Approaching Accurate Description of Molecular Spectroscopies with Multi-reference Electronic Structure Methods

Lixin Lu

A dissertation
submitted in partial fulfillment of the
requirements for the degree of

Doctor of Philosophy

University of Washington

2023

Reading Committee:

Xiaosong Li, Chair

Anne B. McCoy

Munira Khalil

Program Authorized to Offer Degree:

Chemistry

University of Washington

Abstract

Approaching Accurate Description of Molecular Spectroscopies
with Multi-reference Electronic Structure Methods

Lixin Lu

Chair of the Supervisory Committee:
Professor Xiaosong Li
Department of Chemistry

In this dissertation we aim to approach an accurate description of molecular spectroscopy with multi-reference electronic structure methods, for the investigation of real-world problems. Among the challenges that our society is facing now, heavy element chemistry and radiation problems are gaining more attention due to their importance in scientific discovery and technology innovations, requiring a fundamental understanding from the perspective of theoretical chemistry. We start with an introduction of current quantum chemistry approaches, mainly centered on the computation of electronic transitions giving rise to spectroscopic signatures.

The first part of this dissertation focuses on the development on relativistic post-HF electronic structure methods for heavy element spectroscopy. A brief review of relativistic Hamiltonians is given to address the significant work in the field of relativistic electronic structure methods, as well as their linkage and connections, followed by a description of the formalism for the prediction of spectroscopic intensities in the framework of exact-two-component configuration interaction and equation of motion coupled cluster theories. A determinant based Kramers-unrestricted exact-two-component multi-reference second order perturbation theory, which variationally includes relativistic corrections with a perturbative account of dynamic correlation is developed and benchmarked, offering an accurate yet com-

putationally efficient alternative to capture the special relativity and multi-reference nature. The more rigorous four-component multi-reference electronic structure methods including Breit interaction and their benchmark results are presented, representing the most accurate many-body theories before going into the genuine relativistic quantum-electrodynamics theory.

In the second part, we switch gears and focus on the radiation problem — water radiolysis — to explore the origin of reactive species produced by ionizing radiation in aqueous systems. A more complete picture of the ultrafast dynamics and reactive events initiated by photoionization of pure water is provided in an *ab initio* Ehrenfest dynamic study. Stepping beyond outer-valence ionization, the irradiated processes upon ionization of the entire valence band of water is targeted with the first attosecond X-ray pump/X-ray probe transient absorption study in condensed phase, with multi-reference configuration interaction method unraveling the spectroscopic signatures.

TABLE OF CONTENTS

LIST OF FIGURES

GLOSSARY

1PDM: One–particle density matrix

1RDM: One–particle reduced density matrix

2C: 2-component

4C: 4-component

AO: Atomic orbital

BLAS: Basic linear algebra subroutines

BO: Born–Oppenheimer

CAS: Complete active space

CC: Coupled cluster

DC: Dirac-Coulomb

DCB: Dirac-Coulomb-Breit

DCG: Dirac-Coulomb-Gaunt

DFT: Density functional theory

DHF: Dirac Hartree-Fock

EOM: Equation of motion

FCI: Full configuration interaction

GEMM: Matrix–matrix product

GMRES: Generalized minimum residual method

HF: Hartree-Fock

HOMO: Highest Occupied Molecular Orbital

LCAO: Linear combination of atomic orbitals

MCSCF: Multi-configuration self-consistent field

MO: Molecular orbital

MPI: Message passing interface

MRCI: Multi-reference configuration interaction

MRPT2: Multi-reference second-order perturbation theory

RHF: Restricted Hartree-Fock

RAS: Restricted active space

SA: State-Average

SCF: Self-consistent field

SOC: Spin-Orbit Coupling

TDDFT: Time-dependent density functional theory

WFT: Wave-function theory

X2C: Exact two-component

XAS: X-ray absorption spectroscopy

XANES: X-ray absorption near edge structure

ACKNOWLEDGMENTS

Graduate study has been a very important part of my self-exploration journey. COVID has made it difficult, but it gave me enough courage to face the unknown, be curious, read broadly and try new things. My work during PhD is established on top of many brilliant scientists' research. Their books, articles, talks have given me access to their profound understanding and innovative ideas. Moreover, this dissertation will not be done without the supports and help from many people.

The first to thank is my supervisor, Professor Xiaosong Li, who has offered numerous great opportunities to develop my skills and introduced me to various interesting research topics. I appreciate his trust in me to work on different projects which required me to think critically and independently. He has been a strong back bone for my explorations across many different ideas and his challenges helped me gain a lot of growth.

Being involved in IDREAM has been a great experience. Respect from the team greatly help me grow my confidence. Dr. Linda Young is kind and patient in guiding me to understand the experiments and challenging my knowledge. Dr. Carolyn Pearce has been very supportive to my academic development. Dr. Shuai Li and Dr. Emily Nienhuis have been both experimental collaborators and friends, allowing me to ask anything I am curious about in experimental setups and discuss my hypotheses.

I would like to thank everyone with whom I interacted during my time at UW, though COVID has limited our interactions. I appreciate all the help from Dr. Andrew Wildman and Dr. Ryan Beck for my first projects. Many thanks to Hang Hu and Dr. Tianyuan Zhang for their guidance and support for my work in Chronus Quantum. My understanding in theory has grown rapidly through its implementation and discussion with Dr. Andrew

Jenkins, Hang Hu and Dr. Shichao Sun. I thank the rest of the Li group members for challenging me in various topics and strengthen my ability to convey scientific ideas in a cleaner way.

Thanks to Professors Anne McCoy, Munira Khalil and Stephanie Valleau for encouraging me to be confident after my general exam. I appreciate Prof. Anne McCoy for chatting with me which made me feel I am being cared for. I would also like to thank my collaborator Dr. Stefan Knecht for many interesting and helpful discussions via Zoom. Thanks to the great scientists who I have encountered in-person and encouraged me to continue research. I would like to thank my undergraduate supervisors Professors Xin Xu and Igor Ying Zhang for introducing me to Szabo and Ostlund's Modern Quantum Chemistry. Many rules of thumb they told me are still the ones I followed in my research and presentations.

I am fortunate to spend years in Seattle and get to appreciate its mountains, lakes and seas. IMA at UW has given me the peace during the tough times in graduate study.

I am truly grateful to my family for understanding my pursuit and being supportive even though I have not been able to visit them for a long time. Thank you for always letting me choose what I want and what I like without considering too much about other people's comments. Finally, the greatest thank goes to my partner in crime Andrew for everything from the very beginning of the graduate study all the way through now. I have learned a lot from him to start my research. He encouraged me to go through equations when I had doubts in other people or publications. The infinite amount of discussions or even arguments we had about quantum chemistry helped me think deeper and trained my ability to express my ideas better. Thank you for bearing with me when I endlessly talk about research. We have learned a lot more together, in science and in life. It is amazing and fascinating how much beauties we have seen and experienced together, in various interesting theoretical research topics and on top of different peaks. Thank you for putting up with all my frustration through PhD and always encourage me and ensure me that I am doing well.

DEDICATION

to my dear parents, and Andrew

Chapter 1

INTRODUCTION

Out of clutter, find Simplicity.
From discord, find Harmony.
In the middle of difficulty lies Opportunity.
— Albert Einstein

The beautiful and complicated nature of the universe inspires us to question "Why does the observed process happen?" and "How will the process evolve?". Such questions are the driving force of the development of Quantum Chemistry, which aims to deepen our understanding of the fundamental physics behind all the fascinating chemical processes observed in nature, as well as make predictions for their future evolution. The well-known Schrödinger equation has allowed us to describe nature on the atomic and molecular scale in the non-relativistic limit, given in the general form as

$$i\hbar\frac{\partial}{\partial t}|\Psi(t)\rangle = \hat{H}|\Psi(t)\rangle \tag{1.1}$$

where $|\Psi(t)\rangle$ is the wavefunction of the system at time t, and $\hat{H}$ is the Hamiltonian whose form depends on the problem of interest. $\hbar$ is the reduced Planck constant. [6] A combination of quantum mechanics and mathematics has led to the development of theoretical tools and methods to solve Eq. (1.1) properly, and by doing so we can decompose a complicated chemistry problem into the key factors influencing the phenomena we observed. The understanding and advances of the underlying physics are often crucial to cutting-edge innovations and develop solutions to the society's challenges, such as healthcare and medicines, energy crisis and environmental sustainability.

1.1 Modern Quantum Chemistry for Molecular Spectroscopy

Aided by the rapid development of advanced light sources and experimental techniques and methodologies, molecular spectroscopy spanning across different ranges of the electromagnetic field is growing in popularity and impact in a plethora of scientific discoveries. With carefully designed spectroscopic experiments, human beings are able to observe atomic and molecular processes on their natural timescale (as fast as 10^{-18} s). Through the interaction between incident light and the system of interest, molecular rotation and vibration, electronic transitions can be measured, enabling us to study the electronic structure of the system. A wide range of systems from gas-phase to condensed matter can be characterized using spectroscopic techniques. Rich information is encoded in the spectra, many of which cannot be interpreted without computational chemistry and quantum mechanics, especially the spectra from the techniques with increasing complexity. Being highly synergistic, experimental and computational methods together constitute an rather powerful tool in molecular spectroscopy to probe the molecular structures and properties. [7–10]

As the spectra become more and more complicated due to the advanced techniques and the complex processes being probed, better theoretical models that are capable of describing the physical processes and providing accurate predictions are required, which has boosted the development of electronic structure theories for computational spectroscopy. On the other hand, being extremely sensitive to the electronic structure of the system measured, experimental spectra are the best way to verify the reliability and benchmark the accuracy of the theoretical methods. The validated theoretical models can then provide guidance to design experiments based on the predictions of the molecule's electronic structure, properties and chemical reactivity. Readers who are interested in general computational molecular spectroscopy are recommended to Ref. 7 and references therein.

Quantum chemistry has gained a massive growth in the past several decades. [6] Though explicitly solving the Schrödinger equation for real-world problems is still an on-going research topic due to its incredibly high computational cost, modern electronic structure theo-

ries are routinely utilized to describe not only the ground state but also excited states of the molecules based on reasonable approximations to Eq. (1.1), with relatively easy-accessible computing resources. Let us focus on its time-independent form for now:

$$\hat{H}\Psi(\mathbf{r},\mathbf{R}) = E\Psi(\mathbf{r},\mathbf{R}) \tag{1.2}$$

where $\mathbf{r},\mathbf{R}$ are the positions for the electrons and nuclei, respectively, and E contains the energies for the ground state and the excited states corresponding to the chosen Hamiltonian. Firstly, Born–Oppenheimer approximation is introduced to separate the nuclear degree of freedom and electron motions, since the electrons are moving much faster than the nuclei. For a set of nuclear positions, the electronic Schrödinger equation is solved with the nuclei being stationary. If applying the same procedures to other sets of nuclear positions, one can connect the energy solutions and obtain the potential energy surface (PES) as a function of nuclear coordinates. Extensive information can be extracted from PES to study spectroscopic constants, chemistry conformers, chemical reactivity, and further utilized in molecular dynamics. Mean-field theory is another approximation to explore the solutions of the electronic Schrödinger equation, which is implied in the popular Hartree–Fock method and Kohn–Sham (KS) Density Functional Theory (DFT). They effectively reduce the many-body problem to one-body problem and give good predictions for many systems (mainly closed-shell ground state at equilibrium geometry). A single Slater determinant is employed to describe the electronic wavefunction. They are the starting point for many sophisticated many-body electronic structure methods.

The two quantities that are needed to simulate a spectrum are the positions and the relative intensities of the spectral lines. The positions are related to the transitions between the energy levels (rotational, vibrational or electronic transitions). This dissertation will mainly discuss electronic structure methods for computing transitions between different electronic states. To compute the intensity, oscillator strength based upon electric dipole approximation is employed as the electric dipole allowed transitions give rise to the stronger signals

in optical spectroscopies. These two quantities both require the electronic structure method to give accurate description of both the ground and excited states. They are especially important in simulations for the widely-used ultraviolet–visible spectroscopy (UV-Vis) and X-ray absorption/emission spectroscopy, where the sample undergoes electronic transitions upon absorption of the incident light or emission of photons at certain wavelength. UV-Vis spectroscopy probes the valence electrons which are important to study the optical properties, chemical bonding as well as charge-transfer processes. It is routinely used in analytical chemistry for monitoring and characterization. Recent advance in synchrotron and ultrafast light source has led to a renaissance of X-ray techniques. Due to its element specificity and sensitivity to the local electronic and nuclear structure, X-ray spectroscopy has been applied to multiple disciplines including material science and life science.[11] Depending on the energy of the incident X-ray and the electronic structure of the system, one can probe the K-, L- and M-edge. In order to decode the spectra, simulation of core-hole and inner-valence-hole excited states is essential and very challenging.

1.1.1 Excited States Electronic Structure Methods Overview

To describe excited states of large molecules (tens or hundreds of atoms with thousands of basis functions), a main-stream method is linear response (LR) time-dependent density functional theory (TDDFT)[12–15] benefiting from its low scaling. Besides the well-established procedures to study the low-lying excited states, LR-TDDFT has been extended to core-hole excited state region and became a very powerful tool in decoding near-edge X-ray absorption spectroscopy (NEXAS) [16–24] and Resonant Inelastic X-ray Scattering (RIXS)[25].Though DFT captures the dynamic electron correlation through exchange-correlation (XC) functional, its self-interaction error (SIE)[26–29] of electrons posed by the use of an XC functional is a long-standing challenge. In addition, there is not a standard or guidance with regards to the selection of DFT functional, adding in difficulties to the simulation. Nevertheless, the search of new DFT functional is an avid topic and improvements can be expected. [30]

Another group of accurate methods are wavefunction theories (WFT) developed on top

of HF method, *i.e.* post-HF methods. The persistent efforts aiming to approach the exact solution are mainly through: Perturbation theory (PT);[31–35] Configuration interaction (CI);[36] and Coupled-cluster (CC) methods[37, 38].

The usual form of PT used in computational chemistry applications is Møller–Plesset (MP) PT, which improves HF results by adding dynamic correlation on top through Rayleigh–Schrödinger perturbation theory (RS-PT), usually up to 4^{th} order (MP2, MP3 and MP4). CI is the simplest and most straightforward idea to calculate excited states, and its formalism will be introduced in Section 2.2.2. It takes the linear combination of Slater determinants as its wavefunction ansatz. The non-relativistic exact solution of the electronic Schrödinger equation is Full CI at the complete basis set limit, which includes all possible excitations out of the ground state single Slater determinant in the wavefunction expansion. The solutions for the excited states can be obtained at the same time as the ground state when solving the CI problem. Considering the intractable computational cost, it is common to apply truncation on CI expansion (either through truncation of the excitation operators or the truncation of the orbital space – frozen core/virtual orbitals), which will bring in errors, causing it not to be size extensive nor size consistent. There have been several types of size extensivity corrections as discussed and analyzed in Ref. 39. The most widely-used one is Davidson correction [40] and its multi-reference version. For both PT and CI, often used in computational spectroscopy is their multi-reference (MR) extension[41–43], which is the focus of next sub-section. With MRCI being rather computationally expensive, MRPT has been widely used to study spectroscopy for transition metals and more.[44]

Adapting an exponential wavefunction ansatz, CC has desirable properties – size-extensive and size-consistent, making it more favorable for various different areas of physical and chemical problems.[45–47] A series of CC methods from CC singles and doubles (SD) to the often accurate CCSD with noniterative triples CCSD(T) [48, 49], and beyond[50–54], is established with rapid and systematic convergence approaching FCI limit. To obtain the information of electronically excited states, equation-of-motion coupled cluster (EOMCC) is a more explored method and it is size-intensive.[55–57] A brief outline of its formalism is in Section

2.2.3. Similar to CI, the excited states are computed through a diagonalization of the similarity transformed Hamiltonian. If the expansion rank of excitation operators is high enough, EOMCC is expected to approach FCI limit. It is an accurate but relatively computational expensive tools for smaller-sized molecules in spectroscopic simulations.[58–60]

Furthermore, new computational methods for excited states and spectroscopy are emerging every day. As an alternative to TDDFT, the *GW* method and the *GW* plus Bethe-Salpeter equation (*GW*-BSE) method to solve respectively for quasiparticle excitations and optical properties of materials are recently applied to X-ray spectroscopy.[61, 62] A number of methods leverage the sparsity of the wavefunction in order to approach FCI limit, including Full Configuration Interaction Quantum Monte Carlo (FCIQMC) algorithm; [63–65] or by selecting the important electronic configurations on the fly, grouped as selected CI methods;[66–72] or the density matrix renormalization group (DMRG) method[73–77]. Of course there are various other methods in the field and there will be more to come.

1.1.2 Multireference Electronic Structure

The discrepancy between HF and FCI results was defined by Löwdin[6, 78] as electron correlation in a complete basis set. Traditionally, the electron correlation is divided into two categories – static and dynamic correlation. [79] There is not a well-defined separation of the two and there are various terminologies in the literature but the idea does not differ much. Static correlation is related to (near-)degeneracy. For a state of interest, multiple configurations have significant contributions to its wavefunction due to orbital degeneracy, *i.e.*, mathematically, the coefficients of all these configurations are relatively large and non-negligible. Meanwhile, multiple states are very close in energy if not the same. Dynamic correlation mainly is short-ranged, involving a large amount of configurations with small individual contributions. This separation has inspired the development of theories and methods exploiting specilized treatment for each category of electron correlation.

Both Kohn-Sham (KS) DFT and single-reference correlated methods such as MP2, CCSD and CISD are capable of recovering a large amount of dynamic correlation. However, these

well-developed single-configuration (or single Slater determinant) methods break down and have shown their defects when describing chemical systems with a geometry away from equilibrium, open-shell and electronic excited states. The fact that the wavefunction contains more than one dominant determinant/configuration led to the development of multireference (MR) approach. In the past several decades, multi-configuration self-consistent-field (MCSCF) has become a standard treatment for static correlation and is often used to capture the quantitatively correct picture of chemical reaction path, as it has the flexibility in both its wavefunction and orbital optimization to include the electron correlation effects among valence electrons arising from processes such as bond-breaking and avoided-crossing. This additional flexibility allows the wavefunction to describe different regions of the potential energy surfaces on an equal footing and enable the molecular orbital basis to simultaneously describe multiple electronic states of interest. [43, 80–83]

One way to include the important configurations is complete-active-space self-consistent-field (CASSCF)[84–88]. By *a priori* selecting an active space including the orbitals important to the chemical problem, all possible configurations constructed through a "FCI-type" expansion within this space compose the basis of the wavefunction. The wavefunction coefficients (CI coefficients) and the orbital coefficients (MO coefficients) are optimized iteratively based on variational theorem. However, it is well known that the dynamic correlation is missing due to the limited active space. To account for all the small contributions from the configurations external to the selected active space, similar routes to the single-configuration correlated methods are taken: MRPT,[89] MRCI,[43] MRCC,[90, 91] and their variants. The orbital basis and reference wavefunctions have considered the static correlation, and then the dynamic correlation is added on top, *i.e.* "static then dynamic". Note that this is equivalent to a partitioning of the FCI space into model space **P** (for static correlation treatment) and external space **Q** (for dynamic correlation treatment) in literature.

As the cheapest MR approach out of the three, MRPT is still costly for systems with larger size. The quite accurate yet low cost KS-DFT triggers the exploration of combining it with static correlation treatment, leading to long-/short-range separated Multiconfigura-

tion DFT[92, 93], Multiconfiguration Pair-Density Functional Theory (MC-PDFT)[94, 95], DFT/MRCI[96] and others. Nevertheless, the selection of active space is not trivial, and concerns arise with regards to "static then dynamic" scheme, since the static correlation obtained is only based on a limited-size orbital space. There is a need to relax the orbitals in the presence of dynamic correlation. For example, Liu *et al*[97, 98] promoted the "static-dynamic-static" (SDS) family of methods. A variety of emerging approaches for strongly correlated systems are important complementary to the current available treatment for static correlation and significant contributions to advancing the field, which are not covered in this introduction.

1.1.3 Dynamics Simulation and Time-resolved Spectroscopy

In experimental spectroscopy, time-resolved spectroscopy serves as a monitor of the dynamic chemical process of interest, which will take "snapshots" at a certain time interval. One often used technique is transient-absorption spectroscopy, involving a pump and a probe pulse.[99] In the absence of the pump pulse, most species are in their ground state, a spectrum will be measured using the probe pulse at $t < 0$. The pump pulse creates a high population in an excited state (photoexcitation or photoionization) at $t = 0$, and the probe pulse will probe the real-time status of the sample at a time delay Δt. The difference in the spectra at $t < 0$ and $t = \Delta t$ with regards to wavelength generates the delta absorption spectrum, showing the evolution of the excited state. The time delay is tunable depending on the problem at hand. The pump-probe technique is powerful in studying excited state dynamics and possible decay pathways, especially photochemistry.

One desire that many theorists have is to simulate the dynamic physico-chemical processes. There has been a lot of efforts in the development of molecular dynamics (MD) and quantum dynamics. Since the method development is not the focus of this dissertation, it will not be reviewed here. However, it will be worth listing some background for the dynamics simulations in Chapter 5. The genuine dynamics can be derived from the fully coupled electron-nuclei Schrödinger equation. Some efforts are the nuclear-electronic orbital (NEO)

method[100, 101], with specific nuclei being treated on the same level of the electron.

Upon Born–Oppenheimer approximation, the electronic part and nuclear part can be decoupled and treated in separate procedures. The pure electron dynamics is simulated by solving the electronic part of the time-dependent Schrödinger equation (TDSE). Reviews of real-time electronic structure methods can be found in Ref.102 and 103. Though explicitly propagating correlated wavefunctions is rather expensive, it offers the opportunities to study the ultrafast electron dynamics at attosecond to several femtosecond time-scale, where electron correlation dominates.[104]. However, going beyond several femtosecond, nuclear motion is no-longer negligible.

Nuclear dynamics has a wide range of methods varying from numerically exact quantum (path-integral[105] or wave packet propagation[106]) dynamics to approximate but robust fully classical MD, with a flexibility to choose the suitable treatment for electrons, either implicitly (force-field) or explicitly (electronic structure methods). Semi-classical quantum dynamics including surface hopping,[107, 108] Ehrenfest dynamics[109, 110] and multiple-spawning dynamics[111, 112] has filled the gap between the two end. The effects of nuclear motion may disrupt the electronic coherence — decoherence.[113]

The combination of dynamics simulation and time-resolved spectroscopy can decode the ultrafast physico-chemical pathways of excited-state species, and further offer the opportunities to tailor the properties of new materials, prepare new states of matter inaccessible by natural pathways and control the non-equilibrium quantum many-body physics in materials.

1.2 Radiation Problem and Our Curiosity

Among the challenges that our society is facing now, one may not immediately realize the radiation problem and the damage it is causing, which is one of the problem that scientists are working on to gain better understanding. Radiation is the energy emitted by large unstable atoms in order to get rid of the excess energy to become stable, which is more common for elements further down the periodic table, *i.e.* they are highly radioactive. The excess energy can be either in the form of electromagnetic waves (such as sunlight, X-rays, γ-rays,

radar, radio waves), or particles (such as α-particles, neutrons). They will then interact with matter in the environment — the so-called radiation-matter interaction. Radiation is more common than we thought and has significant impact in many fields ranging from daily communication devices and infrastructure, cancer therapies, space travel, to nuclear energy.[114, 115] Heavy elements are becoming more important in frontier materials science as the key components in catalysts, clean energy solar cells,[116–119] quantum information and quantum computing.[120] The wider use of heavy elements also raises serious concerns about the operational safety in industry and nuclear power plants, as well as environmental remediation of legacy nuclear waste and biological damages. Washington state locates the US Department of Energy largest legacy site — the Hanford Site.[121–123] It occupies 586 square miles and there are 56 million gallons of radioactive and chemically hazardous waste in 177 underground storage tanks. Its environmental cleanup project is the work that about 10,000 Hanford workers are involved in today.

Here presents two parts of the radiation problem that this dissertation concerns about: (1) **Heavy element chemistry and characterization**: The much stronger relativistic effects presented in heavy element chemistry, and their more complicated electronic structure give rise to their special properties and potentials in new science and technologies, but pose great challenge to the well-established non-relativistic chemistry. (2) **Radiation-induced chemical processes in complex environment**: High-energy irradiation can ionize and electronically excite target atoms and molecules. The resulting excited states undergo complex relaxation and energy transfer processes at ultrashort timescale that trigger chemical processes within complex energetic landscapes at a longer timescale. Ultimately, the chemistry is driven far from equilibrium, resulting in failure in traditional understanding and models. A fundamental understanding is vital for not only realistic technological and environmental problems, but also our curiosity in nature.

Spectroscopic techniques are powerful probes in both problems as they are capable of not only detecting the structures, chemical bonding and oxidation states, and the electromagnetic properties, but also tracking their changes in a chemical process to investigate the

mechanisms. As stated previously for computational molecular spectroscopy, the theoretical models and computational methods for accurate description and prediction are required.

1.3 Author's Views

As a discipline to provide insights for the physico-chemical processes in nature, and guidance to experimental design and technology innovation, quantum chemistry has become indispensable. Meanwhile, its complexity is growing rapidly and the range of problems it can handle is expanding. Just as all other subjects:

> *Physics is becoming so unbelievably complex that it is taking longer and longer to train a physicist. It is taking so long, in fact, to train a physicist to the place where he understands the nature of physical problems that he is already too old to solve them. — Eugene Wigner*

There are some superficial opinions here for myself in the future, when terrified by the tremendous unknown, to not be panicked.

Good method or bad method?

Centered at solving the Schrödinger equation, a universally applicable model for all does not seem practical, as the underlying physics varies from problem to problem. Indeed, a specific model for specific physics is currently more accepted, leading to a collection of computational methods. A key prerequisite is a thorough understanding of the capability and limitation of the method, in order to utilize it for the correct physics. Some examples are: solvation model is developed to study the chemistry of solutions; classical molecular dynamics provided satisfying prediction to long timescale evolution for proteins. Nevertheless, in exploring the scope of one method, careful analysis should be performed to rule out the possibility of error cancellation, which may cover the true physics. Therefore, the question of whether a method is good or not, becomes whether the chosen method has properly addressed the physics of the problem.

Simplification rather than complication

Allowing non-universal methods does not suggest to complicate quantum chemistry. On the contrary, simplification is the goal. Throughout history, the driving force for creation and inventions is more or less the pursuit of simplifying processes and make our life easier. In quantum chemistry, it is likely to have over-complicated interpretation of the physics, over-complicated computation procedures, and over-complicated codes. Upon simplifying the real-world problem, non-universal methods serve as a factor identifier, to help identify the key physical factor behind the phenomena. What is more, simplified information should be extracted from the usually large amount of data. For example, the computation using genuine relativistic electronic structure methods are notoriously high, while indeed not every system we study requires complete relativistic treatment. The popularity of spin-free relativistic Hamiltonians utilized in systems without strong spin-orbit coupling effects has shown that the development of not so universal methods are indeed helping us simplify the problems.

How accurate is accurate?

Often chemical accuracy (1 kcal/mol) is the goal, while it may be insufficient in some cases, such as in high-resolution spectroscopy and hyperfine structure. It sometimes requires sub-millielectronvolt accuracy for the correct physics. In contrary, in some other scenarios, achieving chemical accuracy only results in extra efforts in computation and time, without altering the physical picture. While high-performance computing resources are becoming more available, affordability should still be one of the factor to be considered in research. Rather than pursuing absolute accuracy, the goal is to provide physical understanding and predictions, with the accuracy being defined by the scale of the chemical phenomena of interest.

In this dissertation, special relativity is considered and combined with high-level electronic structure methods, in order to gain better understanding of the key physics (such as spin-orbit coupling) in heavy element chemistry, to help answer the questions concerning their chemical bonding and spectroscopic properties. However, relativistic methods are not employed in the second part for water radiolysis as it is considered not to be significant in light elements.

New physics drives the method development

Ideally, we hope to find the right method capable of explaining and reproducing what we observed. It may sometimes be a series of trial and error, or sometimes require multiple methods for various aspects of the same problem. If it cannot be answered by any current methods, new physics appears and will drive the development of new models in quantum chemistry. Jumping out of the comfort zone and absorbing knowledge from other fields is necessary for prolonged scientific discovery.

1.4 Outline

Part I includes Chapter 2 to Chapter 4, which focus on development on relativistic post-HF electronic structure methods for heavy element spectroscopy. Chapter 2 starts with a brief review about relativistic Hamiltonians with an aim to give readers an idea about the purpose and the significant work in the field of relativistic electronic structure methods, as well as their linkage and connections. It also includes the documentation of the formalism for oscillator strengths in the framework of two-component configuration interaction and equation of motion coupled cluster theories. Chapter 3 has detailed the formalism and benchmark results of two-component multireference second-order perturbation theory. The more rigorous four-component multireference electronic structure methods including Breit interaction and their benchmark results are presented in Chapter 4, representing the most accurate many-body theories before going into the genuine relativistic quantum-electrodynamics theory.

Then, we switch gear and focus on the other part of the radiation problems — water radiolysis — to explore the origin of reactive species produced by ionizing radiation in aqueous systems. In Chapter 5, a more complete description of the ultrafast dynamics and reactive events initiated by photoionization of pure water is provided in an *ab initio* Ehrenfest dynamic study. In Chapter 6, the irradiated processes upon ionization of the entire valence band of water is targeted with the first attosecond x-ray pump/x-ray probe transient absorption study in condensed phase, with multireference configuration interaction method unraveling the underlying physics of the spectroscopic signatures.

Finally, it concludes with outlook including a brief introduction about a new parallel

implementation of relativistic configuration interaction for advanced computing architectures to extend its capability, as well as remaining challenges in quantum chemistry for real physics and chemistry problems.

Notes on previous published work:

Chapter 3 is adapted with permission from Lixin Lu, Hang Hu, Andrew J. Jenkins, and Xiaosong Li. "Exact-Two-Component Relativistic Multireference Second-Order Perturbation Theory". Journal of Chemical Theory and Computation. 2022, 18 (5), 2983-2992. DOI: 10.1021/acs.jctc.2c00171. Copyright 2022 American Chemical Society.

Chapter 4 is adapted with permission from Chad E. Hoyer, Lixin Lu, Hang Hu, Kirill D. Shumilov, Shichao Sun, Stefan Knecht, Xiaosong Li. "Correlated Dirac–Coulomb–Breit multiconfigurational self-consistent-field methods". J. Chem. Phys. 28 January 2023; 158 (4): 044101. DOI: 10.1063/5.0133741.

Chapter 5 is adapted with permission from Lixin Lu, Andrew Wildman, Andrew J. Jenkins, Linda Young, Aurora E. Clark, and Xiaosong Li. "The "Hole" Story in Ionized Water from the Perspective of Ehrenfest Dynamics". The Journal of Physical Chemistry Letters. 2020, 11 (22), 9946-9951. DOI: 10.1021/acs.jpclett.0c02987. Copyright 2020 American Chemical Society.

Chapter 2

PART I: ELECTRONIC STRUCTURE METHODS FOR HEAVY ELEMENT SPECTROSCOPY

Better understanding of the electronic properties of transition metals and late-row ($\geq$ fourth) elements in the periodic table and their molecular complexes requires an adequate description of both electron correlations and relativistic effects, which presents a challenge to modern electronic structure theory. The two significant relativistic effects are 1) **scalar relativity** – orbitals closer to the nucleus experience a contraction of the radial densities (s and p orbitals); resulting in a stronger shielding effects of the nuclear charge on electrons further apart and therefore experience expansion (d and f orbitals), 2) **spin-orbit coupling (SOC)** – it causes shifts of the energy levels and can be observed in the fine structure splittings in spectral lines.

For heavy-element systems, more valence electrons being unpaired is common, since usually the d or f shell are the valence shells. Additionally, more electrons (valence/inner-valence electrons) have to be included in high-level electronic structure calculations to recover major dynamic correlation. More importantly, their relativistic effects are no longer negligible [124–126] due to the high speed of electrons in the vicinity of heavy nuclei. Although the perturbative treatment of SOC and dynamic correlation is justified for systems including light and medium elements [4], it appears to be insufficient when molecular orbitals (MO) undergo significant mixing or alteration due to strong SOC, as the description of MO is essential to understand chemical bondings in nature. Correlated electronic structure methods that include relativistic effects at the MO level are therefore vigorous and valuable in the field.[127–136] For accurate descriptions of excited states of heavy-element systems to evaluate accurate spectra, high-level wave-function based methods with robust relativistic Hamil-

tonian are required. The following three chapters will focus on relativistic multi-reference electronic structure methods. This Chapter will first present an overview of the relativistic Hamiltonian used throughout Part I of this thesis, followed by a discussion of the exact-two-component (X2C) formalism utlized to compute positions and intensities of spectral lines using Equation-of-Motion Coupled-Cluster (EOMCC) and Configuration Interaction (CI), respectively.

2.1 Relativistic Hamiltonian Overview

Besides molecular electronic structure methods and basis sets, which are the two aspects of theoretical model chemistries introduced by Pople[1, 2], relativistic Hamiltonian has become the third dimension in the combinations of theoretical and computational chemistry[3] and has been getting more and more attention over the past few decades. Other than the single choice of Schrödinger Hamiltonian in the non-relativistic regime, it appears that there are various flavors of Hamiltonians depending on the degree of approximations and the relativistic effects involved. There is no doubt that relativistic calculations will be costly as the spin and spatial symmetries are reduced in the presence of electromagnetic coupling. Hence, theoretical chemists strive for seeking the sweet spots between efficiency and accuracy for the systems of interest. Readers who prefer to get a complete picture of the relativistic domain of theoretical chemistry are referred to more comprehensive textbooks such as Ref. 137 and 138, as well as many other complementary journal articles. Unless otherwise stated, atomic units are employed from now on.

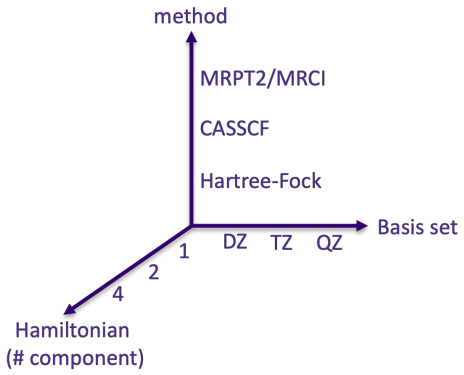

Figure 2.1: Relativity and the theoretical model chemistries introduced by Pople[1–3].

The structure of electronic structure approaches within the Born-Oppenheimer approximation, especially the WFT-based ones, remains essentially the same in a relativistic for-

malism as the non-relativistic counterpart. The general form can be written as

$$\hat{H}|\Psi(t)\rangle = i\partial_t|\Psi(t)\rangle \tag{2.1}$$

$$\hat{H} = V_{NN} + \sum_i \hat{h}(i) + \frac{1}{2}\sum_{i\neq j}\hat{g}(i,j) \tag{2.2}$$

where $|\psi(t)\rangle$ is the time-dependent electronic wavefunction and V_{NN} is the classical repulsion potential of clamped nuclei, evaluated with finite width nuclei assuming a gaussian charge distribution of the nuclei. $\hat{h}(i)$, $\hat{g}(i,j)$ are the one- and two-electron operators and i,j stand for different orbitals.

The second-quantized form is

$$\hat{h} = \sum_{pq} a_p^\dagger a_q (p|h|q) \tag{2.3}$$

$$\hat{g} = \sum_{pqrs} a_p^\dagger a_r^\dagger a_s a_q (pq|rs) \tag{2.4}$$

$$(p|h|q) = \int d\boldsymbol{r_1}\phi_p^*(\boldsymbol{r_1})\hat{h}(\boldsymbol{r_1})\phi_q(\boldsymbol{r_1}) \tag{2.5}$$

$$(pq|rs) = \int d\boldsymbol{r_1}d\boldsymbol{r_2}\phi_p^*(\boldsymbol{r_1})\phi_q(\boldsymbol{r_1})\hat{g}(\boldsymbol{r_1},\boldsymbol{r_2})\phi_r^*(\boldsymbol{r_2})\phi_s(\boldsymbol{r_2}) \tag{2.6}$$

where $|\phi\rangle$ is the set of spatial orbitals/spinors. Their exact forms determine whether Eq. (2.2) is non-relativistic or relativistic, and further for the latter whether it is two-component (2C) or four-component (4C) formalism [3]. $a^\dagger$ and a represent creation and annihilation operators, respectively. Similar to non-relativistic scenario, we will focus on the time-independent form of the equation.

2.1.1 One-Electron Dirac Equation

In 1928, Dirac introduced the famous Dirac equation [139], aiming at a treatment of time and spacial coordinates on an equal footing to ensure Lorentz covariance, which was later found to hold for fermions with a spin of $\frac{1}{2}$ in general. The Dirac Hamiltonian for an electron

in a molecular field

$$\hat{H}_D = c\boldsymbol{\alpha} \cdot \boldsymbol{p} + \boldsymbol{\beta} mc^2 + V_{NN} \tag{2.7}$$

where $\boldsymbol{p} = -i\nabla$ is the momentum operator, and $\boldsymbol{\alpha}$ and $\boldsymbol{\beta}$ are 4×4 Dirac matrices:

$$\boldsymbol{\alpha} = \begin{pmatrix} \mathbf{0}_2 & \boldsymbol{\sigma}_J \\ \boldsymbol{\sigma}_J & \mathbf{0}_2 \end{pmatrix}, \quad J = \{x, y, z\}, \quad \boldsymbol{\beta} = \begin{pmatrix} \boldsymbol{I_2} & \mathbf{0} \\ \mathbf{0} & -\boldsymbol{I_2} \end{pmatrix} \tag{2.8}$$

and $\boldsymbol{\sigma}$ is a vector of Pauli matrices

$$\boldsymbol{\sigma_x} = \begin{pmatrix} 0 & 1 \\ 1 & 0 \end{pmatrix}, \quad \boldsymbol{\sigma_y} = \begin{pmatrix} 0 & -i \\ i & 0 \end{pmatrix}, \quad \boldsymbol{\sigma_z} = \begin{pmatrix} 1 & 0 \\ 0 & -1 \end{pmatrix}. \tag{2.9}$$

Eq. (2.7) leads to an energy spectrum with two parts of the solutions separated by an energy gap of $2mc^2$, which are referred to as negative and positive energy solutions. The four-component Dirac equation can be re-scaled to align with the non-relativistic energy scales by shifting $\boldsymbol{\beta}$ to $\boldsymbol{\beta'} = \boldsymbol{\beta} - \boldsymbol{I_4}$ (Fig. 2.2).

As particles at rest have mc^2, they have positive energy. The "Dirac Sea" was proposed by Dirac to solve the nonphysical dilemma of electrons being de-excited into negative energy levels and emit photons. All the negative-energy levels were hypothesized to be occupied and a "hole" in the Dirac sea was the antimatter counterpart of the electron – the positron, which was later discovered in experiment [140]. It was later better understood in the framework of the rigorous quantum electrodynamics (QED) [124, 125, 141–144].

2.1.2 Two-Electron Interaction

So far, a relativistic free particle in a static potential can be well described by the Dirac equation. In most chemistry problems, the existence of many electrons in the systems requires the many-body interaction to be taken into account. A proper Lorentz-invariant electron-electron interaction can be derived in QED framework from perturbation theory via the

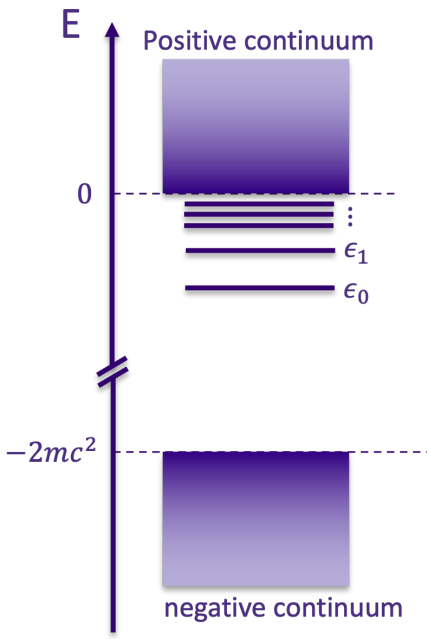

Figure 2.2: Energy spectrum from Dirac Hamiltonian.

exchange of "virtual" photons, considering the fact that the interaction is not instantaneous but there is retardation due to its propagation at the speed of light.[145] As Kenneth Dyall and Knut Fægri discussed in their book, the retardation correction has a relatively small magnitude in the chemical problems of general interest, leading to the approximation of using the frequency-independent terms in the two-electron operators.

Here we revisit the relativistic four-component two-electron operators that will be discussed throughout the rest of the work. The frequency-independent Dirac-Coulomb-Breit operator describes the instantaneous two-electron interaction in the Coulomb gauge, which can be written as

$$V_{ee}^{\mathrm{DCB}} = \sum_{i=1}^{N} \sum_{j>i} (g^C(i,j) + g^B(i,j)) \tag{2.10}$$

$$g^C(i,j) = \frac{1}{r_{ij}} \tag{2.11}$$

$$g^B(i,j) = -\frac{1}{2}\left(\frac{\boldsymbol{\alpha}_i \cdot \boldsymbol{\alpha}_j}{r_{ij}} + \frac{\boldsymbol{\alpha}_i \cdot \mathbf{r}_{ij} \boldsymbol{\alpha}_j \cdot \mathbf{r}_{ij}}{r_{ij}^3} \right) \tag{2.12}$$

where $\{i, j\}$ are electron indices, $\boldsymbol{\alpha}$ is defined in Eq. (2.8) and Eq. (2.9).

While the Coulomb gauge is usually preferred in calculations, a lower cost operator that still carries the magnetic interaction is the Dirac-Coulomb-Gaunt Hamiltonian defined in Feynman gauge:

$$V_{ee}^{\mathrm{DCG}} = \sum_{i=1}^{N} \sum_{j>i} (g^C(i,j) + g^G(i,j)) \tag{2.13}$$

$$g^G(i,j) = -\frac{\boldsymbol{\alpha}_i \cdot \boldsymbol{\alpha}_j}{r_{ij}} \tag{2.14}$$

A more widely-used relativistic four-component Hamiltonian is the one only involves the Dirac-Coulomb operator to account for the leading two-electron interaction.

$$V_{ee}^{\mathrm{DC}} = \sum_{i=1}^{N} \sum_{j>i} g^C(i,j) \tag{2.15}$$

The Dirac Hamiltonian $\hat{H}_D$ (Eq. (2.7)) and the proper choice of the two-electron operators introduced above constitute the four-component Hamiltonian. Although truncation is applied in the fully retarded two-electron operators, Eq. (2.15), Eq. (2.13) and Eq. (2.10) are sufficient to describe the chemical problems upon cautious consideration with regards to which one to use. Eq. (2.15) has the same form as the Coulomb interaction in the non-relativistic domain, but it includes **spin-own orbit coupling** in the underlying physics in four-component framework. By computing the full Breit operator (Eq. (2.12)), **spin-other orbit interaction**, **spin-spin interaction** and **orbit-orbit interaction** are added to the Dirac-Coulomb operator.[3] In theory, both the Coulomb, Gaunt and the Breit terms arise from the same fully retarded interaction in the zero frequency limit, and therefore, they should be treated on a equal footing, unless their difference is negligible for the problem of interest.

2.1.3 Dirac-Hartree-Fock Equation

Once the one- and two-electron part of the Hamiltonian is defined, they can be applied to the well-developed electronic structure approaches with the integrals in Eq. (2.5) and Eq. (2.6) evaluated. First, a Slater determinant with proper atomic-centered basis sets has to be construct for evaluating the expectation value of the Hamiltonian (Eq. (2.16)). Eq. (2.7) indicates the need of describing the wavefunction in a four-spinor form as Eq. (2.17).

$$E = \langle \Psi | \hat{H} | \Psi \rangle, \tag{2.16}$$

$$\phi_p = \begin{pmatrix} \phi_p^L \\ \phi_p^S \end{pmatrix} = \begin{pmatrix} \phi_p^{L\alpha} \\ \phi_p^{L\beta} \\ \phi_p^{S\alpha} \\ \phi_p^{S\beta} \end{pmatrix} = \begin{pmatrix} \sum_\mu c_{p\mu}^{L\alpha} \chi_\mu^L \\ \sum_\mu c_{p\mu}^{L\beta} \chi_\mu^L \\ \sum_\mu c_{p\mu}^{S\alpha} \chi_\mu^S \\ \sum_\mu c_{p\mu}^{S\beta} \chi_\mu^S \end{pmatrix} \tag{2.17}$$

ϕ_p^L and ϕ_p^S are the large and small component of the molecular spinor ϕ_p represented in two-spinor basis $\begin{pmatrix} \chi^\alpha \\ \chi^\beta \end{pmatrix}$, respectively and χ denotes the same spatial basis functions used for α and β parts to reduce the computational cost. The matrix form of Dirac-Hartree-Fock becomes

$$\begin{pmatrix} V & c(\boldsymbol{\sigma} \cdot \boldsymbol{p}) \\ c(\boldsymbol{\sigma} \cdot \boldsymbol{p}) & V - 2mc^2 \end{pmatrix} \begin{pmatrix} \Psi^L \\ \Psi^S \end{pmatrix} = E \begin{pmatrix} \Psi^L \\ \Psi^S \end{pmatrix} \tag{2.18}$$

To connect the concepts here, the positive energy solutions have the larger amplitudes for the large component and negative solutions have the larger amplitudes for the small component.

In non-relativistic framework, one will solve Hartree-Fock equation based on variational theorem and utilize minimization principle to find the lowest energy and determine the molecular spinors, i.e. the so-called orbitals. However, there are several aspects that are different when including special relativity. The DHF solutions are not bound due to the existence of the negative-energy solutions, causing variational collapse. The coupling between

the large and small components should be taken into account when constructing finite basis sets (χ^L and χ^S), whose exact form can be derived from Eq. (2.18). To ensure the correct relationship between large and small finite basis functions at the non-relativistic limit and prevent the variational collapse, *restricted kinetic balance* (RKB) conditions[146, 147] is used to define the relationship between χ^L and χ^S:

$$\chi^S = \frac{1}{2mc}(\boldsymbol{\sigma} \cdot \boldsymbol{p})\chi^L \tag{2.19}$$

Readers can refer to Ref. 148 for a detailed discussion of different types of kinetic balance.

Going into a many-electron model has problems such as Brown-Ravenhall disease [149] (continuum dissolution), to which the solution requires the QED reinterpretation. Take a two-electron system as an example, a true ground state will be the electrons occupied the two lowest spinors with positive energies. However, from relativistic Dirac equation, there exists infinite number of degenerate states where one electron is in the positive continuum while the other is in the negative continuum, resulting in the same total energy. Therefore, the eigenvalue problem using relativistic Hamiltonians has to be solved with caution to avoid contamination from the spinors of the negative continuum. To employ the variational theorem to solve the many-electron eigenvalue problem, Sucher[150] suggested to project the Hamiltonian onto the positive-energy only space — so-called "no-pair" approximation so that it is bounded from below. In fact, the projectors being introduced have to be carefully chosen. A Hartree-Fock based projector was suggested by Mittleman[151]. Rather than using the Aufbau principle to select the bound orbitals for the mean-field potential, i.e. starting from the orbitals with lowest energy, a common way in modern relativistic quantum chemistry computations is to start from the spinor with lowest positive energy. Similar to the SCF procedures in HF, every iteration in solving DHF equation updates the projector. Furthermore, it implies the min-max principle employed in the variational DHF equation,[152, 153] Instead of the minimization principle in the non-relativistic domain, the minimization is applied to the positive-energy solutions, while the negative-energy solution

is maximized. In short, the wavefunction is spanned on a space of Slater determinants with negative-energy spinors treated as frozen, while in the SCF step, negative-energy spinors are a part of the orthogonal spinor basis to be optimized .This procedure in SCF is also important for later MCSCF steps as shown in Chapter 4.

Another aspect is that the spinors and the wavefunction are complex quantities, with complex algebra involved in all operator manipulations in computation, although scalar basis functions are employed. The dimensions of matrices are larger. Along with the loss of spin symmetry is the loss of permutation symmetry of two-electron integrals. A good quantum number for DHF is the total angular momentum, which couples the orbital angular momentum and spin angular momentum, and the z component of the total angular momentum.

As mentioned in the section for two-electron interaction, it is rigorous to include the full Breit operator in calculations. However, the gauge term in the Breit operator arising from the gauge transformation from the Feynman gauge to the Coulomb gauge is the most computational intensive, which hinders its wider applications in correlated many-body calculations. Recent development of the optimal integral–density contraction scheme[154] in the Pauli spinor representation enables the efficient evaluation of Dirac-Coulomb-Breit operator and opens up further exploration of rigorous relativistic multireference electron correlation methods with DCB Hamiltonian, which will be discussed in detail in Chapter 4.

2.1.4 Two-Component Simplification

There have been many years of effort in exploring different efficient algorithms to make four-component calculations become more affordable. These efforts include density fitting [155–158], integral screening [159], symmetry schemes [160] and more [161, 162]. The computational costs of relativistic calculations are still inevitably high. As chemists only care about the positive-energy solutions, it is natural to seek for methods to reduce the problem dimension to two-component, which only involve positive-energy spinors and can still give us the same positive-energy spectrum. Two commonly used approaches are pseudopoten-

tial and all-electron methods. The latter group gives us the flexibility to manipulate core electrons and study core-valence interaction, which are better suited for spectroscopic study involving core regime, such as those employ X-ray.

A natural approach to reduce four-component to two-component formalism is to look for a unitary transformation U to decouple the large and small components, as proposed by Foldy and Wouthuysen[163] and there exist many different flavors of approximate two-component methods[3]. The idea is equivalent to the elimination of the small component, which involves the exact coupling of the large and small components in the transformation[164]. One of the most popular two-component Hamiltonians is the second-order Douglas-Kroll-Hess (DKH)[165, 166] Hamiltonian. A free-particle Foldy-Wouthuysen (FW) transformation is first applied to the Dirac Hamiltonian, followed by further decoupling through a series of unitary transformations in the orders of the external potential V. DKH extension to Higher and even arbitrary order is available.[167–171]. With a different approximation to the exact coupling, zero-order Regular Approximation (ZORA) Hamitonian [172–174] is another widely used approximation, especially in DFT methods. Many well-established quantum chemistry software packages utilize the spin-free forms of these Hamiltonian as they can be easily implemented in the existing non-relativistic codes with real-value algebra. However, the need of including scalar-relativity and spin-orbit coupling on equal footing is increasing in recent years as the rapid development in heavy element chemistry and potential applications in material science and drug discovery.

Among various two-component methods, we adapt the exact-two-component (X2C)[3, 129, 164, 175–188] transformation in all following relativistic two-component method developments. As its name indicated, its formalism is developed to reproduce exactly the positive-energy spectrum of the one-electron part of the parent four-component Dirac Hamiltonian. This one-step transformation scheme is pioneered by Dyall[164]. It greatly benefits from the fact that solving the one-electron Dirac Hamiltonian is inexpensive while giving useful information in the exact coupling of the large and small components. In handling the decoupling transformation, matrix representation and linear algebra alleviate the complication from the

analytical evaluation of integrals. The formalism is reviewed below.

The restricted-kinetic-balanced Dirac equation in spinor basis can be represented in a matrix form as:[137]

$$\begin{pmatrix} \mathbf{V} & \mathbf{T} \\ \mathbf{T} & \frac{1}{4c^2}\mathbf{W} - \mathbf{T} \end{pmatrix} \begin{pmatrix} \mathbf{C}_L^+ & \mathbf{C}_L^- \\ \mathbf{C}_S^+ & \mathbf{C}_S^- \end{pmatrix} = \begin{pmatrix} \mathbf{S} & \mathbf{0}_2 \\ \mathbf{0}_2 & \frac{1}{2c^2}\mathbf{T} \end{pmatrix} \begin{pmatrix} \mathbf{C}_L^+ & \mathbf{C}_L^- \\ \mathbf{C}_S^+ & \mathbf{C}_S^- \end{pmatrix} \begin{pmatrix} \boldsymbol{\epsilon}^+ & \mathbf{0} \\ \mathbf{0} & \boldsymbol{\epsilon}^- \end{pmatrix} \tag{2.20}$$

where c is the speed of light. $\mathbf{V}$, $\mathbf{T}$, and $\mathbf{S}$ are the two-component non-relativistic potential energy, kinetic energy, and overlap matrices, respectively. $\mathbf{W}$ is the relativistic potential matrix, defined as $(\vec{\sigma}\cdot\vec{p})\,\mathbf{V}(\vec{\sigma}\cdot\vec{p})$, where $\vec{p}$ is the linear momentum operator and $\vec{\sigma}$ contains Pauli spin matrices. $\{\epsilon^+\}$, $\{\epsilon^-\}$ are the sets of positive/negative eigenvalues with corresponding molecular orbital coefficients $(\mathbf{C}_L^+ \quad \mathbf{C}_S^+)^T$ for the positive and $(\mathbf{C}_L^- \quad \mathbf{C}_S^-)^T$ for the negative energy solutions. Noted that RKB condition is employed here for the small components' basis set.

The positive-energy part for electrons of Eq. (2.20) is

$$\hat{H}^+\mathbf{C}^+ = \mathbf{S}\mathbf{C}^+\epsilon^+ \tag{2.21}$$

with eigenvalues the same as the positive-energy solutions of Eq. (2.20) if exact decoupling is applied in the transformation. The exact decoupling is determined by the solutions (i.e. eigenvectors) of Eq. (2.20) in their matrix representation, and then used in the construction of the unitary transformation matrix $\boldsymbol{U}$. The four-component Hamiltonian is then block-diagonalized by $\boldsymbol{U}$ in order to decouple the large and small components:

$$\boldsymbol{U}^\dagger\,\hat{H}_{4C}\,\boldsymbol{U} = \begin{pmatrix} \hat{H}^+ & \mathbf{0}_2 \\ \mathbf{0}_2 & \hat{H}^- \end{pmatrix} \tag{2.22}$$

where $\hat{H}^+$ and $\hat{H}^-$ are the two-component Hamiltonians corresponding to the positive and negative energy solutions. A more detailed derivation and implementation can be found in

Ref. 182.

An uncontracted basis (i.e. primitive functions) is necessary for calculating all the matrices needed to evaluate the two-component Hamiltonian for electrons. This is also a requirement for four-component calculations because for a reliable description of electronic orbitals from four-component spinors, the contraction coefficients are different for large component and small component. Therefore, the same contraction coefficients taken from a contracted basis set are not suitable here. After solving the eigenvalue problem, basis contraction can be applied to the two-component, electron-only Hamiltonian. We invoke the no-virtual-pair-approximation where only the positive energy solutions are subject to the correlation treatment.

A key assumption in X2C framework here is that only the one-electron part of the relativistic Hamiltonian is involved, meaning that one-electron scalar relativity and one-electron spin-own orbit coupling (which is the 1e-SOC) are included while the rest are ignored. As scalar-relativity is dominant by the one-electron contribution[189], the spin-free one-electron X2C (sfX2C-1e) Hamiltonian has become a standard option to treat scalar relativistic effects. However, the spin-orbit coupling, especially the contribution from the two-electron part[190], is essential in yielding correct energy splittings and molecular properties, which cannot be simply left out when studying fine structure of molecular spectra and excited states properties. One may wonder if the X2C formalism can be applied to Hamiltonian including two-electron operators. This is not an easy task as a proper two-component form has to be determined for the two-electron part, i.e. a suitable transformation for it. Although the same decoupling transformation constructed using one-electron part could be a consistent option, the cost of the full transformation of the two-electron part will be so high that one would rather just stick to 4C calculations. Some efforts are reported in the literature.[191, 192]

Less expensive routes are to include the approximate two-electron integrals in the form of one-electron potential. The two-electron spin-own orbit and spin-other orbit coupling term effectively shields the one-electron SO interaction. This effect may be efficiently taken into account by using parameterized screened nuclear charges in the evaluation of one-electron

SO integrals[129, 187, 193, 194], such as Boettger factor[195], which is our option for X2C post-HF development. The idea of "from atoms to molecule" [178, 196] works well in DFT framework. Also widely explored is the idea of using atomic mean-field (AMF) as well as molecular mean-field[197–200]. Upon obtaining a mean-field wavefunction (either from SCF or CASSCF step, either with two-electron SO or not), the two-electron SO integrals are then contracted with the density matrix to construct effective one-electron SO integrals for later computation. Though these methods are reported to give small errors, there are still difficulties to be further discussed, such as the reliability of the mean-field wavefunction and picture change errors [201, 202]. The latter is a common concern for two-component methods and the properties they predict.

2.2 Exact-Two-Component Post-HF Methods and Oscillator Strength for Spectroscopy

One key assumption for the common relativistic post-HF methods and the ones discussed in this dissertation is the so-called "no-virtual-pair" approximation (NVPA)[203], which essentially means the correlation space is spanned by Slater determinants constructed from only the positive-energy solutions/spinors. Interesting discussion on including negative-spinor space in correlated methods can be found in Ref. 204–208. With NVPA, the well-developed post-HF methods for excited states and spectroscopy as discussed in Chapter 1 can be easily transferred to work with relativistic Hamiltonians, once the complex arithmetic is carefully taken care of in the equation derivation. As compared to non-relativistic calculations, it increases the storage requirements and the number of floating point operations, as well as the problem dimension considering the use of spinors. A non-exhaustive list of review[83, 209] and journal articles[127–136, 210] about relativistic post-HF methods.

As stated in Chapter 1, the least two quantities – positions and relative intensities of the spectral lines – should be predicted from the relativistic methods we used for heavy-element spectroscopy. In this section, the formalism of two popular methods for excited states – configuration interaction (CI) and equation of motion (EOM) Coupled Cluster (CC) with

X2C Hamiltonian are introduced, and their corresponding oscillator strength formalism are documented. The energies obtained from the two methods correspond to the positions of the spectral lines, while the oscillator strength within the dipole approximation correspond to the intensity, since the interaction between a quantum mechanical system and plane wave light is usually modeled within the electric dipole approximation. Throughout this Section, the labels *i,j,k,l,m,n* refer to molecular orbitals (MOs) that are occupied in the reference configuration, while *a,b,c,d,e,f* refer to MOs that are unoccupied.

2.2.1 General formalism for oscillator strength

For an N-electron system and its normalized wavefunction Ψ, the first-order reduced density matrix, or so-called one-electron reduced density matrix can be constructed as

$$\hat{\gamma} = |\Psi\rangle\langle\Psi| \tag{2.23}$$

$$\gamma_{pq} = \langle\Psi|a_q^\dagger a_p|\Psi\rangle \tag{2.24}$$

which is often used to compute properties, i.e. the expectation value of any operator Θ:

$$\theta = |\langle\Psi|\Theta|\Psi\rangle| \tag{2.25}$$

$$= \mathrm{Tr}(\Theta\gamma) \tag{2.26}$$

For the oscillator strength between initial state Ψ_M and final state Ψ_N in dipole length approximation,

$$D = \langle\Psi_\mathrm{M}|\hat{\boldsymbol{\mu}}|\Psi_\mathrm{N}\rangle\langle\Psi_\mathrm{N}|\hat{\boldsymbol{\mu}}|\Psi_\mathrm{M}\rangle \tag{2.27}$$

$$f = \frac{2}{3}(E_\mathrm{N} - E_\mathrm{M})D \tag{2.28}$$

where D is the dipole strength and f is the oscillator strength. E_M and E_N are the energies for the initial state and final state, respectively.

2.2.2 X2C-CI and oscillator strength

Configuration Interaction is a well-explored method in non-relativistic regime and there are many good textbooks and reviews for detailed introduction and analysis. We refer the readers to Chapter 4 in Szabo and Ostlund's book [6].

A distribution of electrons in the atomic or molecular orbitals is one electronic configuration of the atom or molecule, also called a set of orbital occupancies. An N-electron wavefunction can be described as a linear combination of all possible N-electron Slater determinants constructed from a complete set of spinors/orbitals $\chi(\boldsymbol{r})\}$, which can be obtained from single-reference SCF (HF or DFT) or MCSCF. The wavefunction ansatz for any state of interest is

$$|\Psi\rangle = \sum_I C_I |\Phi_I\rangle \tag{2.29}$$

$$= C_0|\Phi_0\rangle + \sum_{ia} C_i^a |\Phi_i^a\rangle + \sum_{i<j,a<b} C_{ij}^{ab} |\Phi_{ij}^{ab}\rangle + \sum_{i<j<k,a<b<c} C_{ijk}^{abc} |\Phi_{ijk}^{abc}\rangle + ... \tag{2.30}$$

where $|\Phi_I\rangle$ stands for any Slater determinant, and C_I is its coefficient. $|\Phi_i^a\rangle$ is a Slater determinant formed by substituting spinor i in $|\Phi_0\rangle$ with spinor a, and so forth. If Eq. (2.29) is always normalized to 1, the minimum energy E in Eq. (2.16) can be obtained by varying the CI coefficients $\{C_I\}$ of the ansatz based on variational theorem. This is equivalent to the matrix form of Schrödinger equation $\hat{H}C = EC$, if the ground and excited configurations $|\Phi_I\rangle$ are chosen to be orthogonal to each other (which is the case if they are Slater determinants). Solving the eigenvalue problem results in a full set of CI coefficients not only for the ground state but also for all the excited states, which is a very straightforward methodology to simulate excited states and their properties.

If all the possible excitations in Eq. (2.29) are taken into account, the procedure is "full CI", being the exact theory for non-relativistic Schrödinger equation. However, due to the negative solutions for relativistic four-component Hamiltonian, relativistic FCI expansion only includes the excitations between spinors with positive energies, *i.e.* with "No-virtual-

pair approximation" implied. Similar to the non-relativistic CI, truncations are usually employed to reduced the computational cost.

CI is a strict variational electron correlation method, while others are usually not. In theory, if the energy is minimized to be close enough to the exact energy with a large enough basis set, the wavefunction is expected to be near exact, which in turns gives better prediction of other properties. Noted that the values of the properties may not converge as fast as the energy and the CI coefficients may not be optimal for a property other than energy.

The one-particle transition density matrix element between initial state $|\Psi_{\mathrm{M}}\rangle$ and $|\Psi_{\mathrm{N}}\rangle$ in CI is defined as:

$$\gamma_{pq}^{\mathrm{MN}} = \langle\Psi_{\mathrm{M}}|\hat{E}_{qp}|\Psi_{\mathrm{N}}\rangle = \sum_{IJ} C_I^{\mathrm{M}*}\langle\Phi_I|\hat{E}_{qp}|\Phi_J\rangle C_J^{\mathrm{N}} \tag{2.31}$$

where $\hat{E}_{qp} = a_q^\dagger a_p$ is the single excitation operator, C_I^{M} is the CI coefficient for determinant $|\Phi_I\rangle$ of state $|\Psi_{\mathrm{M}}\rangle$, $\langle\Phi_I|\hat{E}_{qp}|\Phi_J\rangle$ is also used in CI calculations so it can be re-used or re-computed. Together with the MO-dipole integrals and following equations in section 2.2.1, oscillator strength can be computed.

2.2.3 X2C-EOMCC and oscillator strength

CC utilizes exponential ansatz for the ground state trial wavefunction,

$$|\Psi_0\rangle = e^{\hat{T}}|\Phi_0\rangle \tag{2.32}$$

where $|\Phi_0\rangle$ is the reference wavefunction which is usually chosen to be the SCF solution, and here it stands for the X2C-HF reference, $\hat{T}$ represents the cluster operator. At the widely used CC with single and double (CCSD) level of theory, it takes the form

$$\hat{T} = \sum_{ia} t_i^a a_a^\dagger a_i + \frac{1}{4}\sum_{ijab} t_{ij}^{ab} a_a^\dagger a_b^\dagger a_j a_i. \tag{2.33}$$

We refer the readers to Ref. 37 for detailed introduction for the basics of coupled-cluster theory. A review for relativistic CC and EOMCC can be found in Ref. 47. At the EOM-CCSD level of theory, excited states $|\Psi_{\rm N}\rangle$ are expanded linearly (CI-like) in terms of excitations out of the CCSD ground-state wave function

$$|\Psi_{\rm N}\rangle = \hat{R}_{\rm N}|\Psi_0\rangle = \left(r_0 + \sum_{ia} r_i^a a_a^\dagger a_i + \frac{1}{4}\sum_{ijab} r_{ij}^{ab} a_a^\dagger a_b^\dagger a_j a_i \right) e^{\hat{T}}|\Phi_0\rangle \tag{2.34}$$

Since both $\hat{R}_{\rm N}$ and $\hat{T}$ are excitation operators, they necessarily commute. The expansion coefficients r_0, r_i^a, and r_{ij}^{ab}, are obtained by solving the right-hand eigenvalue problem

$$\bar{H}_n \hat{R}_{\rm N}|\Phi_0\rangle = \omega_{\rm N}\hat{R}_{\rm N}|\Phi_0\rangle \tag{2.35}$$

$$\bar{H}_n = e^{-\hat{T}}\hat{H}e^{\hat{T}} - E_{\rm CC} \tag{2.36}$$

where $\bar{H}_n$ is the normal-ordered similarity-transformed Hamiltonian, E_{CC} is the ground-state energy from the previous CC step, and $\omega_{\rm N}$ is the difference between the energy of N^{th} excited state and $E_{\rm CC}$, *i.e.* $E_{\rm N} = E_{\rm CC} + \omega_{\rm N}$. The non-hermiticity of $\bar{H}_n$ implies the existence of left-hand excited-state wave functions, the knowledge of which is necessary for the evaluation of excited-state properties (*i.e.*, oscillator strengths). The left-hand excited-state wave functions are expanded in the same manner as the right-hand wave functions, yielding:

$$\langle\widetilde{\Psi}_{\rm N}| = \langle\Phi_0|\hat{L}_{\rm N}e^{-\hat{T}} = \langle\Phi_0|\left(l_0 + \sum_{ia} l_a^i a_i^\dagger a_a + \frac{1}{4}\sum_{ijab} l_{ab}^{ij} a_i^\dagger a_j^\dagger a_b a_a \right) e^{-\hat{T}} \tag{2.37}$$

with $\hat{L}_{\rm N}$ satisfying

$$\langle\Phi_0|\hat{L}_{\rm N}\bar{H}_n = \langle\Phi_0|\hat{L}_{\rm N}\omega_{\rm N}. \tag{2.38}$$

Note that right- and left-hand ground state wave functions can be recovered from Eq. (2.34) and Eq. (2.37) with the choices

$$\hat{R} = \hat{R}_0 = 1 \tag{2.39}$$

$$\hat{L} = \hat{L}_0 = 1 + \hat{\Lambda} \tag{2.40}$$

where $\hat{\Lambda}$ is the usual ground-state de-excitation operator, defined at the CCSD level of theory as

$$\hat{\Lambda} = \sum_{ia} \lambda_a^i a_i^\dagger a_a + \frac{1}{4} \sum_{ijab} \lambda_{ab}^{ij} a_i^\dagger a_j^\dagger a_b a_a \tag{2.41}$$

The t- and λ-amplitudes in Eq. (2.33) and Eq. (2.41) are determined by using a conventional CCSD algorithm,[37, 211, 212] augmented to account for complex arithmetic and spin-broken amplitudes. For low-energy excited-states, the right- and left-hand excited-state wave functions are determined via a modified Davidson algorithm[213–216], which can handle complex arithmetic. For the higher energy excited states relevant to core-level excitations, these wave functions are be determined using the Generalized Preconditioned Locally Harmonic Residual (GPLHR) approach [19, 217] or energy-specific Davidson algorithm.

In order to obtain the oscillator strength of each excitation for X2C-EOM-CCSD, we first need to obtain the r- and l-amplitudes (r_0, r_i^a, r_{ij}^{ab}, l_0, l_a^i, and l_{ab}^{ij} for EOM-CCSD) from the left and right eigenvectors of the Hamiltonian. These r- and l-amplitudes are then used to construct the one-electron transition density matrices, which are then used to calculate properties as described in Ref. 56. Since $\bar{H}$ is non-Hermitian, we must build both transition density matrices, ρ^{MN} and ρ^{NM}, in order to calculate the oscillator strength for the transition from state M to state N. The one-particle transition density matrix between initial state M and final state N is defined as:

$$\rho_{pq}^{\mathrm{MN}} = \langle \widetilde{\Psi}_{\mathrm{M}} | \hat{E}_{qp} | \Psi_{\mathrm{N}} \rangle = \langle \Psi_0 | \hat{L}_{\mathrm{M}} e^{-\hat{T}} \hat{E}_{qp} e^{\hat{T}} \hat{R}_{\mathrm{N}} | \Psi_0 \rangle \tag{2.42}$$

The dipole strength is then defined as:

$$D = \langle \widetilde{\Psi}_{\mathrm{M}} | \mu | \Psi_{\mathrm{N}} \rangle \langle \widetilde{\Psi}_{\mathrm{N}} | \mu | \Psi_{\mathrm{M}} \rangle \tag{2.43}$$

and is more directly calculated as:

$$D = \sum_{\xi} Tr(\rho^{\mathrm{MN}} \mu_{\xi}) Tr(\rho^{\mathrm{NM}} \mu_{\xi}) \tag{2.44}$$

where μ_{ξ} is the matrix representation of a Cartesian component of the dipole operator ($\xi \in x, y, z$). From there, the oscillator strength is calculated as:

$$f_L = \frac{2}{3}(E_{\mathrm{N}} - E_{\mathrm{M}})D \tag{2.45}$$

It should be noted that there is nothing mathematically forcing this oscillator strength value to be real. However, in practice we have found the imaginary component of the oscillator strength to be essentially zero, as it is a physical observable.

The one-particle transition density matrix is defined as Eq. (2.42), in which

$$\rho_{pq} = \begin{bmatrix} \rho_{ij} & \rho_{ia} \\ \rho_{ai} & \rho_{ab} \end{bmatrix} \tag{2.46}$$

where each sub-block is represented by:

$$\rho_{ij} = r_0(t_i^e l_e^j - \frac{1}{2} t_{im}^{fe} l_{fe}^{jm}) - r_i^e l_e^j - \frac{1}{2} r_{im}^{fe} l_{fe}^{jm} - t_i^f r_m^e l_{fe}^{jm} \tag{2.47}$$

$$\rho_{ia} = r_0 l_a^i + l_{ae}^{im} r_m^e \tag{2.48}$$

$$\begin{aligned}\rho_{ai} = {} & r_0(t_{im}^{ae} l_e^m - t_i^e t_m^a l_e^m - \frac{1}{2} t_{in}^{ef} t_m^a l_{ef}^{mn} - \frac{1}{2} t_{mn}^{af} t_i^e l_{ef}^{mn}) \\ & + l_0 r_i^a + r_{im}^{ae} l_e^m - t_m^a r_i^e l_e^m - t_i^e r_m^a l_e^m \\ & - \frac{1}{2} t_{mn}^{af} r_i^e l_{ef}^{mn} - \frac{1}{2} t_{in}^{ef} r_m^a l_{ef}^{mn} - \frac{1}{2} r_{mn}^{af} t_i^e l_{ef}^{mn} - \frac{1}{2} r_{in}^{ef} t_m^a l_{ef}^{mn} \\ & - t_i^e t_m^a r_n^f l_{mn}^{ef} - t_{im}^{ae} r_n^f l_{ef}^{mn}\end{aligned} \tag{2.49}$$

$$\rho_{ab} = r_0(t_m^b l_a^m + \frac{1}{2} t_{mn}^{eb} l_{mn}^{ea}) + r_m^b l_a^m + \frac{1}{2} r_{mn}^{eb} l_{ea}^{mn} + t_n^b r_m^e l_{ea}^{mn} \tag{2.50}$$

Chapter 3

RELATIVISTIC TWO-COMPONENT MULTIREFERENCE SECOND-ORDER PERTURBATION THEORY

As the relativistic corrections become stronger for late-row elements, the fully perturbative treatment of spin-orbit coupling and dynamic correlation may become inadequate for accurate descriptions of chemical properties. In this work, we introduce a determinant based Kramers-unrestricted exact-two-component multi-reference second order perturbation (X2C-MRPT2) method which variationally includes relativistic corrections with a perturbative dynamic correlation. The restricted active space partitioning scheme is employed to provide an adjustable correlation space for the second order perturbation treatment. The multi-state perturbation theory is also developed to improve the descriptions of ground and excited states. Benchmark studies of atomic fine structure splittings and spectroscopic constants of molecular monohydrides using X2C-MRPT2 are compared to the other perturbative and variational approaches. The results suggest that X2C-MRPT2 is a highly accurate alternative to the fully variational multi-reference configuration interaction method at only a small fraction of the computational cost.

3.1 Introduction

Accurate descriptions of chemical reactivities, magnetic properties, and optical responses of systems involving transition-metal, rare earth, and heavy elements require an electronic structure method to be capable of treating relativistic effects (scalar relativity and spin-orbit coupling) and electron correlations (static and dynamic) with a high fidelity. The most accurate approaches are based on the fully variational all-electron two- and four-component multi-reference configuration interaction (MRCI) method that includes relativistic correc-

tions at the molecular orbital level, followed by a multi-configurational self-consistent-field (MCSCF) procedure for static correlation and an additional configuration interaction treatment of the dynamic correlation, such as the exact-two-component MRCI (X2C-MRCI)[188] and the four-component internal-contracted MRCI (4C-ic-MRCI).[218] However, the computational cost of relativistic MRCI is prohibitive except for very small chemical systems.

One approach to reduce the scaling of relativistic MRCI is to treat certain selected physics with perturbation theory. For example, in the four-component multireference perturbation theory[219] and the internally-contracted CASPT2 method (4C-ic-CASPT2),[218, 220, 221] the dynamic correlation is added using the second order perturbation theory while relativistic effects are variationally included at the molecular orbital and MCSCF levels. The perturbation treatment of dynamic correlation can be in a form similar to that in CASPT2[41, 42] or the relativistic generalized Van Vleck second-order perturbation theory.[183] In principle, the perturbative dynamic correlation can be introduced to other types of variational relativistic MCSCF procedure, such as the four-component/two-component Kramers-restricted multi-configurational SCF,[128, 203, 222–224] four-component/two-component complete active space SCF (CASSCF),[129, 225, 226] and four-component density matrix renormalization group (DMRG).[134, 135]

A more drastic yet still accurate approximation to relativistic MRCI is to perturbatively treat both dynamic correlation and spin-orbit coupling, resulting in the very successful CASPT2-SO method.[4] The CASPT2-SO was developed under the assumption that the interplay between the dynamic correlation and spin-orbit coupling can be ignored, and that the dynamic correlation is the same for all spin-orbit coupled microstates. Another advantage of CASPT2-SO is that real-valued MCSCF methods[41–43, 89, 227, 228] can be used in conjunction with the perturbation treatment, giving rise to an additional reduction in computational cost. A very recent work by Zhang and coworkers has introduced a new approach to treat relativistic effects and electron correlations with the iterative configuration interaction and second-order perturbation theory (iCIPT2) method.[229]

In this work, we develop a relativistic two-component multi-state multi-configurational

perturbation theory to introduce the dynamic correlation to relativistic Kramers-unrestricted two-component MCSCF wave function which variationally includes scalar relativistic effects and spin-orbit coupling. A fully uncontracted perturbative formulation is introduced within a determinant basis. Ground and excited fine structure splitting in atomic species as well as spectroscopic constants of molecular monohydrides are used as benchmark systems, compared to other variational and perturbative MCSCF methods and experiments.

3.2 Theory

In this section, the following notations are used, unless otherwise specified:

- μ , ν , λ , κ: atomic orbitals (AOs)
- *p, q, r, s*: general spinor molecular orbitals (MOs)
- *I, J, ...*: Slater determinants in CAS space
- *S, T, ...*: Slater determinants in external space
- *m, n, ...*: states

3.2.1 Kramers-Unrestricted Two-Component CASSCF Reference

The Kramers-unrestricted exact-two-component CASSCF (X2C-CASSCF) wave function, which captures static correlation and relativistic corrections, is utilized as the starting reference of the perturbative treatment of dynamic correlation. For derivation and benchmarking of X2C-CASSCF, we refer readers to Ref. 129.

In this work, the exact-two-component (X2C)[3, 129, 164, 176–188] transformation (see section 2.1.4 in Chapter 2) is used to obtain the two-component electronic Hamiltonian $\mathbb{H}^+$ followed by a self-consistent-field procedure to variationally include the scalar relativistic and spin-orbit coupling effects at the spinor molecular level. In the current implementation, we use the one-step one-electron X2C transformation. To correct for the two-electron spin-orbit coupling, an empirical Boettger[195] factor is employed to scale the one-electron

spin-orbit term. This procedure has been shown to produce accurate spin-orbit splittings for both valence and core electrons.[22, 184, 185, 187, 230, 231] We invoke the no-virtual-pair-approximation where only the positive energy solutions are subject to the correlation treatment.

The X2C transformation yields a set of effective spinor molecular orbitals, which are complex-valued linear combinations of AO spinors.

$$\psi_p^{2c}(\mathbf{q}) = \begin{pmatrix} \phi_p^{\alpha}(\mathbf{r}) \\ \phi_p^{\beta}(\mathbf{r}) \end{pmatrix} = \begin{pmatrix} \sum_{\mu} c_{\mu p}^{\alpha} \chi_{\mu}(\mathbf{r}) \\ \sum_{\mu} c_{\mu p}^{\beta} \chi_{\mu}(\mathbf{r}) \end{pmatrix} \tag{3.1}$$

where coordinate $\mathbf{q}$ includes both the spatial coordinate $\mathbf{r}$ and the spin coordinate.

A multi-configurational wave function based on spinor molecular orbitals can be constructed and optimized, leading to the two-component Kramers-unrestricted complete active space self-consistent-field (X2C-CASSCF) method.[129] Noted that when multiple states are taken into account, all states of interest are treated equally in a state-averaged manner, which allows the recovery of Kramers symmetry for open-shell cases.[18, 130]

3.2.2 Two-Component Multireference Second-Order Perturbation Theory in the Determinant Basis

A relativistic two-component multi-state multi-configurational second-order perturbation theory is developed in an uncontracted determinant basis for the description of dynamic electron correlation, which follows a "perturb then diagonalize" manner.

Single-state perturbation theory

The second-order perturbation is formulated with respect to a single-state multiconfigurational reference wave function $|\Psi_m\rangle$. Based on the Rayleigh-Schrödinger perturbation theory, the exact Hamiltonian $\hat{H}$ from the time-independent Schrödinger equation is partitioned into a zero-order Hamiltonian $\hat{H}_0$ and a perturbation $\hat{V}$ which aims to recover the

"missing" correlation:

$$\hat{H} = \hat{H}^{(0)} + \hat{V} \tag{3.2}$$

In this work, the second-order perturbation is formulated in the determinant basis, while the reference wave function is multi-configurational in nature. Similar to the nonrelativistic CASPT2, $\hat{H^{(0)}}$ is constructed as a one-electron generalized Fock operator $\hat{F}$ projected onto different configuration subspaces (Eq. (3.3)) such that it reduces to Møller–Plesset methods if the CASSCF reference wave function contains only a single determinant.

$$\hat{H}^{(0)} = \hat{P}\hat{F}\hat{P} + \hat{Q}\hat{F}\hat{Q} + \hat{S}\hat{F}\hat{S} \tag{3.3}$$

$$\hat{F} = \sum_{pq} f_{pq} a_p^\dagger a_q \tag{3.4}$$

$$f_{pq} = h_{pq} + \sum_{rs} D_{rs}(g_{pqrs} - g_{psrq}) \tag{3.5}$$

where h_{pq} and g_{pqrs} are the one- and two-electron molecular spinor integrals, and D is the state-specific first-order reduced density matrix (1RDM) with its element $D_{rs} = \langle\Psi|\hat{E}_{rs}|\Psi\rangle$. Here the reference space $\mathbb{P}$ includes CAS determinants in which reference state wave function(s) (*i.e.*, CI vectors of states of interest) are spanned, and the $\mathbb{Q}$ subspace contains the rest of CAS determinants that are not in the $\mathbb{P}$ space, while the external space $\mathbb{S}$ contains determinants that are not included in the CAS space. $\mathbb{P} \oplus \mathbb{Q}$ forms the CAS space. $\hat{P}$, $\hat{Q}$, $\hat{S}$ are the corresponding projection operators.

The zero-order wave functions of the states of interest are the X2C-CASSCF reference:

$$|\Psi_m^{(0)}\rangle = \sum_{mI} C_{m,I}^{(0)} |I\rangle, \quad |I\rangle \in \mathbb{P} \tag{3.6}$$

$$\langle\Psi_m^{(0)}|\Psi_n^{(0)}\rangle = \delta_{mn} \tag{3.7}$$

Determinants in the external space $\mathbb{S}$ can be generated by applying single and double excitation operators to the determinants in the CAS space. The third term of Eq. (3.3) becomes

$|\phi^S\rangle\hat{F}\langle\phi^S| + |\phi^D\rangle\hat{F}\langle\phi^D|$, where $|\phi^S\rangle$ and $|\phi^D\rangle$ are singly and doubly excited determinants, respectively. Under the construction of the zero-order Hamiltonian (Eq. (3.3)), only the determinants in the external space $\mathbb{S}$ contribute to the first-order wavefunction $\Psi^{(1)}$ and the second-order energy $E^{(2)}$ corrections. The first-order wavefunction can be written as,

$$|\Psi_m^{(1)}\rangle = \sum_S C_{m,S}^{(1)}|S\rangle, \quad |S\rangle \in \mathbb{S} \tag{3.8}$$

The expansion coefficients $C_{m,S}^{(1)}$ of the first-order correction to the wave function can be obtained by solving the following linear equation:

$$\sum_S C_{m,S}^{(1)}\langle T|(\hat{H^{(0)}} - E_m^{(0)})|S\rangle = -\langle T|\hat{H}|\Psi_m^{(0)}\rangle, \quad |T\rangle, |S\rangle \in \mathbb{S} \tag{3.9}$$

where $E_m^{(0)}$ is the zero-order energy for the reference state $|\Psi_m^{(0)}\rangle$. The definition of the zero-order Hamiltonian in Eq. (3.3) leads to the "Barycentric" zero-order energy

$$E_m^{(0)} = \sum_I C_{m,I}^{*(0)} C_{m,I}^{(0)}\langle I|\hat{H}^{(0)}|I\rangle, \quad |I\rangle \in \mathbb{P} \tag{3.10}$$

The "Barycentric" zero-order Hamiltonian is superior to the Epstein-Nesbet unperturbed Hamiltonian for relativistic Hamiltonian because of the presence of degenerate or near-degenerate states arising from the time-reversal symmetry.[232]

The second-order perturbative energy for state $|\Psi_m\rangle$ can be evaluated by

$$E_m^{(2)} = \sum_S C_{m,S}^{(1)}\langle\Psi_m^{(0)}|\hat{H}|S\rangle, \quad |S\rangle \in \mathbb{S} \tag{3.11}$$

Multi-state perturbation theory

Because the multi-configurational reference space $\mathbb{P}$ can represent several CI vectors of states, the perturbation theory can be applied to all reference states of interest. When multiple reference states need to be considered in the perturbation theory, determinants

in the external space $\mathbb{S}$ can introduce additional couplings that mix different CASSCF references states. In this scenario, an effective Hamiltonian can be constructed including the first-order $\mathbb{P}$–$\mathbb{S}$ interaction for the CASSCF reference states of interest, leading to the multi-state perturbation theory. The eigenvalues and eigenvectors of the effective Hamiltonian correspond to the perturbed states. A similar approach has been used in the (extended) multi-configuration quasi-degenerate perturbation theory (X)MCQDPT[233, 234] and (X)MS-CASPT2 approaches.[235, 236] Detailed derivation can be found in Ref. 233.

In the multi-state perturbation theory, Eq. (3.5) is used with the state-averaged 1RDM $\bar{D}$ over states of interest, giving rise to the generalized, state-averaged Fock matrix $\bar{f}$. As a result, the zero-order Hamiltonian in the reference space has non-zero off-diagonal elements:

$$\langle \Psi_m^{(0)} | \hat{H}^{(0)} | \Psi_n^{(0)} \rangle = \sum_{IJ} \sum_{pq} \bar{f}_{pq} C^*_{m,I} C_{n,J} \langle I | a_p^\dagger a_q | J \rangle, \quad |I\rangle, |J\rangle \in \mathbb{P} \tag{3.12}$$

In contrast to the simple linear equation for solving for the first order expansion coefficients $C_S^{(1)}$ for single reference state (Eq. (3.9)), the system of linear equations for multi-state perturbation theory takes on a more complicated form:

$$\mathbf{H}_{SP} + \mathbf{H}^{(0)}_{SS} \mathbf{C}_{SP} = \mathbf{C}_{SP} \mathbf{H}^{(0)}_{PP} \tag{3.13}$$

which can be solved iteratively.

In conventional multi-state perturbation theory,[233, 235] the off-diagonal elements in $\mathbf{H}^{(0)}_{PP}$ are ignored so that Eq. (3.13) can be reduced down to Eq. (3.9) for each state and can be solved state-wise. An alternative approach used in MCQDPT[234] and internally-contracted MS-CASPT2[236] first diagonalizes the non-diagonal zero-order Hamiltonian via a unitary transformation $\mathbf{U}$:

$$\mathbf{U}^\dagger \mathbf{H}^{(0)}_{PP} \mathbf{U} = \tilde{\mathbf{H}}^{(0)}_{PP}, \quad |\tilde{\Psi}_m^{(0)}\rangle = \sum_n \mathbf{U}_{mn} |\Psi_n^{(0)}\rangle \tag{3.14}$$

Using the rotated CI vectors and the diagonal elements in $\tilde{\mathbf{H}}_{PP}^{(0)}$ as the zero-order energies for each corresponding perturbed state, the first-order corrections can be obtained using Eq. (3.9) for each state.

The effective Hamiltonian up to second-order is given by:

$$(\mathbf{H}_{eff}^{(0-2)})_{mn} = E_n^{\mathrm{CAS}}\delta_{nm} + \frac{1}{2}\sum_S \left(C_{n,S}^{(1)} \langle \tilde{\Psi}_m^{(0)} | \hat{H} | S \rangle + C_{m,S}^{(1)*} \langle S | \hat{H} | \tilde{\Psi}_n^{(0)} \rangle \right) \tag{3.15}$$

Diagonalizing the effective Hamiltonian gives the perturbed energies of the states of interest up to second-order correction as its eigenvalues, while the perturbed state wave functions are linear combinations of the rotated reference states with coefficients obtained from the eigenvectors. With a single-state reference, the real-valued part of the perturbative (second) term in Eq. (3.15) is the same as that in Eq. (3.11).

3.3 Computational Implementation

3.3.1 RAS book-keeping

Up to second-order of perturbation theory, only the determinants connected with the CAS space through single and double excitations in the external space have contributions to the first-order $\mathbb{P}$–$\mathbb{S}$ interaction. There are several different methods to generate those excited configurations. For example, ic-CASPT2 decomposes the external space into eight subgroups based on the type of excitation operators and computes up to third-order RDMs.[41, 42] GVVPT2 adopts the macroconfiguration approach[237] to construct the CI and external spaces.[238] Similarly, the occupation restricted multiple active space (ORMAS) method[239, 240] can be used to reduce the number of configurations by partitioning the orbitals into subgroups and restricting their electron occupation numbers.

Here we partition the spinor molecular orbitals with a general RAS framework (Fig. 3.1) to generate excited determinants in the external space and utilize the string scheme in Ref. 241 for determinants' book-keeping. This approach has shown its advantages in the previous relativistic X2C-MRCI implementation.[188] In the relativistic second-order perturbation

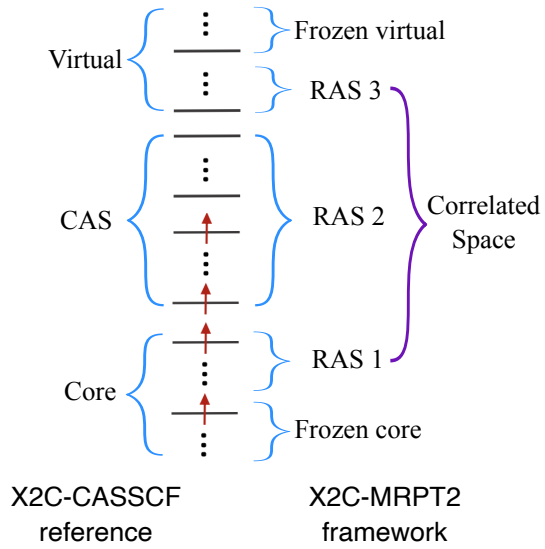

Figure 3.1: Orbital space partitioning in the X2C-MSPT2 framework using the RAS concept.

method introduced in this work, the RAS2 space is identical to the CAS space from the CASSCF calculation, while RAS1 and RAS3 subspaces include spinor orbitals in core and virtual spaces, respectively, allowing for an adjustable correlation space. This is useful if a frozen orbital approximation is needed to reduce the computational cost for larger systems. The restrictions for subspaces are: both the number of holes in RAS1 and the number of electrons in RAS3 must be ≤ 2, in order to construct the external space with only single and double excited determinants.

3.3.2 On-the-fly Matrix-vector Product Evaluation

The left-hand-side in Eq. (3.9) is an $N_S \times N_S$ matrix (N_S is the number of determinants in the external space $\mathbb{S}$). The sparse Hamiltonian matrix required in both the right-hand-side of Eq. (3.9) and the perturbative correction evaluation in Eq. (3.11) or Eq. (3.15) (denoted as $\mathbf{HC}_m^{(1)}$ in matrix form) has dimensions of the total number of determinants, which increases drastically as the size of the correlation space increases.

In order to avoid memory bottlenecks, we adopted the Generalized Minimal Residual

(GMRES) method[242] with a diagonal preconditioner to solve the system of linear equations iteratively. Instead of storing the whole matrices, the matrix-vector products are formed using an 'on-the-fly' direct contraction approach, in the same way as the sigma vector evaluation in the direct CI algorithm.[36]

3.4 Results and discussion

The relativistic two-component multi-state multi-reference second-order perturbation method is implemented in the Chronus Quantum software package.[243] In the X2C calculations, the four-component to two-component transformation is carried out in an uncontracted primitive basis. After the X2C transformation, the basis is recontracted for the SCF and all post-SCF procedures, *i.e.*, X2C-CASSCF, X2C-MRCI, and X2C-MRPT2. In all calculations presented in this work, state averaging is employed over all states of interest in X2C-CASSCF to optimize the reference wave function and the state-averaged 1RDM is used in X2C-MRPT2. Equal state averaging recovers Kramers symmetry in the CASSCF process,[129, 130] which is important for maintaining the correct degeneracy in the later perturbative treatment. An improved virtual orbital scheme[188, 244, 245] is used in the CASSCF reference for the selection of proper virtuals included in the correlation space of both the X2C-MRPT2 and X2C-MRCI methods.

The atomic fine structure splitting plays an important role in molecular bonding as well as spectroscopic characteristics. In this work, we present calculations of ground and excited state fine-structure splittings of selected *s*-, *p*-, *d*-, and *f*-block elements and spectroscopic constants of molecular monohydrides to benchmark the method developed here compared to experiments and results from other relativistic multi-reference methods.

3.4.1 Excited State Fine Structure Splitting in Na ^2P

We examined the performance of the X2C-MRPT2 in the fine structure splitting of sodium atom in Tab. 3.1 using a small 6-31G basis in order to compare to a full CI (FCI) calculation. In the CASSCF part, the valence orbitals ($3s$ and $3p$) are in the active space, *i.e.*, CAS(1,8).

The lowest 8 states are equally weighted. All core and virtual orbitals are included in the external space for the perturbative treatment to capture the dynamic correlation. The result of full space X2C-MRCISD with the same reference wave function is also included for comparison.

	X2C-CASSCF	X2C-MRCISD	X2C-MRPT2	X2C-FCI	CASPT2-SO[4]
$^2P_{1/2} \rightarrow {}^2P_{3/2}$	1.7670	1.7823	1.7828	1.7830	1.4346

Table 3.1: The ^{2}P energy splitting (sodium D-lines, $^2P_{1/2} \rightarrow {}^2P_{3/2}$ in meV) of Na. State-averaging is used in all multi-reference methods (X2C-CASSCF, X2C-MRCISD, and X2C-MRPT2). The CASPT2-SO result is computed using openMolCAS. Splitting between sodium D-lines is experimentally measured to be 2.1 meV.[246]

All methods tested here correctly recover the doubly degenerate ^{2}S ground state as well as the doubly degenerate $^2P_{1/2}$ and the quadruply degenerate $^2P_{3/2}$ excited states. $^2P_{1/2}$ and $^2P_{3/2}$ levels arise from the ^{2}P splitting due to spin-orbit coupling. Static correlation has been captured by CASSCF, while both MRCI and MRPT2 are able to recover over 95% of the dynamic correlation compared to FCI, as shown in Tab. 3.1. The multi-state treatment has almost no effect on the split levels, due to the weak interaction between spin-orbit split microstates that belong to the same ^{2}P term. The off-diagonal values in the effective Hamiltonian (Eq. (3.15)) are less than 1×10^{-6} a.u.

With the same 6-31G basis and orbital partitioning, the CASPT2-SO [4] method computed using openMolCAS [247] gives 1.4346 meV for sodium ^{2}P splitting. The difference is due to how the spin-orbit coupling is included. In the CASPT2-SO method, the spin-orbit coupling is treated perturbatively. As a result, the dynamic correlation treatment in CASPT2 cannot differentiate different levels arising from the ^{2}P term because the spin-orbit coupling is added afterwards. In the X2C-MR methods introduced here, the effect of the spin-orbit is included variationally at the molecular orbital level and hence at the CASSCF level, resulting in a difference in the dynamic correlation computed for $^2P_{1/2}$ and $^2P_{3/2}$ levels and improved excited state fine-structure splitting.

3.4.2 p-Block Elements

In this section, the all-electron X2C-TZVPall-2c [248] basis is used in X2C-MR calculations. 4C-ic-CASPT2 results were obtained with the uncontracted relativistic cc-pVTZ basis set. [5] CASPT2-SO calculations were performed using openMolCAS [247] with a large ANO-RCC basis set.

For group 13 elements, ^{2}P ground state is split into doubly degenerate $^2P_{1/2}$ and quadruply degenerate $^2P_{3/2}$ levels due to spin-orbit coupling. The energy splittings computed using relativistic two-component X2C-CASSCF, X2C-MRCISD, and X2C-MRPT2 are listed in Figure 3.2, compared to the 4C-ic-CASPT2 [5] and perturbative CASPT2-SO [4] methods. The CASSCF reference used an active space including all three valence electrons and eight (bi)spinor s and p orbitals. In Figure 3.2, results of X2C-MRPT2 are obtained with two different orbital partitioning schemes with regards to the frozen orbital approximation to directly compare against results from other methods in the literature. Scheme A includes subvalence electrons as well as first and second Rydberg virtual spinor orbitals in the external space. Scheme B utilizes a more drastic frozen core approximation with all core orbitals outside the CAS space absent in the external space, while all the virtual orbitals outside CAS are included, same as that used in 4C-ic-CASPT2 calculations.

Figure 3.2 shows that X2C-MRPT2 outperforms the 4C-ic-CASPT2 and X2C-CASSCF, and approaches the accuracy of X2C-MRCISD. The error in 4C-ic-CASPT2 relative to X2C-MRPT2 with the same scheme (B) is likely due to the internal contraction. The improvement of X2C-MRPT2 over X2C-CASSCF suggests that dynamic correlation plays an important role in fine structure splitting of p-block elements. While both the perturbative CASPT2-SO and variational X2C-MRPT2 produce better agreement with experiments compared to X2C-CASSCF, the results from X2C-MRPT2 are more accurate for heavier elements (In and Tl). The computed fine-structure splitting from the CASPT2-SO method is independent of the correlation space used for the PT2 treatment because the dynamic correlation is the same for all spin-orbit split microstates that belong to the same J manifold. The excellent

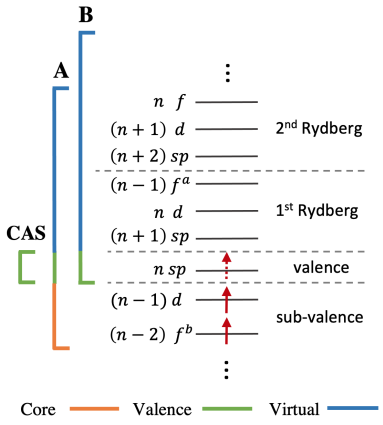

a: only for In and Tl; *b*: only for Tl

	X2C-CASSCF	X2C-MRCISD	X2C-MRPT2		4C-ic-CASPT2[5]	CASPT2-SO[4]	Exp.[246]
		Scheme A	Scheme A	Scheme B	Scheme B		
Ga	90 (−11.8)	100 (−2.0)	99 (−2.9)	97 (−4.9)	93 (−8.8)	99 (−2.9)	102
In	239 (−12.8)	265 (−3.3)	272 (−0.7)	253 (−7.7)	245 (−10.6)	261 (−4.7)	274
Tl	863 (−10.7)	905 (−6.3)	917 (−5.1)	899 (−6.9)	–	893 (−7.5)	966

Figure 3.2: **Top panel**: Definitions of selected correlation spaces. **Bottom panel**: The ground state ^{2}P energy splitting ($^2P_{1/2} \rightarrow {}^2P_{3/2}$ in meV) of group 13 p-block elements. Percentage errors with respect to experiments are reported in parentheses. State-averaging is used in all multi-reference methods (X2C-CASSCF, X2C-MRCISD, and X2C-MRPT2) developed in this work. Calculations using the perturbative CASPT2-SO[4] method and the four-component internal contracted Dirac-Coulomb-Breit CASSCF method[5] are included for comparison.

agreement between X2C-MRPT2 and CASPT2-SO for the 4-th row Ga element suggests that the dynamic correlation and spin-orbit coupling can be treated as separate perturbations for light elements without incurring a noticeable error. As the strength of spin-orbit coupling increases, the discrepancy between CASPT2-SO and X2C-MRPT2 becomes more significant, showing 11 meV and 24 meV differences in fine structure splitting for In and Tl, respectively.

3.4.3 d- and f-Block Elements

In this section, the all-electron X2C-TZVPall-2c[248] basis is used in X2C-MR calculations. CASPT2-SO calculations were performed using openMolCAS [247] with a large ANO-RCC

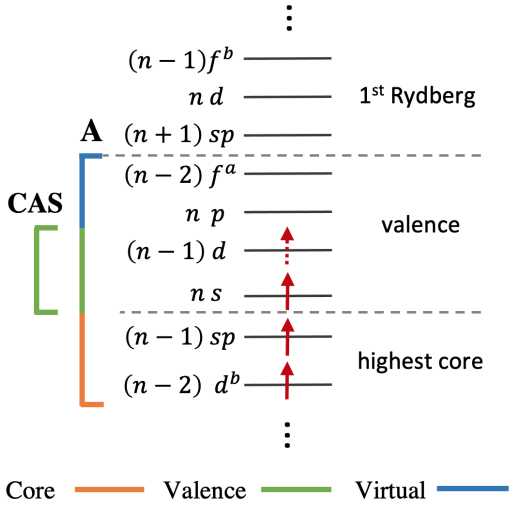

a: only for La; *b*: only for Y and La

	X2C-CASSCF	X2C-MRCISD	X2C-MRPT2	CASPT2-SO	Exp.[246]
Sc	21	23	23	24	21
Y	55	65	62	62	66
La	92	116	116	105	130

Figure 3.3: **Top panel**: Definitions of selected correlation spaces. **Bottom panel**: The ground state ^{2}D energy splittings ($^2D_{3/2} \rightarrow {}^2D_{5/2}$ in meV) of group 3 d-block elements computed using X2C-MRPT2. State-averaging is used in all multi-reference methods (X2C-CASSCF, X2C-MRCISD, and X2C-MRPT2) developed in this work.

basis set. Figure 3.3 shows the ground state fine structure splitting of group 3 d-block elements (Sc, Y and La). The d^1 electron configuration gives rise to ^{2}D ground state term, which is split into quadruply degenerate $^2D_{3/2}$ and 6-fold $^2D_{5/2}$ levels due to spin-orbit coupling. The reference CAS space contains 3 electrons in 12 spinor orbitals (ns and $(n-1)d$). The correlation space in X2C-MRCISD and X2C-MRPT2 calculations includes the highest core electrons ($(n-1)sp$ and $(n-2)d$) and valence virtual orbitals (np and $(n-2)f$). For light d-block elements (Sc and Y), the computed fine structure splittings from X2C-MRPT2 and CASPT2-SO are of a similar accuracy. For the heavier La atom, the variational treatment of spin-orbit in X2C-MRPT2 outperforms the perturbative CASPT2-SO. The result can be improved by using a larger correlation space. For example, including $6p4f7s7p6d5f$ orbitals

in X2C-MRPT2 gives a fine-structure splitting of 123 meV for the La ^{2}D term, only a $\sim$5% error compared to the experimental value.

Table 3.2 shows the fine structure splitting of the ^{4}I term, arising from the f^3 configuration, of the f-block Nd^{3+} ion. The spin-orbit coupling splits the ^{4}I term into $J = 9/2$, 11/2, 13/2, and 15/2 levels. MRCI-SO results using 28-electron relativistic core potential and a quadruple zeta quality ANO basis for the valence orbitals (ECP28MWB ANO) are also included for comparison.[249] For X2C-MR calculations, the reference CAS space contains 3 electrons in 14 spinor orbitals ($4f$). The correlation space for X2C-MRPT2 includes 8 core orbitals ($5sp$) and 124 virtual orbitals outside the CAS space. Table 3.2 shows that even with a limited correlation space the X2C-MRPT2 can improve the X2C-CASSCF results toward the experimental values. Compared to MRCI-SO that perturbatively treats spin-orbit coupling, X2C-MRPT2 results are much more accurate for $J = 11/2$ and 13/2 levels. The X2C-MRPT2 result for the high angular momentum $J = 15/2$ is slightly worse than MRCI-SO, likely due to the limited number of high angular momentum bases used in the X2C-MR calculations.

	MRCI-SO[249]	X2C-CASSCF	X2C-MRPT2	Exp. [250]
$^4I_{9/2} \rightarrow {}^4I_{11/2}$	203.83 (−13.3)	249.17 (5.9)	240.51 (2.3)	235.21
$^4I_{9/2} \rightarrow {}^4I_{13/2}$	444.61 (−8.2)	519.35 (7.2)	498.09 (2.8)	484.44
$^4I_{9/2} \rightarrow {}^4I_{15/2}$	722.58 (−2.7)	804.63 (8.4)	772.66 (4.1)	742.48

Table 3.2: Ground state ^{4}I fine structure splittings of Nd^{3+} computed using the x2c-TZVPall-2c basis set. State-averaging is used in X2C-CASSCF and X2C-MRPT2. Percentage errors with respect to experiments are reported in parentheses.

3.4.4 Molecular Monohydrides

In this section, we examine the performance of X2C-MRPT2 in predicting the splitting of the $^2\Pi$ state of molecular monohydrides (GeH and SnH) and the multi-state potential energy curves of TlH dissociation pathway. The multielectronic term symbols for molecular monohydrides can be derived according to the interplay between the $C_{\infty v}$ point group symmetry

and the spin-orbit coupling.[251, 252]

The ground state term of GeH and SnH is $^2\Pi$ with a $\pi^1\sigma^0$ configuration, which is a quadruply degenerate state in the non-relativistic regime. Spin-orbit coupling splits the $^2\Pi$ term into two doubly degenerate levels, and the splitting is computed and presented in Tab. 3.3. All calculations in Tab. 3.3 use the all-electron X2C-TZVPall-2c basis.[248] The X2C-CASSCF reference used an active space including one electron in six spinors including π and σ orbitals, state-averaged over the four levels split from the $^2\Pi$ term. At the X2C-MRPT2 level, electrons in the sub-valence orbitals (4 electrons for GeH and 14 for SnH determined by the orbital energy separation) are correlated with the CAS active space and all the virtual orbitals. Experimental bond lengths R_e are used in all calculations.[253] Table 3.3 shows that X2C-MRPT2 significantly improves the X2C-CASSCF results and is in excellent agreement with experiments with less than 1% error in the splitting of the $^2\Pi$ ground state.

	R_e (Å)[253]	X2C-CASSCF	X2C-MRPT2	Exp.[253]
GeH	1.5880	926.32 (3.8)	898.63 (0.7)	892.52
SnH	1.7815	2239.75 (2.8)	2197.51 (0.9)	2178.88

Table 3.3: The $^2\Pi$ state energy splitting (in cm^{-1}) of GeH and SnH, compared to experimental measurements. Percentage errors with respect to experiments are reported in parentheses.

To further benchmark the multistate generalization of X2C-MRPT2, here, the potential energy curves of the ground and low-lying excited states of thallium hydride (TlH) are shown in Fig. 3.4. The all-electron X2C-TZVPall-2c[248] basis is used for Tl atom and aug-cc-pVTZ [254, 255] basis for H atom. With the inclusion of spin-orbit coupling effect, the ground state $^1\Sigma^+$ remains to be a singlet bound state $X^1\Sigma^+_{0^+}$, while the first excited state $^3\Pi$ splits into $^3\Pi_{0^+}$, $^3\Pi_{0^-}$, $^3\Pi_1$ and $^3\Pi_2$, which are singly, singly, doubly, and doubly degenerate, respectively. Therefore, state-averaging over seven states of interest are employed in X2C-CASSCF and X2C-MRPT2 calculations. The active space chosen in the X2C-CASSCF reference includes 4 electrons in 10 spinor orbitals (Tl $6s6p$ and H $1s$). In X2C-MRPT2,

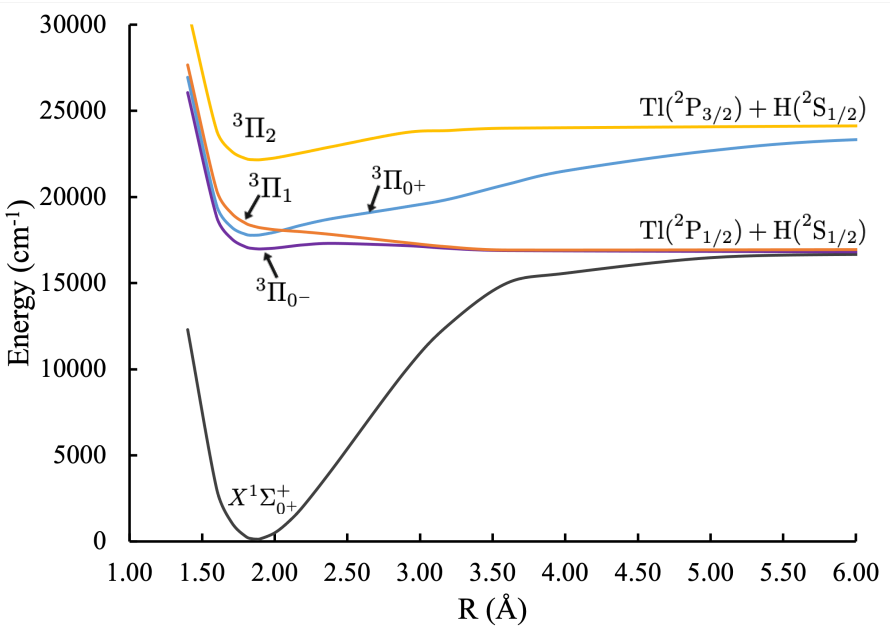

Figure 3.4: The potential energy curves of the 7 low-lying states of TlH at the X2C-MRPT2 level with frozen core orbital approximation.

electrons in Tl $5d$ spinor orbitals are correlated with the CAS space and all the virtual orbitals. The potential energy curves are obtained from single point calculations on a grid of Tl–H distances between 1.4 and 3.6 Å, with grids denser around the minimum in order to obtain the equilibrium internuclear distance R_e. A single point calculation is carried out at a large distance of 9.0 Å for the evaluation of dissociation energy D_e for bound $X^1\Sigma^+_{0+}$ and $^3\Pi_{0+}$ states. The potential energy curves are fitted using the functional form of Morse potential[256]. The harmonic frequencies ω_e are determined by the second derivatives of the fitted functions.

The shape of the potential energy curves shows excellent agreement with the previous theoretical studies. [220, 258, 259, 264, 265] Consistent with experimental observation,[261, 262] the $X^1\Sigma^+_{0+}$ ground state and $^3\Pi_{0+}$ excited state are the two vibrationally bound states with a sufficiently deep potential well. We therefore focus on the benchmark results for these two states. Table 3.4 summarizes the computed spectroscopic constants, including

	X2C-CASSCF	X2C-MRPT2	4C ic-CASPT2 [a]	MCP SO -MCQDPT [b]	(ic-MRCI+Q) -SO [c]	Exp.[d]
$X^1\Sigma^+_{0^+}$						
R_e (Å)	1.924	1.873	1.870	1.876	1.8826	1.872
D_e (eV)	1.52	2.06	1.84	2.03	2.05	2.06
ω_e (cm^{-1})	1439.6	1395.4	–	1391	1390.4	1390.7
$^3\Pi_{0^+}$						
R_e (Å)	1.866	1.858	–	1.887	1.878	1.908
D_e (eV)	0.60	0.77	–	0.79	0.72	0.74
ω_e (cm^{-1})	980.0	1034.4	–	923	943.8	1043.3

[a] It used uncontracted Dyall's cv3z and uncontracted cc-pVTZ basis sets for Tl and H.[218]

[b] Model core potential spin-orbit multiconfigurational quasidegenerate perturbation theory [257, 258] with one-electron SOC treated in the perturbation theory using a large term space. It used uncontracted well-tempered basis set and augmented basis function from aug-cc-pV5Z-PP basis set.

[c] ic-MRCI with Davidson correction (+Q) and SOC treated perturbatively using relativistic effective core potential (ECP60MDF) together with aug-cc-pwCV5Z-PP basis set for Tl, and aug-cc-pV5Z for H. [259]

[d] Experimental data is taken from Ref.260–263.

Table 3.4: Computed spectroscopic constants of TlH using X2C-CASSCF and X2C-MRPT2 methods, compared with experiments and results from other theoretical work. Significant figures are truncated based on the available experimental and theoretical values in literature.

equilibrium bond distances, dissociation energies, and harmonic frequencies, of $X^1\Sigma^+_{0^+}$ and $^3\Pi_{0^+}$ states, as well as results from experiments and other calculations in literature. X2C-MRPT2 yields very accurate results for the ground $X^1\Sigma^+_{0^+}$ state with less than 0.4% error compared to experiment and outperforms the other theoretical results considered here. The inclusion of dynamic correlation significantly improves the X2C-CASSCF results, indicating the correlation of $5d$ orbitals are important to obtain satisfactory spectroscopic constants for TlH. As for the $^3\Pi_{0^+}$ excited state, the dissociation energy and harmonic frequency obtained from X2C-MRPT2 agree well with experiment while the equilibrium internuclear distance deviates slightly further from experiment compared to X2C-CASSCF. Overall, the theoretical prediction of the potential energy curves and the spectroscopic constants at the X2C-MRPT2 level is in excellent agreement with experiments.

3.5 Conclusions

In this work, we introduce a determinant based Kramers-unrestricted exact-two-component multi-reference second order perturbation (X2C-MRPT2) method which variationally includes relativistic corrections with a perturbative dynamic correlation. The restricted active space partitioning scheme is employed to provide an adjustable correlation space for the second order perturbation treatment. The multi-state perturbation theory is also developed to improve the descriptions of ground and excited states.

Benchmark studies of atomic fine structure splitting and spectroscopic constants of molecular monohydrides show that X2C-MRPT2 outperforms the fully perturbative CASPT2-SO for heavier atomic species ($\geq$5th row). This observation suggests that as the strength of the spin-orbit coupling increases, the coupling between relativistic corrections and dynamic correlation also increases and cannot be treated as separate perturbations.

The accuracy of X2C-MRPT2 is similar to the fully variational X2C-MRCI. While both X2C-MRPT2 and X2C-MRCISD produce accurate fine-structure splitting results, X2C-MRPT2, being a perturbation theory for dynamic correlation, is much more computational advantageous than the fully variational X2C-MRCISD. Generally speaking, the current implementation of X2C-MRPT2 is $\sim$7 times faster than X2C-MRCISD with the same orbital partitioning.

As a non-variational approach, the dynamic correlation introduced by the PT2 treatment is sensitive to the choice of correlation space. The improved virtual orbital scheme[188, 244, 245] was used in this work. More advanced virtual space decomposition approaches[229, 266] will be evaluated in a future work.

Chapter 4

RELATIVISTIC FOUR-COMPONENT MULTIREFERENCE ELECTRONIC STRUCTURE METHODS

The fully correlated frequency-independent Dirac-Coulomb-Breit Hamiltonian provides the most accurate description of electron-electron interaction before going to a genuine relativistic quantum electrodynamics theory of many-electron systems. In this work, we introduce a correlated Dirac-Coulomb-Breit multiconfigurational self-consistent-field method within the frameworks of complete active space and density matrix renormalization group. In this approach, the Dirac-Coulomb-Breit Hamiltonian is included variationally in both the mean-field and correlated electron treatment. We also analyze the importance of the Breit operator in electron correlation and the rotation between the positive- and negative-orbital space in the no-virtual-pair approximation. Atomic fine-structure splittings and lanthanide contraction in diatomic fluorides are used as benchmark studies to understand the contribution from the Breit correlation.

4.1 Introduction

In many-body electronic structure theory, the frequency-independent Dirac-Coulomb-Breit operator defined in the Coulomb gauge provides the most accurate description[154, 267–270] of electron-electron interaction before going to a genuine relativistic quantum electrodynam-

ics theory.[124, 125, 141–144] The Dirac-Coulomb-Breit operator can be written as

$$V_{ee}^{\mathrm{DCB}} = \sum_{i=1}^{N} \sum_{j>i} (g^C(i,j) + g^B(i,j)) \tag{4.1}$$

$$g^C(i,j) = \frac{1}{r_{ij}} \tag{4.2}$$

$$g^B(i,j) = -\frac{1}{2}\left(\frac{\boldsymbol{\alpha}_i \cdot \boldsymbol{\alpha}_j}{r_{ij}} + \frac{\boldsymbol{\alpha}_i \cdot \mathbf{r}_{ij} \boldsymbol{\alpha}_j \cdot \mathbf{r}_{ij}}{r_{ij}^3} \right) \tag{4.3}$$

where $\{i, j\}$ are electron indices. The components of the $\boldsymbol{\alpha}$ matrices are defined as

$$\boldsymbol{\alpha}_{i,J} = \begin{pmatrix} \mathbf{0}_2 & \boldsymbol{\sigma}_J \\ \boldsymbol{\sigma}_J & \mathbf{0}_2 \end{pmatrix}, \quad J = \{x, y, z\} \tag{4.4}$$

and $\boldsymbol{\sigma}$ consists of Pauli matrices.

$$\mathbf{I} = \begin{pmatrix} 1 & 0 \\ 0 & 1 \end{pmatrix}, \boldsymbol{\sigma}_x = \begin{pmatrix} 0 & 1 \\ 1 & 0 \end{pmatrix}, \boldsymbol{\sigma}_y = \begin{pmatrix} 0 & -i \\ i & 0 \end{pmatrix}, \boldsymbol{\sigma}_z = \begin{pmatrix} 1 & 0 \\ 0 & -1 \end{pmatrix}. \tag{4.5}$$

The Breit operator (Eq. (4.3)) includes the magnetic interaction and a gauge term, which is the most computational intensive. A lower cost operator that still carries the magnetic interaction is the Dirac-Coulomb-Gaunt Hamiltonian defined in Feynman gauge:

$$V_{ee}^{\mathrm{DCG}} = \sum_{i=1}^{N} \sum_{j>i} (g^C(i,j) + g^G(i,j)) \tag{4.6}$$

$$g^G(i,j) = -\frac{\boldsymbol{\alpha}_i \cdot \boldsymbol{\alpha}_j}{r_{ij}} \tag{4.7}$$

It is generally well understood that the Breit operator in the Coulomb gauge is more accurate than the Gaunt operator in the Feynman gauge,[269, 270] and that the variational treatment of the frequency-independent Breit interaction is important for both correlation calculations and property evaluations.[271, 272]

Although the Dirac-Coulomb and Dirac-Coulomb-Gaunt Hamiltonians have been used in

correlated many-body calculations,[128, 131, 225] due to the large computational cost of the gauge term in the Breit operator, the application of the Dirac-Coulomb-Breit Hamiltonian mostly remains in the mean-field theory or used as perturbative treatment in the correlated methods. Frequency-independent Breit interactions have been implemented with finite difference methods,[273–275] Slater type basis,[276] and Gaussian basis.[154, 158, 226, 277–283] Recently, we introduced a Pauli matrix quaternion representation with an optimal spin- and component-separation algorithm that results in a minimal floating-point count algorithm for building the Dirac-Coulomb-Breit Hamiltonian.[154, 283] The reduced computational cost of the four-component density-integral contraction allows for the development of fully correlated Dirac-Coulomb-Breit many-body methods.

In this work, we introduce the fully correlated Dirac-Coulomb-Breit many-body theory in the variational four-component multiconfigurational self-consistent-field (MCSCF) framework, including the complete active space self-consistent field (CASSCF) and density-matrix renormalization group SCF (DMRGSCF) methods. To the best of our knowledge, this is the first time the Dirac-Coulomb-Breit operator has been applied in the context of DMRG. We will place a special emphasis on the importance of positive-negative-energy orbital rotation in the MCSCF procedure and the contribution of the Breit correlation beyond the Dirac-Coulomb operator.

4.2 Breit Operator at Multiconfiguration Self-consistent-field Level

In this work we develop correlated Dirac-Coulomb-Breit four-component multiconfigurational self-consistent-field methods (DCB-MCSCF) in the frameworks of the complete active space self-consistent field (CASSCF) and density matrix renormalization group self-consistent field (DMRGSCF). Since the fundamental expressions of four-component CASSCF and DMGRSCF are similar to exact-two-component (X2C) implementations, we recommend the readers to Refs. 130 and 136 for more information on Kramers-unrestricted CASSCF and DMRG, respectively. In this section, we focus on methodological developments that are unique to the DCB-MCSCF theory.

In this section the following notation will be used: i, j, k, l label inactive four-spinors; t, u, v, w label active four-spinors; a, b, c, d label virtual four-spinors; p, q, r, s label general four-spinors; I, J, K label Slater determinants. Indices with positive and negative superscript (*e.g.*, i^+, j^+ and a^-, b^-) refer to positive-energy and negative-energy four-spinors, respectively. The following discussions assume all quantities are complex-valued unless stated otherwise.

4.2.1 Four-Component Multiconfigurational Self-consistent-field

Four-Component Multiconfigurational Wave Function in No-Virtual-Pair Approximation

The Dirac equation is cast in a finite Gaussian type basis. The four-spinor molecular orbitals (MO) are expanded in two-spinor basis

$$\psi_p^L = \sum_\tau \sum_{\mu=1}^{N} c_{\mu\tau,p}^L \chi_{\mu\tau}^L, \quad \psi_p^S = \sum_\tau \sum_{\mu=1}^{N} c_{\mu\tau,p}^S \chi_{\mu\tau}^S \tag{4.8}$$

where $\tau \in \{\alpha, \beta\}$ and N is the number of spatial basis functions. The large component basis is defined as

$$\chi_{\mu\alpha}^L = \begin{pmatrix} \chi_\mu \\ 0 \end{pmatrix}, \qquad \chi_{\mu\beta}^L = \begin{pmatrix} 0 \\ \chi_\mu \end{pmatrix} \tag{4.9}$$

where χ_μ are spatial basis functions. The relationship between the large and small component two-spinor basis can be defined via the restricted kinetic balance (RKB) condition which ensures the correct nonrelativistic limit of the positive energy states.[146–148, 180, 284, 285]

$$\chi_\mu^S = \frac{1}{2mc} \boldsymbol{\sigma} \cdot \mathbf{p} \chi_\mu^L \tag{4.10}$$

In the RKB condition, the Dirac–Hartree–Fock Hamiltonian in matrix form can be efficiently built and solved in the Pauli matrix quaternion representation (see Refs. 283 and 154 for Dirac-Coulomb-Gaunt and Dirac-Coulomb-Breit Dirac–Hartree–Fock).

The solution of the four-component Dirac–Hartree–Fock equation consists of sets of pos-

itive and negative eigenvalues $\{\epsilon^+\}$, $\{\epsilon^-\}$ with corresponding molecular orbital coefficients $(\mathbf{C}_L^+ \quad \mathbf{C}_S^+)^T$ for the positive and $(\mathbf{C}_L^- \quad \mathbf{C}_S^-)^T$ for the negative energy solutions. These are mean-field spin-coupled, relativistically-corrected molecular four-spinors that will be used for subsequent correlated calculations. We employ the conventional no-virtual-pair approximation (NVPA) where only positive-energy orbitals $(\mathbf{C}_L^+ \quad \mathbf{C}_S^+)^T$ are considered in the multiconfigurational expansion.[150, 203, 286]

DCB-CASSCF

For NVPA CAS wave function, $|\Psi^+\rangle$ is described as a linear combination or a configuration interaction (CI) expansion of Slater determinants, $|K^+\rangle$, constructed from a subset of the orthonormal positive-energy four-spinors.

$$|\Psi^+\rangle = \sum_{K=1}^{N_{\text{det}}} C_K |K^+\rangle \tag{4.11}$$

where N_{det} is the total number of determinants in the expansion.

The correlated DCB-CASSCF energy is written as,

$$E = \epsilon^c \; + \; \langle \Psi^+ | \hat{H}^{CAS} | \Psi^+ \rangle \tag{4.12}$$

where ϵ^c is the Dirac–Hartree–Fock (*e.g.*, using the Dirac-Coulomb-Breit Hamiltonian) energy of the inactive orbitals (the "core energy") and is defined as

$$\epsilon^c = \sum_{i^+} h_{i^+i^+} + \frac{1}{2} \sum_{i^+j^+} \left[(i^+i^+|V_{ee}^{\text{DCB}}|j^+j^+) - (i^+j^+|V_{ee}^{\text{DCB}}|j^+i^+) \right] \tag{4.13}$$

where V_{ee}^{DCB} is the Dirac-Coulomb-Breit operator in Eq. (4.1). $\hat{H}^{CAS}$ is the active space

Hamiltonian and is defined as

$$\hat{H}^{CAS} = \sum_{t^+u^+} h^c_{t^+u^+} \hat{E}_{t^+u^+} + \frac{1}{2} \sum_{t^+u^+v^+w^+} (t^+u^+|V^{\mathrm{DCB}}_{ee}|v^+w^+) \left(\hat{E}_{t^+u^+} \hat{E}_{v^+w^+} - \delta_{u^+v^+} \hat{E}_{t^+w^+} \right) \tag{4.14}$$

where h^c is the core Dirac–Fock matrix, and is given by

$$h^c_{t^+u^+} = h_{t^+u^+} + \sum_{i^+} \left[(t^+u^+|V^{\mathrm{DCB}}_{ee}|i^+i^+) - (t^+i^+|V^{\mathrm{DCB}}_{ee}|i^+u^+) \right] \tag{4.15}$$

and $\hat{E}_{p^+q^+}$ is an operator that excites from four-spinor orbital q^+ to p^+ and can be written using the usual creation and annihilation operators $\hat{E}_{p^+q^+} = a^\dagger_{p^+} a_{q^+}$. The excitation list is generated using Handy's string based approach [36] adapted to the four-component orbital space.

In NVPA DCB-CASSCF, only positive-energy four-spinors are used in the CI expansion and energy evaluation, and all corresponding two-electron integrals in both mean-field and correlation treatments are evaluated with the Dirac-Coulomb-Breit operator.

DCB-DMRGSCF

The DMRG wave function can be written as

$$|\Psi\rangle = \sum_I C^{I_1 I_2 \ldots I_N} |\boldsymbol{I}\rangle \,, \;\; |\boldsymbol{I}\rangle = |I_1, ..., I_N\rangle \tag{4.16}$$

where $C^{I_1 I_2 \ldots I_N}$ are complex-valued configuration-interaction coefficients, N is the number of active four-spinors, and $|I\rangle$ is an occupation number vector comprised of Kramers-unrestricted four-spinor orbitals. Upon refactoring to the matrix-product state (MPS) ansatz, the no-pair wave function used in DMRGSCF is

$$\left|\Psi^+\right\rangle = \sum_{I_1,...,I_N} \sum_{a_1,...,a_{N-1}} M^{I_1}_{1a_1} M^{I_2}_{a_1 a_2} \cdots M^{I_N}_{a_{N-1}1} |I_1, ..., I_N\rangle = \sum_{\boldsymbol{I}} M^{I_1} M^{I_2} \cdots M^{I_N} |\boldsymbol{I}\rangle \tag{4.17}$$

where $\{I_p\}$ are occupations and $\{a_i\}$ are the virtual indices (bond dimension) that are capped by the parameter $m_{\max} = 2^{N/2}$, commonly referred to as *number of renormalized block states*.[287] Variational relativistic DMRG methods are an emerging area of research.[134–136, 288]

We enforce the NVPA on the Kramers-unrestricted MPS wave function by placing constraints on occupations (I_p in Eq. (4.16)). We restrict negative-energy four-spinors (p^-) to be unoccupied (vac), but allow positive-energy four-spinors (p^+) to be unoccupied or occupied (occ),[134, 135]

$$I_p \in \begin{cases} \{|\text{occ}\rangle, |\text{vac}\rangle\} \text{ for } p^+ \\ \{|\text{vac}\rangle\} \text{ for } p^-. \end{cases} \tag{4.18}$$

Positive-Negative-Energy Orbital Rotation

The four-component multiconfigurational wave function is optimized by making the energy stationary with respect to variations of *both* the configuration parameters and the four-spinor coefficients. For the complex configuration interaction (CI) coefficients, this is achieved via solution of the CASCI eigenvalue equation.

The complex four-spinor orbitals are optimized via a unitary transformation of the existing orbitals

$$\psi'_{p^+}(\mathbf{q}) = R_{p^+q}\psi_q(\mathbf{q}) \tag{4.19}$$

where the $\mathbf{R}$ matrix may be written in terms of an anti-Hermitian orbital-rotation matrix $\mathbf{X}$:

$$\mathbf{R} = \exp(\mathbf{X}) \tag{4.20}$$

$$X_{p^+q} = -X^*_{q^+p} \tag{4.21}$$

The CASSCF wavefunction is optimized when

$$\frac{\partial E}{\partial \mathbf{C}} = 0 \;\; ; \;\; \frac{\partial E}{\partial \mathbf{X}} = 0 \tag{4.22}$$

There are three orbital optimization strategies investigated in this work:

- No orbital rotation: In this scheme, the four-component multiconfigurational methods become DCB-CASCI and DCB-DMRG using positive- and negative-energy four-spinors from the solution of Dirac-Coulomb-Breit Hartree–Fock without further orbital optimization.

- Rotation within positive-energy orbitals only: In this scheme, the orbital rotation matrix (Eq. (4.21)) is restricted to positive-energy space only, *i.e.*, $X_{p^+q^+}$. The negative-energy four-spinors are from the solution of Dirac-Coulomb-Breit Hartree–Fock without further orbital optimization.

- Rotation in the full space including positive- and negative-energy orbitals: In this scheme, the orbital rotation matrix (Eq. (4.21)) also considers the rotation between positive- and negative-orbital space in CASSCF and DMRGSCF energy minimization, *i.e.*, $X_{p^+q^\pm}$.

For Dirac–Hartree–Fock we use rotation in the full space including both positive- and negative-energy orbitals and enforce NVPA by restricting the density construction to only positive-energy spinors (our single determinant has no negative-energy spinor occupation).

AO-Direct Integral Transformation of Dirac-Coulomb-Breit Hamiltonian

The correlated Dirac-Coulomb-Breit many-body theory requires two-electron repulsion integrals (ERIs) in the form of $(pq|V_{ee}^{\mathrm{DCB}}|rs)$ where $\{p, q, r, s\}$ are general four-component orbitals and V_{ee}^{DCB} is defined in Eq. (4.1). In correlated relativistic treatment, the integral transformation from the atomic orbital to four-spinor basis is the most computational expensive

step. Particularly, in the correlated DCB Hamiltonian, the gauge integral transformation is the most complicated and computational dominant procedure.

The contraction scheme in the Pauli quaternion representation[154, 283] recently developed by the team allows for fast transformation directly, without going through an in-core assembly of spinor integrals, from quantities computed in the atomic orbital basis to ERIs in four-spinor basis. For example, the AO-direct transformation of the gauge term starts from four basic types of scalar gauge integrals in the atomic orbital basis (see Reference 154 for detailed derivations):

$$(\mu\nu|\boldsymbol{\nabla}_\nu \cdot \mathbf{r}_{12}\, \mathbf{r}_{12} \cdot \boldsymbol{\nabla}_\kappa|\kappa\lambda)_3 \tag{4.23}$$

$$(\mu\nu|(\mathbf{r}_{12} \times \boldsymbol{\nabla}_\nu)_J(\mathbf{r}_{12} \cdot \boldsymbol{\nabla}_\kappa)|\kappa\lambda)_3 \tag{4.24}$$

$$(\mu\nu|(\boldsymbol{\nabla}_\nu \cdot \mathbf{r}_{12})(\boldsymbol{\nabla}_\kappa \times \mathbf{r}_{12})_J|\kappa\lambda)_3 \tag{4.25}$$

$$(\mu\nu|(\mathbf{r}_{12} \times \boldsymbol{\nabla}_\nu)_J(\boldsymbol{\nabla}_\kappa \times \mathbf{r}_{12})_K|\kappa\lambda)_3 \tag{4.26}$$

$$J, K \in \{x, y, z\}$$

where the subscript "3" denotes that the integral is $\frac{1}{r_{12}^3}$ in contrast to $\frac{1}{r_{12}}$. The contraction between scalar AO integrals with density ($\mathcal{O}(N^6)$ method) or four-spinor coefficients ($\mathcal{O}(N^5)$ method) can be easily carried out in the Pauli quaternion representation. This approach results in an efficient transformation procedure that leads to the AO-direct-enabled correlated Dirac-Coulomb-Breit many-body theory. Although the technical advances are non-trivial to implement, the theoretical foundation is well illustrated in references 154 and 283.

4.2.2 Results and discussion

The Dirac-Coulomb-Breit-CASSCF calculations were performed in the Chronus Quantum[243] software package. All calculations in this work are all electron and use a Kramers-unrestricted spinor basis in the no-virtual-pair approximation. The Dirac-Coulomb-Breit-DMRGSCF implementation is built off our previous modular interface between QCMaquis[289–291] and

Chronus Quantum[243] computational packages.[136] The integrals for the four-component Hamiltonians and orbital optimizations were computed in Chronus Quantum, and the matrix-product state optimizations were performed in QCMaquis. For more information on four-component integral evaluation, see References 154 and 283. We use a "state-specific" approach for optimization of the matrix-product-state wave function,[292] and a "state-averaged" approach for orbital optimization.[293] The matrix product state utilized no additional reordering of orbitals. Unlike CASSCF, the active-active orbital rotations are non-redundant for DMRGSCF (with unconverged m); however, we did not include them in this study.[294, 295] Orbital optimizations were performed with an approximated quasi-second-order Newton-Raphson method.[188]

Importance of Positive-Negative-Energy Orbital Rotation

Core Electrons

In the no-virtual-pair approximation (NVPA), only positive energy molecular orbitals are used in the correlated wave function treatment, such as the configuration interaction expansion. However, positive- and negative-energy orbitals are not completely disentangled from each other due to the kinetic-balance condition. Therefore, the orbital rotation in the correlated relativistic method should be carefully examined. In this section, three strategies are examined within NVPA: no orbital rotation (*e.g.*, CASCI), orbital rotation within the positive energy space (denoted as CASSCF^{+}), and orbital rotation in the full four-component space (denoted as CASSCF$^{\pm}$). In the full orbital rotation including both positive and negative energy spaces, the negative energy orbitals are treated as virtuals.

We first examine the importance of orbital rotation for core-electrons. The ground state energy of Rn^{84+} was computed using three Hamiltonians, including Dirac-Coulomb (DC), Dirac-Coulomb-Gaunt (DCG), and Dirac-Coulomb-Breit (DCB), in the correlated CAS(2,10) treatment. The CAS(2,10) consisted of the ns, $(n+1)s$, and $(n+1)p$. Uncontracted ANO-RCC-MB (255 basis functions including up to f function) is used in this study. In this basis set, the tightest atomic s-orbital has an exponent of $53,906,998$. Table 4.1 compares the

Table 4.1: Electron correlation energies (in eV) of Rn^{84+} computed using different orbital rotation schemes. Correlation energy, E_c, is defined as the difference between calculations using correlated method and Dirac–Hartree–Fock theory. Superscript $\pm$ refers to calculations with positive-negative-energy orbital rotations, whereas superscript + only does orbital rotations in the positive energy space. The CASCI method does not do orbital rotations. CAS(2,10) is used.

	E_c (eV)
E(DCB-CASSCF$^{\pm}$)$-E$(DCB-HF)	-3.099
E(DCB-CASSCF^{+})$-E$(DCB-HF)	-3.404
E(DCB-CASCI)$-E$(DCB-HF)	-0.155
E(DCG-CASSCF$^{\pm}$)$-E$(DCG-HF)	-3.804
E(DCG-CASSCF^{+})$-E$(DCG-HF)	-4.237
E(DCG-CASCI)$-E$(DCG-HF)	-0.181
E(DC-CASSCF$^{\pm}$)$-E$(DC-HF)	-1.141
E(DC-CASSCF^{+})$-E$(DC-HF)	-1.225
E(DC-CASCI)$-E$(DC-HF)	-0.059

correlation energy computed using the three different orbital rotation strategies in correlated CAS calculations. The correlation energy, E_c, is defined as the energy difference between four-component correlated calculation and the four-component Hartree-Fock mean-field theory with the same relativistic operator.

Table 4.1 suggests that the orbital rotation plays a very important role in recovering the correlation energy, exemplified by the large difference between CASCI and CASSCF^{+}/CASSCF$^{\pm}$ calculations. When comparing the partial orbital rotation within the positive energy space in CASSCF^{+} and the full rotation in CASSCF$^{\pm}$, a $\sim$10% over-estimation of the correlation energy was observed for DCB-CASSCF^{+}, DCG-CASSCF^{+}, and DC-CASSCF^{+}. This analysis suggests that orbital rotation in the full four-component space including both positive and negative energy orbitals is essential in accurate correlated treatment of core electrons and cannot be neglected at the correlated level.[128]

Valence Electrons

Table 4.2: Electron correlation energies (in eV) of alkaline earth metals (Be to Ra) computed using different orbital rotation schemes. Superscript ± refers to calculations with positive-negative-energy orbital rotations, whereas superscript + only does orbital rotations in the positive energy space. The CASCI method does not do orbital rotations. CAS(2,36) is used.

	Be	Mg	Ca	Sr	Ba	Ra
E(DCB-CASSCF$^{\pm}$)$-E$(DCB-HF)	−1.192	−0.854	−0.748	−0.683	−0.636	−0.560
E(DCB-CASSCF^{+})$-E$(DCB-HF)	−1.192	−0.854	−0.748	−0.683	−0.636	−0.560
E(DCB-CASCI)$-E$(DCB-HF)	−0.319	−0.332	−0.665	−0.559	−0.458	−0.262
E(DCG-CASSCF$^{\pm}$)$-E$(DCG-HF)	−1.194	−0.854	−0.748	−0.683	−0.635	−0.560
E(DCG-CASSCF^{+})$-E$(DCG-HF)	−1.194	−0.854	−0.748	−0.683	−0.635	−0.560
E(DCG-CASCI)$-E$(DCG-HF)	−0.319	−0.332	−0.665	−0.559	−0.458	−0.262
E(DC-CASSCF$^{\pm}$)$-E$(DC-HF)	−1.192	−0.854	−0.748	−0.683	−0.636	−0.561
E(DC-CASSCF^{+})$-E$(DC-HF)	−1.192	−0.854	−0.748	−0.683	−0.636	−0.561
E(DC-CASCI)$-E$(DC-HF)	−0.319	−0.332	−0.665	−0.559	−0.458	−0.262

We now focus on the importance of positive-negative orbital rotation on valence electrons. We report in Table 4.2 correlation energy of CASCI, CASSCF^{+}, and CASSCF$^{\pm}$ for alkaline earth metals of Be to Ra with an active space consisting of the outermost ns electrons and the ns, np, $(n+1)s$, and $(n+1)p$ orbitals (CAS(2,16)) for Be-Ca and the ns, np, $(n-1)d$, $(n+1)s$, $(n+1)p$, and nd orbitals for Sr-Ra (CAS(2,36)). It is obvious that CASCI with no orbital optimization, compared to CASSCF (both "$^{+}$" and "$^{\pm}$"), misses a large part of the electron correlation. In contrast to the case for core electrons, doing the full positive-negative orbital rotation in CASSCF$^{\pm}$ for valence electrons does not significantly change the correlation energy compared to CASSCF^{+}. This observation suggests that positive-negative orbital rotation with CASSCF becomes less important for valence electrons further away from the nucleus and can be treated at the Dirac–Hartree–Fock level. Comparing correlation energies computed using three different relativistic Hamiltonians will be discussed in the next section.

Importance of Breit Operator in Correlation Energy

Table 4.1 and Table 4.2 also compare the correlation energy computed using the three different relativistic Hamiltonians in correlated calculations. Figure 4.1 shows the trend of CAS(2,10) correlation energy in He-like two-electron systems as the nuclear charge increases. Larger active spaces, including CAS(2,18) and CAS(2,46), were also tested (see SI). For CASSCF^{+} and CASSCF$^{\pm}$, large active spaces do not change the results, suggesting that the benchmark tests show in Figure 4.1 have reached the full MCSCF limit. This is not the case for CASCI calculations which need a much larger active space to reach the full CI limit.

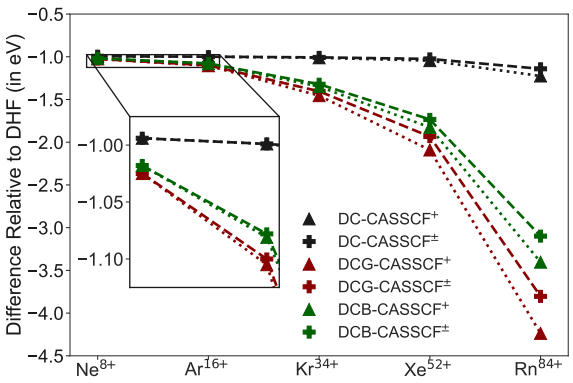

Figure 4.1: Electron correlation energies for CASSCF^{+} and CASSCF$^{\pm}$ relative to Dirac–Hartree–Fock with DC, DCG, and DCB Hamiltonians (in eV) for He-like two-electron systems. CAS(2,10) is used.

From Table 4.1, it is obvious that the correlation energy for Rn^{84+} arising from the Breit operator ($-3.099 - (-1.141) = -1.958$ eV) is much bigger than that from the Dirac-Coulomb term (-1.141 eV). This observation suggests that the Breit correlation becomes the dominant contribution for deep core electrons.[124] Compared to the Dirac-Coulomb-Breit result (DCB-CASSCF$^{\pm}$), the Dirac-Coulomb-Gaunt Hamiltonian over-estimates the correlation energy by ∼25% whereas the Dirac-Coulomb term under-estimates it by ∼63%. These behaviors can be understood from the nature of the corresponding Hamiltonians. The Dirac-Coulomb Hamiltonian lacks the magnetic and gauge interactions which play a

significant role in the electron-electron interaction of deep core electrons. The Gaunt term is twice the magnetic interaction in the Breit Hamiltonian which has an additional gauge term. As discussed in Ref. 154, the difference between the Gaunt and Breit Hamiltonians results in ∼20% difference in relativistic mean-field energy correction.[154] Table 4.1 suggests that this difference is also manifested in the correlation energy.

Figure 4.1 shows that while the difference in correlation energy between DC, DCG, and DCB is relatively small for core electrons in light elements, it quickly becomes significant as the nuclear charge increases (see SI for all computed results, including CASCI). For Ne^{8+}, the DC-CASSCF$^{\pm}$ and DCG-CASSCF$^{\pm}$ differ by 31 meV, and DCG-CASSCF$^{\pm}$ and DCB-CASSCF$^{\pm}$ correlation energies differ by 7 meV. They quickly increase to 101 meV between DC-CASSCF$^{\pm}$ and DCG-CASSCF$^{\pm}$ and 22 meV between DCG-CASSCF$^{\pm}$ and DCB-CASSCF$^{\pm}$ for Ar^{16+} – noticeable differences among three different relativistic operators. In addition, the difference between CASSCF$^{\pm}$ and CASSCF^{+} orbital rotation schemes also becomes noticeable starting at Ar^{16+}.

In contrast, for valence electrons, we find no strong dependence of electron correlation on the Breit operator as shown in Table 4.2. In addition, the CASSCF (both "+" and "±") correlation energy for the valence electrons decreases as atomic number increases, exhibiting an opposite trend compared to that for the core electrons. The CASCI results do not display the same trend as CASSCF due to a lack of optimization of the virtual orbitals.

Atomic Fine-Structure Splitting

In Table 4.3 we report atomic fine-structure splitting for Ga, In, Tl, La, and Te using state-average Dirac-Coulomb, Dirac-Coulomb-Gaunt, and Dirac-Coulomb-Breit 4C-CASSCF$^{\pm}$ and 4C-DMRGSCF$^{\pm}$. For the atomic systems, an uncontracted ANO-RCC-VTZP basis set was used.[296, 297] The wave functions used a valence active space and averaged over the total number of m_J states involved in the fine-structure splitting. For Ga, In, and Tl we used a SA(6)-CAS(3,8), for La we used a SA(10)-CAS(3,12), and for Te we used a SA(9)-CAS(6,8). SA(N) denotes a CASSCF obital optimization averaged over N number of states. Conver-

Table 4.3: Atomic fine-structure splitting (in eV) computed using state-average 4C-CASSCF$^{\pm}$ and 4C-DMRGSCF$^{\pm}$. In DMRG calcualtions, we used $m = m_{\max}$ where $m_{\max} = 2^{N_{\text{orb}}/2}$.

		4C-CASSCF$^{\pm}$	4C-DMRGSCF$^{\pm}$	Expt.[246]
Ga ($^2P_{1/2} \rightarrow {}^2P_{3/2}$)	DC	0.087	0.087	
	DCG	0.085	0.085	0.102
	DCB	0.085	0.085	
In ($^2P_{1/2} \rightarrow {}^2P_{3/2}$)	DC	0.233	0.233	
	DCG	0.230	0.230	0.274
	DCB	0.230	0.230	
Tl ($^2P_{1/2} \rightarrow {}^2P_{3/2}$)	DC	0.849	0.849	
	DCG	0.839	0.839	0.966
	DCB	0.839	0.839	
La ($^2D_{3/2} \rightarrow {}^2D_{5/2}$)	DC	0.086	0.086	
	DCG	0.083	0.083	0.131
	DCB	0.083	0.083	
Te ($^3P_2 \rightarrow {}^3P_0$)	DC	0.589	0.589	
	DCG	0.584	0.584	0.584
	DCB	0.584	0.584	

gence thresholds of 10^{-7} au in energy and 5×10^{-4} au in orbital rotation gradient were used for 4C-CASSCF$^{\pm}$ and 4C-DMRGSCF$^{\pm}$.

The computed results shown in Table 4.3 show a good agreement with experimental measurements, with an error ranging from 10 meV (or 1.7%) in Te to 127 meV (or 13%) in Tl. Both 4C-CASSCF$^{\pm}$ and 4C-DMRGSCF$^{\pm}$ converge to the same results as expected, given the large value of m. Even though the valence space CAS calculations lack dynamical correlation, the error could be reduced further by increasing the size of the active space. For Ga atom, increasing the size of the active space to a CAS(3,26) improves the Ga splitting to 0.093 eV with DC-DMRGSCF$^{\pm}(m = 150)$ compared to experimental value of 0.102 eV. We defer the discussion on correlation convergence using the Dirac-Coulomb-Breit MCSCF approach to a future study as the goal of this section is to analyze the importance of the Breit Hamiltonian beyond the Coulomb operator for spectroscopic properties.

As we go down the periodic table, the inclusion of the Gaunt or the Breit operator consistently decreases the fine-structure splitting, *e.g.*, by 2 meV for Ga to 10 meV for Tl. The improvement brought about by Gaunt or Breit operator seems to deviate away from

experiments except for Te. This is mainly because the correlation effect is not fully converged in a small active space. In other words, the "better" Dirac-Coulomb results are false positive due to unconverged electron correlation treatment.

Comparing the Gaunt and the Breit electron correlations, the difference for the atomic systems tested here is less than a meV. This agrees with our alkaline earth metal findings regarding the importance of correlated Breit treatments for valence electrons.

4.3 Breit Operator in Dynamic Correlation

In this section, we would like to provide an accurate benchmark of correlated Dirac-Coulomb-Breit multi-reference methods without much approximations, aiming to fully understand the effects of relativistic two-electron interactions and correlation space on spin-orbit coupling, as the start of our exploration of reliable approximations to get the right answer with the right reasons. We benchmarked the spin-orbit splittings of the ground and first-excited states and analyzed the effect of frozen core/virtual approximations on atomic cases, from which we showcase the importance of the inclusion of inner-valence orbitals for obtaining sub-meV accuracy, as well as the important role of Breit interaction.

4.3.1 Four-Component Multireference Configuration Interaction and Multireference Second-order Perturbation Theory

With the aforementioned four-component (4C) MCSCF wavefunction as our reference, 4C Hamiltonians at different approximation levels can be extended in post-MCSCF level of the methods, such as multireference configuration interaction (MRCI) and multireferce second-order perturbation theory (MRPT). With no-virtual pair approximation (NVPA)[150, 203, 286], the formalism of post-MCSCF methods for four-component are the same as the ones for exact-two-component Hamiltonian (X2C), as introduced in Section 2.2.2 for CI and Chapter 3 for MRPT2. Despite the use of the conventional NVPA, both 4C-MRCI and 4C-MRPT2 utilize the molecular spinors optimized with 4C-CASSCF including positive-negative-energy orbital rotation, *i.e.* 4C-CASSCF$^{\pm}$. [203, 210]

However, 4C-post-MCSCF methods are still more expensive than their two-component variants due to: (1) Expensive integral transformation in four spinor basis; (2) the lack of basis set contraction scheme results in the use of uncontracted basis in the correlation methods, *i.e.* a large number of spinors in the correlated space to fully capture dynamic correlation. The computational cost from using multi-reference methods with the frequency independent Dirac-Coulomb-Breit (DCB) Hamiltonian is so high that one should investigate possible approaches to lower the scaling. In non-relativistic regime, when high-level post-CASSCF methods have been extended to predict larger scale systems, various approaches to reduce the cost are needed and it has been an important research topic. One group of the techniques is the low-rank approximations to the electron repulsion integrals (ERIs) including resolution of identity and the cholesky decomposition (CD) and density-fitting. With those, the dimension of the linear equation systems is still large, which makes it very computational demanding to solve. Therefore, further approximations aim at reducing the size of the equations and the coefficients of the first-order wavefunctions. For example, Frozen Natural Orbitals (FNO) by Aquilante *et al*[298], use of Tensor Hyper-contraction (THC) in combination with the supporting subspace technique by Song and Martinez,[299] Local pair-natural-orbital (LPNO) type of methods [300], as well as the simplest frozen core/virtual approximation. Similarly, these approximations can be extended into relativistic regime after careful examination. The four-component CASSCF, MRCI and CASPT2 implemented in Bagel[301] utilized density-fitting directly tied to sigma formation to reduce memory requirement. However, the auxiliary basis sets may need to be developed for relativistic calculations. In Ref. 158, the density fitting error has been analyzed at the Dirac-Hartree-Fock level and it shows that using the standard basis sets with Dirac-Coulomb Hamiltonian gives similar error compare to non-relativistic HF, but larger error with Gaunt and Breit terms included. The authors addressed the need for the development of fitting basis sets for DCG and DCB.[158] On the other hand, FNO has been extended into relativistic couple-cluster methods[302].

Our work aims to provide a better understanding of four-component Hamiltonian espe-

cially the Breit interaction in dynamic correlation, as the first step towards exploration of efficient approximations.

4.3.2 Atomic Fine Structure Splitting

A simple case – Na

Na is the first simple case we would like to use to demonstrate the effect of different levels of four-component Hamiltonians, as well as verifying the effects of frozen core/virtual approximation on its fine structure splitting. The results using different four-component Hamiltonians with CASSCF$^{\pm}$, MRCI and MRPT2 are shown in Tab. 4.4, with *fc/v* and textitall representing two different correlated spaces. CASSCF calculation includes an active space of 1 electron in 8 spinors $(2s, 2p)$. *fc/v* here stands for frozen 1s core spinors and high-lying virtual spinors with eigenvalues larger than 6 Hartree upon Improved virtual orbitals (IVO)[188, 244, 245]. *all* here stands for all electrons and all virtuals are correlated in both MRCI and MRPT2 calculations. Uncontracted ANO-RCC-VTZP basis set[303–306] is emplyed.

Splittings (meV)	Theory	Space	DC	DCG	DCB	Exp
$^2S_{1/2} \rightarrow {}^2P_{1/2}$	CASSCF	(1e, 8o)	1976.638 (-6.0)	1976.601 (-6.0)	1976.567 (-6.0)	2102.297
	MRPT2	fc/v	2063.407 (-1.8)	2063.443 (-1.8)	2063.384 (-1.8)	
		all	2077.001 (-1.2)	2077.086 (-1.2)	2077.008 (-1.2)	
	MRCI	fc/v	2093.745 (-0.4)	2093.786 (-0.4)	2093.724 (-0.4)	
		all	2087.144 (-0.7)	2087.123 (-0.7)	2087.073 (-0.7)	
$^2P_{1/2} \rightarrow {}^2P_{3/2}$	CASSCF	(1e, 8o)	2.012 (-5.6)	1.871 (-12.2)	1.870 (-12.3)	2.132
	MRPT2	fc/v	2.236 (+4.9)	2.079 (-2.5)	2.078 (-2.5)	
		all	2.234 (+4.8)	2.072 (-2.8)	2.072 (-2.8)	
	MRCI	fc/v	2.269 (+6.4)	2.110 (-1.0)	2.110 (-1.0)	
		all	2.240 (+5.1)	2.076 (-2.6)	2.076 (-2.6)	

Table 4.4: Na fine structure splittings (in meV). *fc/v* here stands for frozen 1s core spinors and high-lying virtual spinors with eigenvalues larger than 6 Hartree upon Improved virtual orbitals (IVO)[188, 244, 245]. *all* here stands for all electrons and all virtuals are correlated. Percentage error is shown in parentheses.

Different two-electron operators have tiny impacts on $^2S_{1/2} \rightarrow {}^2P_{1/2}$ splittings because

it is not dominant by two-electron SOC, but the dynamic correlation greatly improved the splitting. However, the $^2P_{1/2} \rightarrow {}^2P_{3/2}$ splittings are affected a lot by the two electron operators. Both DC-MRCI and DC-MRPT2 overestimated the splitting, while adding on Breit interaction corrects the overestimation. *fc/v* gives satisfactory results with a lower computational cost compared to correlating all electrons and all orbitals, indicating that the accurate description of valence electron and low-lying excited states can be achieved without correlating the core electrons and high-lying virtual orbitals above a certain threshold.

To further understand the role of different two-electron operators in dynamic correlation, the difference between MRCI energy and CASSCF energy is obtained as an evaluation of dynamic correlation for the corresponding state and Hamiltonian. At each state, the difference of dynamic correlation energies between two 4C operators is calculated to reflect the effects of certain two-electron terms. Tab. 4.5 shows the effects of different two-electron operators on dynamic correlation energies (in meV) for Na ground state and excited states.

MRCI	Na	ΔE_s^d	ΔE_{gaunt}^d	ΔE_{gauge}^d
fc/v	$^2S_{1/2}$	-8.703 (0.27)	-4.108 (0.13)	0.991 (-0.03)
	$^2P_{1/2}$	-8.791 (0.28)	-4.030 (0.13)	0.964 (-0.03)
	$^2P_{3/2}$	-8.864 (0.28)	-4.048 (0.13)	0.964 (-0.03)
all	$^2S_{1/2}$	-19.077 (0.27)	-57.547 (0.77)	15.259 (-0.20)
	$^2P_{1/2}$	-19.279 (0.27)	-57.530 (0.78)	15.242 (-0.20)
	$^2P_{3/2}$	-19.339 (0.27)	-57.553 (0.78)	15.242 (-0.20)

Table 4.5: Effects of different two-electron operators on dynamic correlation energies (in meV) for Na ground state and excited states. $\Delta E_s^d = E_{DC}^d - E_{bareC}^d$, $\Delta E_{gaunt}^d = E_{DCG}^d - E_{DC}^d$, $\Delta E_{gauge}^d = E_{DCB}^d - E_{DCG}^d$. Superscript d stands for dynamic correlation. Numbers in the parentheses show the ratio $\Delta E_x^d / E_{bareC}^d$ (x = s, gaunt, gauge) in percentage.

While the dynamic correlation for MRCI *all* are 2.3 $\sim$ 2.4 times compared to the *fc/v* case, the contributions from small (s), gaunt, and gauge terms are very different. Despite that their contributions to dynamic correlation energies are very small (within 1%), it shows that Breit interaction is more pronounced when core and high-lying virtuals are correlated to describe the dynamic correlation. The same analysis with MRPT2 are included in appendix.

Since the contributions to dynamic correlation from gaunt terms of each energy levels differ at the scale of 0.01 meV, their effects on the fine structure splittings are negligible. The same behavior is observed for gauge contributions. That being said, the overestimation ($> 5\%$) of Na $^2P_{1/2} \rightarrow {}^2P_{3/2}$ splittings using DC Hamiltonian originates from the CASSCF level using DC Hamiltonian. For post-CASSCF methods, the molecular transformation is a lot more computational expensive and time-consuming due to a much larger correlation space involved. Therefore, the dynamic correlation can be approximated utilizing Dirac-Coulomb level two-electron operator when extremely accurate predictions are not required. Starting with DCB-CASSCF results, if we add on dynamic correlation computed as the difference between DC-MRCI(*all*) and DC-CASSCF, we can get 2087.074 meV and 2.099 meV for sodium $^2S_{1/2} \rightarrow {}^2P_{1/2}$ and $^2P_{1/2} \rightarrow {}^2P_{3/2}$, respectively.

Atomic fine structure splittings

Benchmark results with four-component Dirac-Coulomb (DC), DC-Gaunt (DCG) and DC-Breit (DCB) for d, p-Block elements are listed in Tab. 4.6, which is complementary to Tab. 4.3. Comparing the aforementioned two tables, it clearly shows the necessity to include dynamic correlation for a more accurate description.

For group 3 d-block atoms, the d^1 electron configuration gives rise to ^2D ground state term, which is split into quadruply degenerate $^2D_{3/2}$ and 6-fold $^2D_{5/2}$ levels due to spin-orbit coupling. Three electrons and 12 spinors (ns and $(n-1)d$) are included in the reference CAS space. For Sc and Y, 8 sub-valence electrons ($(n-1)sp$ orbitals) and unoccupied virtual spinors up to 4 Hartree are correlated. For La, 10 more sub-valence electrons are included in the correlated space. For group 13 elements, ^2P ground state is split into doubly degenerate $^2P_{1/2}$ and quadruply degenerate $^2P_{3/2}$ levels. The CASSCF reference used an active space including three valence electrons and eight spinors (s and p orbitals). Ten sub-valence electrons (d orbitals) and unoccupied virtual spinors up to 4 Hartree are included in the correlated space in 4C-MRCI and 4C-MRPT2. Uncontracted ANO-RCC-VTZP basis set is employed.[304–307]

Transition	Element	Z	Theory	DC	DCG	DCB	Exp
$^2D_{3/2} \rightarrow {}^2D_{5/2}$	Sc	21	CASSCF	21.055	17.444	17.439	20.871
			MRPT2	23.613	20.141	20.136	
	Y	39	CASSCF	50.434	47.415	47.396	65.755
			MRPT2	69.237	65.966	65.943	
	La	57	CASSCF	85.858	82.779	82.782	130.576
			MRPT2	125.080	121.308	121.342	
$^2P_{1/2} \rightarrow {}^2P_{3/2}$	Ga	31	CASSCF	86.693	84.884	84.891	102.435
			MRPT2	99.997	97.895	97.898	
			MRCI	99.649	95.986	97.568	
	In	49	CASSCF	232.976	229.739	229.772	274.327
			MRPT2	278.372	274.543	274.550	
			MRCI	263.854	260.176	260.202	
	Tl	81	CASSCF	848.792	839.145	839.369	966.172
			MRPT2	951.996	941.801	941.990	

Table 4.6: Atomic fine structure splittings (in meV) computed using state-average 4C-CASSCF$^{\pm}$, 4C-MRPT2, and 4C-MRCI for Ga and In.

Similar to Na, results with DC Hamiltonian tend to overestimate the splittings, while including Breit interaction corrects them. However, one may find DC results closer to experimental values, which is indeed due to error cancellation. The source of error cancelled with DC Hamiltonian comes from the deficiency of dynamic correlation. For La, In and Tl, limited by the high computational cost, we are not able to add in more sub-valence electrons and more higher-lying virtual orbitals. For Ga, if we correlate six more sub-valence electrons, and include virtual spinors up to 15 Hartree, DC-MRPT2 yields 103.812 meV while DCG-MRPT2 and DCB-MRPT2 give 101.623 and 101.624 meV, respectively. Therefore, we can expect the rest of the results can be improved by enlarging the correlated space. Careful consideration is required when choosing the correlated space. As shown in our previous work, and also in previous study by Fleig *et al*[308], it is very important to correlate enough sub-valence electrons for reliable dynamic correlation. A balanced correlated space contains not only a large amount of virtual orbitals, but also a simultaneously increase in the number of inner-valence or core electrons. Some previous benchmark results from other

work[5, 218] that did not consider the importance of correlating sub-valence electrons, showing that 4C-CASSCF is better than 4C-CASPT2, may due to error cancellation and should be re-examined carefully.

Breit interaction are essential in correlated methods to get a true answer. The fine structure splittings in Tab. 4.6 have shown no impact from gauge dependence, which indicates Gaunt interaction provides a useful approximation to the full Breit interaction for valence electrons and low-lying excited states. From analysis on Na results, gauge dependence showed up in the dynamical correlation energies when core electrons and high-lying virtuals are included in the correlated space. The full Breit operator may be necessary for the description of core electrons in applications such as K-edge X-ray absorption spectroscopy and study about Auger decay.

Possible Approximation

The valence space is the most relevant to chemistry and condensed matter systems. Our previous benchmark study presented here is rather important to provide an understanding of the Breit interaction in correlated methods, while emphasize the significance of choosing a balanced correlated space. A convergence test with increasing correlated space size is needed to ensure the chosen space is capable of capturing full dynamic correlation. Based upon the knowledge that Gaunt term and Gauge term's contribution to dynamic correlation do not differ much among the ground state and low-lying excited states, leading to negligible fine structure splittings, we can perform DC-MRCI or DC-MRPT2 to obtain dynamic correlation, since the correlated space is usually large and the computational cost is demanding. However, the Breit operator has to be considered in the MCSCF step because the molecular spinors should be optimized with respect to the full spin-orbit coupling, as also mentioned by Pernpointner[309].

4.4 Conclusions

In this work, we introduce a fully correlated Dirac-Coulomb-Breit multiconfigurational self-consistent-field method within the frameworks of complete active space and density matrix renormalization group. In this approach, the Dirac-Coulomb-Breit Hamiltonian is included variationally in both the mean-field and correlated electron treatment.

Benchmark studies suggest that the positive-negative-energy orbital rotation in the no-virtual-pair approximation is important for deep-core electrons. Rotation only the positive-energy orbital space will lead to an overestimation of electron correlation by $\sim$10%, whereas no orbital rotation severely underestimate the correlation energy. Calculations on the correlation energy of valence electrons suggest that positive-negative orbital rotation becomes less important for electrons further away from the nucleus.

Calculations on He-like two-electron systems show that the Breit correlation becomes increasingly important as the atomic number increases and accounts for more than 50% of core electron correlation for heavier elements. On the other hand, we find no strong dependence of electron correlation on the Breit operator for valence electrons. Atomic fine structure study suggests that spectroscopic properties computed using only the correlated Dirac-Coulomb operator can produce false positive results. High-accuracy calculations require the fully correlated Gaunt or Breit operator and a large active space. Studies of lanthanide contraction due to the relativistic effect show excellent agreement with experiment.

This work lays the theoretical foundation for using correlated Breit operator for high-accuracy computational chemistry within a multireference framework, representing the non-quantum-electrodynamics limit of the many-body theory. DMRG's true potential in fast convergence toward the full CI limit is not fully explored in the proof-of-concept numerical examples presented herein, and will be an subject of study for highly correlated chemical systems.

The accuracy of the correlated Breit CASSCF and DMRG methods can be improved with additional dynamic correlations in the form of perturbation theory or multireference

configuration interaction, which is also presented. The benchmark results have shown the importance of including Breit operator in the CASSCF step, while for description of valence electrons and low-lying excited states, the dynamic correlation can be approximated by just using DC Hamiltonian when the calculation is too demanding.

Chapter 5

PART II: THE "HOLE" STORY IN IONIZED WATER

Starting from this Chapter, we switch gears and focus on the other part of the radiation problems — **water radiolysis**. The radiolysis of liquid water and the radiation-matter interactions that happen in aqueous environments are important to the fields of chemistry, materials, and environmental sciences, as well as biological and physiological response to extreme conditions and medical treatments. The initial stage of radiolysis is the ultrafast response, or hole dynamics, that trigger chemical processes within complex energetic landscapes that may include reactivity.

A fundamental understanding necessitates the use of theoretical methods that are capable of simulating both ultrafast coherence and non-adiabatic energy transfer pathways. In this chapter, we carry out an *ab initio* Ehrenfest dynamics study in order to provide a more complete description of the ultrafast dynamics and reactive events initiated by photoionization of water. After sudden ionization, the range of processes that include hole trapping and transfer, large OH oscillations, proton transfer and subsequent relay, formation of the metastable Zundel complex, and long-lived coherence, are identified and new insights into their driving forces are elucidated from the perspective of Ehrenfest dynamics.

5.1 Introduction

Water radiolysis initiates a suite of important reactions that impact many fields of study, such as radiotherapy, photocatalysis, and environmental science. Consider that the use of water as a coolant in nuclear reactors, and the associated water radiolysis process, is impactful to environmental management and remediation, as well as the production of unwanted waste byproducts and corrosion.[310] Within the medical field, water radiolysis and subsequent

reactivity is fundamental to radiation therapy and the effects of exposure to biologically damaging radiation.[114] With such a wide ranging relevance, it is no wonder that the study of water radiolysis persists as an active area of research to this day.

Despite many years of study, a *complete* understanding of the processes that occur after water ionization remains elusive. The difficulty with providing an exhaustive description of this process stems from both the capture of accurate molecular structures in liquid water [311] and the challenge of correctly describing non-equilibrium molecular dynamics. Nevertheless, some general reaction pathways in liquid water after ionization have been identified; one of the them is the formation of a hydrated electron and a cationic hole that decays to a hydronium molecule and a hydroxide radical.[310, 312, 313] The detection and dynamics of the hydrated electron has been the subject of many studies, [314–319] whereas the study of the dynamics of the cationic hole and subsequent proton transfer has increased in recent years.[320–322] Many studies have been able to resolve the spectrum of various protonated structures in water, including both the Eigen ($H_3O(H_2O)_3{}^+$) and Zundel ($H_5O_2^+$) moieties.[323–331] Extending these studies, the proton transfer mechanisms and dynamics in non-ionized liquid water have been heavily studied. [332–342] Direct experimental observation of the cationic hole in ionized liquid water has remained a great challenge as a result of its ultrashort lifetime and lack of characteristic spectral lines. Recently, ultrafast X-ray spectroscopy has been able to provide evidence for the existence of H_2O^+ as well as the decay to an OH radical via proton transfer.[322] However, a full account of the driving forces behind hole localization and subsequent ultrafast chemical processes has yet to be given.

In this work, we hope to provide a more complete ultrafast dynamic landscape of the reaction dynamics upon photoionization of water. Particularly, the driving forces behind hole localization and proton transfer are proposed, and a full account of the processes that occur after sudden ionization are identified.

5.2 Ab Initio Ehrenfest Dynamics Simulations and Computational Details

An ensemble of water $(H_2O)_{27}$ nanodroplet configurations shown in (Fig. 5.1), is used throughout this study. The initial configuration of the nanodroplet was carved from a classical simulation of bulk water using the SPC/E model[343] to identify a representative ground state configuration having an hydrogen bond distribution similar to the bulk.[344]

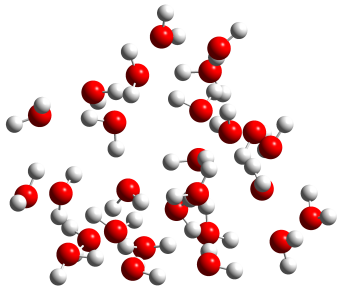

Figure 5.1: 27-water cluster model system.

Ultrafast photochemical dynamics, where electronic degrees of freedom are in the non-equilibrium condition, require a simulation protocol that is capable of treating electronic coherence as well as non-equilibrium non-adiabatic energy transfer pathways. Recent works have demonstrated the importance of modeling nuclear motion using non-adiabatic methods after ionization both in small water systems [345–348] and in liquid water. [349–352] In this work, we carried out *ab initio* on-the-fly Ehrenfest dynamics[103, 109, 353, 354] to simulate the ultrafast hole dynamics and its interplay with molecular vibrations. In the *ab initio* Ehrenfest dynamics, the time-dependent many-electron wavefunction is propagated explicitly in the time-domain, while the nuclear degrees of freedom are evolved classically using the mean force computed on-the-fly. The high density-of-state nature of the water cluster model used in this work makes the Ehrenfest dynamics an ideal approach to simulate quantum dynamics of the photoionized hole within the time-dependent Schödinger equation framework.

All calculations in this chapter are performed using the development version of the Gaus-

sian computational program.[355] The real-time time-dependent density functional theory (RT-TDDFT)[102, 103] with the BH&H functional[356] and the 6-31G(d,p) basis set is used in the Ehrenfest dynamics. Other functional and basis set combinations have been tested, showing similar behavior and initial conditions, so this level of theory has been chosen for its ability to produce excellent agreement with the experimentally measured bulk water photoabsorption and neutron scattering results.[357] Initial conditions for the *ab initio* Ehrenfest molecular dynamics were sampled from the thermalized neutral ground state trajectory at 298 K.[358–360] A total of 21 vibrationally bound initial conditions, *i.e.*, geometries and velocities, were sampled.[357]

To model the sudden ionization of water, the electron from the highest occupied molecular orbital (HOMO) of the neutral water cluster was removed (*i.e.*, vertical ionization), without changing the molecular geometry or velocity. With the purpose of investigating the attosecond electronic dynamics after ionization as well as the role of molecular vibration, both quantum electron dynamics[103, 353, 361] with fixed nuclei and *ab initio* on-the-fly Ehrenfest[103, 109, 353, 354] simulations were performed. It is worth noting that the semi-classical character of Ehrenfest dynamics necessarily neglect quantum nuclear effects[362–365]; it is expected that these may change the quantitative rates and lifetimes presented in this work, but that the general processes still occur.

The step size of the pure electronic dynamics simulations with fixed nuclei using RT-TDDFT is set to 0.02 a.u. (0.0004838 fs). There are three time step sizes — Δt_N, Δt_{Ne}, Δt_e — in the *ab initio* Ehrenfest dynamics scheme.[109] It was found that $\Delta t_N = 0.05$ fs, $\Delta t_{Ne} = 0.005$ fs, $\Delta t_e = 0.0005$ fs, satisfies the total energy conservation criteria (< 10 meV). The electronic spin densities from Mulliken population analysis[366] condensed to each water molecule in the cluster, was employed to measure of the extent of the delocalization of the hole in the ionized droplet.

During the reaction dynamics, the proton transfer pathway may not be along the O–O bond due to molecular rotation and vibration. In the following analysis, we use the OH bond ratio to quantify the proton transfer dynamics. The OH bond ratio is defined as the ratio

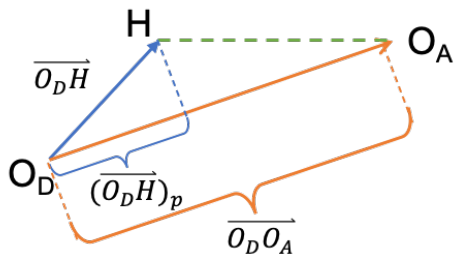

Figure 5.2: A diagram of the ratio between the scalar projection of O_D–H bond and the O–O distance between the donor(D) and acceptor(A). When the proton is equally shared by the two oxygens, the ratio is equal to 0.5.

between the scalar projection of the donor O_D–H bond and the O_D–O_A distance between the donor and acceptor (see Fig. 5.2).

5.3 Results and discussion

Previous theoretical and experimental studies have shown that photoionization of water results in an ultrafast hole localization process.[321, 322] Detailed analyses of *ab initio* Ehrenfest simulations lead to a more complex picture of reaction mechanism beyond the ultrafast hole localization. In this work, several characteristic dynamical behaviors of water nanodroplets have been observed within the first ∼70 fs after photoionization. Results of *ab initio* Ehrenfest and fixed-nuclei real-time electronic dynamics[361] simulations are compared to illustrate the important interplay between electronic and nuclear degrees of freedom in modulating the hole and proton dynamics.

5.3.1 Hole Trapping

A distinguishing characteristic in all the simulated Ehrenfest dynamics is the ultrafast localization of the hole, quickly formed after the ionization of the water nanodroplet. The spatial extent of the photoionized hole depends on the overlap/mixing of the $1b_1$ orbitals of the water molecules. Most of the photoionized holes have significant contributions from 2-4

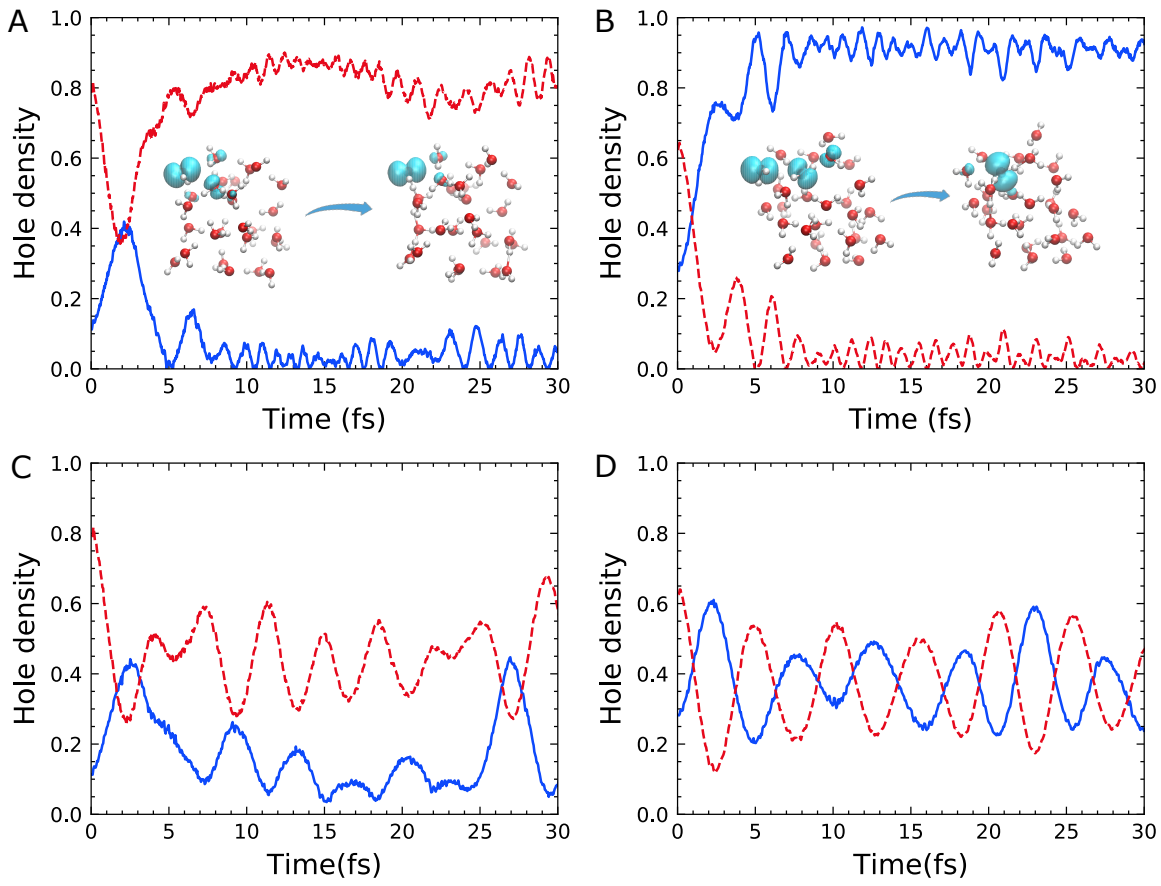

Figure 5.3: (A) and (B): Time-resolved hole density plots of selected simulations using *ab initio* Ehrenfest dynamics. (C) and (D): fixed-nuclei real-time electronic dynamics using the same initial conditions as in (A) and (B), respectively. Hole densities are computed as Mulliken spin densities projected on oxygen atoms. The two largest hole densities are plotted.

water nearest molecules, as shown in Fig. 5.3A and Fig. 5.3B. All simulations exhibit a quick hole localization process within the first 10 fs, with a representative dynamic simulation shown in Fig. 5.3A. This observation agrees with the previous theoretical and experimental results.[321, 322] However, hole localization is not observed from the pure electronic dynamics (Fig. 5.3C), which do not take the nuclear motions into account. This comparison suggests that molecular motions play a crucial role in hole dynamics, and, as shown later, hole-coupled proton dynamics.

In Fig. 5.3A, there is a coherent oscillation of the hole density among several nearby water $1b_1$ orbitals within the first 5 fs. As the molecular motion starts to be effective, the coherence of electronic degrees of freedom decays and the photoionized hole is localized to a single water molecule within the first 10 fs. In ~70% of the trajectories, the hole localized to the water molecule with the greatest proportion of hole character initially. This process leads to a persistent hole trapping within the simulation time, followed by a suite of reaction pathways triggered by the photoionization.

5.3.2 Hole Transfer

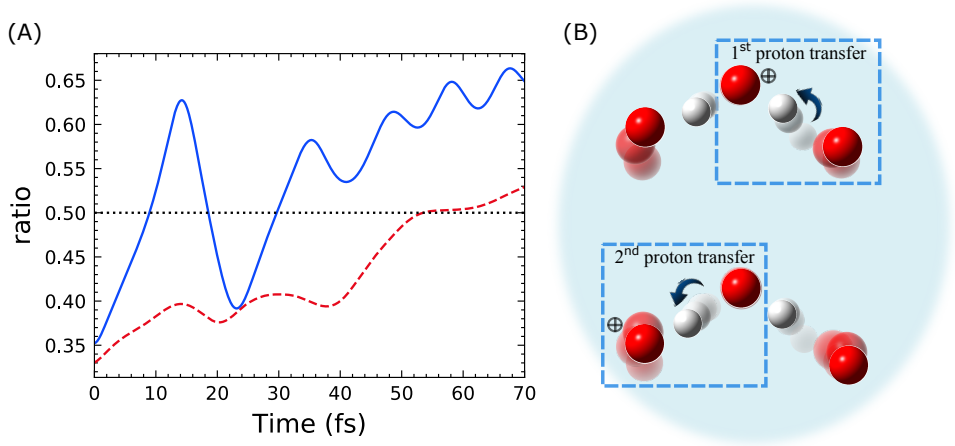

Figure 5.4: (A) Ratio plots of *ab initio* Ehrenfest dynamics for trajectory B after the ionization, indicating the first (blue, solid) and second (red, dashed) proton transfer processes. (B) illustrative figures of the first and second proton transfer.

An interesting hole behavior observed from the Ehrenfest simulations is the hole transfer process. This can be seen in Fig. 5.3B, indicated by the crossing of the hole/spin densities of two adjacent water molecules. The reaction starts from a relatively delocalized hole orbital with a significant amount of hole density on an adjacent water molecule. As time evolves, the hole density on the ionized water decreases as it increases on the nearest neighbor water, indicating a hole transfer event. This process is completed within the first 10 fs. During this

process, all protons remain in their original water molecules. This is still a hole localization event but with the distinct signature that the final localized hole is not on the initially photoionized water. In the study, 20% of simulations underwent a hole transfer process.

Molecular vibrations play an important role in modulating where the hole is localized. In the first 5 fs, the hole dynamics is dominated by electronic coherence as suggested by the similarity between the pure coherent electronic dynamics and Ehrenfest dynamics. After ∼5 fs, molecular motions caused by the change of the electronic structure come into effect and subsequently alter the electron movement, leading to a trapping of the hole, which is defined as decoherence.[367, 368] When the molecular vibration induced decoherence takes place, the hole can be "trapped" at different water molecules depending on the location of the maximum probability of the hole density during the coherent dynamics. In the simulation timescale, this process is irreversible, leading to persistent hole localization and hole transfer.

5.3.3 Large Amplitude Proton Oscillation

The ultrafast hole localization after photoionization can be considered as a relaxation process through which the electronic energy is relaxed to create locally activated molecular vibrations. An apparent phenomenon as a result of this relaxation process is how it modulates the bound proton oscillation without proton or hydrogen transfer. The hole localization triggers proton oscillations with a larger magnitude compared to those before the photoionization. Figure 5.4A plots the time-evolution of the relative O_D–H bond length with respect to the O_D–O_A distance for the dynamics shown in Fig. 5.3B. A value of 0.5 indicates a scenario when the proton is equally shared by two oxygens. In this dynamics, although the hole is localized and transferred within the first 10 fs, the proton continues to exhibit a large oscillatory behavior near the 0.5 value in the first 40 fs. Such a large protonic vibration amplitude does not appear before the photoionization. This observation suggests that in contrast to the repulsive potential energy surface (PES) on the excited state,[357] the photoionized PES is still attractive with a smaller curvature. Such a change of PES characteristics gives rise to a larger vibrational amplitude observed in the simulation. In all simulated radiolysis dy-

namics, ∼24% of them show larger proton oscillation amplitude with no observed proton or hydrogen transfer within the simulation time.

5.3.4 Proton Transfer

In photoexcited water cluster, a proton transfer event was observed mainly due to the repulsive excited state potential energy surface and the relaxation of photoexcited electron.[357] In contrast to the spontaneous dissociation in photoexcited water or water dimer ionization,[369] in which the proton transfer happens immediately after photoexcitation, the proton transfer event was experimentally observed 46 ± 10 fs after the ionization of liquid water.[322]

As discussed in the previous section, the hole localization/relaxation leads to locally activated OH vibrations. The consequence of activated OH vibrations is that many of them eventually undergo a proton transfer process. Figure 5.4 illustrates the dynamic characteristics of the proton transfer event following the photoionization. The simulation shows that activated OH bond undergoes several large amplitude vibrations before a proton is fully transferred to a neighboring water, leaving behind an OH radical. In the simulated dynamics, the proton transfer event is considered complete when the OH bond ratio is greater than 0.5 and the OH bond vibration does not return below 0.5 bond ratio. Among all simulations, 76% of dynamics exhibit proton transfers that complete 30∼40 fs after the photoionization. This time scale is in agreement with the experiment,[322] but is longer than that on the excited state because the latter occurs on a repulsive excited state surface.[357]

5.3.5 Formation of Zundel Complex and Proton Relay

In the condensed phase, nearby water molecules in the hydrogen bonding network stabilize the dissociated proton, through a proton relay. During the proton relay, one proton is shuttled from one oxygen to one of its nearest neighbors in the hydrogen bonding network. This process leads to a vibrationally hot hydronium H_3O^+ that eventually shuttles one of its protons to another nearest neighbor water molecule (see Fig. 5.4). Careful examination of the dynamics suggests that the proton relay event is not a concerted process, *i.e.*, the

second proton transfer is 10∼20 fs delayed after the formation of the hydronium H_3O^+. The OH ratio plot in Fig. 5.4 suggests that in this second stage of proton transfer a metastable $H(H_2O)_2^+$ Zundel complex is formed with a lifetime of 10∼20 fs. The lifetime of Zundel complex is much shorter than the excess proton in liquid water,[370] mainly due to the large reorganization energy arising from the photoionization.

In photoexcited water droplets, the proton relay event can reach as far as the third nearest neighboring water molecule. In contrast, on the photoionized ground state, the proton relay can only reach up to two nearest neighboring water within 70 fs. In addition, 10% of proton transfer processes may include a back transfer to the previous neighboring water molecule.

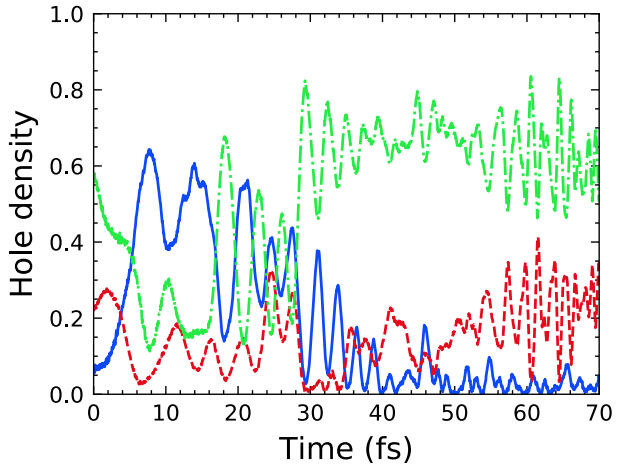

Figure 5.5: Time-resolved spin density plots of three different water molecules.

5.3.6 Long-lived Coherent Hole Dynamics

Within the simulation time, there are two trajectories that exhibit a long-lived hole coherence. As shown in Fig. 5.5, photoionization creates a delocalized hole with significant spin densities distributed among three water molecules. In the first 30 fs, strong coherence gives rise to the observed oscillation of hole density among the three water molecules without obvious hole localization. After 30 fs, three-site coherence is reduced to two-site. The coherence becomes even more prominent, as suggested by the nearly exact out-of-phase hole oscillation

between two water molecules (green and red curves). Note that electronic states could be overly coherence due to the mean-field nature of the Ehrenfest dynamics. The life-times of these coherent hole dynamics may be shortened if a better decoherence mechanism is implemented.[371–376] From the theoretical point of view, this phenomenon is sustainable only if molecular vibrations have a small effect on the energetics of orbitals that are involved in the coherence.[377] Analyses show that in this particular case delocalized molecular orbitals involved in the hole dynamics exhibit little fluctuations during the simulation time. Although this likely is a rare event at high temperature, we hypothesize that long-lived hole coherence is sustainable in ordered water structures, *e.g.* ice, at low temperature.

5.4 Conclusions

In this work, *ab initio* Ehrenfest dynamics simulations of radiolysis of water revealed unique ultrafast dynamical processes within ∼70 fs timeframe after the photoionization, including hole trapping, hole transfer, long-lived coherence, large OH oscillation, and proton transfer and relay, and the formation of the metastable Zundel complex. The hole localization process can be classified into hole trapping to the photoionized water and hole transfer to a nearby water. This process is considered the 'gateway' that triggers large OH oscillations. A fraction of the dynamics undergo a proton transfer and unconcerted proton relay process. These results not only match the earlier ultrafast X-ray experiment[322], but also provide a more thorough understanding of the evolution of ionized water on an ultrafast timescale. We also hypothesize that the probability of long-lived hole coherence increases at low temperature and in ordered water structures.

Chapter 6

ATTOSECOND ORIGINS OF WATER RADIOLYSIS

6.1 Introduction

Understanding radiation-induced chemical processes and reactive species in condensed phase has importance for applications ranging from cancer therapies and space travel to environmental remediation of legacy nuclear waste, as mentioned in section 1.3. Radiation-matter interactions involving high-energy electromagnetic wave such as γ-ray and X-ray, can ionize electrons from the matter. Ionization in aqueous systems will trigger the ejection of energetic primary electrons, resulting in highly damaging slower secondary electrons via inelastic and non-adiabatic processes. These processes happen on the physico-chemical timescale, *i.e.* within 10^{-12} s. The reactive radical species produced during this stage, for example, the hydrated electron [315, 316] and hydroxyl radical [322, 378], will react with H atoms and other particles in the system in the subsequent stages, initiating radiation damage, which can be observed in a longer timescale up to decades. However, it is the ultrafast processes and the reactive species that lead to the long-term effects that we observed.

Stepping beyond the ideal pure water radiolysis, the possible processes and reactions are more complicated upon radiolysis in complex aqueous systems where solute species are present. Besides the ultrafast proton transfer process, many studies suggested that the cationic hole could initiate *in situ* oxidation processes via electron transfer both in the homogeneous solutions and in interfacial biological systems prior to the generation of the OH radical. The ionization of the complex species also exists. [379] It is crucial to identify the initial products subsequent to the interaction of high-energy radiation with liquid water to understand the possible damage in aqueous condensed matter.

Core-level ionization or inner-valence ionization can be followed by several non-adiabatic

electronic decay pathways. Auger decay occurs locally within an atomic or molecular entity, whose outer valence electron fills the inner vacancy and a secondary electron (Auger electron) is ejected by the excess energy. Interatomic or intermolecular Coulombic decay (ICD) is a nonlocal electronic decay mechanism occurring in weakly bound matter, first proposed by Cederbaum *et al.* [380] The inner valence hole on an atomic or molecular moiety is filled by an outer valence electron on the same site, followed by the ejection of an outer valence electron from the neighboring species in the complex. Two adjacent single-hole sites then undergo Coulomb repulsion. An additional non-local decay pathway is electron-transfer-mediated decay (ETMD), with the inner vacancy filled by an electron transfer from a neighboring atom or molecule, and the released energy then ionizes the outer valence electron in the donor or another neighboring species. [381] At liquid/solid interfaces, radiation can stimulate interfacial reactions with various reactivities that may impact the structure of both the solid and liquid phase, and subsequently affect reactions on a longer timescale, such as molecular H_2 production. The energy transfer pathways and the dynamics of highly reactive radicals generated by radiation exposure on the physico-chemical timescale is not yet clear. Jones *et al* [382] revealed the ICD and ETMD energy dissipation pathways in their low-energy electron irradiation experiment on micro-solvated boehmite (AlOOH) nanoplatelets. The highly reactive radicals generated upon radiolysis have ultrashort lifetime, with ultrafast energy transfer pathways on the sub-picosecond timescale.

Here, X-ray spectroscopy is a promising candidate for observing the transient intermediates and investigating the time-resolved structural changes that occur in complex solutions. X-ray free electron laser (X-FEL) radiation or single x-ray photon at synchrotron facilities is promising to obtain experimental spectra of the ultrafast processes. In April 2022, a team led by Young *et al* has performed the world's first attosecond x-ray pump/x-ray probe experiment in condensed phase targeting liquid water. The electrons in the full valence band can be ionized using the high-energy X-ray pump.

Interpreting the information given by the experimental spectrum and revealing the underlying energy transfer mechanisms require theoretical simulations. To describe the elec-

tronic structure when the radiation triggers the ionization of electrons in the inner-shell orbitals, higher level theory is required. As illustrated in Chapter 1, the single-determinant approximation has shown its defects when describing chemical systems with a geometry far from equilibrium, open-shell and electronic excited states, and especially photochemical processes. An actual stationary state can be treated as superpositions of different electronic configurations, namely configuration interaction. It requires a multiconfigurational treatment such as complete-active-space self-consistent field (CASSCF) [227] approach to recover the static correlation arising from quasidegeneracy that involves several near-degenerate orbitals. Multi-reference restricted active space configuration interaction (MRRASCI) is employed to simulate the oxygen K-edge X-ray absorption spectrum upon inner-valence ionization.

6.1.1 Experimental XAS

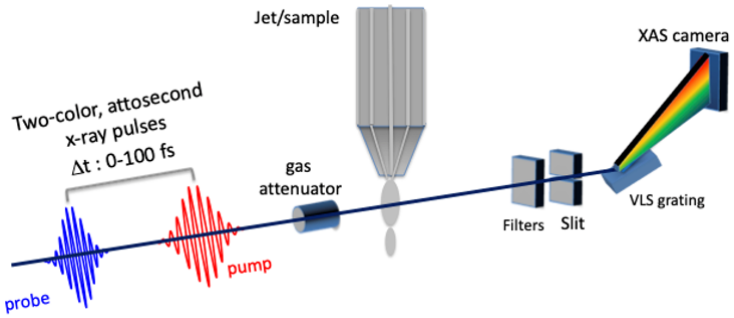

Figure 6.1: Configuration for attosecond x-ray pump probe studies of radiolysis via transient absorption.

As shown in Fig. 6.1, the red light first interacts with the sample as the pump to create excited-state species (ionized species in our case). Then after a certain time delay Δt, the blue light is utilized to probe the oxygen K-edge of the sample. LCLS's unique XLEAP w/2w mode allowed ionization of the entire valence band whilst simultaneously probing the valence hole and pre-edge region in liquid water. Only the 0.6 fs time delay point was properly overlapped.

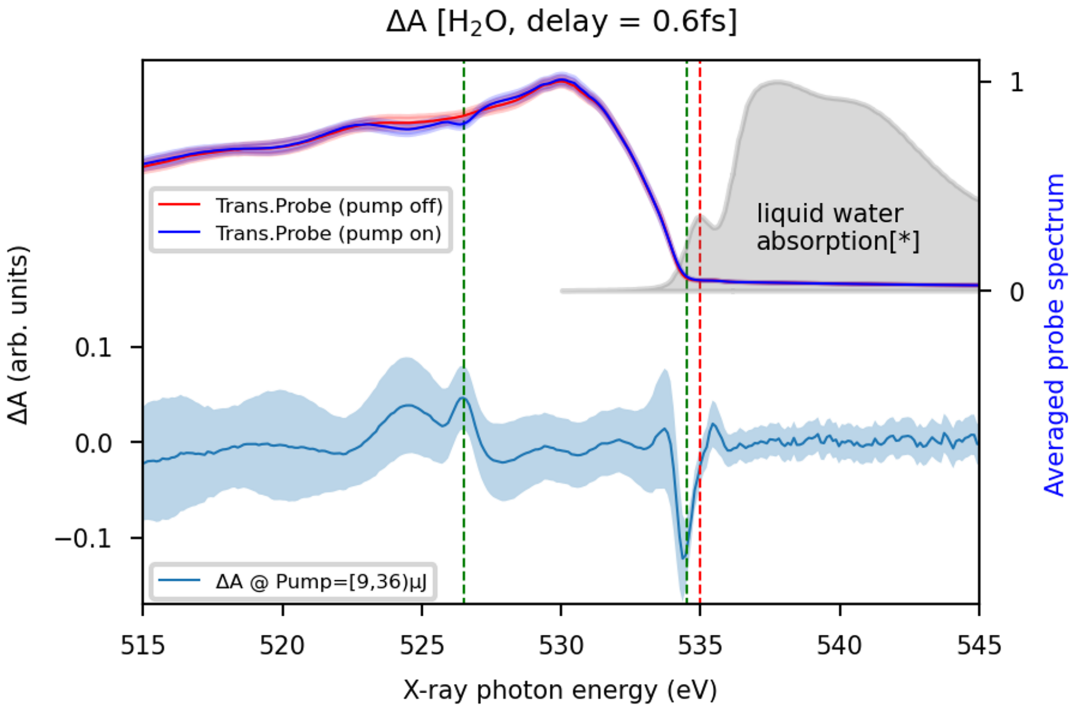

Figure 6.2: Experimental differential absorption spectrum over the valence hole and pre-edge region, attributed to Shuai Li, Kai Li, Emily Nienhuis, Gilles Doumy, Zheming Wang, Zhi-Heng Loh, Georgi Dakovski, Kristjan Kunnus, Dan DePonte, Giacomo Coslovich, Thomas Wolf, Linda Young and Carolyn Pearce.

From the experimental delta absorption spectrum, there are two regions showing significant response. One is around 525 eV, while the other is the bleach right before the neutral water pre-edge feature.

6.2 Theoretical Simulation of XAS with Multi-reference Methods

Here we investigate three water species: monomer, dimer and pentamer, aiming to understand the electronic structure upon attosecond X-ray Pump/Probe. The theoretical X-ray absorption spectra were computed using multi-reference restricted-active-space configuration-interaction as implemented in the development version of Gaussian, [383] with tetrahedrally coordinated $(H_2O)_5$, as it is the simplest cluster mimicking the first solvation shell in "bulk

water". For better understanding, same simulations are performed with water monomer and water dimer. The time scale being 0.6 femtosecond is only a very small fraction compared to the shortest nuclear motion – hydrogen vibration – 10 fs. Therefore, we consider no nuclear motion at 0.6 fs and freeze all nuclear degrees of freedom when computing the spectra with the aforementioned water models.

6.2.1 Geometry Optimization

The pentamer structure is optimized at the MP2/aug-cc-pVTZ level of theory, with O-O-O angles fixed at 109.5° to maintain the tetrahedrality of the system. [384] Note that this arrangement is not a stationary point on the potential energy surface and it will collapse to cyclic minimum if one performs full geometry optimization. Fig. C.1, together with Tab. C.1, shows the distance between atoms of the central water to atoms of its neighboring water to help visualize the pentamer structure. Both the water monomer and dimer geometries are fully optimized using coupled cluster single and double(CCSD) with 6-311++g** basis set [304–306, 385, 386]. All calculations are carried out using he development version of Gaussian. [383]

6.2.2 X-ray Absorption Spectrum Calculation

Two species of each water model $(H_2O)_x$ $(x = 1, 2, 5)$ are studied using multi-reference *ab initio* methods with 6-311++G** basis set to simulate the delta XAS spectrum from experiment, being the neutral water and water cation with +1 charge to mimic the species before and after X-ray pump, respectively. The XAS spectra for each species were then computed with restricted-active-space configuration interaction(RASCI)[387] method using proper reference wavefunction of the states of interest. RAS technique allows us to divide the active space of correlated molecular orbitals into three spaces RAS 1, RAS 2, and RAS 3. The configurations are then constructed based on maximum number of holes and electrons allowed in RAS 1 and RAS 3, respectively, while no restrictions apply to RAS 2. Excited states above

a certain energy threshold were converged using energy-specific Davidson algorithm with $1e^{-8}$ convergence criteria on eigenvector amplitudes of desired states.

Upon RASCI calculations, the energies between initial states and final states give the positions of the corresponding transitions in the spectrum, with their intensities determined by the oscillator strength computed within the dipole approximation. The X-ray absorption spectral lines of the two species are plotted in the same plot with a global shift applied to align the pre-edge (535 eV) and the $1b_1$ (526.5 eV) features. With the peak position and relative intensity determined, the spectrum is adjusted by a Gaussian broadening (0.7) to account for both lifetime and experimental broadening. The delta XAS is produced by the difference between the two spectral lines.

The calculation setup are illustrated in detail here for water pentamer. The electronic structure of closed-shell neutral water pentamer is first computed with restricted Hartree-Fock (RHF) method. To capture the XAS of neutral species, the transitions between ground state and excited states with $1s$ core-hole are computed. RAS 1 included the five $1s$ orbitals with ten electrons. RAS 2 comprised the 15 inner-valence and valence orbitals ($1b_1$, $3a_1$, $1b_2$ from each water molecule) and 30 electrons. RAS 3 included all the unoccupied orbitals with orbital energies up to 0.5 Hartree ($\approx$ 13.61 electronVolt), in order to lower the computational cost while maintaining a accurate description of the pre-edge feature. Up to one hole is allowed in RAS 1 to simulate both the initial states and $1s$ core-hole states, while up to 2 electrons are allowed in RAS 3 not only to describe the pre-edge features, but also to capture enough dynamic correlation. 200 core-hole states are computed for neutral water O K-edge XAS.

In order to describe the multiple-hole excited-state physics created upon 250 eV X-ray pump, the reference molecular orbitals for the open-shell water cation were optimized using state-averaged(SA) complete-active-space self-consistent-field(CASSCF) with an active space including 29 electrons in 15 inner-valence and valence orbitals ($1b_1$, $3a_1$, $1b_2$ from each water molecule). The 15 one-hole states were treated with averaged weights in the orbital optimization step to capture the orbital relaxation upon X-ray pump. In order to simulate

the two regions in the experimental oxygen K-edge delta XAS – 520 $\sim$ 527 eV and 530 $\sim$ 536 eV, three main types of electronic transitions are taken into account, as shown in Fig. 6.3: a) 1s electron is excited into the hole vacancies of the same water; b) 1s electron is excited into the unoccupied orbitals without any hole in the same water; c) The hole being a spectator while the 1s electron is excited into unoccupied virtual orbitals. These transitions are computed in a RASCI calculation. The three restricted active spaces were constructed in the same manner as the neutral species, except that RAS 2 now has 29 electrons in 15 valence/inner-valence orbitals. 550 core-hole states in total are computed for the pre-edge part of the spectrum, whose energies are high enough to describe all the transitions before the large water absorption signals. For signals in the region of inner-valence/valence holes, a global shift of 13.5 eV is applied, while 15.3 eV shift is applied to the pre-edge region. The difference is due to the fact that the dynamic correlation is not fully recovered upon the frozen virtual approximation. (Different shifts are applied to Fig. C.4 and Fig. 6.4 using the 526.5 eV and 535 eV as calibration, which worths further discussion.)

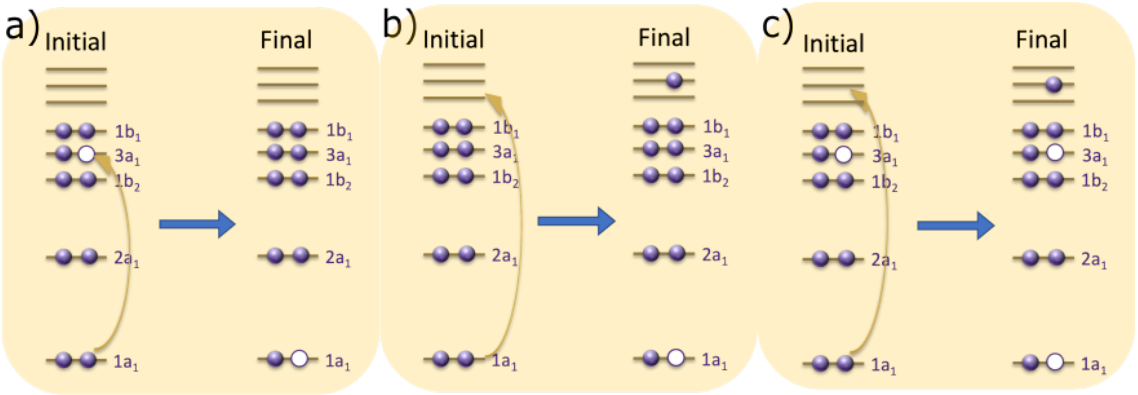

Figure 6.3: Three types of transitions for O K-edge XAS being considered: a) 1s electron is excited into the hole vacancies of the same water; b) 1s electron is excited into the unoccupied orbitals without any hole in the same water; c) The hole being a spectator while the 1s electron is excited into unoccupied virtual orbitals.

6.2.3 Transition Analysis

The hole configurations of all states are analyzed using the diagonal elements of their one-particle reduced density matrices (1RDMs), computed in the RASCI calculations.

$$\gamma_{pq}^{\mathrm{M}} = \langle \Psi_{\mathrm{M}} | \hat{E}_{qp} | \Psi_{\mathrm{M}} \rangle \tag{6.1}$$

where Ψ_{M} is the CI wavefunction for state M, $\hat{E}_{qp}$ is the single excitation operator and p, q refer to molecular orbitals (MOs) in the correlated space. By comparing the hole configurations of the initial and final states, the mechanism of each transition can be revealed.

To further visualize and characterize the orbitals participated in the hole-particle transitions, natural transition orbitals (NTOs) were generated by finding the sets of orbital representations which diagonalize the one-particle transition density matrix (1TDM) of a specific transition.[388]

$$\gamma_{pq}^{\mathrm{MN}} = \langle \Psi_{\mathrm{M}} | \hat{E}_{qp} | \Psi_{\mathrm{N}} \rangle \tag{6.2}$$

where M and N stand for initial and final states, respectively. The unitary transformation matrices $\mathbf{U}$ and $\mathbf{V}$ to generate NTOs are defined by a singular value decomposition (SVD) of 1TDM.

$$\gamma_{pq}^{\mathrm{MN}} = \mathbf{U}\mathbf{S}\mathbf{V}^{\dagger} \tag{6.3}$$

Transforming the canonical molecular orbitals by $\mathbf{U}$ generates the particle NTOs, while transforming by $\mathbf{V}$ results in the hole NTOs. The diagonal matrix $\mathbf{S}$ contains the singular values, representing the amplitudes. It is well-known that NTOs provide essential information with regards to what extent two electronic states are related to each other by a one-electron excitation, as the transition is represented by a more condensed set of orbitals (usually a pair of NTOs).

6.3 Results and Discussion

The computed XAS for each water model $(H_2O)_x$ $(x = 1, 2, 5)$ are shown from Fig. C.2, Fig. C.3, Fig. C.4 and Fig. 6.4. In the XAS of neutral species in each water model, only type b) transitions happen and give rise to the pre-, main- and post-edge signatures, while for the cationic species, type a) transitions account for the signals before pre-edge and type b) and c) transitions account for the pre-, main- and post-edge signals.

Fig. C.2 has shown the accuracy of the method as it has correctly predicted the energy difference (∼14 eV) between $1b_1$ peak and the pre-edge peak of the water cation, which agrees well with a recent study on X-ray absorption spectrum of H_3O^+ and H_2O^+. [389] More importantly, the pre-edge signals of the cation H_2O^+ being above 540 eV shows that there is no absorption from H_2O^+ itself in the pre-edge region of the neutral water (around $535 \sim 537$ eV).

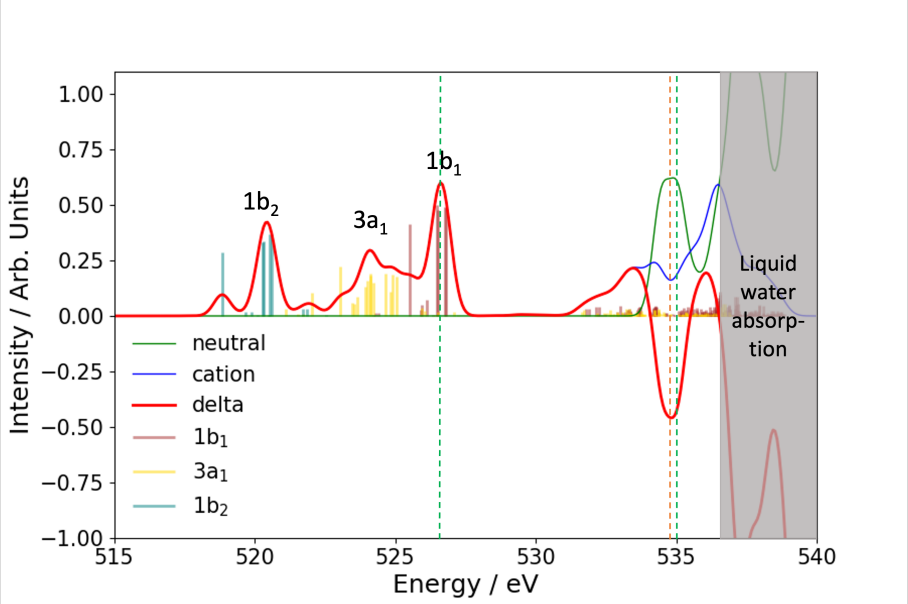

Figure 6.4: Computed spectrum for pentamer with 1*s* core-hole from all water in our simulation. For signals in the region of inner-valence/valence holes, a global shift of 13.5 eV is applied, while 15.3 eV shift is applied to the pre-edge region.

The computed spectra for water pentamer are shown in Fig. 6.4 and Fig. C.4. All

three types of transitions (Fig. 6.3) gave rise to signals. The broken hydrogen bond when considering all the 1s orbitals from all water in the pentamer causes a larger neutral pre-edge, account for the strong bleach signal, indicating the existence of broken hydrogen bonds in liquid water. The electronic configuration of the initial and final states of each transition can be analyzed though the diagonal element of the 1RDM. Therefore the peaks in Fig. 6.4 can be characterized. The signals from 520 to 526 eV arise from type a) transitions, in which the 1s core electron is excited to fill the inner-valence hole. The pre-edge features are more complicated and the transition mechanism is shown in Fig. 6.5. The transition itself falls into b) type but with a neighboring valence or inner-valence presented, leading to its shift and broadening. Further analysis to investigate the nature of the peak shift with NTO are still on-going.

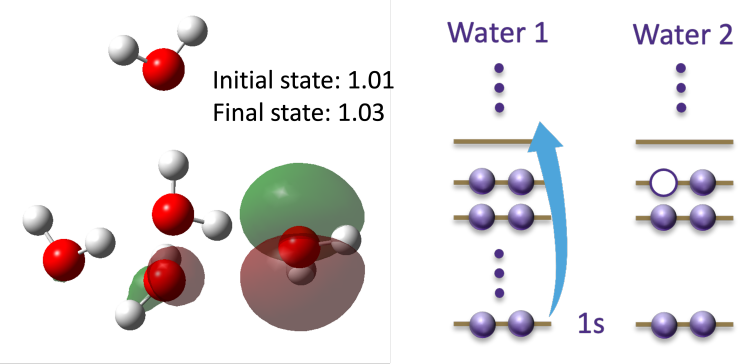

Figure 6.5: One transition with $1b_1$ hole as spectator at 531.9 eV, together with its electron densities at the initial state and final state. Figure on the right shows the transition mechanism. Water 1 stands for the central water, and water 2 represents the neighboring water with the valence hole.

Chapter 7

CONCLUSIONS AND OUTLOOK

At the last chapter of my dissertation, I am very fortunate to have undertaken several research projects built upon great endeavors of many brilliant scientists. I will not be this far without the contributions from previous researchers, my peers and my collaborators. The work presented in this dissertation centered at the development and application of multi-reference electronic structure methods to address heavy element spectroscopy and radiation problems that society is facing, as well as deepen our understanding of the complicated nature of heavy element chemistry and radiolysis. In part I, we have developed and benchmarked multi-reference electronic structure methods with special relativity to approach accurate description of heavy element spectroscopy. Part II introduced a fundamental understanding of the ultrafast chemical processes upon water radiolysis, and further illustrated that ultrafast X-ray spectroscopy and computational chemistry are highly synergistic in advancing our knowledge. The methods and the analysis tools developed continue to be used in heavy element spectroscopy to investigate the metal $M-$edge, $L-$edge and ligand $K-$edge XAS, to understand the chemical bonding in Lanthanides and Actinides complexes. They will further be applied to solve more chemistry problems.

More research is on-going, as there are still new physics and chemistry that current quantum chemistry cannot interpret and predict. As system size becomes larger, the computational cost of multi-reference electronic structure grow exponentially. What is more, many problems in heavy-element chemistry will require relativistic MCSCF and MRCI being able to handle larger active spaces such as one including $5d$, $6sp$, $5f$, $6d$, $7sp$, and $8s$ and key ligand orbitals for Actinide complexes. One attempt we are taking is to extending our implementation to adapt to the advanced high-performance computing architectures. Current

scientific computing facilities such as the National Energy Research Scientific Computing Center (NERSC) have clusters built from a large number of processors and a high-speed interconnect network aiming at accelerating scientific discovery through computation. It offers enormous computing power and further poses a challenge for quantum chemistry software packages, requiring them to be massively parallelized. To ensure the portability for our implementation, the parallel algorithm is designed utilizing the standard message passing interface (MPI) as it is generally available on most parallel computers and it provides library functions to fully exploit multi-node computing power. Considering the fact that matrix-vector product formation (*i.e.* σ-formation) in the direct-CI approach accounts for almost the entire computer time of a CI calculation, it is naturally our first choice to parallel its scheme. Inspired by the success of the generalized active space (GAS) approach [53, 308, 390–403] in which orbitals can be arbitrarily partitioned into any number of active spaces, in the upcoming work, we introduce a new implementation of relativistic configuration interaction with a GAS framework aiming at combining the strength of the process- and thread-based programming paradigms. Its performance is further analyzed in HPC clusters, which provides insights for future users and developers. With 512 nodes on NERSC, the averaged sigma build time for a CASCI calculation with 138 billion determinants took just over an hour. It will provide us the capability to accelerate scientific discovery.

The work in this dissertation has only addressed a small part of the challenges in quantum chemistry and the development of electronic structure theories will continue for predictions for new phenomena and physics. For example, multi-reference electronic structure methods are accurate treatments for excited states but their computational cost is limiting their further applications even with high-performance computing, especially in relativistic regime. More understanding in dynamic correlation and efforts in better approximations in terms of unoccupied virtual orbitals will be meaningful in extending multi-reference methods into larger molecules and condensed phases. Continuing the study on water radiolysis, unraveling the whole energy dissipation landscape requires accurate descriptions for resonance states and continuum in order to capture two-hole one-particle states in various decay processes,

together with dynamics simulations. Its development will also help understand the main- and post-edge features in XAS spectra. Last but not least, there are a lot of exciting theories for different physical and chemical problems to learn and explore. This dissertation will hopefully serve as an introduction for many more interesting methodology development in the future.

BIBLIOGRAPHY

[1] Hehre, W. J.; Radom, L.; von R. Schleyer, P.; Pople, J. A. *Ab Initio Molecular Orbital Theory*; John Wiley & Sons, New York, 1986.

[2] Pople, J. A. Nobel Lecture: Quantum Chemical Models. *Rev. Mod. Phys.* **1999**, *71*, 1267–1274.

[3] Saue, T. Relativistic Hamiltonians for Chemistry: A Primer. *ChemPhysChem* **2011**, *12*, 3077–3094.

[4] Roos, B. O.; Malmqvist, P.-Å. Relativistic Quantum Chemistry: The Multiconfigurational Approach. *Phys. Chem. Chem. Phys.* **2004**, *6*, 2919–2927.

[5] Zhang, B.; Vandezande, J. E.; Reynolds, R. D.; Schaefer, H. F. Spin-Orbit Coupling via Four-Component Multireference Methods: Benchmarking on p-Block Elements and Tentative Recommendations. *J. Chem. Theory Comput.* **2018**, *14*, 1235–1246.

[6] Szabo, A.; Ostlund, N. S. *Modern Quantum Chemistry: Introduction to Advanced Electronic Structure Theory*, 3rd ed.; Dover Publications, Inc.: New York, 1996.

[7] Barone, V.; Alessandrini, S.; Biczysko, M.; Cheeseman, J. R.; Clary, D. C.; McCoy, A. B.; DiRisio, R. J.; Neese, F.; Melosso, M.; Puzzarini, C. Computational Molecular Spectroscopy. *Nat. Rev. Methods Primers* **2021**, *1*, 38.

[8] Wang, F. Future of Computational Molecular Spectroscopy—from Supporting Interpretation to Leading The Innovation. *Phys. Chem. Chem. Phys.* **2023**, *25*, 7090–7105.

[9] Barone, V.; Puzzarini, C. Gas-Phase Computational Spectroscopy: The Challenge of the Molecular Bricks of Life. *Annu. Rev. Phys. Chem.* **2023**, *74*, 29–52.

[10] Giovannini, T.; Egidi, F.; Cappelli, C. Molecular Spectroscopy of Aqueous Solutions: A Theoretical Perspective. *Chem. Soc. Rev.* **2020**, *49*, 5664–5677.

[11] Norman, P.; Dreuw, A. Simulating X-ray Spectroscopies and Calculating Core-Excited States of Molecules. *Chem. Rev.* **2018**, *118*, 7208–7248.

[12] Isborn, C. M.; Luehr, N.; Ufimtsev, I. S.; Martínez, T. J. Excited-State Electronic Structure with Configuration Interaction Singles and Tamm–Dancoff Time-Dependent Density Functional Theory on Graphical Processing Units. *J. Chem. Theory Comput.* **2011**, *7*, 1814–1823.

[13] Dreuw, A.; Head-Gordon, M. Single-Reference Ab Initio Methods for The Calculation of Excited States of Large Molecules. *Chem. Rev.* **2005**, *105*, 4009–4037.

[14] Marques, M.; Gross, E. Time-Dependent Density Functional Theory. *Annu. Rev. Phys. Chem.* **2004**, *55*, 427–455.

[15] Burke, K.; Werschnik, J.; Gross, E. K. U. Time-dependent Density Functional Theory: Past, Present, And Future. *J. Chem. Phys.* **2006**, *123*, 062206.

[16] Carter-Fenk, K.; Cunha, L. A.; Arias-Martinez, J. E.; Head-Gordon, M. Electron-Affinity Time-Dependent Density Functional Theory: Formalism and Applications to Core-Excited States. *J. Phys. Chem. Lett.* **2022**, *13*, 9664–9672.

[17] Cruzeiro, V. W. D.; Wildman, A.; Li, X.; Paesani, F. Relationship between Hydrogen-Bonding Motifs and the $^1b_1$ Splitting in the X-ray Emission Spectrum of Liquid Water. *J. Phys. Chem. Lett.* **2021**, *12*, 3996–4002.

[18] Kasper, J. M.; Stetina, T. F.; Jenkins, A. J.; Li, X. Ab Initio Methods for L-edge X-ray Absorption Spectroscopy. *Chem. Phys. Rev.* **2020**, *1*, 011304.

[19] Stetina, T. F.; Kasper, J. M.; Li, X. Modeling $L_{2,3}$-Edge X-ray Absorption Spectroscopy with Linear Response Exact Two-Component Relativistic Time-Dependent Density Functional Theory. *J. Chem. Phys.* **2019**, *150*, 234103.

[20] Stetina, T.; Clark, A.; Li, X. X-ray Absorption Signatures of Hydrogen-bond Structure in Water-Alcohol Solutions. *Int. J. Quant. Chem.* **2019**, *119*, e25802.

[21] Wildman, A.; Martinez-Baez, E.; Fulton, J.; Schenter, G.; Pearce, C.; Clark, A.; Li, X. Anticorrelated Contributions to Pre-Edge Features of Aluminate Near-Edge X-ray Absorption Spectroscopy in Concentrated Electrolytes. *J. Phys. Chem. Lett.* **2018**, *9*, 2444–2449.

[22] Kasper, J. M.; Lestrange, P. J.; Stetina, T. F.; Li, X. Modeling $L_{2,3}$-Edge X-ray Absorption Spectroscopy with Real-Time Exact Two-Component Relativistic Time-Dependent Density Functional Theory. *J. Chem. Theory Comput.* **2018**, *14*, 1998–2006.

[23] Lestrange, P. J.; Nguyen, P. D.; Li, X. Calibration of Energy-Specific TDDFT for Modeling K-Edge XAS Spectra of Light Elements. *J. Chem. Theory Comput.* **2015**, *11*, 2994–2999.

[24] George, S. D.; Petrenko, T.; Neese, F. Time-dependent Density Functional Calculations of Ligand K-edge X-ray Absorption Spectra. *Inorg. Chim. Acta* **2008**, *361*, 965–972, Protagonists in Chemistry: Professor Edward I Solomon.

[25] Nascimento, D. R.; Biasin, E.; Poulter, B. I.; Khalil, M.; Sokaras, D.; Govind, N. Resonant Inelastic X-ray Scattering Calculations of Transition Metal Complexes Within a Simplified Time-Dependent Density Functional Theory Framework. *J. Chem. Theory Comput.* **2021**, *17*, 3031–3038.

[26] Perdew, J. P.; Zunger, A. Self-interaction Correction to Density-functional Approximations for Many-electron Systems. *Phys. Rev. B* **1981**, *23*, 5048–5079.

[27] POLO, V.; KRAKA, E.; CREMER, D. Electron Correlation and The Self-Interaction Error of Density Functional Theory. *Mol. Phys.* **2002**, *100*, 1771–1790.

[28] Mori-Sánchez, P.; Cohen, A. J.; Yang, W. Many-electron Self-interaction Error in Approximate Density Functionals. *J. Chem. Phys.* **2006**, *125*, 201102.

[29] Gräfenstein, J.; Kraka, E.; Cremer, D. The Impact of The Self-interaction Error on The Density Functional Theory Description of Dissociating Radical Cations: Ionic And Covalent Dissociation Limits. *J. Chem. Phys.* **2004**, *120*, 524–539.

[30] Cohen, A. J.; Mori-Sánchez, P.; Yang, W. Challenges for Density Functional Theory. *Chem. Rev.* **2012**, *112*, 289–320.

[31] Pople, J. A.; Binkley, J. S.; Seeger, R. Theoretical Models Incorporating Electron Correlation. *Int. J. Quant. Chem.* **1976**, *10*, 1–19.

[32] Pople, J.; Krishnan, R.; Schlegel, H.; Binkley, J. Electron Correlation Theories And Their Application to The Study of Simple Reaction Potential Surfaces. *Int. J. Quant. Chem.* **1978**, *10*, 545–560.

[33] Krishnan, R.; Frisch, M. J.; Pople, J. A. Contribution of Triple Substitutions to The Electron Correlation Energy in Fourth Order Perturbation Theory. *J. Chem. Phys.* **1980**, *72*, 4244–4245.

[34] Nobes, R. H.; Pople, J. A.; Radom, L.; Handy, N. C.; Knowles, P. J. Slow Convergence of The Møller-plesset Perturbation Series: The Dissociation Energy of Hydrogen Cyanide And The Electron Affinity of The Cyano Radical. *Chem. Phys. Lett.* **1987**, *138*, 481–485.

[35] Knowles, P. J.; Andrews, J. S.; Amos, R. D.; Handy, N. C.; Pople, J. A. Restricted Møller—Plesset Theory for Open-shell Molecules. *Chem. Phys. Lett.* **1991**, *186*, 130–136.

[36] Knowles, P. J.; Handy, N. C. A New Determinant-based Full Configuration Interaction Method. *Chem. Phys. Lett.* **1984**, *111*, 315–321.

[37] Crawford, D. T.; Schaefer III, H. F. *Rev Comp Chem*; 2007; Vol. 14; pp 33–136.

[38] Koch, H.; Jörgensen, P. Coupled Cluster Response Functions. *J. Chem. Phys.* **1990**, *93*, 3333–3344.

[39] Duch, W.; Diercksen, G. H. F. Size-extensivity Corrections in Configuration Interaction Methods. *J. Chem. Phys.* **1994**, *101*, 3018–3030.

[40] Langhoff, S. R.; Davidson, E. R. Configuration Interaction Calculations on The Nitrogen Molecule. *Int. J. Quant. Chem.* **1974**, *8*, 61–72.

[41] Andersson, K.; Malmqvist, P. Å.; Roos, B. O.; Sadlej, A. J.; Wolinski, K. Second-Order Perturbation Theory with A CASSCF Reference Function. *J. Phys. Chem.* **1990**, *94*, 5483–5488.

[42] Andersson, K.; Malmqvist, P. Å.; Roos, B. O. Second-Order Perturbation Theory with A Complete Active Space Self-Consistent Field Reference function. *J. Chem. Phys.* **1992**, *96*, 1218–1226.

[43] Szalay, P. G.; Müller, T.; Gidofalvi, G.; Lischka, H.; Shepard, R. Multiconfiguration Self-Consistent Field and Multireference Configuration Interaction Methods and Applications. *Chem. Rev.* **2012**, *112*, 108–181.

[44] PIERLOOT, K. The CASPT2 Method in Inorganic Electronic Spectroscopy: from Ionic Transition Metal to Covalent Actinide Complexes. *Mol. Phys.* **2003**, *101*, 2083–2094.

[45] Zhang, I. Y.; Grüneis, A. Coupled Cluster Theory in Materials Science. *Frontiers in Materials* **2019**, *6*.

[46] Jagau, T.-C.; Bravaya, K. B.; Krylov, A. I. Extending Quantum Chemistry of Bound States to Electronic Resonances. *Annu. Rev. Phys. Chem.* **2017**, *68*, 525–553.

[47] Liu, J.; Cheng, L. Relativistic Coupled-cluster And Equation-of-motion Coupled-cluster Methods. *WIREs Comput. Mol. Sci.* **2021**, *11*, e1536.

[48] Raghavachari, K.; Trucks, G. W.; Pople, J. A.; Head-Gordon, M. A Fifth-order Perturbation Comparison of Electron Correlation Theories. *Chem. Phys. Lett.* **1989**, *157*, 479–483.

[49] Stanton, J. F. Why CCSD(T) Works: A Different Perspective. *Chem. Phys. Lett.* **1997**, *281*, 130–134.

[50] Lee, Y. S.; Kucharski, S. A.; Bartlett, R. J. A Coupled Cluster Approach with Triple Excitations. *J. Chem. Phys.* **1984**, *81*, 5906–5912.

[51] Jozef Noga, R. J. B. The Full CCSDT Model for Molecular Electronic Structure. *J. Chem. Phys.* **1987**, *86*, 7041–7050.

[52] Kucharski, S.; Bartlett, R. Recursive Intermediate Factorization And Complete Computational Linearization of The Coupled-Cluster Single, Double, Triple, And Quadruple Excitation Equations. *Theor. Chem. Acc. 80*.

[53] Olsen, J. The Initial Implementation And Applications of A General Active Space Coupled Cluster Method. *J. Chem. Phys.* **2000**, *113*, 7140–7148.

[54] Kállay, M.; Surján, P. R. Higher Excitations in Coupled-Cluster Theory. *J. Chem. Phys.* **2001**, *115*, 2945–2954.

[55] Krylov, A. I. Equation-of-Motion Coupled-Cluster Methods for Open-Shell and Electronically Excited Species: The Hitchhiker's Guide to Fock Space. *Annu. Rev. Phys. Chem.* **2008**, *59*, 433–462.

[56] Stanton, J. F.; Bartlett, R. J. The Equation of Motion Coupled-Cluster Method. A Systematic Biorthogonal Approach to Molecular Excitation Energies, Transition Probabilities, and Excited State Properties. *J. Chem. Phys.* **1993**, *98*, 7029–7039.

[57] Koch, H.; Jørgen Aa. Jensen, H.; Jørgensen, P.; Helgaker, T., et al. Excitation Energies From the Coupled Cluster Singles and Doubles Linear Response Function (CCSDLR). Applications to Be, CH+, CO, and H2O. *J. Chem. Phys.* **1990**, *93*, 3345–3350.

[58] Peng, B.; Lestrange, P. J.; Goings, J. J.; Caricato, M.; Li, X. Energy-Specific Equation-of-Motion Coupled-Cluster Methods for High-Energy Excited States: Application to K-Edge X-Ray Absorption Spectroscopy. *J. Chem. Theory Comput.* **2015**, *11*, 4146–4153.

[59] Vidal, M. L.; Pokhilko, P.; Krylov, A. I.; Coriani, S. Equation-of-Motion Coupled-Cluster Theory to Model L-Edge X-ray Absorption and Photoelectron Spectra. *J. Phys. Chem. Lett.* **2020**, *11*, 8314–8321.

[60] Andersen, J. H.; Nanda, K. D.; Krylov, A. I.; Coriani, S. Probing Molecular Chirality of Ground and Electronically Excited States in the UV–vis and X-ray Regimes: An EOM-CCSD Study. *J. Chem. Theory Comput.* **2022**, *18*, 1748–1764.

[61] Aoki, T.; Ohno, K. Ab Initio Simulations of X-ray Emission Spectroscopy with The GW+Bethe-Salpeter Equation Method. *Phys. Rev. B* **2019**, *100*, 075149.

[62] Tang, F.; Li, Z.; Zhang, C.; Louie, S. G.; Car, R.; Qiu, D. Y.; Wu, X. Many-body Effects in The X-ray Absorption Spectra of Liquid Water. *Proc. Natl. Acad. Sci. U.S.A.* **2022**, *119*, e2201258119.

[63] Otis, L.; Neuscamman, E. A Promising Intersection of Excited-state-specific Methods from Quantum Chemistry And Quantum Monte Carlo. *WIREs Comput. Mol. Sci. n/a*, e1659.

[64] Booth, G. H.; Chan, G. K.-L. Communication: Excited States, Dynamic Correlation Functions and Spectral Properties from Full Configuration Interaction Quantum Monte Carlo. *J. Chem. Phys.* **2012**, *137*, 191102.

[65] Blunt, N. S.; Smart, S. D.; Booth, G. H.; Alavi, A. An Excited-state Approach within Full Configuration Interaction Quantum Monte Carlo. *J. Chem. Phys.* **2015**, *143*, 134117.

[66] Tubman, N. M.; Lee, J.; Takeshita, T. Y.; Head-Gordon, M.; Whaley, K. B. A Deterministic Alternative to The Full Configuration Interaction Quantum Monte Carlo Method. *J. Chem. Phys.* **2016**, *145*, 044112.

[67] Holmes, A. A.; Tubman, N. M.; Umrigar, C. J. Heat-Bath Configuration Interaction: An Efficient Selected Configuration Interaction Algorithm Inspired by Heat-Bath Sampling. *J. Chem. Theory Comput.* **2016**, *12*, 3674–3680.

[68] Levine, D. S.; Hait, D.; Tubman, N. M.; Lehtola, S.; Whaley, K. B.; Head-Gordon, M. CASSCF with Extremely Large Active Spaces Using the Adaptive Sampling Configuration Interaction Method. *J. Chem. Theory Comput.* **2020**, *16*, 2340–2354.

[69] Schriber, J. B.; Evangelista, F. A. Communication: An Adaptive Configuration Interaction Approach for Strongly Correlated Electrons with Tunable Accuracy. *J. Chem. Phys.* **2016**, *144*, 161106.

[70] Yao, Y.; Umrigar, C. J. Orbital Optimization in Selected Configuration Interaction Methods. *J. Chem. Theory Comput.* **2021**, *17*, 4183–4194.

[71] Zhang, N.; Liu, W.; Hoffmann, M. R. Iterative Configuration Interaction with Selection. *J. Chem. Theory Comput.* **2020**, *16*, 2296–2316.

[72] Guo, Y.; Zhang, N.; Lei, Y.; Liu, W. iCISCF: An Iterative Configuration Interaction-Based Multiconfigurational Self-Consistent Field Theory for Large Active Spaces. *J. Chem. Theory Comput.* **2021**, *17*, 7545–7561.

[73] White, S. R. Density Matrix Formulation for Quantum Renormalization Groups. *Phys. Rev. Lett.* **1992**, *69*, 2863–2866.

[74] Chan, G. K.-L.; Head-Gordon, M. Highly Correlated Calculations with a Polynomial Cost Algorithm: A Study of the Density Matrix Renormalization Group. *J. Chem. Phys.* **2002**, *116*, 4462–4476.

[75] Moritz, G.; Wolf, A.; Reiher, M. Relativistic DMRG Calculations on the Curve Crossing of Cesium Hydride. *J. Chem. Phys.* **2005**, *123*, 184105.

[76] Kurashige, Y.; Yanai, T. High-Performance Ab Initio Density Matrix Renormalization Group Method: Applicability to Large-Scale Multireference Problems for Metal Compounds. *J. Chem. Phys.* **2009**, *130*, 234114.

[77] Olivares-Amaya, R.; Hu, W.; Nakatani, N.; Sharma, S.; Yang, J.; Chan, G. K.-L. The Ab-Initio Density Matrix Renormalization Group in Practice. *J. Chem. Phys.* **2015**, *142*, 034102.

[78] Löwdin, P.-O. *Advances in Chemical Physics*; John Wiley & Sons, Ltd, 1958; pp 207–322.

[79] Hollett, J. W.; Gill, P. M. W. The Two Faces of Static Correlation. *J. Chem. Phys.* **2011**, *134*, 114111.

[80] Hartree, D. R.; Hartree, W.; Swirles, B. Self-Consistent Field, Including Exchange and Superposition of Configurations, with Some Results for Oxygen. *Philosophical Transactions of the Royal Society of London. Series A, Mathematical and Physical Sciences* **1939**, *238*, 229–247.

[81] Das, G.; Wahl, A. C. Extended Hartree—Fock Wavefunctions: Optimized Valence Configurations for H2 and Li2, Optimized Double Configurations for F2. *J. Chem. Phys.* **1966**, *44*, 87–96.

[82] Schmidt, M. W.; Gordon, M. S. The Construction and Interpretation of MCSCF Wavefunctions. *Annu. Rev. Phys. Chem.* **1998**, *49*, 233–266.

[83] Fleig, T. Relativistic Wave-function Based Electron Correlation Methods. *Chem. Phys.* **2012**, *395*, 2–15.

[84] Olsen, J. The CASSCF Method: A Perspective and Commentary: CASSCF Method. *Int. J. Quant. Chem.* **2011**, *111*, 3267–3272.

[85] Roos, B. r. O.; Taylor, P. R.; Sigbahn, P. E. A Complete Active Space SCF Method (CASSCF) Using A Density Matrix Formulated Super-CI Approach. *Chem. Phys.* **1980**, *48*, 157–173.

[86] Roos, B. O. The Complete Active Space SCF method in a Fock-Matrix-Based Super-CI Formulation. *Int. J. Quant. Chem.* **1980**, *18*, 175–189.

[87] Siegbahn, P. E.; Heiberg, A.; Roos, B.; Levy, B. A Comparison of the Super-CI and the Newton-Raphson Scheme in the Complete Active Space SCF Method. *Physica Scripta* **1980**, *21*, 323.

[88] Siegbahn, P. E. M.; Almlö f, J.; Heiberg, A.; Roos, B. r. O. The Complete Active Space SCF (CASSCF) Method in A Newton–Raphson Formulation with Application to the HNO Molecule. *J. Chem. Phys.* **1981**, *74*, 2384–2396.

[89] Lindh, R.; Galván, I. F. *Quantum Chemistry and Dynamics of Excited States*; John Wiley & Sons, Ltd, Chapter 10, pp 299–353.

[90] Lyakh, D. I.; Musiał, M.; Lotrich, V. F.; Bartlett, R. J. Multireference Nature of Chemistry: The Coupled-Cluster View. *Chem. Rev.* **2012**, *112*, 182–243.

[91] Evangelista, F. A. Perspective: Multireference Coupled Cluster Theories of Dynamical Electron Correlation. *J. Chem. Phys.* **2018**, *149*, 030901.

[92] Pernal, K.; Hapka, M. Range-separated Multiconfigurational Density Functional Theory Methods. *WIREs Comput. Mol. Sci.* **2022**, *12*, e1566.

[93] Fromager, E.; Toulouse, J.; Jensen, H. J. A. On The Universality of The Long-/short-range Separation in Multiconfigurational Density-functional Theory. *J. Chem. Phys.* **2007**, *126*, 074111.

[94] Li Manni, G.; Carlson, R. K.; Luo, S.; Ma, D.; Olsen, J.; Truhlar, D. G.; Gagliardi, L. Multiconfiguration Pair-Density Functional Theory. *J. Chem. Theory Comput.* **2014**, *10*, 3669–3680.

[95] Gagliardi, L.; Truhlar, D. G.; Li Manni, G.; Carlson, R. K.; Hoyer, C. E.; Bao, J. L. Multiconfiguration Pair-Density Functional Theory: A New Way To Treat Strongly Correlated Systems. *Acc. Chem. Res.* **2017**, *50*, 66–73.

[96] Marian, C. M.; Heil, A.; Kleinschmidt, M. The DFT/MRCI Method. *WIREs Comput. Mol. Sci.* **2019**, *9*, e1394.

[97] Liu, W.; Hoffmann, M. In *Isaiah Shavitt: A Memorial Festschrift from Theoretical Chemistry Accounts*; Shepard, R., Pitzer, R. M., Dunning, T., Eds.; Springer, Berlin, Heidelberg.

[98] Song, Y.; Guo, Y.; Lei, Y.; Zhang, N.; Liu, W. In *New Horizons in Computational Chemistry Software*; Filatov, M., Choi, C. H., Olivucci, M., Eds.; Springer International Publishing, 2022; pp 181–236.

[99] Porter, G.; Norrish, R. G. W. Flash photolysis and spectroscopy. A new method for the study of free radical reactions. *Proceedings of the Royal Society of London. Series A. Mathematical and Physical Sciences* **1950**, *200*, 284–300.

[100] Pavošević, F.; Culpitt, T.; Hammes-Schiffer, S. Multicomponent Quantum Chemistry: Integrating Electronic and Nuclear Quantum Effects via the Nuclear–Electronic Orbital Method. *Chem. Rev.* **2020**, *120*, 4222–4253.

[101] Hammes-Schiffer, S. Nuclear–electronic Orbital methods: Foundations and Prospects. *J. Chem. Phys. 155*.

[102] Li, X.; Govind, N.; Isborn, C.; DePrince, A. E.; Lopata, K. Real-Time Time-Dependent Electronic Structure Theory. *Chem. Rev.* **2020**, *120*, 9951–9993.

[103] Goings, J. J.; Lestrange, P. J.; Li, X. Real-Time Time-Dependent Electronic Structure Theory. *WIREs Comput. Mol. Sci.* **2018**, *8*, e1341.

[104] Kuleff, A. I.; Cederbaum, L. S. Ultrafast Correlation-Driven Electron Dynamics. *J. Phys. B* **2014**, *47*, 124002.

[105] Marx, D.; Parrinello, M. Ab Initio Path Integral Molecular Dynamics: Basic Ideas. *J. Chem. Phys. 104*.

[106] Meyer, H.-D.; Manthe, U.; Cederbaum, L. The Multi-configurational Time-dependent Hartree Approach. *Chem. Phys. Lett.* **1990**, *165*, 73–78.

[107] Subotnik, J. E.; Jain, A.; Landry, B.; Petit, A.; Ouyang, W.; Bellonzi, N. Understanding the Surface Hopping View of Electronic Transitions and Decoherence. *Annu. Rev. Phys. Chem.* **2016**, *67*, 387–417.

[108] Tully, J. C. Molecular Dynamics with Electronic Transitions. *J. Chem. Phys. 93*.

[109] Li, X.; Tully, J. C.; Schlegel, H. B.; Frisch, M. J. Ab Initio Ehrenfest Dynamics. *J. Chem. Phys.* **2005**, *123*, 084106.

[110] Vacher, M.; Mendive-Tapia, D.; Bearpark, M. J.; Robb, M. A. In *Isaiah Shavitt: A Memorial Festschrift from Theoretical Chemistry Accounts*; Shepard, R., Pitzer, R. M., Dunning, T., Eds.; Springer Berlin Heidelberg: Berlin, Heidelberg, 2016; pp 325–336.

[111] Martínez, T. J.; Ben-Nun, M.; Levine, R. D. Multi-Electronic-State Molecular Dynamics: A Wave Function Approach with Applications. *J. Phys. Chem.* **1996**, *100*, 7884–7895.

[112] Ben-Nun, M.; Martínez, T. J. A Multiple Spawning Approach to Tunneling Dynamics. *J. Chem. Phys. 112*.

[113] Robb, M. A.; Jenkins, A. J.; Vacher, M. *Isaiah Shavitt: A Memorial Festschrift from Theoretical Chemistry Accounts*.

[114] Huels, M. A.; Boudaïffa, B.; Cloutier, P.; Hunting, D.; Sanche, L. Single, Double, and Multiple Double Strand Breaks Induced in DNA by 3- 100 eV Electrons. *J. Am. Chem. Soc.* **2003**, *125*, 4467–4477.

[115] Cutler, C. S.; Hennkens, H. M.; Sisay, N.; Huclier-Markai, S.; Jurisson, S. S. Radiometals for Combined Imaging and Therapy. *Chem. Rev.* **2013**, *113*, 858–883.

[116] Nehra, K.; Dalal, A.; Hooda, A.; Bhagwan, S.; Saini, R. K.; Mari, B.; Kumar, S.; Singh, D. Lanthanides β-Diketonate Complexes as Energy-Efficient Emissive Materials: A Review. *J. Mol. Struct.* **2022**, *1249*, 131531.

[117] Pressler, K.; Snoeren, T. J.; Walsh, K. M.; Gamelin, D. R. Magnetic Amplification at Yb3+ "Designer Defects" in the van Der Waals Ferromagnet CrI3. *Nano Lett.* **2023**, *23*, 1320–1326.

[118] Milstein, T. J.; Kroupa, D. M.; Gamelin, D. R. Picosecond Quantum Cutting Generates Photoluminescence Quantum Yields Over 100% in Ytterbium-Doped CsPbCl3 Nanocrystals. *Nano Lett.* **2018**, *18*, 3792–3799.

[119] Yao, J.-S.; Ge, J.; Han, B.-N.; Wang, K.-H.; Yao, H.-B.; Yu, H.-L.; Li, J.-H.; Zhu, B.-S.; Song, J.-Z.; Chen, C.; Zhang, Q.; Zeng, H.-B.; Luo, Y.; Yu, S.-H. Ce3+-Doping to Modulate Photoluminescence Kinetics for Efficient CsPbBr3 Nanocrystals Based Light-Emitting Diodes. *J. Am. Chem. Soc.* **2018**, *140*, 3626–3634.

[120] Lino, J. B. d. R.; Gonçalves, M. A.; Sauer, S. P. A.; Ramalho, T. C. Extending NMR Quantum Computation Systems by Employing Compounds with Several Heavy Metals as Qubits. *Magnetochemistry* **2022**, *8*.

[121] Peterson, R. A.; Buck, E. C.; Chun, J.; Daniel, R. C.; Herting, D. L.; Ilton, E. S.; Lumetta, G. J.; Clark, S. B. Review of the Scientific Understanding of Radioactive Waste at the U.S. DOE Hanford Site. *Environmental Science & Technology* **2018**, *52*, 381–396.

[122] Colburn, H. A.; Peterson, R. A. A History of Hanford Tank Waste, Implications for Waste Treatment, and Disposal. *Environmental Progress & Sustainable Energy* **2021**, *40*, e13567.

[123] Page, J. S.; Reynolds, J. G.; Cooke, G. A.; Wells, B. E. Large Cemented Gibbsite Agglomerates in Alkaline Nuclear Waste at the Hanford Site and The Impacts to Remediation. *Journal of Hazardous Materials* **2020**, *384*, 121318.

[124] Pyykkö, P. The Physics behind Chemistry and the Periodic Table. *Chem. Rev.* **2012**, *112*, 371–384.

[125] Pyykkö, P. Relativistic Effects in Chemistry: More Common Than You Thought. *Annu. Rev. Phys. Chem.* **2012**, *63*, 45–64.

[126] Autschbach, J. Perspective: Relativistic Effects. *J. Chem. Phys.* **2012**, *136*, 150902.

[127] Fleig, T.; Jensen, H. J. A.; Olsen, J.; Visscher, L. The Generalized Active Space Concept for the Relativistic Treatment of Electron Correlation. III. Large-scale Configuration Interaction and Multiconfiguration Self-Consistent-Field Four-Component Methods with Application to UO_2. *J. Chem. Phys.* **2006**, *124*, 2963–2971.

[128] Thyssen, J.; Fleig, T.; Jensen, H. J. A. A Direct Relativistic Four-Component Multiconfiguration Self-Consistent-Field Method for Molecules. *J. Chem. Phys.* **2008**, *129*, 034109.

[129] Jenkins, A. J.; Liu, H.; Kasper, J. M.; Frisch, M. J.; Li, X. Variational Relativistic Complete Active Space Self-Consistent Field Method. *J. Chem. Theory Comput.* **2019**, *15*, 2974–2982.

[130] Kasper, J. M.; Jenkins, A. J.; Sun, S.; Li, X. Perspective on Kramers Symmetry Breaking and Restoration in Relativistic Electronic Structure Methods for Open-Shell Systems. *J. Chem. Phys.* **2020**, *153*, 090903.

[131] Visscher, L.; Lee, T. J.; Dyall, K. G. Formulation and Implementation of a Relativistic Unrestricted Coupled-Cluster Method including Noniterative Connected Triples. *J. Chem. Phys.* **1996**, *105*, 8769.

[132] Liu, J.; Cheng, L. Relativistic Coupled-Cluster and Equation-of-Motion Coupled-Cluster Methods. *WIREs Comput. Mol. Sci.* **2021**, *11*, 1536.

[133] Pototschnig, J. V.; Papadopoulos, A.; Lyakh, D. I.; Repisky, M.; Halbert, L. ı. c.; Severo Pereira Gomes, A.; Jensen, H. J. A.; Visscher, L. Implementation of Relativistic Coupled Cluster Theory for Massively Parallel GPU-Accelerated Computing Architectures. *J. Chem. Theory Comput.* **2021**, *17*, 5509–5529, PMID: 34370471.

[134] Knecht, S.; Legeza, O.; Reiher, M. Communication: Four-component Density Matrix Renormalization Group. *J. Chem. Phys.* **2014**, *140*, 041101.

[135] Battaglia, S.; Keller, S.; Knecht, S. Efficient Relativistic Density-Matrix Renormalization Group Implementation in a Matrix-Product Formulation. *J. Chem. Theory Comput.* **2018**, *14*, 2353–2369.

[136] Hoyer, C. E.; Hu, H.; Lu, L.; Knecht, S.; Li, X. Relativistic Kramers-Unrestricted Exact-Two-Component Density Matrix Renormalization Group. *J. Phys. Chem. A* **2022**, *126*, 5011–5020.

[137] Dyall, K. G.; Fægri, Jr., K. *Introduction to Relativistic Quantum Chemistry*; Oxford University Press, 2007.

[138] Reiher, M.; Wolf, A. *Relativistic Quantum Chemistry*, 2nd ed.; Wiley-VCH, 2015.

[139] Dirac, P. A. M.; Fowler, R. H. The Quantum Theory of The Electron. *Proc. Roy. Soc. (London)* **1928**, *117*, 610–624.

[140] Anderson, C. D. The Positive Electron. *Phys. Rev.* **1933**, *43*, 491–494.

[141] Thierfelder, C.; Schwerdtfeger, P. Quantum Electrodynamic Corrections for the Valence Shell in Heavy Many-electron Atoms. *Phys. Rev. A* **2010**, *82*, 062503.

[142] Liu, W.; Lindgren, I. Going beyond "No-pair Relativistic Quantum Chemistry". *J. Chem. Phys.* **2013**, *139*, 014108.

[143] Liu, W. Advances in Relativistic Molecular Quantum Mechanics. *Phys. Rep.* **2014**, *537*, 59–89.

[144] Liu, W. Essentials of Relativistic Quantum Chemistry. *J. Chem. Phys.* **2020**, *152*, 180901.

[145] Dyall, K. G.; Fægri Jr, K. *Introduction to Relativistic Quantum Chemistry*; Oxford University Press, 2007.

[146] Stanton, R. E.; Havriliak, S. Kinetic Balance: A Partial Solution to the Problem of Variational Safety in Dirac Calculations. *J. Chem. Phys.* **1984**, *81*, 1910–1918.

[147] Dyall, K. G.; Fægri, K. Kinetic Balance and Variational Bounds Failure in the Solution of the Dirac Equation in a Finite Gaussian Basis Set. *Chem. Phys. Lett.* **1990**, *174*, 25 – 32.

[148] Sun, Q.; Liu, W.; Kutzelnigg, W. Comparison of Restricted, Unrestricted, Inverse, and Dual Kinetic Balances for Four-Component Relativistic Calculations. *Theor. Chem. Acc.* **2011**, *129*, 423–436.

[149] Brown, G. E.; Ravenhall, D. On the Interaction of Two Electrons. *Proc. R. Soc. London, Ser. A* **1951**, *208*, 552–559.

[150] Sucher, J. Foundations of the Relativistic Theory of Many-Electron Atoms. *Phys. Rev. A* **1980**, *22*, 348.

[151] Mittleman, M. H. Theory of Relativistic Effects on Atoms: Configuration-Space Hamiltonian. *Phys. Rev. A* **1981**, *24*, 1167–1175.

[152] Talman, J. D. Minimax Principle for The Dirac Equation. *Phys. Rev. Lett.* **1986**, *57*, 1091–1094.

[153] LaJohn, L.; Talman, J. Minimax Variational Solution of The Dirac Equation in Molecular Geometries. *Chem. Phys. Lett.* **1992**, *189*, 383–389.

[154] Sun, S.; Ehrman, J. N.; Sun, Q.; Li, X. Efficient Evaluation of the Breit Operator in the Pauli Spinor Basis. *J. Chem. Phys.* **2022**, *157*, 064112.

[155] Liu, W.; Hong, G.; Dai, D.; Li, L.; Dolg, M. The Beijing Four-Component Density Functional Program Package (BDF) And Its Application to EuO, EuS, YbO And YbS. *Theor. Chem. Acc.* **1997**, *96*, 75–83.

[156] Varga, S.; Engel, E.; Sepp, W.-D.; Fricke, B. Systematic Study of The Ib Diatomic Molecules Cu_2, Ag_2, And Au_2 Using Advanced Relativistic Density Functionals. *Phys. Rev. A* **1999**, *59*, 4288–4294.

[157] Belpassi, L.; Tarantelli, F.; Sgamellotti, A.; Quiney, H. M. Electron Density Fitting for The Coulomb Problem in Relativistic Density-Functional Theory. *J. Chem. Phys.* **2006**, *124*, 124104.

[158] Kelley, M. S.; Shiozaki, T. Large-Scale Dirac–Fock–Breit Method Using Density Fitting and 2-Spinor Basis Functions. *J. Chem. Phys.* **2013**, *138*, 204113.

[159] Saue, T.; gri, K. F.; Helgaker, T.; Gropen, O. Principles of Direct 4-Component Relativistic SCF: Application to Caesium Auride. *Mol. Phys.* **1997**, *91*, 937–950.

[160] Saue, T.; Jensen, H. J. A. Quaternion Symmetry in Relativistic Molecular Calculations: The Dirac–Hartree–Fock Method. *J. Chem. Phys.* **1999**, *111*, 6211–6222.

[161] Visscher, L. Quaternion Symmetry in Relativistic Molecular Calculations: The Dirac–Hartree–Fock Method. *Theor. Chem. Acc.* **1997**, *98*, 68–70.

[162] Nakajima, T.; Hirao, K. Pseudospectral Approach to Relativistic Molecular Theory. *J. Chem. Phys.* **2004**, *121*, 3438–3445.

[163] Foldy, L. L.; Wouthuysen, S. A. On the Dirac Theory of Spin 1/2 Particles and Its Non-Relativistic Limit. *Phys. Rev.* **1950**, *78*, 29–36.

[164] Iliaš, M.; Saue, T. An Infinite-Order Relativistic Hamiltonian by a Simple One-Step Transformation. *J. Chem. Phys.* **2007**, *126*, 064102.

[165] Douglas, M.; Kroll, N. M. Quantum Electrodynamical Corrections to the Fine Structure of Helium. *Ann. Phys.* **1974**, *82*, 89–155.

[166] Hess, B. A. Relativistic Electronic-Structure Calculations Employing a Two-Component No-Pair Formalism with External-Field Projection Operators. *Phys. Rev. A* **1986**, *33*, 3742–3748.

[167] Nakajima, T.; Hirao, K. The Higher-Order Douglas–Kroll Transformation. *J. Chem. Phys.* **2000**, *113*, 7786–7789.

[168] Wolf, A.; Reiher, M.; Hess, B. A. The Generalized Douglas–Kroll Transformation. *J. Chem. Phys.* **2002**, *117*, 9215–9226.

[169] van Wüllen, C. Relation Between Different Variants of The Generalized Douglas–Kroll Transformation Through Sixth Order. *J. Chem. Phys.* **2004**, *120*, 7307–7313.

[170] Reiher, M.; Wolf, A. Exact Decoupling of the DIrac Hamiltonian. II. The Generalized Douglas-Kroll-Hess Transformation Up to Arbitrary Order. *J. Chem. Phys.* **2004**, *121*, 10945.

[171] Peng, D.; Hirao, K. An Arbitrary Order Douglas–Kroll Method with Polynomial Cost. *J. Chem. Phys.* **2009**, *130*, 044102.

[172] Chang, C.; Pelissier, M.; Durand, P. Regular Two-Component Pauli-Like Effective Hamiltonians in Dirac Theory. *Phys. Scripta* **1986**, *34*, 394.

[173] van Lenthe, E.; Baerends, E. J.; Snijders, J. G. Relativistic Total Energy Using Regular Approximations. *J. Chem. Phys.* **1994**, *101*, 9783–9792.

[174] van Lenthe, E.; Snijders, J. G.; Baerends, E. J. The Zero-order Regular Approximation for Relativistic Effects: The Effect of Spin–orbit Coupling in Closed Shell Molecules. *J. Chem. Phys.* **1996**, *105*, 6505–6516.

[175] Dyall, K. G. Interfacing Relativistic And Nonrelativistic Methods. I. Normalized Elimination of The Small Component in The Modified Dirac Equation. *J. Chem. Phys.* **1997**, *106*, 9618–9626.

[176] Kutzlenigg, W.; Liu, W. Quasirelativistic Theory Equivalent to Fully Relativistic Theory. *J. Chem. Phys.* **2005**, *123*, 241102.

[177] Liu, W.; Peng, D. Infinite-Order Quasirelativistic Density Functional Method Based on the Exact Matrix Quasirelativistic Theory. *J. Chem. Phys.* **2006**, *125*, 044102.

[178] Peng, D.; Liu, W.; Xiao, Y.; Cheng, L. Making Four- and Two-component Relativistic Density Functional Methods fully Equivalent based on the Idea of 'from Atoms to Molecule'. *J. Chem. Phys.* **2007**, *127*, 104106.

[179] Liu, W.; Peng, D. Exact Two-component Hamiltonians Revisited. *J. Chem. Phys.* **2009**, *131*, 031104.

[180] Liu, W. Ideas of Relativistic Quantum Chemistry. *Mol. Phys.* **2010**, *108*, 1679–1706.

[181] Li, Z.; Xiao, Y.; Liu, W. On the Spin Separation of Algebraic Two-Component Relativistic Hamiltonians. *J. Chem. Phys.* **2012**, *137*, 154114.

[182] Peng, D.; Middendorf, N.; Weigend, F.; Reiher, M. An Efficient Implementation of Two-Component Relativistic Exact-Decoupling Methods for Large Molecules. *J. Chem. Phys.* **2013**, *138*, 184105.

[183] Tamukong, P. K.; Hoffmann, M. R.; Li, Z.; Liu, W. Relativistic GVVPT2 Multireference Perturbation Theory Description of the Electronic States of Y_2 and Tc_2. *J. Phys. Chem. A* **2014**, *118*, 1489–1501.

[184] Egidi, F.; Goings, J. J.; Frisch, M. J.; Li, X. Direct Atomic-Orbital-Based Relativistic Two-Component Linear Response Method for Calculating Excited-State Fine Structures. *J. Chem. Theory Comput.* **2016**, *12*, 3711–3718.

[185] Goings, J. J.; Kasper, J. M.; Egidi, F.; Sun, S.; Li, X. Real Time Propagation of the Exact Two Component Time-Dependent Density Functional Theory. *J. Chem. Phys.* **2016**, *145*, 104107.

[186] Konecny, L.; Kadek, M.; Komorovsky, S.; Malkina, O. L.; Ruud, K.; Repisky, M. Acceleration of Relativistic Electron Dynamics by Means of X2C Transformation: Application to the Calculation of Nonlinear Optical Properties. *J. Chem. Theory Comput.* **2016**, *12*, 5823–5833.

[187] Egidi, F.; Sun, S.; Goings, J. J.; Scalmani, G.; Frisch, M. J.; Li, X. Two-Component Non-Collinear Time-Dependent Spin Density Functional Theory for Excited State Calculations. *J. Chem. Theory Comput.* **2017**, *13*, 2591–2603.

[188] Hu, H.; Jenkins, A. J.; Liu, H.; Kasper, J. M.; Frisch, M. J.; Li, X. Relativistic Two-Component Multireference Configuration Interaction Method with Tunable Correlation Space. *J. Chem. Theory Comput.* **2020**, *16*, 2975–2984.

[189] Dyall, K. G. Interfacing Relativistic and Nonrelativistic Methods. II. One- and Two-Electron Scalar Approximations. *J. Chem. Phys.* **2001**, *115*, 9136–9143.

[190] Fedorov, D. G.; Gordon, M. S. A Study of The Relative Importance of One And Two-electron Contributions to Spin–orbit Coupling. *J. Chem. Phys.* **2000**, *112*, 5611–5623.

[191] Nakajima, T.; Hirao, K. Extended Douglas–Kroll Transformations Applied to The Relativistic Many-electron Hamiltonian. *J. Chem. Phys.* **2003**, *119*, 4105–4111.

[192] Seino, J.; Hada, M. Examination of Accuracy of Electron–electron Coulomb Interactions in Two-component Relativistic Methods. *Chem. Phys. Lett.* **2008**, *461*, 327–331.

[193] Chalupský, J.; Yanai, T. Flexible Nuclear Screening Approximation to The Two-electron Spin–orbit Coupling Based on Ab Initio Parameterization. *J. Chem. Phys.* **2013**, *139*, 204106.

[194] Filatov, M.; Zou, W.; Cremer, D. Spin-Orbit Coupling Calculations with the Two-Component Normalized Elimination of the Small Component Method. *J. Chem. Phys.* **2013**, *139*, 014106.

[195] Boettger, J. C. Approximate Two-Electron Spin-Orbit Coupling Term For Density-Functional-Theory DFT Calculations Using The Douglas-Kroll-Hess Transformation. *Phys. Rev. B* **2000**, *62*, 7809–7815.

[196] van Wüllen, C.; Michauk, C. Spin-orbit Coupling Calculations With The Two-component Normalized Elimination of The Small Component Method. *J. Chem. Phys.* **2005**, *123*, 204113.

[197] Heß, B. A.; Marian, C. M.; Wahlgren, U.; Gropen, O. A Mean-Field Spin-Orbit Method Applicable to Correlated Wavefunctions. *J. Chem. Phys.* **1996**, *251*, 365–371.

[198] Schimmelpfennig, B.; Maron, L.; Wahlgren, U.; Teichteil, C.; Fagerli, H.; Gropen, O. On the Efficiency of An Effective Hamiltonian in Spin-orbit CI Calculations. *Chem. Phys. Lett.* **1998**, *286*, 261–266.

[199] Sikkema, J.; Visscher, L.; Saue, T.; Ilias, M. The Molecular Mean-field Approach for Correlated Relativistic Calculations. *J. Chem. Phys.* **2009**, *131*, 124116.

[200] Marian, C. M. Spin-Orbit Coupling and Intersystem Crossing in Molecules. *WIREs Comp. Mol. Sci.* **2012**, *2*, 187–203.

[201] š Bučinský, L.; Kucková, L.; Malček, M.; šek, J. K. i.; Biskupič, S.; Jayatilaka, D.; chel, G. E. B.; Arion, V. B. Picture Change Error in Quasirelativistic Electron/Spin Density, Laplacian And Bond Critical Points. *Chem. Phys.* **2014**, *438*, 37–47.

[202] Knecht, S.; Repisky, M.; Jensen, H. J. A.; Saue, T. Exact Two-component Hamiltonians for Relativistic Quantum Chemistry: Two-electron Picture-change Corrections Made Simple. *J. Chem. Phys.* **2022**, *157*, 114106.

[203] Almoukhalalati, A.; Knecht, S.; Jensen, H. J. A.; Dyall, K. G.; Saue, T. Electron Correlation within the Relativistic No-pair Approximation. *J. Chem. Phys.* **2016**, *145*, 074104.

[204] Watanabe, Y.; Nakano, H.; Tatewaki, H. Effect of Removing The No-virtual-pair Approximation on The Correlation Energy of The He Isoelectronic Sequence. *J. Chem. Phys.* **2007**, *126*, 174105.

[205] Tatewaki, H.; Watanabe, Y. Necessity of Including The Negative Energy Space in Four-component Relativistic Calculations for Accurate Solutions. *Chem. Phys.* **2011**, *389*, 58–63.

[206] Liu, W. Going Beyond "No-pair Relativistic Quantum Chemistry". *J. Chem. Phys.* **2013**, *139*, 014108.

[207] Liu, W. Effective Quantum Electrodynamics Hamiltonians: A Tutorial Review. *Int. J. Quant. Chem.* **2015**, *115*, 631–640.

[208] Sunaga, A.; Salman, M.; Saue, T. 4-component Relativistic Hamiltonian with Effective QED Potentials for Molecular Calculations. *J. Chem. Phys.* **2022**, *157*, 164101.

[209] Dolg, M. *Computational Methods in Lanthanide and Actinide Chemistry, 1st edition*; John Wiley & Sons, New York.

[210] Hoyer, C. E.; Lu, L.; Hu, H.; Shumilov, K. D.; Sun, S.; Knecht, S.; Li, X. Correlated Dirac–Coulomb–Breit Multiconfigurational Self-Consistent-Field Methods. *J. Chem. Phys.* **2023**, *158*, 044101.

[211] Stanton, J. F.; Gauss, J.; Watts, J. D.; Bartlett, R. J. A Direct Product Decomposition Approach for Symmetry Exploitation in Many-Body Methods. I. Energy Calculations. *J. Chem. Phys.* **1991**, *94*, 4334–4345.

[212] Gauss, J.; Stanton, J. F. Coupled-Cluster Calculations of Nuclear Magnetic Resonance Chemical Shifts. *J. Chem. Phys.* **1995**, *103*, 3561–3577.

[213] Davidson, E. R. The Iterative Calculation of a Few of the Lowest Eigenvalues and Corresponding Eigenvectors of Large Real-symmetric Matrices. *J. Chem. Phys.* **1975**, *17*, 87–94.

[214] Hirao, K.; Nakatsuji, H. A Generalization of the Davidson's Method to Large Nonsymmetric Eigenvalue Problems. *J. Comput. Phys.* **1982**, *45*, 246–254.

[215] Caricato, M.; Trucks, G. W.; Frisch, M. J. A Comparison of Three Variants of the Generalized Davidson Algorithm for the Partial Diagonalization of Large Non-Hermitian Matrices. *J. Chem. Theory Comput.* **2010**, *6*, 1966–1970.

[216] Weiss, H.; Ahlrichs, R.; Häser, M. A Direct Algorithm for Self-Consistent-Field Linear Response Theory and Application to C60: Excitation Energies, Oscillator Strengths, and Frequency-Dependent Polarizabilities. *J. Chem. Phys.* **1993**, *99*, 1262–1270.

[217] Vecharynski, E.; Yang, C.; Xue, F. Generalized Preconditioned Locally Harmonic Residual Method for Non-Hermitian Eigenproblems. *SIAM J. Sci. Comp.* **2016**, *38*, A500–A527.

[218] Shiozaki, T.; Mizukami, W. Relativistic Internally Contracted Multireference Electron Correlation Methods. *J. Chem. Theory Comput.* **2015**, *11*, 4733–4739.

[219] Vilkas, M. J.; Ishikawa, Y.; Koc, K. Relativistic Multireference Many-body Perturbation Theory for Quasidegenerate Systems: Energy Levels of Ions of the Oxygen Isoelectronic Sequence. *Phys. Rev. A* **1999**, *60*, 2808–2821.

[220] Abe, M.; Nakajima, T.; Hirao, K. The Relativistic Complete Active-Space Second-Order Perturbation Theory with the Four-Component Dirac Hamiltonian. *J. Chem. Phys.* **2006**, *125*, 234110.

[221] Vlaisavljevich, B.; Shiozaki, T. Nuclear Energy Gradients for Internally Contracted Complex Active Space Second-Order Perturbation Theory: Multistate Extensions. *J. Chem. Theory Comput.* **2016**, *12*, 3781–3787.

[222] Jensen, H. J. A.; Dyall, K. G.; Saue, T.; Fægri, K. Relativistic Four-Component Multiconfigurational Self-Consistent-Field Theory for Molecules: Formalism. *J. Chem. Phys.* **1996**, *104*, 4083–4097.

[223] Kim, I.; Lee, Y. S. Two-Component Multi-Configurational Second-Order Perturbation Theory with Kramers Restricted Complete Active Space Self-Consistent Field Reference Function and Spin-Orbit Relativistic Effective Core Potential. *J. Chem. Phys.* **2014**, *141*, 164104.

[224] Knecht, S.; Jensen, H. J. A.; Saue, T. Relativistic Quantum Chemical Calculations Show that the Uranium Molecule U_2 has a Quadruple Bond. *Nat. Chem.* **2019**, *11*, 40–44.

[225] Bates, J. E.; Shiozaki, T. Fully Relativistic Complete Active Space Self-Consistent Field for Large Molecules: Quasi-second-order Minimax Optimization. *J. Chem. Phys.* **2015**, *142*, 044112.

[226] Reynolds, R. D.; Yanai, T.; Shiozaki, T. Large-scale Relativistic Complete Active Space Self-Consistent Field with Robust Convergence. *J. Chem. Phys.* **2018**, *149*, 014106.

[227] Roos, B. O. *Advances in Chemical Physics; Ab Initio Methods in Quantum Chemistry II*; John Wiley & Sons, Ltd, Chapter 69, p 399.

[228] Lischka, H.; Shepard, R.; Brown, F. B.; Shavitt, I. New Implementation of the Graphical Unitary Group Approach for Multireference Direct Configuration Interaction Calculations. *Int. J. Quant. Chem.* **1981**, *20*, 91–100.

[229] Zhang, N.; Xiao, Y.; Liu, W. SOiCI and iCISO: Combining Iterative Configuration Interaction with Spin–Orbit Coupling in Two Ways. *J. Phys.–Condens. Mat.* **2022**, *34*, 224007.

[230] Williams-Young, D.; Egidi, F.; Li, X. Relativistic Two-Component Particle-Particle Tamm-Dancoff Approximation. *J. Chem. Theory Comput.* **2016**, *12*, 5379–5384.

[231] Petrone, A.; Williams-Young, D. B.; Sun, S.; Stetina, T. F.; Li, X. An Efficient Implementation of Two-Component Relativistic Density Functional Theory with Torque-Free Auxiliary Variables. *Euro. Phys. J. B* **2018**, *91*, 169.

[232] Huron, B.; Malrieu, J. P.; Rancurel, P. Iterative Perturbation Calculations of Ground and Excited State Energies from Multiconfigurational Zeroth-order Wavefunctions. *J. Chem. Phys.* **1973**, *58*, 5745–5759.

[233] Nakano, H. Quasidegenerate Perturbation Theory with Multiconfigurational Self-Consistent-Field Reference Functions. *J. Chem. Phys.* **1993**, *99*, 7983–7992.

[234] Granovsky, A. A. Extended Multi-Configuration Quasi-Degenerate Perturbation Theory: The New Approach to Multi-state Multi-Reference Perturbation Theory. *J. Chem. Phys.* **2011**, *134*, 214113.

[235] Finley, J.; Malmqvist, P. Å.; Roos, B. O.; Serrano-Andrés, L. The Multi-State CASPT2 Method. *Chem. Phys. Lett.* **1998**, *288*, 299–306.

[236] Shiozaki, T.; Győrffy, W.; Celani, P.; Werner, H.-J. Communication: Extended Multi-State Complete Active Space Second-Order Perturbation Theory: Energy and Nuclear Gradients. *J. Chem. Phys.* **2011**, *135*, 081106.

[237] Khait, Y. G.; Song, J.; Hoffmann, M. R. Macroconfigurations in Molecular Electronic Structure Theory. *Int. J. Quant. Chem.* **2004**, *99*, 210–220.

[238] Khait, Y. G.; Song, J.; Hoffmann, M. R. Explication and Revision of Generalized Van Vleck Perturbation Theory for Molecular Electronic Structure. *J. Chem. Phys.* **2002**, *117*, 4133–4145.

[239] Ivanic, J. Direct Configuration Interaction and Multiconfigurational Self-Consistent-Field Method for Multiple Active Spaces with Variable Occupations. I. Method. *J. Chem. Phys.* **2003**, *119*, 9364–9376.

[240] Roskop, L.; Gordon, M. S. Quasi-Degenerate Second-order Perturbation Theory for Occupation Restricted Multiple Active Space Self-Consistent Field Reference Functions. *J. Chem. Phys.* **2011**, *135*, 044101.

[241] Klene, M.; Robb, M. A.; Blancafort, L.; Frisch, M. J. A New Efficient Approach to the Direct Restricted Active Space Self-Consistent Field Method. *J. Chem. Phys.* **2003**, *119*, 713–728.

[242] Saad, Y.; Schultz, M. H. GMRES: A Generalized Minimal Residual Algorithm for Solving Nonsymmetric Linear Systems. *SIAM J. Sci. and Stat. Comput.* **1986**, *7*, 856–869.

[243] Williams-Young, D. B.; Petrone, A.; Sun, S.; Stetina, T. F.; Lestrange, P.; Hoyer, C. E.; Nascimento, D. R.; Koulias, L.; Wildman, A.; Kasper, J.; Goings, J. J.; Ding, F.; DePrince III, A. E.; Valeev, E. F.; Li, X. The Chronus Quantum (ChronusQ) Software Package. *WIREs Comput. Mol. Sci.* **2020**, *10*, e1436.

[244] Hunt, s. J.; Goddard, W. A. Excited States of H_2O Using Improved Virtual Orbitals. *Chem. Phys. Lett.* **1969**, *3*, 414–418.

[245] Hirao, K.; Huzinaga, S. Improved Virtual Orbitals in the Potential of the SCF Ion. *Chem. Phys. Lett.* **1977**, *45*, 55–58.

[246] Kramida, A.; Ralchenko, Y.; Reader, J.; NIST ASD Team, NIST Atomic Spectra Database (version 5.6.1). https://physics.nist.gov/asd, 2018; National Institute of Standards and Technology, Gaithersburg, MD.

[247] Fdez. Galván, I. et al. OpenMolcas: From Source Code to Insight. *J. Chem. Theory Comput.* **2019**, *15*, 5925–5964.

[248] Pollak, P.; Weigend, F. Segmented Contracted Error-Consistent Basis Sets of Double- and Triple-Valence Quality for One- and Two-Component Relativistic All-Electron Calculations. *J. Chem. Theory Comput.* **2017**, *13*, 3696–3705.

[249] VanGundy, R. A.; Persinger, T. D.; Heaven, M. C. Low Energy States of NdO^+ Probed by Photoelectron Spectroscopy. *J. Chem. Phys.* **2019**, *150*, 114302.

[250] Wyart, J.-F.; Meftah, A.; Tchang-Brillet, W. L.; Champion, N.; Lamrous, O.; Spector, N.; Sugar, J. Analysis of The Free Ion Nd^{3+} Spectrum (Nd IV). *J. Phys. B* **2007**, *40*, 3957–3972.

[251] Butler, P. H. *Point Group Symmetry Applications: Methods and Tables*; Plenum Press, New York, NY, USA, 1981.

[252] Zimmermann, P.; Hunault, M. O. J. Y.; de Groot, F. M. F. 1s2p RIXS Calculations for 3d Transition Metal Ions in Octahedral Symmetry. *J. Spectrosc.* **2018**, *2018*, 3618463.

[253] Huber, K. P.; Herzberg, G. H. In *NIST Chemistry WebBook, NIST Standard Reference Database Number 69*; Linstrom, P., Mallard, W., Eds.; National Institute of Standards and Technology, Gaithersburg MD, 20899, (retrieved January 15, 2022).

[254] Dunning, T. H. Gaussian Basis Sets for Use in Correlated Molecular Calculations. I. The Atoms Boron through Neon and Hydrogen. *J. Chem. Phys.* **1989**, *90*, 1007–1023.

[255] Kendall, R. A.; Dunning, T. H.; Harrison, R. J. Electron Affinities of the First-row Atoms Revisited. Systematic Basis Sets and Wave Functions. *J. Chem. Phys.* **1992**, *96*, 6796–6806.

[256] Morse, P. M. Diatomic Molecules According to the Wave Mechanics. II. Vibrational Levels. *Phys. Rev.* **1929**, *34*, 57–64.

[257] Fedorov, D. G.; Finley, J. P. Spin-orbit Multireference Multistate Perturbation Theory. *Phys. Rev. A* **2001**, *64*, 042502.

[258] Zeng, T.; Fedorov, D. G.; Klobukowski, M. Multireference Study of Spin-orbit Coupling in the Hydrides of the 6p-block Elements Using the Model Core Potential Method. *J. Chem. Phys.* **2010**, *132*, 2014–2019.

[259] Liu, Y.; Liu, R.; Li, L.; Yan, B. Low-lying Electronic States in Thallium Hydride with Multireference Configuration Interaction Calculation. *J. Quant. Spectrosc. Radiat. Transf.* **2021**, *270*, 107667.

[260] Titov, A. V.; Mosyagin, N. S.; Alekseyev, A. B.; Buenker, R. J. GRECP/MRD-CI Calculations of Spin-orbit Splitting in Ground State of Tl and of Spectroscopic Properties of TlH. *Int. J. Quant. Chem.* **2001**, *81*, 409–421.

[261] Grundström, B.; Valberg, P. The Band Spectrum of Thallium Hydride. I. *Z. Phys.* **1938**, *108*, 326–337.

[262] Neuhaus, H.; Muld, V. . The Band Spectrum of Thallium Deuterides. *Z. Phys.* **1959**, *153*, 412–422.

[263] Urban, R.-D.; Bahnmaier, A. H.; Magg, U.; Jones, H. The Diode Laser Spectrum of Thallium Hydride (^{205}TlH and ^{203}TlH) in Its Ground Electronic State. *Chem. Phys. Lett.* **1989**, *158*, 443–446.

[264] Rakowitz, F.; Marian, C. M. An Extrapolation Scheme for Spin–orbit Configuration Interaction Energies Applied to The Ground And Excited Electronic States of Thallium Hydride. *Chem. Phys.* **1997**, *225*, 223–238.

[265] Jeong Choi, Y.; Han, Y.-K.; Lee, Y. S. The Convergence of Spin–orbit Configuration Interaction Calculations for TlH and (113)H. *J. Chem. Phys.* **2001**, *115*, 3448–3453.

[266] Song, Y.; Guo, Y.; Lei, Y.; Zhang, N.; Liu, W. The Static–Dynamic–Static Family of Methods for Strongly Correlated Electrons: Methodology and Benchmarking. *Top. Curr. Chem.* **2021**, *379*, 43.

[267] Mann, J. B.; Johnson, W. R. Breit Interaction in Multielectron Atoms. *Phys. Rev. A* **1971**, *4*, 41–51.

[268] Huang, K.-N.; Aoyagi, M.; Chen, M. H.; Crasemann, B.; Mark, H. Neutral-Atom Electron Binding Energies from Relaxed-Orbital Relativistic Hartree-Fock-Slater Calculations $2 \leq Z \leq 106$. *At. Data Nucl. Data Tables* **1976**, *18*, 243–291.

[269] Chantler, C.; Nguyen, T.; Lowe, J.; Grant, I. Convergence of the Breit Interaction in Self-Consistent and Configuration-Interaction Approaches. *Phys. Rev. A* **2014**, *90*, 062504.

[270] Kozioł, K.; Giménez, C. A.; Aucar, G. A. Breit Corrections to Individual Atomic and Molecular Orbital Energies. *J. Chem. Phys.* **2018**, *148*, 044113.

[271] Grant, I. P.; Penney, W. G. Relativistic Self-Consistent Fields. *Proc. R. Soc. London, Ser. A* **1961**, *262*, 555–576.

[272] Lindroth, E.; Martensson-Pendrill, A.-M.; Ynnerman, A.; Oster, P. Self-Consistent Treatment of the Breit Interaction, with Application to the Electric Dipole Moment in Thallium. *J. Phys. B* **1989**, *22*, 2447–2464.

[273] Desclaux, J. A Multiconfiguration Relativistic DIRAC-FOCK Program. *Comp. Phys. Comm.* **1975**, *9*, 31–45.

[274] Grant, I.; McKenzie, B. The Transverse Electron-Electron Interaction in Atomic Structure Calculations. *J. Phys. B* **1980**, *13*, 2671.

[275] Dyall, K.; Grant, I.; Johnson, C.; Parpia, F.; Plummer, E. GRASP: A General-Purpose Relativistic Atomic Structure Program. *Comp. Phys. Comm.* **1989**, *55*, 425–456.

[276] Quiney, H. M.; Grant, I. P.; Wilson, S. The Dirac Equation in the Algebraic Approximation. V. Self-Consistent Field Studies Including the Breit Interaction. *J. Phys. B* **1987**, *20*, 1413–1422.

[277] Quiney, H. M.; Skaane, H.; Grant, I. P. Relativistic Calculation of Electromagnetic Interactions in Molecules. *J. Phys. B* **1997**, *30*, L829–L834.

[278] Quiney, H.; Skaane, H.; Grant, I. Relativistic, Quantum Electrodynamic and Many-Body Effects in the Water Molecule. *Chem. Phys. Lett.* **1998**, *290*, 473–480.

[279] Ishikawa, Y. Dirac–Fock Gaussian Basis Calculations: Inclusion of the Breit Interaction in the Self-Consistent Field Procedure. *Chem. Phys. Lett.* **1990**, *166*, 321–325.

[280] Ishikawa, Y.; Quiney, H. M.; Malli, G. L. Dirac-Fock-Breit Self-Consistent-Field Method: Gaussian Basis-Set Calculations on Many-Electron Atoms. *Phys. Rev. A* **1991**, *43*, 3270–3278.

[281] Parpia, F. A.; Mohanty, A. K.; Clementi, E. Relativistic Calculations for Atoms: Self-Consistent Treatment of Breit Interaction and Nuclear Volume Effect. *J. Phys. B* **1992**, *25*, 1–16.

[282] Shiozaki, T. Communication: An Efficient Algorithm for Evaluating the Breit and Spin-Spin Coupling Integrals. *J. Chem. Phys.* **2013**, *138*, 111101.

[283] Sun, S.; Stetina, T. F.; Zhang, T.; Hu, H.; Valeev, E. F.; Sun, Q.; Li, X. Efficient Four-Component Dirac–Coulomb–Gaunt Hartree–Fock in the Pauli Spinor Representation. *J. Chem. Theory Comput.* **2021**, *17*, 3388–3402.

[284] Ishikawa, Y.; Binning, R.; Sando, K. Dirac-Fock Discrete-Basis Calculations on the Beryllium Atom. *Chem. Phys. Lett.* **1983**, *101*, 111 – 114.

[285] Sun, S.; Stetina, T. F.; Zhang, T.; Li, X. In *Rare Earth Elements and Actinides: Progress in Computational Science Applications*; Penchoff, D. A., Windus, T. L., C., P. C., Eds.; American Chemical Society, 2021; Vol. 1388; Chapter Chapter 10 - On the Finite Nuclear Effect and Gaussian Basis Set for Four-Component Dirac Hartree-Fock Calculations., pp 207–218.

[286] Saue, T.; Visscher, L. In *Theoretical Chemistry and Physics of Heavy and Superheavy Elements*; Wilson, S., Kaldor, U., Eds.; Kluwer, Dordrecht, 2003; pp 211–261.

[287] White, S. R. Density-Matrix Algorithms for Quantum Renormalization Groups. *Phys. Rev. B* **1993**, *48*, 10345.

[288] Zhai, H.; Chan, G. K.-L. A Comparison Between the One- and Two-Step Spin–Orbit Coupling Approaches Based on the *ab initio* Density Matrix Renormalization Group. *J. Chem. Phys.* **2022**, *157*, 164108.

[289] Keller, S.; Dolfi, M.; Troyer, M.; Reiher, M. An Efficient Matrix Product Operator Representation of the Quantum Chemical Hamiltonian. *J. Chem. Phys.* **2015**, *143*, 244118.

[290] Keller, S.; Reiher, M. Spin-Adapted Matrix Product States and Operators. *J. Chem. Phys.* **2016**, *144*, 134101.

[291] Knecht, S.; Hedegaard, E. D.; Keller, S.; Kovyrshin, A.; Ma, Y.; Muolo, A.; Stein, C. J.; Reiher, M. New Approaches for Ab Initio Calculations of Molecules with Strong Electron Correlation. *Chimia* **2016**, *70*, 244–251.

[292] McCulloch, I. P. From Density-Matrix Renormalization Group to Matrix Product States. **2007**, P10014.

[293] Werner, H.-J.; Meyer, W. A Quadratically Convergent MCSCF Method for the Simultaneous Optimization of Several States a Quadratically Convergent MCSCF Method for the Simultaneous Optimization of Several States. *J. Chem. Phys.* **1981**, *74*, 5794.

[294] Wouters, S.; Van Neck, D. The Density Matrix Renormalization Group for Ab Initio Quantum Chemistry. *Euro. Phys. J. D* **2014**, *68*, 1–20.

[295] Helgaker, T.; Jørgensen, P.; Olsen, J. *Molecular Electronic-Structure Theory*, 1st ed.; John Wiley and Sons, Ltd: West Sussex, U.K., 2000.

[296] Roos, B. O.; Lindh, R.; Malmqvist, P.-Å.; Veryazov, V.; Widmark, P.-O. Main Group Atoms and Dimers Studied with a New Relativistic ANO Basis Set. *J. Phys. Chem. A* **2004**, *108*, 2851–2858.

[297] Roos, B. O.; Lindh, R.; Malmqvist, P.-Å.; Veryazov, V.; Widmark, P.-O.; Borin, A. C. New Relativistic Atomic Natural Orbital Basis Sets for Lanthanide Atoms with Applications to the Ce Diatom and LuF_3. *J. Phys. Chem. A* **2008**, *112*, 11431–11435.

[298] Segarra-Martí, J.; Garavelli, M.; Aquilante, F. Multiconfigurational Second-Order Perturbation Theory with Frozen Natural Orbitals Extended to the Treatment of Photochemical Problems. *J. Chem. Theory Comput.* **2015**, *11*, 3772–3784.

[299] Song, C.; Martínez, T. J. Reduced Scaling Extended Multi-state CASPT2 (XMS-CASPT2) Using Supporting Subspaces and Tensor Hyper-contraction. *J. Chem. Phys.* **2020**, *152*, 234113.

[300] Saitow, M.; Uemura, K.; Yanai, T. A Local Pair-natural Orbital-based Complete-active Space Perturbation Theory Using Orthogonal Localized Virtual Molecular Orbitals. *J. Chem. Phys.* **2022**, *157*, 084101.

[301] Shiozaki, T. BAGEL : Brilliantly Advanced General Electronic-structure Library. *WIREs Comput. Mol. Sci.* **2018**, *8*, e1331.

[302] Yuan, X.; Visscher, L.; Gomes, A. S. P. Assessing MP2 Frozen Natural Orbitals in Relativistic Correlated Electronic Structure Calculations. *J. Chem. Phys.* **2022**, *156*, 224108.

[303] Veryazov, V.; Widmark, P.-O.; Roos, B. O. Relativistic Atomic Natural Orbital Type Basis Sets for The Alkaline and Alkaline-earth Atoms Applied to The Ground-state Potentials for The Corresponding Dimers. *Theor. Chem. Acc.* **2004**, *111*, 345–351.

[304] Pritchard, B. P.; Altarawy, D.; Didier, B.; Gibsom, T. D.; Windus, T. L. A New Basis Set Exchange: An Open, Up-to-date Resource for the Molecular Sciences Community. **2019**, *59*, 4814–4820.

[305] Feller, D. The Role of Databases in Support of Computational Chemistry Calculations. *J. Comput. Chem.* **1996**, *17*, 1571–1586.

[306] Schuchardt, K. L.; Didier, B. T.; Elsethagen, T.; Sun, L.; Gurumoorthi, V.; Chase, J.; Li, J.; Windus, T. L. Basis Set Exchange: A Community Database for Computational Sciences. **2007**, *47*, 1045–1052.

[307] Roos, B. O.; Lindh, R.; Malmqvist, P. Å.; Veryazov, V.; Widmark, P.-O. Main Group Atoms and Dimers Studied with a New Relativistic ANO Basis Set. *J. Phys. Chem. A* **2004**, *108*, 2851–2858.

[308] Fleig, T.; Olsen, J.; Visscher, L. The Generalized Active Space Concept for The Relativistic Treatment of Electron Correlation. II. Large-scale Configuration Interaction Implementation Based on Relativistic 2- and 4-spinors and Its Application. *J. Chem. Phys.* **2003**, *119*, 2963–2971.

[309] Pernpointner, M. The Effect of the Gaunt Interaction on The Electric fField Gradient. *Journal of Physics B: Atomic, Molecular and Optical Physics* **2002**, *35*, 383.

[310] Garrett, B. C. et al. Role of Water in Electron-Initiated Processes and Radical Chemistry: Issues and Scientific Advances. *Chem. Rev.* **2005**, *105*, 355–390.

[311] Franks, F., Ed. *Water: A Comprehensive Treatise*; Plenum Press, 1972; Vol. 1.

[312] Draganić, I. G.; Draganić, Z. D. In *The Radiation Chemistry of Water*; Loebl, E. M., Ed.; Elsevier, 1971; Vol. 26.

[313] Gauduel, Y.; Pommeret, S.; Migus, A.; Antonetti, A. Some Evidence of Ultrafast H_2O^+-Water Molecule Reaction in Femtosecond Photoionization of Pure Liquid Water: Influence on Geminate Pair Recombination Dynamics. *Chem. Phys.* **1990**, *149*, 1–10.

[314] Walker, D. C. The Hydrated Electron. **1967**, *21*, 79–108.

[315] Hart, E. J.; Boag, J. Absorption Spectrum of the Hydrated Electron in Water and in Aqueous Solutions. *J. Am. Chem. Soc.* **1962**, *84*, 4090–4095.

[316] Herbert, J. M.; Coons, M. P. The Hydrated Electron. *Annu. Rev. Phys. Chem.* **2017**, *68*, 447–472.

[317] Boero, M.; Parrinello, M.; Terakura, K.; Ikeshoji, T.; Liew, C. C. First-Principles Molecular-Dynamics Simulations of a Hydrated Electron in Normal and Supercritical Water. *Phys. Rev. Lett.* **2003**, *90*, 226403.

[318] Uhlig, F.; Marsalek, O.; Jungwirth, P. Unraveling the Complex Nature of the Hydrated Electron. *J. Phys. Chem. Lett.* **2012**, *3*, 3071–3075.

[319] Long, F. H.; Lu, H.; Eisenthal, K. B. Femtosecond Studies of the Presolvated Electron: An Excited State of the Solvated Electron? *Phys. Rev. Lett.* **1990**, *64*, 1469–1472.

[320] Kamarchik, E.; Kostko, O.; Bowman, J. M.; Ahmed, M.; Krylov, A. I. Spectroscopic Signatures of Proton Transfer Dynamics in The Water Dimer Cation. *J. Chem. Phys.* **2010**, *132*, 194311.

[321] Marsalek, O.; Elles, C. G.; Pieniazek, P. A.; Pluhařová, E.; VandeVondele, J.; Bradforth, S. E.; Jungwirth, P. Chasing Charge Localization and Chemical Reactivity Following Photoionization in Liquid Water. *J. Chem. Phys.* **2011**, *135*, 224510.

[322] Loh, Z.-H. et al. Observation of the Fastest Chemical Processes in the Radiolysis of Water. *Science* **2020**, *367*, 179–182.

[323] Asmis, K. R.; Pivonka, N. L.; Santambrogio, G.; Brümmer, M.; Kaposta, C.; Neumark, D. M.; Wöste, L. Gas-Phase Infrared Spectrum of the Protonated Water Dimer. *Science* **2003**, *299*, 1375–1377.

[324] Headrick, J. M.; Diken, E. G.; Walters, R. S.; Hammer, N. I.; Christie, R. A.; Cui, J.; Myshakin, E. M.; Duncan, M. A.; Johnson, M. A.; Jordan, K. D. Spectral Signatures of Hydrated Proton Vibrations in Water Clusters. *Science* **2005**, *308*, 1765–1769.

[325] Guasco, T. L.; Johnson, M. A.; McCoy, A. B. Unraveling Anharmonic Effects in the Vibrational Predissociation Spectra of H_5O_{2+} and Its Deuterated Analogues. *J. Phys. Chem. A* **2011**, *115*, 5847–5858.

[326] Xu, J.; Zhang, Y.; Voth, G. A. Infrared Spectrum of the Hydrated Proton in Water. *J. Phys. Chem. Lett.* **2011**, *2*, 81–86.

[327] Park, M.; Shin, I.; Singh, N. J.; Kim, K. S. Eigen and Zundel Forms of Small Protonated Water Clusters: Structures and Infrared Spectra. *J. Phys. Chem. A* **2007**, *111*, 10692–10702.

[328] Kim, J.; Schmitt, U. W.; Gruetzmacher, J. A.; Voth, G. A.; Scherer, N. E. The Vibrational Spectrum of the Hydrated Proton: Comparison of Experiment, Simulation, and Normal Mode Analysis. *J. Chem. Phys.* **2002**, *116*, 737–746.

[329] Kulig, W.; Agmon, N. A 'Clusters-In-Liquid' Method for Calculating Infrared Spectra Identifies the Proton-Transfer Mode in Acidic Aqueous Solutions. *Nat. Chem.* **2013**, *5*, 29–35.

[330] Vendrell, O.; Gatti, F.; Meyer, H.-D. Full Dimensional (15-Dimensional) Quantum-Dynamical Simulation of the Protonated Water Dimer. II. Infrared Spectrum and Vibrational Dynamics. *J. Chem. Phys.* **2007**, *127*, 184303.

[331] Wolke, C. T.; Fournier, J. A.; Dzugan, L. C.; Fagiani, M. R.; Odbadrakh, T. T.; Knorke, H.; Jordan, K. D.; McCoy, A. B.; Asmis, K. R.; Johnson, M. A. Spectroscopic Snapshots of the Proton-Transfer Mechanism in Water. *Science* **2016**, *354*, 1131–1135.

[332] Hassanali, A.; Giberti, F.; Cuny, J.; Kühne, T. D.; Parrinello, M. Proton Transfer through the Water Gossamer. *Proc. Natl. Acad. Sci. U.S.A.* **2013**, *110*, 13723–13728.

[333] Berkelbach, T. C.; Lee, H.-S.; Tuckerman, M. E. Concerted Hydrogen-Bond Dynamics in the Transport Mechanism of the Hydrated Proton: A First Principles Molecular Dynamics Study. *Phys. Rev. Lett.* **2009**, *103*, 238302.

[334] Markovitch, O.; Chen, H.; Izvekov, S.; Paesani, F.; Voth, G. A.; Agmon, N. Special Pair Dance and Partner Selection: Elementary Steps in Proton Transport in Liquid Water. *J. Phys. Chem. B* **2008**, *112*, 9456–9466.

[335] Kornyshev, A.; Kuznetsov, A.; Spohr, E.; Ulstrup, J. Kinetics of Proton Transport in Water. *J. Phys. Chem. B* **2003**, *107*, 3351–3366.

[336] Vuilleumier, R.; Borgis, D. An Extended Empirical Valence Bond Model for Describing Proton Transfer in $H^+(H_2O)_n$ Clusters and Liquid Water. *Chem. Phys. Lett.* **1998**, *284*, 71–77.

[337] Tuckerman, M.; Laasonen, K.; Sprik, M.; Parrinello, M. Ab Initio Molecular Dynamics Simulation of the Solvation and Transport of H_3O^+ and OH^- Ions in Water. *J. Phys. Chem.*

[338] Lapid, H.; Agmon, N.; Petersen, M. K.; Voth, G. A. A Bond-Order Analysis of the Mechanism for Hydrated Proton Mobility in Liquid Water. *J. Chem. Phys.* **2005**, *122*, 014506.

[339] Geissler, P. L.; Dellago, C.; Chandler, D.; Hutter, J.; Parrinello, M. Autoionization in Liquid Water. *Science* **2001**, *291*, 2121–2124.

[340] Marx, D. Proton Transfer 200 Years after von Grotthuss: Insights from Ab Initio Simulations. *Comp. Phys. Comm.* **2006**, *7*, 1848–1870.

[341] Marx, D.; Tuckerman, M. E.; Hutter, J.; Parrinello, M. The Nature of the Hydrated Excess Proton in Water. *Nature* **1999**, *397*, 601–604.

[342] Agmon, N. The Grotthuss Mechanism. *Chem. Phys. Lett.* **1995**, *244*, 456–462.

[343] Berendsen, H.; Grigera, J.; Straatsma, T. The Missing Term in Effective Pair Potentials. *J. Phys. Chem.* **1987**, *91*, 6269–6271.

[344] Ozkanlar, A.; Clark, A. E. ChemNetworks: A Complex Network Analysis Tool for Chemical Systems. *J. Comput. Chem.* **2014**, *35*, 495–505.

[345] Yuan, K.; Dixon, R. N.; Yang, X. Photochemistry of the Water Molecule: Adiabatic Versus Nonadiabatic Dynamics. *Acc. Chem. Res.* **2011**, *44*, 369–378.

[346] Hu, X.; Zhou, L.; Xie, D. State-to-State Photodissociation Dynamics of the Water Molecule. *WIREs Comput. Mol. Sci.* **2018**, *8*, e1350.

[347] Zhou, L.; Xie, D. Full-Dimensional Quantum Dynamics of Vibrational Mediated Photodissociation of HOD in its B Band. *J. Phys. Chem. A* **2015**, *119*, 12062–12072.

[348] Wang, Z.; Xu, X.; Zhang, F.; Qian, C. TDDFT Investigation of Excitation of Water Tetramer under Femtosecond Laser Pulse Irradiation. *Int. J. Mod. Phys. B* **2018**, *32*, 1850113.

[349] Yuan, K.; Cheng, Y.; Cheng, L.; Guo, Q.; Dai, D.; Wang, X.; Yang, X.; Dixon, R. N. Nonadiabatic Dissociation Dynamics in H_2O: Competition Between Rotationally and Nonrotationally Mediated Pathways. *Proc. Natl. Acad. Sci. U.S.A.* **2008**, *105*, 19148–19153.

[350] Chmura, B.; Lan, Z.; Rode, M. F.; Sobolewski, A. L. Photochemistry of the Water Dimer: Time-Dependent Quantum Wave-Packet Description of the Dynamics at the S_1-S_0 conical intersection. *J. Chem. Phys.* **2009**, *131*, 134307.

[351] Zhou, L.; Xie, D.; Guo, H. Signatures of Non-Adiabatic Dynamics in the Fine-Structure State Distributions of the OH ($\tilde{X}/\tilde{A}$) Products in the B-band Photodissociation of H_2O. *J. Chem. Phys.* **2015**, *142*, 124317.

[352] Wang, Z.; Dinh, P. M.; Reinhard, P.-G.; Suraud, E. Ultrafast Nonadiabatic Dynamics of a Water Dimer in Femtosecond Laser Pulses. **2014**, *24*, 106004.

[353] Li, X.; Smith, S. M.; Markevitch, A. N.; Romanov, D. A.; Levis, R. J.; Schlegel, H. B. A Time-Dependent Hartree-Fock Approach for Studying the Electronic Optical Response of Molecules in Intense Fields. *Phys. Chem. Chem. Phys.* **2005**, *7*, 233–239.

[354] Williams-Young, D.; Goings, J. J.; Li, X. Accelerating Real-Time Time-Dependent Density Functional Theory with a Non-Recursive Chebyshev Expansion of the Quantum Propagator. *J. Chem. Theory Comput.* **2016**, *12*, 5333–5338.

[355] Frisch, M. J. et al. Gaussian Development Version Revision I.13+. Gaussian Inc., Wallingford CT 2018.

[356] Becke, A. D. Density-Functional Thermochemistry. III. The Role of Exact Exchange. *Chem. Phys* **1993**, *98*, 5648–5652.

[357] Stetina, T. F.; Sun, S.; Lingerfelt, D. B.; Clark, A.; Li, X. The Role of Excited-State Proton Relays in the Photochemical Dynamics of Water Nanodroplets. *J. Phys. Chem. Lett.* **2019**, *10*, 3694–3698.

[358] Li, X.; Millam, J. M.; Schlegel, H. B. Ab Initio Molecular Dynamics Studies of the Photodissociation of Formaldehyde, $H_2CO \rightarrow H_2 + CO$: Direct Classical Trajectory Calculations by MP2 and Density Functional Theory. *J. Chem. Phys.* **2000**, *113*, 10062–10067.

[359] Li, X.; Millam, J. M.; Schlegel, H. B. Glyoxal Photodissociation. An Ab Initio Direct Classical Trajectory Study of $C_2H_2O_2 \rightarrow H_2 + 2CO$. *J. Chem. Phys.* **2001**, *114*, 8897–8904.

[360] Li, X.; Millam, J. M.; Schlegel, H. B. Glyoxal Photodissociation. II. An Ab Initio Direct Classical Trajectory Study of $C_2H_2O_2 \rightarrow CO + H_2CO$. *J. Chem. Phys.* **2001**, *115*, 6907–6912.

[361] Liang, W.; Chapman, C. T.; Li, X. Efficient First-Principles Electronic Dynamics. *J. Chem. Phys.* **2011**, *134*, 184102.

[362] Morrone, J. A.; Car, R. Nuclear Quantum Effects in Water. *Phys. Rev. Lett.* **2008**, *101*, 017801.

[363] Sun, Z.; Zheng, L.; Chen, M.; Klein, M. L.; Paesani, F.; Wu, X. Electron-Hole Theory of the Effect of Quantum Nuclei on the X-Ray Absorption Spectra of Liquid Water. *Phys. Rev. Lett.* **2018**, *121*, 137401.

[364] Pavese, M.; Chawla, S.; Lu, D.; Lobaugh, J.; Voth, G. A. Quantum Effects and the Excess Proton in Water. *J. Chem. Phys.* **1997**, *107*, 7428–7432.

[365] Napoli, J. A.; Marsalek, O.; Markland, T. E. Decoding the Spectroscopic Features and Time Scales of Aqueous Proton Defects. *J. Chem. Phys.* **2018**, *148*, 222833.

[366] Mulliken, R. S. Electronic Population Analysis on LCAO–MO Molecular Wave Functions. I. *J. Chem. Phys.* **1955**, *23*, 1833–1840.

[367] Vacher, M.; Albertani, F. E.; Jenkins, A. J.; Polyak, I.; Bearpark, M. J.; Robb, M. A. Electron and Nuclear Dynamics Following Ionisation of Modified Bismethylene-Adamantane. *Faraday Discuss.* **2016**, *194*, 95–115.

[368] Vacher, M.; Bearpark, M. J.; Robb, M. A.; Malhado, J. P. Electron Dynamics upon Ionization of Polyatomic Molecules: Coupling to Quantum Nuclear Motion and Decoherence. *Phys. Rev. Lett.* **2017**, *118*, 083001.

[369] Pieniazek, P. A.; VandeVondele, J.; Jungwirth, P.; Krylov, A. I.; Bradforth, S. E. Electronic Structure of the Water Dimer Cation. *J. Phys. Chem. A* **2008**, *112*, 6159–6170.

[370] Thämer, M.; De Marco, L.; Ramasesha, K.; Mandal, A.; Tokmakoff, A. Ultrafast 2D IR Spectroscopy of the Excess Proton in Liquid Water. *Science* **2015**, *350*, 78–82.

[371] Subotnik, J. E.; Shenvi, N. A New Approach to Decoherence and Momentum Rescaling in the Surface Hopping Algorithm. *J. Chem. Phys.* **2011**, *134*, 024105.

[372] Bittner, E. R.; Rossky, P. J. Quantum Decoherence in Mixed Quantum-Classical Systems - Nonadiabatic Processes. *J. Chem. Phys.* **1995**, *103*, 8130–8143.

[373] Bedard-Hearn, M. J.; Larsen, R. E.; Schwartz, B. J. Mean-Field Dynamics with Stochastic Decoherence (MF-SD): A New Algorithm for Nonadiabatic Mixed Quantum/Classical Molecular-Dynamics Simulations with Nuclear-Induced Decoherence. *J. Chem. Phys.* **2005**, *123*, 234106.

[374] Shenvi, N.; Subotnik, J. E.; Yang, W. Simultaneous-Trajectory Surface Hopping: A Parameter-Free Algorithm for Implementing Decoherence in Nonadiabatic Dynamics. *J. Chem. Phys.* **2011**, *134*, 144102.

[375] Jaeger, H. M.; Fischer, S.; Prezhdo, O. V. Decoherence-Induced Surface Hopping. *J. Chem. Phys.* **2012**, *137*, 22A545.

[376] Truhlar, D. G. In *Quantum Dynamics of Complex Molecular Systems*; Micha, D. A., Burghardt, I., Eds.; Springer Berlin Heidelberg: Berlin, Heidelberg, 2007; pp 227–243.

[377] Radler, J. J.; Lingerfelt, D. B.; Castellano, F. N.; Chen, L. X.; Li, X. Role of Vibrational Dynamics on Excited-State Electronic Coherence in a Binuclear Platinum Complex. *J. Phys. Chem. A* **2018**, *122*, 5071–5077.

[378] Kjellsson, L. et al. Resonant Inelastic X-Ray Scattering Reveals Hidden Local Transitions of the Aqueous OH Radical. *Phys. Rev. Lett.* **2020**, *124*, 236001.

[379] Ma, J.; Wang, F.; Mostafavi, M. Ultrafast Chemistry of Water Radical Cation, H2O•+, in Aqueous Solutions. *Molecules* **2018**, *23*, 244.

[380] Cederbaum, L. S.; Zobeley, J.; Tarantelli, F. Giant Intermolecular Decay and Fragmentation of Clusters. *Phys. Rev. Lett.* **1997**, *79*, 4778–4781.

[381] Jahnke, T.; Hergenhahn, U.; Winter, B.; Dörner, R.; Frühling, U.; Demekhin, P. V.; Gokhberg, K.; Cederbaum, L. S.; Ehresmann, A.; Knie, A.; Dreuw, A. Interatomic and Intermolecular Coulombic Decay. *Chem. Rev.* **2020**, *120*, 11295–11369.

[382] Jones, B. M.; Hu, H.; Alexsandrov, A.; Smith, W.; Clark, A. E.; Li, X.; Orlando, T. M. Efficient Intermolecular Energy Exchange and Soft Ionization of Water at Nanoplatelet Interfaces. *J. Phys. Chem. Lett.* **2020**, *11*, 10088–10093.

[383] Frisch, M. J. et al. Gaussian Development Version Revision J.14+.

[384] Herman, K. M.; Xantheas, S. S. An Extensive Assessment of the Performance of Pairwise and Many-body Interaction Potentials in Reproducing Ab Initio Benchmark Binding Energies for Water Clusters n = 2 – 25. *Phys. Chem. Chem. Phys.* **2023**, *25*, 7120–7143.

[385] Clark, T.; Chandrasekhar, J.; Spitznagel, G. n. W.; Schleyer, P. V. R. Efficient Diffuse Function-Augmented Basis Sets for Anion Calculations. III. The 3-21+G Basis Set for First-Row Elements, Li-F. *J. Comput. Chem.* **1983**, *4*, 294–301.

[386] Krishnan, R.; Binkley, J. S.; Seeger, R.; Pople, J. A. Self-Consistent Molecular Orbital Methods. XX. A Basis Set for Correlated Wave Functions. *J. Chem. Phys.* **1980**, *72*, 650–654.

[387] Jenkins, A. J.; Hu, H.; Lu, L.; Frisch, M. J.; Li, X. Two-Component Multireference Restricted Active Space Configuration Interaction for the Computation of L-Edge X-ray Absorption Spectra. *J. Chem. Theory Comput.* **2022**, *18*, 141–150.

[388] Martin, R. L. Natural transition orbitals. *J. Chem. Phys.* **2003**, *118*, 4775–4777.

[389] Schwarz, J.; Kielgast, F.; Baev, I.; Reinwardt, S.; Trinter, F.; Klumpp, S.; Perry-Sassmannshausen, A.; Buhr, T.; Schippers, S.; Muller, A.; Bari, S.; Mondes, V.; Flesch, R.; Rühl, E.; Martins, M. X-Ray Absorption Spectroscopy of H_3O^+. *Phys. Chem. Chem. Phys.* **2022**, *24*, 23119–23127.

[390] Olsen, J.; Roos, B. O.; Jørgensen, P.; Jensen, H. J. A. Determinant Based Configuration Interaction Algorithms for Complete and Restricted Configuration Interaction Spaces. *J. Chem. Phys.* **1988**, *89*, 2185–2192.

[391] Fleig, T.; Olsen, J.; Marian, C. M. The Generalized Active Space Concept for The Relativistic Treatment of Electron Correlation. I. Kramers-Restricted Two-Component Configuration Interaction. *J. Chem. Phys.* **2001**, *114*, 4775–4790.

[392] Fleig, T.; Jensen, H. J. A.; Olsen, J.; Visscher, L. The Generalized Active Space Concept for The Relativistic Treatment of Electron Correlation. III. Large-Scale Configuration Interaction And Multiconfiguration Self-Consistent-Field Four-Component Methods with Application to UO2. *J. Chem. Phys.* **2006**, *124*, 104106.

[393] Knecht, S.; Jensen, H. J. A.; Fleig, T. Large-Scale Parallel Configuration Interaction. I. Nonrelativistic And Scalar-Relativistic General Active Space Implementation with Application to (Rb–Ba)$^+$. *J. Chem. Phys.* **2008**, *128*, 014108.

[394] Knecht, S.; Jensen, H. J. A.; Fleig, T. Large-scale Parallel Configuration Interaction. II. Two and Four-Component Double-Group General Active Space Implementation with Application to BiH. *J. Chem. Phys.* **2010**, *132*, 014108.

[395] Vogiatzis, K. D.; Ma, D.; Olsen, J.; Gagliardi, L.; de Jong, W. A. Pushing Configuration-Interaction to the Limit: Towards Massively Parallel MCSCF Calculations. *J. Chem. Phys.* **2017**, *147*, 184111.

[396] Ma, D.; Li Manni, G.; Gagliardi, L. The Generalized Active Space Concept in Multiconfigurational Self-Consistent Field Methods. *J. Chem. Phys.* **2011**, *135*, 044128.

[397] Vogiatzis, K. D.; Li Manni, G.; Stoneburner, S. J.; Ma, D.; Gagliardi, L. Systematic Expansion of Active Spaces beyond the CASSCF Limit: A GASSCF/SplitGAS Benchmark Study. *J. Chem. Theory Comput.* **2015**, *11*, 3010–3021.

[398] Odoh, S. O.; Manni, G. L.; Carlson, R. K.; Truhlar, D. G.; Gagliardi, L. Separated-Pair Approximation And Separated-Pair Pair-Density Functional Theory. *Chem. Sci.* **2016**, *7*, 2399–2413.

[399] Ghosh, S.; Cramer, C. J.; Truhlar, D. G.; Gagliardi, L. Generalized-Active-Space Pair-Density Functional Theory: An Efficient Method to Study Large, Strongly Correlated, Conjugated Systems. *Chem. Sci.* **2017**, *8*, 2741–2750.

[400] Ma, D.; Li Manni, G.; Olsen, J.; Gagliardi, L. Second-Order Perturbation Theory for Generalized Active Space Self-Consistent-Field Wave Functions. *J. Chem. Theory Comput.* **2016**, *12*, 3208–3213.

[401] Huang, M.; Li, C.; Evangelista, F. A. Theoretical Calculation of Core-Excited States along Dissociative Pathways beyond Second-Order Perturbation Theory. *J. Chem. Theory Comput.* **2022**, *18*, 219–233.

[402] Huang, M.; Evangelista, F. A. A Benchmark Study of Core-Excited States of Organic Molecules Computed with The Generalized Active Space Driven Similarity Renormalization Group. 2022; https://arxiv.org/abs/2212.04369.

[403] Weser, O.; Guther, K.; Ghanem, K.; Li Manni, G. Stochastic Generalized Active Space Self-Consistent Field: Theory and Application. *J. Chem. Theory Comput.* **2022**, *18*, 251–272.

Appendix A

SUPPORTING INFORMATION FOR RELATIVISTIC TWO-COMPONENT MULTIREFERENCE SECOND-ORDER PERTURBATION THEORY

Spin-Free vs. Variational Inclusion of Spin-Orbit

In this Appendix section, we compare X2C-MRPT2 calculations using spin-free orbitals (sf-X2C-MRPT2(SO)) to those using variationally optimized orbitals at the X2C-CASSCF level with spin-orbit couplings. Calculations presented here use the same active space and basis set as in Sec. 3.4.2. For PT2 calculations, all virtual spinor orbitals are correlated to recover the dynamic correlation and avoid the error introduced by the frozen virtual orbital approximation. The results are shown in Tab. A.1.

Ga	sf-X2C-CASSCF	sf-X2C-MRPT2(SO)	X2C-MRPT2	Exp.
1	−1942.181826	−1942.337628	−1942.400843	
2	−1942.181826	−1942.337628	−1942.400843	
3	−1942.181826	−1942.334341	−1942.397130	
4	−1942.181826	−1942.334341	−1942.397130	
5	−1942.181826	−1942.334341	−1942.397130	
6	−1942.181826	−1942.334341	−1942.397129	
splitting (meV)	0	89.5	101.0	102

Table A.1: The ground state ^{2}P energy splitting ($^2P_{1/2} \rightarrow {}^2P_{3/2}$ in meV) of Ga. Energies of microstates that belong to $^2P_{1/2}$ and $^2P_{3/2}$ levels are presented. State-averaging is used in all multi-reference methods developed in this work.

All the six states remain degenerate in spin-free X2C-CASSCF (sf-X2C-CASSCF) calculations due to the lack of spin-orbit coupling. When spin-orbit coupling is included in the Hamiltonian of MRPT2 calculation with sf-X2C-CASSCF orbitals, the ground states split into 2- and 4-fold degenerate microstates. Comparing the fine-structure splitting using

spin-free orbitals and that computed using variationally optimized orbitals with spin-orbit coupling (*e.g.*, X2C-MRPT2), sf-X2C-MRPT2(SO) splitting has a larger error compared to the X2C-MRPT2 result. This test demonstrates the significant improvement when the spin-orbit coupling is included variationally at the reference level.

Appendix B

SUPPORTING INFORMATION FOR THE VALENCE HOLE DYNAMICS OF WATER CLUSTER

B.1 Spatial Extent of Hole

The vertical ionization of the vibrationally bound initial states of water $(H_2O)_{27}$ nanodroplet results in a non-localized hole in our simulations. In order to demonstrate the factors that affect the spatial extent of the photoionized hole, the highest occupied molecular orbital (HOMO) of a water dimer with different O–O distance and orientation was shown in the following figures. The initial conditions (geometry and momentum) have an effect on the spacial extent of the photoionized hole via the degree of the orbital overlap/mixing. The calculations are performed with the same density functional and basis set as in the main text, *i.e.*, BH&H and 6-31g(d,p) basis set.

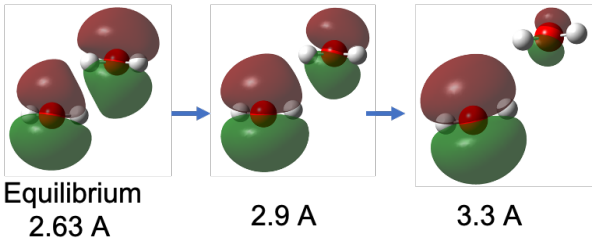

Figure B.1: The highest occupied molecular orbital (HOMO) distribution of a water dimer with different O–O distance. Compared to the equilibrium geometry, the further apart in terms of the two water molecules, the more localized is the HOMO. (A refers to Angstrom)

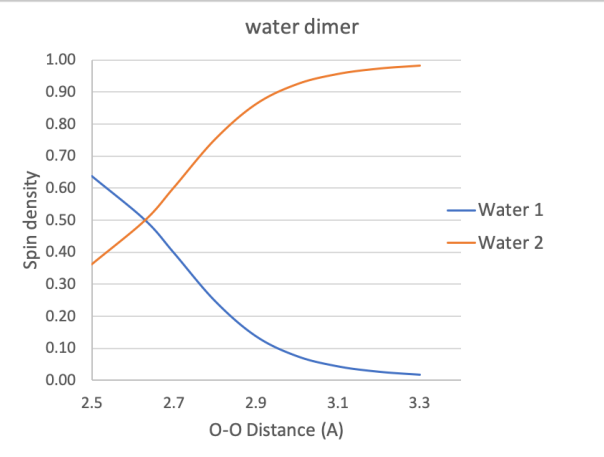

Figure B.2: The plot of spin density condensed to each water molecule of the water dimer with different O–O distance.Same conclusion can be drawn as Fig. B.1.

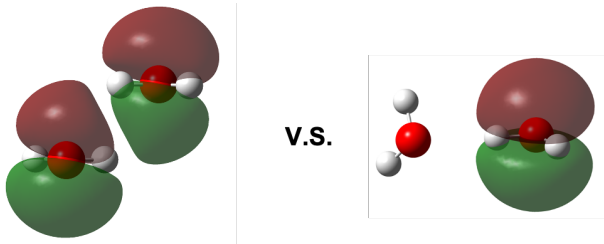

Figure B.3: The highest occupied molecular orbital (HOMO) distribution of a water dimer with different orientation. The HOMO is more delocalized when the two water molecules are closer to a stacking style geometry.

B.2 Force Analysis

Large protonic vibration amplitude is observed after photoionization. In order to get further understanding of the vibrational normal modes, frequency calculations of the water $(H_2O)_{27}$ nanodroplet before and after the vertical ionization are performed using the same version Gaussian software. The vibrational normal modes relevant to the symmetric and asymmetric O–H stretching of the H_2O where the hole localized are extracted and their force constants

are compared before and after photoionization, as shown in the following table.

After photoionization, there are several vibrational normal modes containing part of the symmetric O–H stretching and similar for the asymmetric O–H stretching. However, the conclusion can still be obtained from the force constant averaged over them. The force constants of both types of O–H stretching decrease upon vertical ionization.

Table B.1: Vibrational normal modes analysis of one of the initial states of water $(H_2O)_{27}$ nanodroplet before and after photoionization.

	Symmetric O–H stretching		Asymmetric O–H stretching	
	Vibrational mode #	Force constant	Vibrational mode #	Force constant
Before	216	9.5686	229	10.4143
After	194	7.9132		
	196	8.0714	223	10.0315
	198	8.4644		
	201	8.7583		
	206	9.2420	225 (main)	10.1930
	209	9.3742		
	212	9.4862		
	214	9.5369	226	10.1352
	215	9.6554		

B.3 Initial States

The 21 vibrationally bound initial conditions of water $(H_2O)_{27}$ nanodroplet, *i.e.*, geometries and momenta in terms of the mass-weighted velocities (MWV), are listed in the following

tables.

Table B.2: Vibrationally bound initial condition 1 of water $(H_2O)_{27}$ nanodroplet.

State #1	Coordinates (Å)			MWV ($amu^2 * bohr/sec$)		
#atom	x	y	z	v_x	v_y	v_z
O 1	-1.454014	5.056822	0.074424	-6.1083e+12	-4.3257e+13	1.4328e+13
H 2	-1.845518	4.548512	0.811073	3.5485e+13	-2.6656e+13	2.1991e+12
H 3	-1.887753	5.908071	0.059652	-5.1690e+12	-2.1579e+13	7.9594e+12
O 4	-1.975307	2.173640	-0.573026	-1.3186e+13	1.2428e+13	5.8268e+13
H 5	-1.286497	2.841247	-0.501138	3.0765e+12	-9.1771e+12	2.6835e+13
H 6	-2.514611	2.359012	0.221851	5.5139e+12	-1.9746e+13	1.9830e+13
O 7	-0.226684	-0.491348	-2.175120	5.1213e+13	8.7305e+12	5.0161e+13
H 8	-0.523976	-1.413606	-2.231987	6.2375e+13	-1.7348e+13	-8.6844e+12
H 9	-0.923854	-0.018288	-2.682340	-2.5938e+13	9.2341e+12	2.0473e+13
O10	2.039765	-2.348660	-2.001208	-3.6766e+13	-6.5716e+12	1.2453e+13
H11	1.225336	-2.710415	-2.407362	5.0278e+12	-3.8444e+13	5.6445e+12
H12	2.038660	-2.676354	-1.092103	7.0097e+12	-1.6672e+13	-3.3213e+12
O13	5.437274	-0.189052	1.570729	-4.3469e+11	2.9238e+12	4.1552e+13
H14	4.849803	0.458381	1.968826	-1.8690e+13	-6.8482e+12	-4.3188e+12
H15	5.607331	0.080390	0.664802	3.0542e+12	-5.4754e+13	-1.6836e+12
O16	0.474772	2.382569	3.203650	-4.9731e+13	-2.3388e+13	-2.7346e+13
H17	0.451525	3.341774	3.221825	1.8885e+13	-3.0405e+12	-5.7270e+13
H18	0.750942	2.154516	2.299256	4.1314e+13	-4.1191e+13	1.4722e+11
O19	-0.368595	-3.172097	0.844741	-5.4901e+13	9.1360e+13	1.3648e+13
H20	-0.968249	-3.843463	1.227851	-3.8041e+13	7.2302e+12	-6.6652e+12
H21	-0.610528	-2.273517	1.132218	2.2858e+13	3.1766e+13	1.7774e+13

Continuation of Table B.2						
State #1	Coordinates (Å)			MWV ($amu^2 * bohr/sec$)		
#atom	x	y	z	v_x	v_y	v_z
O22	-0.944493	-0.442060	1.118880	-5.5539e+13	-5.4363e+13	-2.1347e+12
H23	0.006284	-0.202913	1.053370	5.6079e+12	-2.7813e+13	-2.7080e+13
H24	-1.355236	-0.089360	0.312716	2.9709e+12	-6.7209e+13	-2.7651e+13
O25	-4.218289	-3.304940	0.004293	3.1377e+13	3.7035e+12	-2.2055e+13
H26	-4.321968	-2.695348	0.740452	6.1213e+13	-4.8565e+13	3.2290e+13
H27	-4.932565	-3.141428	-0.618907	-5.2190e+13	-1.0994e+13	7.5174e+13
O28	3.566028	3.616513	-0.348675	-5.2146e+13	6.7499e+12	4.5076e+12
H29	4.517087	3.586985	-0.428655	-1.4450e+13	4.9137e+12	3.8887e+12
H30	3.234476	4.259600	-0.973751	-2.9169e+13	-1.6542e+13	-9.8718e+12
O31	1.728628	0.219421	-4.064501	-1.2708e+13	3.2821e+13	2.1511e+13
H32	1.100957	0.095438	-3.333320	1.7997e+13	2.2677e+13	9.7165e+12
H33	2.308344	0.967557	-3.859265	2.4265e+12	7.1030e+12	-1.5012e+13
O34	-3.403834	-0.564762	-2.339113	4.6743e+13	-1.4462e+13	2.0621e+13
H35	-3.217960	0.022089	-1.607601	3.7354e+13	-1.4762e+13	4.8204e+12
H36	-3.634415	-0.019315	-3.096096	-4.5045e+13	-1.2912e+13	2.8659e+13
O37	-2.605768	-4.602333	1.566243	6.8386e+12	3.6842e+13	-2.5072e+13
H38	-3.232645	-4.319055	0.874830	-1.2252e+13	-2.4529e+13	-7.4284e+12
H39	-2.543693	-5.556221	1.497942	-1.4560e+13	1.8704e+12	7.4179e+13
O40	-3.177837	2.215954	-3.004035	5.9785e+13	-1.3560e+12	2.1320e+13
H41	-2.686053	2.235319	-2.157594	1.4197e+13	-4.4399e+12	4.2687e+13
H42	-3.401613	3.111269	-3.258777	4.6675e+12	-3.0791e+12	1.4087e+13
O43	-1.517955	0.800854	-4.154979	5.5907e+13	-3.1990e+13	5.6112e+13
H44	-0.816507	1.194834	-4.686895	-2.8799e+13	3.1622e+13	-7.3819e+12
H45	-2.172587	1.489335	-3.932898	-4.1609e+13	-5.7205e+13	-5.0898e+12

Continuation of Table B.2						
State #1	Coordinates (Å)			MWV ($amu^2 * bohr/sec$)		
#atom	x	y	z	v_x	v_y	v_z
O46	1.338993	2.050856	0.708934	2.6859e+13	-5.2476e+13	3.8917e+13
H47	2.088674	2.600750	0.442239	7.3879e+12	-2.3630e+13	-9.9777e+12
H48	1.597630	1.111409	0.562011	-7.9731e+12	-1.9364e+13	-3.6992e+13
O49	-2.033021	1.769434	3.182235	6.8785e+13	-2.3191e+13	-3.1685e+13
H50	-1.070877	1.947593	3.329461	2.3845e+13	-3.1599e+13	-2.0740e+13
H51	-2.185348	0.814611	3.135105	-1.0283e+12	3.3738e+12	-1.1972e+13
O52	4.010050	-1.053451	-2.127133	-4.4671e+13	-2.8177e+11	-1.7103e+13
H53	3.109961	-1.408446	-2.285123	-3.4754e+13	4.6242e+12	-6.7321e+12
H54	4.483588	-1.433609	-2.873942	-2.0626e+13	-6.4090e+13	2.4258e+13
O55	1.603281	-0.302068	0.005893	-3.2755e+13	2.1525e+13	-1.7671e+13
H56	2.371260	-0.891161	0.161797	3.8508e+13	9.1876e+12	-3.9401e+13
H57	1.159903	-0.483179	-0.841719	-4.5578e+13	1.7164e+13	1.3246e+13
O58	-0.533963	-3.093665	-1.766768	4.3379e+12	2.7537e+13	-2.6917e+13
H59	-0.509796	-3.080065	-0.786826	4.4390e+13	-3.5061e+12	2.7267e+13
H60	-1.373971	-3.496943	-2.007320	1.4756e+13	-3.7185e+13	1.1388e+13
O61	-2.928792	3.258149	1.658681	1.6545e+12	-2.5840e+13	-4.8375e+13
H62	-3.790900	3.629741	1.830267	1.4586e+13	1.0515e+13	-9.9305e+12
H63	-2.588725	2.599341	2.376853	2.6187e+13	2.9883e+13	-1.2607e+13
O64	-2.773549	-0.950361	3.101055	7.0631e+13	7.2759e+13	-7.7417e+13
H65	-2.896810	-1.475585	3.892873	-1.0991e+13	3.8578e+12	-3.6805e+13
H66	-2.188508	-1.438166	2.507961	-9.6446e+12	4.0010e+13	-5.7020e+13
O67	3.650855	-1.976458	0.478750	-6.3461e+13	6.0033e+13	2.7403e+12
H68	4.123255	-1.938504	-0.370921	-1.2968e+13	1.0036e+13	-8.3699e+12
H69	4.277465	-1.642082	1.158311	5.1656e+12	5.7966e+13	-4.2589e+13

Continuation of Table B.2						
State #1	Coordinates (Å)			MWV ($amu^2 * bohr/sec$)		
#atom	x	y	z	v_x	v_y	v_z
O70	2.214660	-3.639333	2.117425	-1.5636e+13	3.1838e+13	-4.8291e+13
H71	2.689620	-3.086266	1.490069	-1.1353e+13	-1.7963e+13	-3.1316e+13
H72	1.310695	-3.636681	1.782351	2.8848e+12	-1.8614e+13	-5.3197e+12
O73	3.406654	1.490721	-2.507993	-1.5476e+13	-2.0511e+13	1.4922e+13
H74	2.889814	1.681099	-1.722830	7.7034e+11	-5.6510e+12	1.7320e+12
H75	3.784523	0.591406	-2.398584	2.1620e+13	2.2517e+12	-2.5302e+13
O76	-3.638067	-0.472600	0.543065	2.7134e+13	-1.3646e+13	4.1227e+13
H77	-3.283137	-0.875834	1.327922	1.1864e+13	2.5487e+13	7.3968e+12
H78	-4.355167	0.088501	0.838942	2.5792e+13	1.5467e+13	-9.2234e+12
O79	2.511876	1.439522	4.841099	-2.3230e+13	-5.8221e+12	-5.5664e+13
H80	2.596183	0.745295	5.492504	8.0215e+12	2.6781e+13	1.6876e+12
H81	1.647064	1.424792	4.414388	-1.4460e+13	2.5200e+13	2.2390e+13
End of Table						

Table B.3: Vibrationally bound initial condition 2 of water $(H_2O)_{27}$ nanodroplet.

State #2	Coordinates (Å)			MWV ($amu^2 * bohr/sec$)		
#atom	x	y	z	v_x	v_y	v_z
O 1	-1.459459	5.128587	0.068808	6.4864e+12	-2.4980e+13	-2.4979e+11
H 2	-2.065896	4.683359	0.672815	1.9225e+13	-1.8169e+13	9.3919e+12
H 3	-1.720295	6.026009	-0.094617	-2.0352e+13	-1.2573e+13	1.7856e+13
O 4	-1.959705	2.155075	-0.686515	2.5698e+11	3.8979e+12	5.5773e+13

Continuation of Table B.3						
State #2	Coordinates (Å)			MWV ($amu^2 * bohr/sec$)		
#atom	x	y	z	v_x	v_y	v_z
H 5	-1.213575	2.754886	-0.785961	-1.7756e+13	2.8242e+13	2.7023e+13
H 6	-2.498008	2.559270	0.015914	-2.0962e+13	-2.5078e+13	1.1929e+13
O 7	-0.316485	-0.495850	-2.270117	2.3665e+13	-6.1157e+12	4.3479e+13
H 8	-0.800231	-1.293272	-2.020260	3.0401e+13	-2.5421e+13	-2.2710e+13
H 9	-0.869340	0.017163	-2.912290	5.3100e+13	1.1597e+13	2.0733e+13
O10	2.058656	-2.369346	-2.010856	7.4747e+12	1.7422e+13	-3.2462e+12
H11	1.143820	-2.336068	-2.322781	2.5620e+13	-3.9684e+13	-1.4615e+13
H12	2.024431	-2.799542	-1.152164	-6.4444e+12	5.3715e+13	1.5064e+13
O13	5.424095	-0.178723	1.481749	1.1422e+13	-8.7871e+12	4.1887e+13
H14	5.072892	0.375280	2.181778	-3.8144e+13	2.4521e+13	-3.1609e+13
H15	5.639945	0.338744	0.710449	-5.9985e+12	-2.2990e+13	-4.0895e+12
O16	0.541030	2.427342	3.245476	-1.8294e+13	-2.6219e+13	-1.4869e+13
H17	0.585165	3.266239	3.714236	-4.4182e+13	2.4422e+13	-5.8282e+13
H18	0.778201	2.556883	2.274405	-3.6167e+13	-2.2580e+13	-3.1000e+12
O19	-0.268396	-3.329713	0.837769	-3.4710e+13	6.3748e+13	-3.7274e+12
H20	-1.018029	-3.874277	1.191617	2.5979e+13	9.2726e+12	3.1046e+12
H21	-0.559640	-2.400411	0.867345	-4.3490e+13	6.7723e+11	2.6734e+13
O22	-0.859667	-0.346042	1.134181	-3.0601e+13	-4.7363e+13	-1.5271e+13
H23	0.097841	-0.221826	0.941272	-2.8645e+13	3.7667e+13	4.5174e+13
H24	-1.318447	0.337997	0.630664	-2.1339e+12	-2.7514e+13	-3.3507e+13
O25	-4.321622	-3.281742	0.033164	6.4016e+13	-3.4009e+13	1.6314e+13
H26	-4.536128	-2.353881	0.192078	-2.3587e+13	-2.7684e+13	5.7789e+13
H27	-3.998804	-3.263503	-0.884803	-1.4878e+14	5.6955e+13	-5.4572e+13
O28	3.654974	3.603659	-0.352281	-3.7920e+13	6.8343e+12	1.1463e+12

Continuation of Table B.3						
State #2	Coordinates (Å)			MWV ($amu^2 * bohr/sec$)		
#atom	x	y	z	v_x	v_y	v_z
H29	4.582383	3.415303	-0.489204	-9.1625e+11	3.5237e+13	9.9824e+12
H30	3.417056	4.339754	-0.916597	-1.7274e+13	-5.2499e+12	-8.3049e+12
O31	1.724099	0.156433	-4.117611	1.7253e+13	2.9389e+13	2.3508e+13
H32	1.128191	-0.271383	-3.501095	-1.7398e+13	7.3579e+13	2.7952e+13
H33	2.264140	0.750003	-3.579370	-2.5332e+12	2.7467e+13	-2.0068e+13
O34	-3.501421	-0.540165	-2.388953	4.8564e+13	-5.8824e+12	2.6980e+13
H35	-3.510683	-0.053838	-1.565010	2.1666e+13	3.0985e+13	-4.9716e+12
H36	-3.125646	0.013914	-3.078525	-6.5192e+13	-4.8826e+11	-2.8504e+13
O37	-2.596311	-4.680832	1.592269	-2.1462e+13	3.2656e+13	4.5077e+11
H38	-3.178318	-4.122478	1.035063	1.6188e+13	-9.3963e+12	-4.0716e+13
H39	-2.466364	-5.523592	1.159654	7.0052e+12	-2.3594e+12	2.0795e+13
O40	-3.296146	2.252075	-3.037209	5.2317e+13	-3.4785e+13	8.0116e+12
H41	-2.925217	2.277831	-2.109390	3.7232e+13	6.8536e+12	-2.9490e+13
H42	-3.588981	3.132073	-3.268190	4.8720e+13	-4.8714e+12	3.3528e+11
O43	-1.585655	0.852743	-4.276989	1.3147e+13	-1.0619e+13	5.9873e+13
H44	-0.684312	0.832438	-4.611779	-7.3238e+12	2.0208e+13	7.7385e+12
H45	-1.872493	1.720382	-3.964834	-2.6097e+13	-1.3110e+13	2.0668e+13
O46	1.286200	2.189476	0.665657	2.3586e+13	-8.4930e+13	1.1194e+13
H47	2.053402	2.762799	0.549922	-1.4027e+12	-1.6964e+13	-7.8299e+11
H48	1.559994	1.303844	0.358677	2.0084e+13	-2.2677e+13	4.4229e+13
O49	-2.141779	1.746687	3.319744	3.6956e+13	3.8548e+13	-9.2218e+13
H50	-1.185183	1.964112	3.278092	3.5195e+12	1.8414e+13	1.2881e+13
H51	-2.181324	0.794624	3.184930	2.2413e+13	3.3571e+12	-6.4552e+12
O52	4.158310	-1.026219	-2.097839	-9.1895e+13	-3.0342e+13	-1.8676e+13

Continuation of Table B.3						
State #2	Coordinates (Å)			MWV ($amu^2 * bohr/sec$)		
#atom	x	y	z	v_x	v_y	v_z
H53	3.352152	-1.586409	-2.291299	-3.8414e+13	3.6728e+13	2.0024e+13
H54	4.655432	-0.939606	-2.911351	-1.8663e+13	-3.3142e+13	4.0916e+11
O55	1.659115	-0.354896	0.048090	-2.2275e+13	2.4772e+13	-2.4840e+13
H56	2.336422	-1.030062	0.312962	-3.6606e+13	1.2042e+13	4.9035e+12
H57	1.363590	-0.527739	-0.854736	-6.1287e+12	9.2945e+12	-8.1488e+12
O58	-0.567238	-3.143419	-1.739289	2.0262e+13	1.4853e+13	-8.4098e+11
H59	-0.583748	-3.360390	-0.760549	-6.4110e+12	8.0125e+13	-8.1767e+12
H60	-1.406066	-3.225180	-2.194155	8.1363e+12	-1.4035e+13	1.2920e+13
O61	-2.970866	3.359117	1.685127	3.9086e+13	-6.6453e+13	1.8374e+13
H62	-3.876039	3.574632	1.891093	1.3580e+13	-8.7917e+12	1.1431e+11
H63	-2.657401	2.630223	2.337217	-2.2165e+13	-3.5382e+13	1.3311e+13
O64	-2.881079	-1.122336	3.247861	3.1769e+13	8.8785e+13	-6.6837e+13
H65	-3.078429	-1.370978	4.150535	4.6840e+13	-1.9786e+13	-1.7970e+13
H66	-1.950171	-1.283273	3.048158	-1.4119e+13	-5.0628e+13	-6.9178e+13
O67	3.761882	-2.101228	0.475637	-5.7355e+13	6.1310e+13	5.8914e+12
H68	4.219014	-1.824628	-0.343895	1.7675e+13	-1.6548e+13	1.7085e+13
H69	4.404616	-1.754810	1.108757	-2.0024e+13	-3.2618e+13	1.4248e+13
O70	2.224938	-3.691010	2.209932	9.0835e+11	2.0384e+13	-4.9542e+13
H71	2.855415	-3.231898	1.657044	-1.8576e+13	5.1641e+13	-5.9913e+11
H72	1.362517	-3.525191	1.827349	-9.2692e+12	-4.0385e+12	4.2266e+12
O73	3.441644	1.534295	-2.509229	-1.2690e+13	-2.1505e+13	-9.3807e+12
H74	2.993739	1.985910	-1.792250	-3.5771e+13	-6.1981e+13	1.1470e+13
H75	3.652388	0.620602	-2.253404	-2.1288e+12	-6.4983e+12	-3.4246e+13
O76	-3.720429	-0.455886	0.473603	5.2825e+13	-1.3859e+12	2.3523e+13

Continuation of Table B.3						
State #2	Coordinates (Å)			MWV ($amu^2 * bohr/sec$)		
#atom	x	y	z	v_x	v_y	v_z
H77	-3.277838	-0.742030	1.275361	-1.5267e+13	-4.0118e+13	1.4256e+13
H78	-4.456990	0.081714	0.748068	1.0552e+13	-1.7595e+13	2.7487e+13
O79	2.556483	1.438423	4.948141	-2.1729e+13	3.0480e+12	-4.9369e+13
H80	2.466456	0.597066	5.380268	2.2153e+13	1.9232e+13	2.0051e+13
H81	1.877537	1.543816	4.275090	-3.4386e+13	-4.3316e+13	1.0649e+13
End of Table						

Table B.4: Vibrationally bound initial condition 3 of water $(H_2O)_{27}$ nanodroplet.

State #3	Coordinates (Å)			MWV ($amu^2 * bohr/sec$)		
#atom	x	y	z	v_x	v_y	v_z
O 1	-1.449283	4.955957	0.109828	3.4560e+12	-5.1099e+13	2.5124e+13
H 2	-1.916313	4.400505	0.760309	-3.0913e+13	-2.6067e+13	-1.8143e+13
H 3	-1.949689	5.775310	0.144869	8.3958e+12	-8.9685e+12	-5.2754e+12
O 4	-2.000551	2.169780	-0.485682	-1.0474e+13	-2.0243e+13	2.2654e+13
H 5	-1.207704	2.717896	-0.459894	6.8294e+12	-2.2774e+13	-9.3357e+12
H 6	-2.529777	2.465916	0.285149	-1.8243e+12	4.6667e+13	-8.2651e+12
O 7	-0.124809	-0.457670	-2.054592	5.1902e+13	2.5188e+13	6.6591e+13
H 8	-0.295094	-1.408704	-2.195869	-2.3082e+13	1.7703e+13	1.8612e+13
H 9	-0.721161	-0.037804	-2.706824	6.2180e+13	-6.9070e+12	-1.6901e+13
O10	1.920952	-2.414219	-1.959761	-6.5072e+13	-5.0253e+13	2.7386e+13
H11	1.128853	-2.840409	-2.322074	-4.2734e+13	-6.6030e+12	1.7384e+13

Continuation of Table B.4						
State #3	Coordinates (Å)			MWV ($amu^2 * bohr/sec$)		
#atom	x	y	z	v_x	v_y	v_z
H12	2.136361	-2.890734	-1.153503	4.7617e+12	-4.2280e+13	-6.4929e+12
O13	5.416383	-0.209392	1.644071	-2.6701e+13	-1.3788e+13	2.3363e+13
H14	4.827619	0.509706	1.891365	1.2282e+13	1.1896e+13	1.5446e+13
H15	5.677996	0.012723	0.744575	3.7351e+13	1.6351e+13	2.3282e+13
O16	0.421612	2.330777	3.115350	1.1611e+13	-2.7935e+13	-5.4402e+13
H17	0.527401	3.282698	3.100025	-1.5924e+13	-5.4645e+12	1.6710e+13
H18	0.959440	1.974033	2.327590	-5.9393e+12	-4.0425e+12	-1.0273e+13
O19	-0.465318	-3.023578	0.878430	-5.0095e+13	5.8026e+13	1.6333e+13
H20	-1.310144	-3.434731	1.083532	-1.0820e+13	2.4836e+13	-1.4418e+13
H21	-0.625424	-2.073899	1.033169	-1.1941e+13	1.7228e+13	-4.3996e+13
O22	-1.017004	-0.562626	1.097986	-1.4051e+13	-6.5644e+13	-1.8531e+13
H23	-0.075376	-0.457020	0.925756	7.6632e+11	3.6421e+12	-1.6112e+13
H24	-1.517066	-0.478535	0.270065	-3.8702e+13	-1.6605e+13	1.8040e+13
O25	-4.166596	-3.318625	-0.014849	1.7406e+13	-8.4789e+12	7.8120e+12
H26	-3.891170	-2.578301	0.561386	6.3252e+13	5.5090e+13	-9.2777e+13
H27	-5.105558	-3.177086	-0.169395	2.0232e+12	-1.1075e+13	2.0425e+13
O28	3.439937	3.622715	-0.330264	-6.8502e+13	2.6452e+12	6.7327e+12
H29	4.381198	3.573681	-0.504124	-2.0929e+13	-1.8780e+13	-5.2158e+12
H30	3.082433	4.091935	-1.086091	-2.8677e+13	-2.7637e+13	-9.8431e+12
O31	1.686730	0.278291	-4.050689	-2.9853e+13	2.7438e+13	2.2865e+11
H32	1.084294	0.081612	-3.309883	-2.2561e+13	-3.1017e+13	-1.7716e+13
H33	2.316466	0.920704	-3.700803	5.3947e+12	-6.8612e+12	3.2061e+13
O34	-3.313630	-0.609920	-2.296903	4.2186e+13	-1.8473e+13	2.3198e+13
H35	-3.088875	-0.176780	-1.467207	3.5072e+12	-5.4378e+13	3.0118e+13

Continuation of Table B.4						
State #3	Coordinates (Å)			MWV ($amu^2 * bohr/sec$)		
#atom	x	y	z	v_x	v_y	v_z
H36	-3.806365	0.075459	-2.770410	1.5005e+12	1.5363e+13	4.4982e+13
O37	-2.581552	-4.543730	1.513099	1.3981e+13	2.3478e+13	-2.5829e+13
H38	-3.266729	-4.573402	0.822995	-6.9144e+12	-2.3748e+13	1.0487e+13
H39	-2.644468	-5.294435	2.103488	-2.0264e+12	6.2478e+13	5.9981e+13
O40	-3.079788	2.236564	-2.916423	3.4319e+13	2.3030e+13	7.1095e+13
H41	-2.712491	2.245583	-1.987676	5.7456e+12	-9.0783e+12	-1.2879e+13
H42	-3.418266	3.114155	-3.103558	-8.3137e+12	-3.2521e+12	8.8411e+12
O43	-1.394231	0.711337	-4.061229	6.5822e+13	-6.1851e+13	4.0311e+13
H44	-0.876990	1.261229	-4.654642	2.2918e+13	-6.6222e+12	1.2911e+13
H45	-2.209334	1.202444	-3.845574	3.5490e+13	-7.0174e+11	3.1617e+13
O46	1.406816	1.979560	0.804282	3.6596e+13	-6.4653e+12	5.5767e+13
H47	2.113831	2.580211	0.537658	4.5335e+12	9.7540e+12	2.0813e+13
H48	1.424628	1.150935	0.276056	6.1376e+12	-4.6852e+12	5.9804e+12
O49	-1.895538	1.687662	3.174506	4.7693e+13	-4.0943e+13	6.2551e+12
H50	-0.922981	1.813275	3.043017	1.1678e+13	1.7818e+12	-2.9894e+13
H51	-2.204734	0.783574	3.058652	6.6138e+12	-7.9374e+12	1.4519e+13
O52	3.966527	-1.057008	-2.164746	-9.4767e+12	-3.2035e+12	-1.0796e+13
H53	3.016953	-1.342259	-2.317823	2.7472e+13	-1.0905e+13	-2.9226e+13
H54	4.478405	-1.698662	-2.663450	3.9940e+12	-6.1245e+12	8.4057e+12
O55	1.517399	-0.287305	-0.045229	-6.8549e+13	-1.8792e+12	-4.6942e+13
H56	2.276678	-0.876043	-0.021328	-4.8931e+13	-1.1362e+13	2.8553e+13
H57	1.002752	-0.376537	-0.894985	1.0719e+13	-6.5282e+12	-2.3291e+13
O58	-0.512102	-3.061530	-1.799951	1.9414e+13	-9.0785e+11	-2.0511e+12
H59	-0.410954	-3.121391	-0.807666	-2.4731e+13	1.5390e+13	-2.9411e+13

Continuation of Table B.4						
State #3	Coordinates (Å)			MWV ($amu^2 * bohr/sec$)		
#atom	x	y	z	v_x	v_y	v_z
H60	-1.271660	-3.604303	-2.021131	-1.7102e+12	1.0422e+13	-2.5315e+13
O61	-2.937444	3.254780	1.529277	-1.4462e+13	9.9330e+12	-4.6846e+13
H62	-3.737351	3.662979	1.865995	1.0256e+12	4.2928e+12	-4.4789e+12
H63	-2.561565	2.655129	2.261480	1.3530e+13	-1.8839e+13	-4.2305e+13
O64	-2.636736	-0.816728	2.942283	7.6575e+13	5.3647e+13	-7.8702e+13
H65	-2.907634	-1.530217	3.521465	5.4975e+12	-5.2738e+12	-5.0024e+13
H66	-1.731937	-0.965495	2.591122	5.7098e+13	8.5398e+13	5.2989e+13
O67	3.556141	-1.836733	0.447376	-4.5412e+13	7.3875e+13	-3.8459e+13
H68	3.868223	-1.812597	-0.466521	7.0988e+10	3.8599e+13	-2.5046e+12
H69	4.141913	-1.305690	1.019350	-1.0245e+13	1.2334e+13	1.0708e+13
O70	2.171382	-3.588079	2.021199	-2.7239e+13	1.5302e+13	-4.6661e+13
H71	2.723764	-3.187385	1.337811	1.8407e+12	8.1993e+12	-2.1054e+12
H72	1.261502	-3.625744	1.689865	-5.1655e+12	3.1632e+13	-2.3903e+13
O73	3.404029	1.485513	-2.475547	9.2968e+12	9.3450e+12	2.7544e+13
H74	2.984121	1.629157	-1.622864	1.6545e+13	1.4562e+13	1.1964e+13
H75	3.743109	0.576509	-2.416093	5.3592e+11	-5.2650e+12	-5.8951e+12
O76	-3.609649	-0.495388	0.609278	-1.7510e+12	2.5575e+12	4.5055e+13
H77	-3.304369	-0.456995	1.543322	-6.1401e+12	2.9940e+13	6.3874e+12
H78	-4.187482	0.284297	0.540303	2.0083e+13	4.5786e+12	-1.0659e+14
O79	2.480882	1.436614	4.722953	-1.8558e+13	-1.8119e+12	-5.6801e+13
H80	2.437720	0.861063	5.491894	-1.9872e+13	1.2319e+13	-5.1611e+12
H81	1.566505	1.732923	4.566379	7.7594e+12	5.2591e+13	-1.0544e+13
End of Table						

Table B.5: Vibrationally bound initial condition 4 of water $(H_2O)_{27}$ nanodroplet.

State #4	Coordinates (Å)			MWV $(amu^2 * bohr/sec)$		
#atom	x	y	z	v_x	v_y	v_z
O 1	-1.441050	4.856944	0.158350	1.0446e+13	-4.8961e+13	1.5700e+13
H 2	-2.095117	4.414658	0.718067	-1.4498e+13	4.1268e+13	2.8650e+13
H 3	-1.747942	5.753362	0.020855	3.1583e+13	2.6962e+11	-1.4557e+13
O 4	-2.012803	2.102864	-0.485960	1.1022e+11	-4.9429e+13	-2.6730e+13
H 5	-1.116564	2.450340	-0.542118	1.3005e+13	-3.3872e+13	1.4060e+13
H 6	-2.530194	2.691121	0.071528	1.3872e+13	5.3102e+12	-5.3423e+12
O 7	-0.055214	-0.411490	-1.965736	1.7417e+13	2.4097e+13	2.4199e+13
H 8	-0.529899	-1.251926	-1.917169	-3.7301e+13	2.1767e+13	1.5107e+13
H 9	-0.530713	0.114097	-2.673119	-3.2762e+13	-6.2679e+11	6.3413e+12
O10	1.820854	-2.535397	-1.903748	-2.3718e+13	-6.1254e+13	2.5742e+13
H11	0.895652	-2.773212	-2.070433	-6.5386e+12	8.5286e+12	3.1902e+13
H12	2.175585	-3.166054	-1.283058	9.7161e+12	-2.7135e+13	-1.3576e+13
O13	5.340783	-0.226844	1.666230	-4.0571e+13	-1.2933e+12	6.0392e+12
H14	5.036023	0.509756	2.202089	3.0000e+13	-1.9562e+13	5.1311e+13
H15	6.053488	0.144758	1.139374	4.0524e+13	8.6332e+12	7.3216e+13
O16	0.500559	2.288304	3.027319	6.1227e+13	1.7227e+12	-4.1601e+13
H17	0.300406	3.221653	3.139716	-4.7668e+13	-1.7272e+13	1.6398e+13
H18	0.894078	2.217501	2.093833	-1.5396e+13	3.1606e+12	1.3641e+13
O19	-0.547557	-2.966472	0.860180	-3.0898e+13	-1.2143e+13	-3.4258e+13
H20	-1.211076	-3.598735	1.218531	3.2435e+13	-1.7563e+13	1.7514e+13
H21	-0.871924	-2.046153	0.984700	-4.1668e+13	-1.8630e+13	2.6108e+13
O22	-0.965321	-0.640370	1.029970	5.3315e+13	1.9341e+13	-7.0898e+13

Continuation of Table B.5						
State #4	Coordinates (Å)			MWV ($amu^2 * bohr/sec$)		
#atom	x	y	z	v_x	v_y	v_z
H23	-0.208792	-0.233747	0.545547	2.1487e+12	-1.3465e+13	-2.9089e+13
H24	-1.778070	-0.221241	0.677646	-3.1817e+13	3.1866e+13	1.1092e+14
O25	-4.127911	-3.300594	0.003495	8.4160e+12	3.0656e+13	-5.9064e+12
H26	-3.788272	-2.508661	-0.426928	1.0922e+13	-3.4780e+13	-8.9305e+13
H27	-5.072317	-3.199349	-0.139621	-8.4540e+12	-2.0832e+13	-1.0336e+12
O28	3.293889	3.618919	-0.321720	-7.7525e+13	-8.5479e+12	1.3764e+12
H29	4.193340	3.397694	-0.574094	-2.6484e+13	-1.7874e+13	-1.3949e+13
H30	2.875838	3.902685	-1.137927	-1.9897e+13	-1.4668e+13	-2.9187e+12
O31	1.620341	0.333004	-4.063898	-3.7603e+13	3.1209e+13	-9.3560e+12
H32	1.131402	-0.250375	-3.470910	2.7009e+13	-6.4398e+13	-2.0554e+13
H33	2.153003	0.872306	-3.473493	-2.3686e+13	7.3788e+11	8.1433e+12
O34	-3.241988	-0.644610	-2.239726	3.0133e+13	-2.6994e+13	3.2657e+13
H35	-3.015809	-0.673126	-1.307309	1.6472e+13	-3.5700e+13	5.1338e+12
H36	-3.551994	0.249662	-2.446820	6.8664e+13	3.7885e+13	4.9174e+13
O37	-2.535092	-4.511396	1.482092	3.0448e+13	1.4059e+12	2.6570e+12
H38	-3.409247	-4.375522	1.078644	-1.3110e+12	9.0661e+13	3.2892e+13
H39	-2.652750	-4.847039	2.370247	1.0566e+12	4.2494e+13	1.4792e+13
O40	-3.033676	2.264590	-2.774314	1.7644e+13	3.8917e+12	6.8888e+13
H41	-2.612559	2.344992	-1.893022	1.1014e+13	1.1930e+13	4.4164e+13
H42	-3.406554	3.119062	-2.983523	5.4382e+12	6.7469e+12	3.8919e+12
O43	-1.251517	0.589217	-3.984415	7.9467e+13	-5.4495e+13	4.4123e+13
H44	-0.529370	1.001412	-4.465845	6.2366e+13	-5.2231e+13	2.3196e+13
H45	-1.812392	1.286594	-3.610067	3.5977e+13	2.1123e+13	-1.3771e+12
O46	1.487045	2.002727	0.906854	5.2850e+13	1.7601e+13	3.4929e+13

Continuation of Table B.5						
State #4	Coordinates (Å)			MWV ($amu^2 * bohr/sec$)		
#atom	x	y	z	v_x	v_y	v_z
H47	2.195460	2.594925	0.625711	1.5308e+13	-3.7817e+12	2.5653e+12
H48	1.629224	1.074727	0.604756	-8.5092e+12	1.2355e+13	3.8057e+13
O49	-1.872427	1.668362	3.157785	-1.4297e+13	1.9606e+13	-1.9140e+13
H50	-0.875986	1.733427	3.189326	-1.9397e+13	-1.2980e+13	4.2485e+13
H51	-2.180133	0.787614	3.420019	-5.3570e+12	1.9354e+13	6.2358e+13
O52	3.963090	-1.085969	-2.192431	7.7286e+12	-1.5220e+13	-1.4877e+13
H53	3.102762	-1.555793	-2.332849	-5.5245e+12	-6.0193e+13	2.2036e+13
H54	4.668468	-1.474370	-2.707181	1.9822e+13	4.1714e+13	-1.9142e+13
O55	1.355444	-0.288275	-0.129050	-7.3631e+13	9.8946e+12	-8.0899e+12
H56	1.972873	-0.963833	0.260826	-2.2243e+13	-1.3269e+13	-8.6819e+12
H57	1.081896	-0.490958	-1.039070	2.4070e+12	-1.0890e+13	-1.2846e+13
O58	-0.510999	-3.079675	-1.795378	-2.9014e+13	-9.2750e+12	1.2049e+13
H59	-0.620774	-3.149423	-0.815813	-2.0752e+13	-3.4820e+13	2.7342e+13
H60	-1.282797	-3.396842	-2.253896	-4.0358e+12	2.5656e+13	-2.9298e+13
O61	-2.974750	3.262113	1.490259	-2.8538e+13	-3.9091e+12	6.4808e+12
H62	-3.759602	3.605171	1.919263	-1.0816e+13	-9.6532e+12	1.2576e+13
H63	-2.575417	2.604900	2.159826	6.6978e+12	-1.1957e+12	1.1754e+13
O64	-2.501906	-0.726505	2.845025	5.7575e+13	2.8433e+13	-6.5050e+12
H65	-2.710798	-1.586647	3.211643	2.0933e+13	-7.6646e+12	-2.8919e+13
H66	-1.579751	-0.813087	2.520895	-1.0621e+13	-1.7675e+13	-9.0452e+13
O67	3.482203	-1.689524	0.360353	-2.3201e+13	7.3288e+13	-3.9167e+13
H68	3.869896	-1.383592	-0.483436	-3.3822e+13	4.2714e+13	-1.4895e+13
H69	4.058026	-1.402007	1.073708	-1.3709e+13	-9.4986e+12	2.1522e+12
O70	2.100054	-3.567334	1.916366	-4.3778e+13	1.1481e+13	-5.9451e+13

Continuation of Table B.5						
State #4	Coordinates (Å)			MWV ($amu^2 * bohr/sec$)		
#atom	x	y	z	v_x	v_y	v_z
H71	2.729119	-3.017835	1.443628	2.7417e+12	1.8657e+13	1.4480e+13
H72	1.229236	-3.287351	1.595366	-1.4576e+13	3.6062e+13	8.7845e+11
O73	3.439310	1.518624	-2.408389	2.5443e+13	2.1137e+13	4.0316e+13
H74	3.114720	1.710136	-1.523460	1.0343e+13	-3.6962e+12	1.5134e+13
H75	3.811371	0.620883	-2.317830	-3.5612e+12	1.5169e+13	2.3669e+13
O76	-3.631224	-0.501834	0.637820	-1.5257e+13	-1.6482e+13	-2.5959e+13
H77	-3.464027	-0.198717	1.542205	-2.7480e+13	3.4424e+13	-6.2542e+12
H78	-3.938544	0.244129	0.115137	1.6713e+13	3.7297e+13	1.8198e+13
O79	2.452516	1.440476	4.615240	5.1516e+11	6.1274e+12	-5.3291e+13
H80	2.197307	1.002051	5.425961	-5.4280e+13	2.4858e+13	-8.8699e+12
H81	1.667505	1.848534	4.224895	-3.5767e+12	-3.4400e+13	-7.0499e+13
End of Table						

Table B.6: Vibrationally bound initial condition 5 of water $(H_2O)_{27}$ nanodroplet.

State #5	Coordinates (Å)			MWV ($amu^2 * bohr/sec$)		
#atom	x	y	z	v_x	v_y	v_z
O 1	-1.423958	4.776853	0.182581	1.4039e+13	-3.8537e+13	8.7513e+12
H 2	-2.005817	4.675243	0.944185	1.6027e+13	2.5938e+13	5.9674e+12
H 3	-1.351989	5.683721	-0.100653	4.8456e+13	-8.9689e+12	4.6316e+11
O 4	-1.987584	1.997531	-0.522469	2.8393e+13	-5.6917e+13	1.7190e+13
H 5	-1.037489	2.107883	-0.413733	1.0794e+13	-4.3111e+13	-4.2295e+12

Continuation of Table B.6						
State #5	Coordinates (Å)			MWV ($amu^2 * bohr/sec$)		
#atom	x	y	z	v_x	v_y	v_z
H 6	-2.428717	2.518576	0.202458	-2.9150e+12	-4.0222e+13	6.4216e+12
O 7	-0.103051	-0.386139	-1.979956	-4.5423e+13	-3.4319e+12	-1.8056e+13
H 8	-0.514538	-1.218722	-1.724073	2.2461e+13	-6.8191e+12	7.3056e+12
H 9	-0.595877	0.057311	-2.735053	-1.4738e+13	-1.7534e+13	2.7244e+12
O10	1.862464	-2.640781	-1.854752	5.4567e+13	-5.5364e+13	2.6325e+13
H11	0.878873	-2.811902	-1.973191	-6.8238e+11	-7.2159e+11	-1.2471e+13
H12	2.143075	-3.352685	-1.275378	-7.9167e+12	-8.7420e+12	1.3139e+13
O13	5.280712	-0.184737	1.694861	-2.4417e+13	3.4703e+13	2.6246e+13
H14	5.021478	0.028950	2.599592	-1.6042e+13	-8.4871e+13	2.3520e+13
H15	6.238500	-0.138961	1.663212	8.2708e+11	-6.0412e+13	6.5726e+13
O16	0.571366	2.312482	3.028597	4.0665e+12	1.5612e+13	2.5370e+13
H17	0.240912	3.197733	3.178879	4.6128e+13	2.2575e+13	2.1738e+12
H18	0.998657	2.313614	2.142693	1.1583e+13	2.4433e+13	1.6140e+13
O19	-0.580485	-3.061052	0.770032	1.0690e+12	-6.7570e+13	-5.9266e+13
H20	-1.148952	-3.746264	1.181669	-2.3788e+13	-1.0555e+13	1.8647e+12
H21	-0.903641	-2.143147	0.877174	1.2362e+13	-1.8534e+13	-3.4794e+13
O22	-0.896300	-0.539183	0.896191	1.9136e+12	7.4106e+13	-6.3232e+13
H23	0.018040	-0.427225	0.476534	5.9279e+13	-1.7841e+13	4.6816e+13
H24	-1.444498	0.176596	0.508475	1.1139e+14	3.1143e+13	-1.3351e+14
O25	-4.132727	-3.232587	-0.034197	2.5059e+12	3.2332e+13	-2.5842e+13
H26	-3.822887	-2.757011	-0.801785	-3.8601e+13	-1.7471e+12	-2.4609e+13
H27	-5.069720	-3.323341	-0.180545	-3.4404e+12	-1.4455e+12	-1.0626e+13
O28	3.150212	3.590651	-0.336806	-6.6117e+13	-1.7964e+13	-1.2498e+13
H29	4.025826	3.339203	-0.637624	-1.6150e+13	1.0523e+13	-2.1970e+13

Continuation of Table B.6						
State #5	Coordinates (Å)			MWV ($amu^2 * bohr/sec$)		
#atom	x	y	z	v_x	v_y	v_z
H30	2.649604	3.905248	-1.091211	-2.1118e+13	1.3446e+13	7.6357e+12
O31	1.524252	0.382975	-4.083244	-4.8077e+13	2.0438e+13	-8.2702e+12
H32	1.523921	-0.479467	-3.672174	5.2842e+13	1.3091e+12	-2.0680e+13
H33	2.102500	0.912502	-3.499551	-7.9237e+12	1.0449e+13	-2.6916e+13
O34	-3.183916	-0.682456	-2.145260	3.6080e+13	-1.5798e+13	6.2375e+13
H35	-2.829773	-0.846218	-1.267189	1.2686e+13	-7.2440e+12	1.3643e+13
H36	-2.936617	0.215963	-2.383009	5.5900e+13	-3.3135e+13	-3.9567e+13
O37	-2.491011	-4.517710	1.525419	2.4328e+13	-7.8717e+11	3.4740e+13
H38	-2.959907	-3.751871	1.174774	3.5751e+13	1.2543e+13	1.6714e+12
H39	-2.701485	-4.657406	2.447218	-2.5182e+13	1.9888e+13	5.4703e+12
O40	-2.997686	2.258519	-2.661017	1.9171e+13	-1.5922e+13	3.0562e+13
H41	-2.562162	2.381139	-1.761784	1.7777e+12	2.0910e+13	-2.0798e+13
H42	-3.357811	3.075886	-2.987591	1.3171e+12	-2.4757e+11	1.1991e+13
O43	-1.091003	0.521064	-3.901172	8.0732e+13	-1.6185e+13	2.5003e+13
H44	-0.160226	0.623688	-4.192375	1.7085e+13	-8.3365e+12	2.1815e+13
H45	-1.584407	1.346296	-3.951170	3.6413e+13	-1.2242e+13	-4.3203e+13
O46	1.605726	2.036114	0.924460	6.5382e+13	7.0394e+12	-2.1918e+13
H47	2.324902	2.577895	0.568567	4.7469e+12	1.2931e+13	-1.2216e+13
H48	1.485713	1.176726	0.439625	-1.3771e+13	1.3374e+13	-2.3799e+13
O49	-1.921781	1.733613	3.143395	-2.6509e+13	5.3364e+13	3.3973e+12
H50	-0.940866	1.725842	3.126166	1.1382e+12	-1.2374e+13	-4.1854e+13
H51	-2.301485	0.949773	3.547607	-7.6934e+12	-8.2771e+12	-3.2383e+13
O52	3.960889	-1.119480	-2.220526	-6.9562e+12	-2.4841e+13	-2.4898e+13
H53	3.243953	-1.810166	-2.292092	-2.2589e+12	2.1837e+13	1.4504e+12

Continuation of Table B.6						
State #5	Coordinates (Å)			MWV ($amu^2 * bohr/sec$)		
#atom	x	y	z	v_x	v_y	v_z
H54	4.628615	-1.314615	-2.876515	-5.5755e+12	9.6977e+12	-1.2275e+13
O55	1.265563	-0.271536	-0.069621	-2.3998e+13	1.8595e+13	4.1589e+13
H56	1.983698	-0.892144	0.097892	3.9443e+13	2.1347e+13	-1.2936e+13
H57	0.871282	-0.229914	-1.033799	-3.8000e+13	4.7437e+13	2.4149e+13
O58	-0.625227	-3.096680	-1.740694	-7.3880e+13	-4.8854e+12	3.4521e+13
H59	-0.791320	-3.282018	-0.752318	-1.9296e+13	7.4774e+12	-8.0997e+12
H60	-1.332066	-3.350540	-2.329649	-1.3885e+13	-1.3684e+13	1.6176e+13
O61	-3.045646	3.247679	1.551760	-3.3071e+13	-4.8249e+12	4.2190e+13
H62	-3.891632	3.485443	1.926724	-2.7124e+13	-2.6376e+13	-6.5164e+12
H63	-2.591636	2.644004	2.252045	-3.7452e+13	-8.2101e+11	3.0177e+13
O64	-2.400104	-0.725323	2.895793	3.0291e+13	-2.2125e+13	4.7456e+13
H65	-2.676477	-1.620192	3.086381	1.5816e+13	-9.8772e+12	3.4130e+12
H66	-1.660889	-0.759613	2.212907	2.5467e+13	1.5017e+13	2.2728e+13
O67	3.435861	-1.563623	0.305151	-5.9767e+12	6.5914e+13	-1.6877e+13
H68	3.787412	-1.289589	-0.559097	-8.9688e+12	-4.0497e+13	-2.6272e+13
H69	4.099680	-1.153692	0.890854	-1.9939e+13	3.9151e+13	-1.4748e+13
O70	2.000254	-3.535011	1.796454	-5.2560e+13	2.0028e+13	-6.0766e+13
H71	2.646817	-2.961454	1.379223	-2.0300e+13	2.2510e+12	-2.7367e+13
H72	1.141485	-3.197995	1.539823	-1.5018e+13	-1.3702e+13	-2.2045e+13
O73	3.489209	1.560946	-2.299519	2.0124e+13	1.9342e+13	5.7401e+13
H74	3.026695	1.689236	-1.467391	-2.1999e+13	-1.8399e+13	8.2865e+12
H75	3.686783	0.596085	-2.344182	-2.2316e+13	-7.6891e+12	6.8226e+12
O76	-3.676304	-0.469290	0.561886	-2.5030e+13	2.3417e+13	-4.7001e+13
H77	-3.643893	-0.537564	1.514328	-1.0839e+13	-3.6717e+13	-2.9679e+13

Continuation of Table B.6						
State #5	Coordinates (Å)			MWV ($amu^2 * bohr/sec$)		
#atom	x	y	z	v_x	v_y	v_z
H78	-3.919895	0.377852	0.206946	-1.5958e+13	2.3544e+13	3.2374e+13
O79	2.451765	1.447719	4.516557	1.2306e+13	-5.5656e+12	-4.7069e+13
H80	1.875325	1.211937	5.236574	-3.5541e+13	2.3799e+13	-2.9345e+13
H81	1.864467	1.589843	3.770885	2.2334e+13	3.9876e+12	-1.5603e+13
End of Table						

Table B.7: Vibrationally bound initial condition 6 of water $(H_2O)_{27}$ nanodroplet.

State #6	Coordinates (Å)			MWV ($amu^2 * bohr/sec$)		
#atom	x	y	z	v_x	v_y	v_z
O 1	-1.375256	4.705764	0.185125	2.9803e+13	-3.4166e+13	-1.4740e+12
H 2	-2.041791	4.637952	0.893288	-1.2430e+13	-4.3941e+13	-2.2878e+13
H 3	-1.064694	5.600049	0.090158	2.6910e+13	-8.8377e+12	4.0018e+13
O 4	-1.899205	1.855246	-0.429568	6.7762e+13	-7.1477e+13	7.2739e+13
H 5	-1.010720	2.224184	-0.358980	-4.7453e+12	3.9994e+13	-2.6994e+12
H 6	-2.319833	2.356525	0.293049	-1.3970e+13	-9.3415e+12	6.9327e+12
O 7	-0.175891	-0.446130	-1.946274	-3.9750e+13	-7.0877e+13	5.2527e+13
H 8	-0.490610	-1.376956	-1.936532	-1.0009e+13	-1.4860e+13	-3.8033e+13
H 9	-0.721824	0.023692	-2.630301	3.8096e+13	3.0202e+13	-9.9930e+12
O10	1.978094	-2.753574	-1.814567	5.8334e+13	-5.7474e+13	1.5216e+13
H11	1.048217	-2.821678	-2.007689	1.4242e+13	-1.9179e+13	6.0804e+12
H12	2.106232	-3.364849	-1.078719	-2.9866e+12	1.2453e+13	2.4043e+13

Continuation of Table B.7						
State #6	Coordinates (Å)			MWV ($amu^2 * bohr/sec$)		
#atom	x	y	z	v_x	v_y	v_z
O13	5.244136	-0.126033	1.795153	-1.9271e+13	1.6638e+13	6.9586e+13
H14	4.683786	-0.384818	2.538624	-5.1935e+13	-2.0829e+12	-2.1587e+13
H15	6.056736	-0.630636	1.859057	-3.8095e+13	-5.1279e+13	-9.0727e+12
O16	0.544872	2.371727	3.063183	-2.4064e+13	3.4174e+13	9.5536e+12
H17	0.663347	3.274569	3.360627	4.5412e+13	4.4353e+11	4.4418e+12
H18	0.974615	2.249812	2.139832	5.9180e+12	2.2413e+13	-2.3924e+13
O19	-0.570509	-3.190649	0.658465	3.5715e+12	-5.4844e+13	-3.5858e+13
H20	-1.191979	-3.695904	1.225440	5.6425e+12	6.8637e+12	-2.0708e+13
H21	-0.832699	-2.241136	0.702520	1.9523e+13	1.2974e+12	-9.6424e+12
O22	-0.908745	-0.392494	0.790066	-3.8312e+13	5.0437e+13	-1.5590e+13
H23	0.067313	-0.455996	1.009999	3.5042e+12	4.9535e+13	-7.9984e+12
H24	-0.977360	-0.051764	-0.119107	3.4375e+13	-4.7244e+13	-3.0599e+13
O25	-4.130483	-3.171211	-0.117149	8.5228e+12	2.4089e+13	-4.8078e+13
H26	-3.999380	-2.429690	-0.738543	-3.3438e+13	5.6862e+13	5.5100e+13
H27	-5.053975	-3.372086	-0.014748	4.2916e+12	1.7220e+13	9.1386e+12
O28	3.055512	3.584888	-0.396783	-2.8363e+13	2.2853e+13	-5.3003e+13
H29	3.893861	3.422552	-0.832604	-1.4954e+13	-1.6549e+12	-2.7150e+13
H30	2.486815	4.088095	-0.981195	-1.8543e+13	3.0953e+13	1.9637e+13
O31	1.468059	0.428140	-4.111566	-5.0476e+12	2.7580e+13	-2.8015e+13
H32	1.710342	-0.415558	-3.731752	1.5492e+12	3.1224e+13	1.5457e+13
H33	2.067028	1.093100	-3.732179	1.2981e+13	1.0853e+13	-6.8759e+12
O34	-3.099297	-0.748513	-2.023675	5.4084e+13	-4.4783e+13	6.6994e+13
H35	-2.986870	-0.412118	-1.112792	-6.6696e+13	8.1493e+13	-5.7260e+12
H36	-2.770180	-0.046280	-2.590071	-2.6228e+13	-3.5323e+13	-2.4510e+13

Continuation of Table B.7						
State #6	Coordinates (Å)			MWV ($amu^2 * bohr/sec$)		
#atom	x	y	z	v_x	v_y	v_z
O37	-2.457269	-4.492960	1.614692	-1.4119e+13	2.8881e+13	4.4937e+13
H38	-3.179807	-4.251316	0.975360	1.3056e+13	-1.1508e+14	-2.2763e+13
H39	-2.849959	-4.635041	2.475322	-2.4355e+12	-2.1530e+13	6.1708e+12
O40	-2.966735	2.235190	-2.679519	1.5056e+13	-1.3156e+13	-4.7816e+13
H41	-2.528071	2.296872	-1.812087	-3.2827e+12	-3.0888e+13	2.6664e+13
H42	-3.428004	3.026135	-2.922732	-1.1732e+13	-3.6515e+12	1.5981e+13
O43	-0.970207	0.532267	-3.937319	2.1084e+13	2.6786e+13	-5.2460e+13
H44	-0.011289	0.653131	-4.142584	1.7941e+13	1.7141e+13	6.7328e+12
H45	-1.540676	1.313957	-3.976529	5.0825e+11	4.2403e+11	2.0619e+13
O46	1.707090	2.045768	0.882827	2.5922e+13	-6.7251e+12	-2.4502e+12
H47	2.301182	2.631507	0.391417	1.4405e+12	-3.0044e+12	-1.4263e+13
H48	1.644426	1.131003	0.529213	2.7816e+13	3.8088e+12	1.4295e+13
O49	-1.971554	1.825676	3.177791	-1.9398e+13	2.9579e+13	2.4121e+13
H50	-1.004949	1.950826	2.982210	-1.7173e+13	7.8953e+13	3.2925e+13
H51	-2.228180	0.898883	3.131866	1.0630e+13	1.2276e+13	-2.2725e+13
O52	3.929951	-1.157592	-2.288187	-1.6700e+13	-1.2165e+13	-4.5217e+13
H53	3.129828	-1.717982	-2.375027	-1.8866e+13	-1.9972e+13	2.2602e+12
H54	4.551858	-1.463294	-2.948367	-1.9224e+13	-3.8613e+13	-8.4749e+12
O55	1.291411	-0.200678	0.002271	5.8144e+13	3.9761e+13	2.6109e+13
H56	2.180349	-0.662183	-0.081530	3.3216e+12	8.7329e+12	-3.6945e+12
H57	0.797146	-0.341998	-0.841545	1.1920e+13	-1.5652e+13	3.0060e+13
O58	-0.766134	-3.087429	-1.708030	-6.4163e+13	1.2025e+13	-1.0481e+13
H59	-0.753593	-3.318958	-0.759735	1.7561e+13	-2.3806e+13	-7.9115e+12
H60	-1.530951	-3.466343	-2.137647	-2.5994e+13	-3.4203e+12	2.8724e+13

Continuation of Table B.7						
State #6	Coordinates (Å)			MWV ($amu^2 * bohr/sec$)		
#atom	x	y	z	v_x	v_y	v_z
O61	-3.131281	3.247343	1.640582	-4.8520e+13	8.5635e+12	2.8955e+13
H62	-4.080525	3.311348	1.646705	-1.3366e+13	-2.7598e+13	-3.1444e+13
H63	-2.711048	2.652257	2.364399	-2.3724e+13	1.3914e+13	1.5207e+13
O64	-2.355405	-0.785274	2.992129	1.8682e+13	-3.0856e+13	3.6458e+13
H65	-2.272041	-1.703923	3.252080	7.9679e+13	4.6785e+12	2.8363e+13
H66	-1.793075	-0.653125	2.196074	-4.2567e+13	-2.3799e+13	-3.0067e+13
O67	3.431801	-1.438486	0.272591	9.0308e+12	5.4181e+13	-1.4393e+13
H68	3.938305	-1.685124	-0.518455	2.8719e+13	-2.9211e+13	2.6050e+13
H69	4.085092	-0.857767	0.736098	2.0447e+13	3.0029e+13	-2.8531e+13
O70	1.903129	-3.490996	1.665984	-4.5607e+13	2.3551e+13	-7.6331e+13
H71	2.447141	-2.862812	1.177388	-3.0270e+13	2.8422e+13	-6.1515e+12
H72	1.006822	-3.436941	1.282036	-2.0506e+12	-3.3464e+13	-2.8209e+13
O73	3.495911	1.567653	-2.181489	-1.0331e+13	-5.3248e+12	5.7150e+13
H74	2.893833	1.652447	-1.444003	-1.4710e+13	-2.9835e+10	1.8881e+12
H75	3.789455	0.655494	-2.216866	3.6250e+13	4.4509e+12	2.5234e+13
O76	-3.745176	-0.422826	0.456132	-4.3703e+13	3.5453e+13	-2.9150e+13
H77	-3.398404	-0.610998	1.353626	5.5384e+13	-3.5913e+13	-5.4956e+13
H78	-3.993441	0.501877	0.448256	-1.7239e+12	3.9908e+12	-1.7584e+13
O79	2.497769	1.411361	4.444841	2.8459e+13	-2.3748e+13	-2.8048e+13
H80	1.832956	1.334812	5.123475	2.7113e+13	-4.2772e+12	7.1654e+12
H81	2.019003	1.875203	3.741925	3.2193e+13	2.9336e+13	5.3112e+12
End of Table						

Table B.8: Vibrationally bound initial condition 7 of water $(H_2O)_{27}$ nanodroplet.

State #7	Coordinates (Å)			MWV ($amu^2 * bohr/sec$)		
#atom	x	y	z	v_x	v_y	v_z
O 1	-1.311199	4.624242	0.172971	3.1269e+13	-4.2013e+13	-4.7830e+12
H 2	-2.045580	4.285504	0.712385	2.4586e+12	-5.1353e+13	-1.8271e+13
H 3	-1.091089	5.450292	0.599307	-1.5417e+13	-4.0369e+13	6.3282e+13
O 4	-1.774330	1.769623	-0.282790	4.6927e+13	-1.3591e+13	6.2684e+13
H 5	-1.095991	2.455405	-0.373146	-1.9658e+13	2.2080e+13	1.1943e+13
H 6	-2.343684	2.172301	0.401472	3.7629e+13	-2.4034e+13	2.8418e+13
O 7	-0.242779	-0.607861	-1.823434	-1.9272e+13	-7.4999e+13	5.7714e+13
H 8	-0.778396	-1.413012	-1.951165	-3.3410e+13	-1.8494e+13	4.5704e+13
H 9	-0.426681	-0.036429	-2.618838	-1.5695e+13	-2.8176e+13	1.3679e+13
O10	2.064056	-2.881729	-1.778782	2.9019e+13	-6.9892e+13	2.2884e+13
H11	1.114334	-2.970245	-2.030737	3.2924e+13	-1.2540e+13	1.1373e+13
H12	2.170238	-3.231551	-0.877462	-1.2579e+13	6.5952e+12	2.5169e+13
O13	5.181854	-0.114866	1.915318	-4.5486e+13	-9.0871e+12	5.5229e+13
H14	4.541505	-0.132605	2.640429	1.0560e+13	7.6143e+13	3.9650e+13
H15	5.683435	-0.928128	1.991520	-4.2692e+13	-1.7241e+13	3.5894e+13
O16	0.514679	2.477371	3.046296	-7.2268e+12	6.8387e+13	-1.4439e+13
H17	0.714505	3.361494	3.355414	-2.0463e+13	2.1527e+13	-9.0084e+12
H18	0.915141	2.324182	2.087642	-6.4347e+12	-9.3182e+11	4.7771e+12
O19	-0.551260	-3.262737	0.630179	1.0499e+13	-1.9381e+13	1.4166e+12
H20	-1.318302	-3.678273	1.105623	-1.8028e+13	4.9682e+10	1.4187e+13
H21	-0.642044	-2.308262	0.742177	1.6378e+13	-6.6376e+12	2.2057e+13
O22	-0.999971	-0.362983	0.800078	-6.6870e+13	-3.0556e+13	2.0492e+13

Continuation of Table B.8						
State #7	Coordinates (Å)			MWV ($amu^2 * bohr/sec$)		
#atom	x	y	z	v_x	v_y	v_z
H23	-0.110128	-0.038646	0.857703	-2.1629e+12	4.6593e+13	-3.5536e+13
H24	-1.296065	-0.335344	-0.126357	-6.1917e+13	4.2236e+12	2.6971e+13
O25	-4.121807	-3.120253	-0.219201	-4.1148e+12	3.2568e+13	-5.1889e+13
H26	-3.927774	-2.165925	-0.186803	5.3221e+13	-2.0222e+12	5.5794e+13
H27	-5.051636	-3.223124	-0.025950	6.4140e+12	2.6406e+12	-5.4271e+12
O28	3.031687	3.679482	-0.526413	4.9543e+12	6.8482e+13	-7.9490e+13
H29	3.631755	3.350491	-1.211729	-5.4983e+13	-2.7872e+13	-4.7019e+13
H30	2.486392	4.357540	-0.924731	2.9467e+12	3.4195e+13	6.5889e+12
O31	1.534132	0.505672	-4.162657	6.2282e+13	4.0869e+13	-1.6596e+13
H32	1.480104	-0.255564	-3.560636	-4.8273e+13	2.8937e+13	4.3284e+12
H33	2.181631	1.099254	-3.780961	3.4184e+13	1.3798e+12	-2.1039e+12
O34	-2.988491	-0.825989	-1.906037	5.4609e+13	-3.5290e+13	3.4332e+13
H35	-3.433139	-0.203986	-1.328732	-3.7310e+13	-1.3286e+13	-1.8186e+13
H36	-3.082339	-0.479215	-2.804028	-2.7044e+13	-7.6346e+13	-7.5017e+12
O37	-2.499952	-4.461029	1.706198	-2.5898e+13	2.2224e+12	4.6247e+13
H38	-3.077750	-4.622551	0.941146	-1.5797e+13	2.0046e+13	-6.4057e+12
H39	-2.917336	-4.851051	2.470974	-1.9229e+12	-2.7094e+13	5.2572e+12
O40	-2.920421	2.194760	-2.780098	2.6582e+13	-2.4789e+13	-3.8378e+13
H41	-2.613642	1.999198	-1.867838	1.0355e+13	-4.2585e+13	-5.0694e+13
H42	-3.440799	2.994483	-2.732160	1.3332e+13	-1.5097e+13	9.4628e+12
O43	-0.985399	0.613717	-4.046513	-2.5371e+13	6.0036e+13	-5.0601e+13
H44	-0.105269	0.889270	-4.341534	-2.2956e+13	1.1314e+13	-5.4958e+13
H45	-1.501935	1.392952	-3.773396	-1.9760e+13	1.2046e+12	2.7812e+13
O46	1.724349	2.049241	0.939370	-4.1300e+12	1.8056e+13	5.5413e+13

Continuation of Table B.8						
State #7	Coordinates (Å)			MWV ($amu^2 * bohr/sec$)		
#atom	x	y	z	v_x	v_y	v_z
H47	2.325471	2.658055	0.469718	-9.6745e+12	1.2629e+13	1.9650e+13
H48	1.603931	1.176148	0.476133	-3.4124e+12	6.8259e+12	-1.2848e+13
O49	-2.019208	1.897659	3.246882	-1.4218e+13	2.3027e+13	5.4886e+13
H50	-1.077348	2.186023	3.323023	4.2772e+11	3.8203e+13	1.0872e+13
H51	-1.919951	0.933128	3.323127	-1.4792e+13	9.2514e+12	4.1446e+13
O52	3.894990	-1.197974	-2.398212	-1.7502e+13	-2.5479e+13	-5.0681e+13
H53	3.142068	-1.794055	-2.150925	8.8115e+12	3.8946e+10	-2.0002e+13
H54	4.412206	-1.658838	-3.059029	-2.8457e+13	-1.5545e+13	-2.1374e+13
O55	1.446736	-0.145826	0.017717	7.3010e+13	2.2933e+13	-8.2955e+12
H56	2.172151	-0.774227	0.106761	1.2217e+13	-8.2485e+12	1.8275e+13
H57	0.921857	-0.279323	-0.814322	1.1183e+13	-2.5438e+13	-1.9686e+13
O58	-0.868085	-3.078523	-1.798347	-4.6026e+13	-5.6933e+12	-7.7695e+13
H59	-0.777694	-3.285662	-0.817353	-2.0510e+13	2.6460e+13	-9.4504e+12
H60	-1.768334	-3.304746	-2.059401	-2.6724e+13	3.9828e+13	-3.3268e+12
O61	-3.237483	3.277400	1.644923	-6.4749e+13	1.5113e+13	-2.1526e+13
H62	-4.187131	3.187443	1.629217	-1.3657e+13	1.3731e+13	1.6016e+13
H63	-2.836082	2.717006	2.370554	2.1373e+13	-4.4178e+12	-1.4042e+13
O64	-2.307336	-0.863952	3.005721	3.9855e+13	-4.4821e+13	-1.2023e+13
H65	-1.768801	-1.402725	3.595276	2.9126e+13	6.3764e+13	4.5154e+13
H66	-1.746626	-0.778839	2.191105	4.1053e+13	7.3941e+11	3.2756e+13
O67	3.520201	-1.352664	0.262090	6.1083e+13	2.5121e+13	1.0671e+13
H68	3.919943	-1.681408	-0.547309	1.9304e+13	5.4494e+13	-1.9863e+13
H69	4.121681	-0.732071	0.693703	2.5581e+13	-1.6042e+12	-7.8109e+12
O70	1.845218	-3.451051	1.492586	-8.0793e+12	2.0289e+13	-9.8195e+13

Continuation of Table B.8						
State #7	Coordinates (Å)			MWV ($amu^2 * bohr/sec$)		
#atom	x	y	z	v_x	v_y	v_z
H71	2.177408	-2.558551	1.339964	-3.2637e+13	2.8205e+13	4.1611e+13
H72	0.924632	-3.463138	1.188984	-2.3256e+13	1.8135e+13	8.4642e+12
O73	3.469765	1.549927	-2.079106	-1.8534e+13	-2.2463e+13	5.5924e+13
H74	2.769124	1.496820	-1.420182	-1.4258e+13	-1.7540e+13	-4.8228e+12
H75	3.862377	0.657284	-2.055589	-8.0215e+12	1.2925e+13	-1.8920e+13
O76	-3.861251	-0.357240	0.398414	-6.8265e+13	4.6356e+13	-1.3757e+13
H77	-3.163947	-0.642282	1.017528	1.7388e+13	-1.6696e+13	-3.2398e+13
H78	-3.911552	0.557257	0.700704	-6.0028e+12	-5.3027e+12	4.3312e+13
O79	2.599636	1.356722	4.409175	6.1022e+13	-2.9338e+13	-1.1978e+13
H80	2.015998	1.206229	5.152935	3.6822e+13	-3.0139e+13	4.0303e+12
H81	1.973745	1.732304	3.759835	-2.6203e+13	-5.7467e+13	-5.7215e+12
End of Table						

Table B.9: Vibrationally bound initial condition 8 of water $(H_2O)_{27}$ nanodroplet.

State #8	Coordinates (Å)			MWV ($amu^2 * bohr/sec$)		
#atom	x	y	z	v_x	v_y	v_z
O 1	-0.939039	3.741676	0.720868	4.1766e+13	-7.6595e+13	2.4639e+13
H 2	-1.874771	3.988037	0.857943	2.4634e+13	5.1551e+13	3.0592e+13
H 3	-0.535982	3.550618	1.572808	-2.9781e+13	-7.3801e+13	1.7665e+13
O 4	-2.173947	1.592140	0.071460	2.0776e+13	-2.4895e+12	2.8924e+13
H 5	-1.430398	2.232761	0.088023	1.5261e+12	3.5672e+13	-1.1804e+12

Continuation of Table B.9						
State #8	Coordinates (Å)			MWV ($amu^2 * bohr/sec$)		
#atom	x	y	z	v_x	v_y	v_z
H 6	-2.817892	2.054482	0.654356	2.6999e+13	2.9695e+13	8.6624e+12
O 7	0.470717	-1.050586	-2.416188	8.0798e+13	-5.6464e+13	-1.2155e+13
H 8	0.149127	-1.910063	-2.720774	-1.5719e+13	-8.6759e+12	-3.5656e+12
H 9	-0.124872	-0.400168	-2.882183	1.0842e+13	-1.6055e+13	7.5303e+12
O10	2.167877	-3.623623	-2.422575	-3.4855e+13	-4.0459e+13	-5.0070e+13
H11	1.206537	-3.761156	-2.384781	1.4414e+13	8.4653e+12	-4.0284e+13
H12	2.394583	-3.528352	-1.498185	-4.6525e+13	-5.3849e+13	-2.1550e+12
O13	5.062511	-0.093560	2.601845	5.9648e+13	-2.6771e+13	-5.0224e+13
H14	5.376217	0.716987	3.016373	-1.7273e+13	-2.4161e+13	5.3705e+13
H15	4.181835	-0.224496	2.961826	-7.8325e+10	-1.7689e+13	-6.1033e+13
O16	0.448331	3.277894	3.425693	1.7995e+13	2.3086e+13	-8.6242e+12
H17	0.676738	3.910054	4.097740	3.7206e+12	2.1244e+13	-1.5712e+13
H18	1.058469	3.297183	2.684504	2.9495e+12	-2.6873e+13	-8.0089e+12
O19	-0.928847	-3.376909	0.425561	2.1762e+13	-3.1029e+11	-4.2897e+13
H20	-1.519074	-3.772526	1.074586	-2.1528e+13	1.4266e+13	7.0282e+12
H21	-0.963081	-2.425317	0.502995	-4.2264e+13	1.2154e+13	-1.0930e+13
O22	-0.849839	-0.579834	0.853458	3.2490e+13	-4.8414e+13	8.2179e+13
H23	0.131668	-0.414402	0.866374	6.8484e+12	2.5587e+13	-2.4558e+13
H24	-1.305876	0.163979	0.421704	2.2207e+13	-4.4926e+12	3.3028e+13
O25	-4.043925	-3.164101	-0.433875	-6.2805e+12	1.1510e+13	-5.3625e+13
H26	-3.608458	-2.314900	-0.638688	1.5876e+12	1.2955e+12	-6.7708e+12
H27	-4.864132	-3.216620	-0.920560	-4.3920e+13	-4.2402e+12	5.6355e+13
O28	2.830548	3.725208	-1.303351	-4.8799e+13	-6.1193e+12	9.4083e+12
H29	3.066122	2.946798	-1.841864	2.3570e+13	1.3494e+13	7.0819e+12

Continuation of Table B.9						
State #8	Coordinates (Å)			MWV ($amu^2 * bohr/sec$)		
#atom	x	y	z	v_x	v_y	v_z
H30	2.078034	4.135375	-1.732744	2.4865e+12	-1.5335e+13	-3.3431e+13
O31	1.727309	1.189208	-4.249349	-7.8190e+12	8.1225e+13	-5.2689e+13
H32	1.783425	2.125793	-4.458421	-5.5856e+13	2.0960e+13	2.1934e+13
H33	2.096248	1.031964	-3.363078	2.1584e+13	3.4565e+12	-8.8946e+12
O34	-2.885185	-1.063508	-1.616662	2.1019e+13	3.9558e+13	5.9219e+13
H35	-2.023013	-1.288958	-1.992759	-1.1241e+13	-1.9315e+13	1.6790e+11
H36	-3.265797	-0.410614	-2.227043	6.0703e+13	3.2267e+13	8.9534e+11
O37	-3.379577	-4.186414	1.882260	-3.6801e+13	3.5670e+13	-9.2179e+12
H38	-3.771044	-3.794446	1.061408	-1.2603e+12	-3.2162e+13	-1.8723e+13
H39	-3.367118	-5.131769	1.713922	-2.1001e+12	-5.3152e+12	6.0807e+13
O40	-2.832537	1.767128	-2.633474	-3.2831e+13	-8.9514e+13	-4.8856e+13
H41	-2.738732	1.509934	-1.668984	-6.9084e+12	3.1335e+13	4.3380e+12
H42	-3.593493	2.343393	-2.684479	3.1612e+13	2.7730e+13	-6.8054e+13
O43	-0.626797	0.356189	-4.140457	2.0175e+13	-2.8268e+13	2.2307e+13
H44	0.250593	0.798147	-4.268098	2.9655e+13	-2.4584e+13	9.2348e+12
H45	-1.250308	1.096763	-4.077030	-5.9502e+12	-3.9008e+13	5.7062e+13
O46	1.746449	3.053356	1.119708	-2.3424e+13	4.5733e+13	2.5653e+13
H47	2.188161	3.453008	0.341871	7.2233e+12	9.2267e+12	2.3232e+13
H48	1.752519	2.128608	0.845604	-3.2399e+13	3.4594e+13	-3.0339e+13
O49	-2.387672	2.044440	3.588488	3.2200e+13	3.7180e+13	1.7629e+13
H50	-1.564021	2.511046	3.742837	-8.0028e+12	2.5937e+13	4.1652e+13
H51	-2.140463	1.092234	3.592431	-3.1717e+13	-3.7345e+12	-7.2356e+13
O52	3.776081	-1.256815	-2.407428	2.6886e+13	2.9614e+13	-5.7925e+11
H53	2.834550	-1.372870	-2.565742	1.0443e+13	2.7100e+13	4.5499e+12

Continuation of Table B.9						
State #8	Coordinates (Å)			MWV ($amu^2 * bohr/sec$)		
#atom	x	y	z	v_x	v_y	v_z
H54	4.201008	-1.998267	-2.835146	-2.8180e+13	4.3271e+12	-2.4514e+13
O55	1.617307	-0.114219	0.095235	1.0266e+13	1.7932e+12	-8.0488e+12
H56	2.452786	-0.632638	0.294621	-1.2870e+13	-1.5040e+13	3.2164e+13
H57	1.262248	-0.439359	-0.729798	-1.4098e+13	-1.6992e+13	2.1273e+11
O58	-1.166039	-3.363311	-2.219832	6.0625e+13	6.5598e+10	1.9282e+13
H59	-0.967276	-3.485844	-1.265391	-2.8158e+13	1.0339e+14	1.2113e+13
H60	-1.843421	-4.008886	-2.438571	4.8176e+13	-3.4039e+13	4.0396e+13
O61	-3.387981	3.164587	1.551518	-3.9363e+13	-2.9661e+13	3.3048e+13
H62	-4.288130	3.128216	1.231964	-9.0983e+12	7.4104e+13	-4.3794e+12
H63	-3.215420	2.787741	2.467689	-1.8731e+13	2.5627e+13	1.5265e+13
O64	-2.096530	-0.444932	3.397559	-9.1690e+12	2.1576e+13	-3.1813e+13
H65	-2.609895	-1.086548	3.893142	6.2363e+13	-2.7394e+13	2.2948e+13
H66	-1.713443	-0.805994	2.565107	1.9786e+13	3.7740e+13	-2.8012e+13
O67	4.123451	-1.261182	0.202118	-5.3348e+13	2.5919e+13	5.9600e+13
H68	4.346219	-1.578880	-0.674266	-3.3350e+13	5.3460e+13	-7.7572e+12
H69	4.831978	-0.830625	0.711015	-5.2303e+13	5.4726e+13	3.7651e+13
O70	2.085715	-3.146094	0.671506	-3.0003e+13	-9.9473e+11	-7.3066e+13
H71	2.599676	-2.770890	1.382497	1.1855e+13	-4.1668e+13	3.6493e+12
H72	1.207908	-3.411585	0.946755	-1.2973e+13	9.7839e+12	-1.8380e+12
O73	3.253713	1.224843	-2.041127	1.9733e+13	-8.4076e+13	-2.0134e+13
H74	2.922927	0.913100	-1.168633	-2.2364e+13	1.3627e+12	-4.6610e+12
H75	3.883617	0.572026	-2.359359	2.3981e+13	1.1060e+13	-4.1218e+13
O76	-4.114518	0.400839	0.844385	-1.7725e+13	2.0637e+13	1.6752e+13
H77	-4.204564	0.105435	1.755164	1.6790e+13	5.8741e+12	1.5166e+13

Continuation of Table B.9						
State #8	Coordinates (Å)			MWV ($amu^2 * bohr/sec$)		
#atom	x	y	z	v_x	v_y	v_z
H78	-3.313411	-0.039786	0.575959	-9.4183e+12	-1.0450e+13	2.3683e+13
O79	2.609981	1.157248	4.376355	-8.2308e+13	3.8519e+13	2.7922e+13
H80	2.021763	1.712493	4.877590	-3.5327e+13	-1.0550e+12	6.0050e+12
H81	2.252130	1.231185	3.491308	-9.5112e+12	1.9365e+13	4.7815e+12
End of Table						

Table B.10: Vibrationally bound initial condition 9 of water $(H_2O)_{27}$ nanodroplet.

State #9	Coordinates (Å)			MWV ($amu^2 * bohr/sec$)		
#atom	x	y	z	v_x	v_y	v_z
O 1	-0.856860	3.625270	0.789452	4.8810e+13	-3.9153e+13	4.3013e+13
H 2	-1.607717	4.162874	1.036527	-1.4628e+12	-5.5006e+12	7.7469e+12
H 3	-0.540177	3.212040	1.595139	2.7931e+13	-7.2264e+12	1.3194e+12
O 4	-2.072499	1.589481	0.060575	6.4536e+13	-1.5812e+13	-3.8850e+13
H 5	-1.467579	2.336672	0.042247	-1.0128e+13	1.2700e+13	3.5619e+13
H 6	-2.817151	1.846143	0.640007	-1.8232e+13	-3.6854e+13	-3.1199e+13
O 7	0.640938	-1.164755	-2.403953	9.9752e+13	-5.4292e+13	2.6369e+13
H 8	0.240616	-2.035564	-2.479719	2.6436e+13	-2.1665e+13	4.7672e+13
H 9	0.192511	-0.583892	-3.054956	3.8146e+13	-4.5293e+13	-3.4410e+13
O10	2.101462	-3.693970	-2.491276	-2.8928e+13	-3.3594e+13	-2.4253e+13
H11	1.184532	-3.773857	-2.833897	-3.8806e+12	-9.9462e+12	-3.8492e+13
H12	2.066453	-3.853471	-1.534370	-5.2625e+13	-1.6200e+13	-2.3375e+13

Continuation of Table B.10						
State #9	Coordinates (Å)			MWV ($amu^2 * bohr/sec$)		
#atom	x	y	z	v_x	v_y	v_z
O13	5.156873	-0.133932	2.504583	3.5660e+13	-1.8247e+13	-4.8910e+13
H14	5.336652	0.421318	3.263022	2.2524e+12	-3.6054e+13	1.7653e+13
H15	4.264120	-0.467751	2.625483	2.1978e+13	-3.6902e+13	-1.6812e+13
O16	0.479972	3.304351	3.411362	2.8250e+13	1.6128e+13	-1.0729e+13
H17	0.711795	4.144656	3.811032	-2.9900e+13	1.8644e+13	-2.4887e+13
H18	1.059041	3.295407	2.583430	-3.0453e+13	-1.2900e+13	-1.7424e+13
O19	-0.907284	-3.330009	0.385162	-6.1105e+12	5.3838e+13	-7.0192e+11
H20	-1.669291	-3.741030	0.804207	4.2099e+12	2.3443e+12	-4.4559e+13
H21	-0.926087	-2.342722	0.567578	3.4934e+13	-1.8594e+13	3.3073e+13
O22	-0.798614	-0.671596	1.027365	1.0434e+13	-4.3696e+13	9.1870e+13
H23	0.124391	-0.498306	0.798934	1.6817e+13	-1.1894e+13	1.5525e+13
H24	-1.374323	0.074194	0.700522	-3.7582e+11	-1.8084e+13	2.1798e+12
O25	-4.062573	-3.150918	-0.532488	-2.3055e+13	1.2935e+13	-5.8128e+13
H26	-3.794997	-2.343600	-1.006899	-6.2314e+12	-1.0603e+13	-2.9438e+13
H27	-5.014489	-3.053266	-0.472709	2.5792e+12	8.8360e+12	6.4079e+13
O28	2.729451	3.720061	-1.281647	-4.7572e+13	2.2846e+12	1.9489e+13
H29	3.200073	2.922460	-1.583969	-1.0770e+13	-1.8342e+13	2.9497e+13
H30	2.148409	4.018377	-1.980241	1.9444e+13	-2.8535e+13	-3.6211e+13
O31	1.728259	1.360819	-4.338178	1.0906e+13	9.8851e+13	-3.3357e+13
H32	1.520756	2.302835	-4.358753	-1.6138e+13	1.9182e+13	-1.3305e+13
H33	2.324310	1.223433	-3.580628	1.3375e+13	1.4036e+13	-3.7666e+13
O34	-2.826187	-0.976073	-1.509814	3.0510e+13	3.5276e+13	6.2129e+13
H35	-2.225749	-1.610589	-1.924779	-2.8498e+13	-7.6344e+12	-2.4783e+13
H36	-2.880311	-0.149781	-2.006485	5.0981e+13	2.1924e+13	1.8537e+13

Continuation of Table B.10						
State #9	Coordinates (Å)			MWV ($amu^2 * bohr/sec$)		
#atom	x	y	z	v_x	v_y	v_z
O37	-3.419250	-4.118707	1.853608	9.2125e+11	3.8353e+13	-1.3402e+13
H38	-3.747813	-4.011072	0.947383	-2.9931e+12	-2.5393e+13	-1.4333e+13
H39	-3.515571	-5.009833	2.177031	-4.0945e+13	2.2558e+13	3.0941e+13
O40	-2.892530	1.574165	-2.697622	-2.1445e+13	-8.9396e+13	-1.8519e+13
H41	-2.639514	1.910174	-1.835653	2.4232e+13	1.3150e+13	-1.1037e+13
H42	-3.227895	2.326959	-3.182766	4.6588e+13	-4.9453e+13	-7.2295e+13
O43	-0.628711	0.295446	-4.087915	-1.5544e+13	-3.6651e+13	3.2361e+13
H44	0.177236	0.797825	-4.307304	-5.2652e+13	3.6766e+13	-3.7785e+12
H45	-1.203115	0.896170	-3.570725	2.7357e+13	-6.7783e+12	4.6615e+13
O46	1.721008	3.103732	1.172034	-4.9573e+12	6.9359e+12	3.6035e+13
H47	2.168086	3.641269	0.487211	-1.5332e+13	4.2838e+12	-1.2693e+13
H48	1.413863	2.318003	0.684198	-2.0924e+13	3.6611e+13	-3.0276e+13
O49	-2.344252	2.158797	3.624086	2.2096e+13	6.8010e+13	1.9413e+13
H50	-1.435917	2.374546	3.873632	1.2843e+13	-2.7756e+13	-1.5969e+13
H51	-2.226454	1.191490	3.463020	-6.5575e+11	1.0132e+13	6.2867e+13
O52	3.818156	-1.234896	-2.437418	1.1360e+12	-8.3215e+12	-2.5756e+13
H53	2.835567	-1.280772	-2.349869	1.6143e+13	-9.4279e+12	3.0988e+13
H54	4.038603	-1.992905	-2.988562	-6.8682e+11	-4.6364e+12	7.4408e+12
O55	1.646970	-0.106606	0.045227	4.2309e+12	-1.1015e+13	-5.4753e+13
H56	2.331718	-0.710742	0.352227	1.3942e+13	6.8913e+12	2.3892e+13
H57	1.202377	-0.604265	-0.699894	2.0131e+12	2.9518e+13	5.3470e+12
O58	-1.028165	-3.339873	-2.174742	6.2107e+13	2.1756e+13	2.3061e+13
H59	-1.148780	-3.188018	-1.190894	4.0756e+13	-3.2680e+13	3.1906e+13
H60	-1.477608	-4.188016	-2.287870	5.2075e+13	-1.3135e+13	-2.5931e+13

Continuation of Table B.10						
State #9	Coordinates (Å)			MWV ($amu^2 * bohr/sec$)		
#atom	x	y	z	v_x	v_y	v_z
O61	-3.489139	3.157191	1.611413	-6.8775e+13	2.0011e+13	3.2221e+13
H62	-4.373825	3.507860	1.636869	-6.4453e+12	2.3390e+13	5.5087e+13
H63	-3.275296	2.821941	2.504963	5.1231e+13	4.2358e+12	8.5245e+12
O64	-2.111070	-0.421125	3.302698	1.8356e+12	-6.7645e+12	-6.6824e+13
H65	-1.981335	-1.243167	3.775732	5.8673e+13	1.0772e+13	-9.4113e+12
H66	-1.502345	-0.564983	2.560148	2.9861e+13	3.8610e+13	2.2567e+12
O67	3.993758	-1.196884	0.357544	-5.9895e+13	4.9678e+13	7.7189e+13
H68	4.111275	-0.996814	-0.579594	-4.7888e+13	4.4625e+12	1.7563e+13
H69	4.600769	-0.576441	0.772688	-1.1687e+13	9.2593e+12	3.6535e+13
O70	2.008952	-3.149311	0.509839	-5.0918e+13	3.3316e+11	-9.1433e+13
H71	2.670728	-3.170890	1.192013	4.0708e+12	-5.2402e+13	-4.1841e+13
H72	1.117083	-3.288967	0.839180	-8.6021e+11	3.4880e+12	-2.4209e+13
O73	3.273670	1.111549	-2.085131	1.1281e+13	-4.3058e+13	-1.7288e+13
H74	2.807745	0.689626	-1.347247	-6.1063e+13	-2.6895e+11	-1.5870e+13
H75	3.882161	0.391044	-2.325689	-1.8534e+13	-8.0451e+12	-1.0305e+13
O76	-4.179264	0.406555	0.911631	-4.9671e+13	1.2533e+12	3.2597e+13
H77	-4.155751	0.132771	1.828072	4.4496e+13	-4.0285e+13	4.4431e+12
H78	-3.492387	-0.024648	0.396283	-5.0021e+13	-1.8234e+13	-7.2011e+12
O79	2.446535	1.235110	4.412667	-8.2263e+13	3.8368e+13	1.1130e+13
H80	1.778007	1.628762	4.968477	-2.3987e+13	-1.6768e+13	3.2086e+12
H81	2.155623	1.448599	3.523340	-1.3753e+13	4.0690e+13	1.1360e+13
End of Table						

Table B.11: Vibrationally bound initial condition 10 of water $(H_2O)_{27}$ nanodroplet.

State #10	Coordinates (Å)			MWV ($amu^2 * bohr/sec$)		
#atom	x	y	z	v_x	v_y	v_z
O 1	-0.778564	3.592569	0.882208	1.4020e+13	6.6357e+11	6.5977e+13
H 2	-1.699612	3.839556	1.042792	-7.2881e+12	-3.8949e+13	-2.9164e+13
H 3	-0.378700	3.494313	1.757558	2.1513e+13	6.0733e+13	1.0785e+13
O 4	-1.967251	1.532901	-0.055602	3.2502e+13	-3.8251e+13	-7.5030e+13
H 5	-1.488503	2.254716	0.425058	2.2481e+13	-3.9781e+13	1.6012e+13
H 6	-2.882947	1.457705	0.266242	1.7954e+13	-7.2378e+13	-3.0123e+13
O 7	0.871655	-1.264419	-2.333373	1.2702e+14	-4.8681e+13	3.5734e+13
H 8	0.430221	-2.101576	-2.150952	1.7144e+13	3.7244e+12	2.8686e+13
H 9	0.338425	-0.854338	-3.053057	1.0608e+13	6.5576e+12	4.0661e+13
O10	2.044198	-3.767912	-2.535022	-1.3847e+13	-4.1311e+13	-1.2866e+13
H11	1.247766	-3.829892	-3.060293	-2.2523e+13	-2.8431e+12	-3.7683e+13
H12	1.824526	-3.746999	-1.585698	-8.5473e+12	3.8046e+13	2.2045e+12
O13	5.205805	-0.177506	2.430015	1.5469e+13	-2.8082e+13	-2.0184e+13
H14	5.450638	0.297635	3.220484	3.3852e+13	1.4852e+13	-2.8707e+13
H15	4.492424	-0.772044	2.678038	3.4356e+13	-3.7796e+13	8.4177e+12
O16	0.517905	3.324132	3.387007	7.1360e+12	1.2972e+13	-1.8044e+13
H17	0.431521	4.239432	3.667846	-3.2276e+13	-2.4726e+12	-2.8778e+12
H18	1.120221	3.363998	2.609999	4.2224e+13	9.9245e+12	2.8488e+13
O19	-0.906564	-3.218531	0.405160	-5.0416e+12	4.6062e+13	3.6386e+13
H20	-1.695814	-3.644974	0.805176	1.9462e+13	-7.8756e+12	8.7248e+12
H21	-0.938447	-2.291070	0.723619	1.3839e+13	6.0147e+13	-2.8349e+13
O22	-0.761709	-0.728200	1.184376	4.2403e+13	-3.8503e+12	4.9464e+13

Continuation of Table B.11						
State #10	Coordinates (Å)			MWV ($amu^2 * bohr/sec$)		
#atom	x	y	z	v_x	v_y	v_z
H23	0.183011	-0.504453	1.028713	2.4414e+12	-2.8977e+13	3.0645e+13
H24	-1.246030	-0.229593	0.506903	-1.2856e+13	-5.0850e+13	-2.1066e+13
O25	-4.132906	-3.141312	-0.645964	-4.8802e+13	8.1994e+12	-4.9271e+13
H26	-3.759816	-2.273203	-0.927489	2.8300e+13	-3.4687e+12	3.1598e+13
H27	-4.915669	-2.833733	-0.176389	1.4372e+13	3.0511e+13	4.0505e+12
O28	2.643714	3.699511	-1.247684	-3.9727e+13	-2.1230e+13	1.8556e+13
H29	3.082458	2.846211	-1.327566	-5.1021e+12	-2.7775e+12	2.0307e+13
H30	2.286157	3.923151	-2.102089	1.1455e+13	4.8583e+12	-1.2046e+12
O31	1.738477	1.569144	-4.412088	2.7228e+12	1.0953e+14	-3.2560e+13
H32	1.738245	2.526578	-4.502161	4.7063e+13	3.7629e+13	-3.7330e+13
H33	2.316855	1.403275	-3.624652	-1.4977e+13	1.3412e+13	8.7982e+12
O34	-2.751317	-0.930306	-1.403272	4.3780e+13	1.3562e+13	4.4223e+13
H35	-2.252762	-1.554234	-1.943965	2.5761e+13	-4.1999e+12	3.6810e+13
H36	-2.841136	-0.081720	-1.863262	-4.2225e+13	-3.1180e+12	1.9461e+13
O37	-3.393875	-4.051294	1.814770	2.0702e+13	3.0203e+13	-2.7086e+13
H38	-3.732009	-3.974207	0.912052	9.0636e+12	3.3504e+13	-2.4961e+12
H39	-3.834922	-4.757167	2.277723	-2.9571e+13	3.8351e+13	3.7874e+11
O40	-2.890529	1.392192	-2.712692	2.0036e+13	-9.7034e+13	6.2132e+12
H41	-2.639398	1.938354	-1.943533	-9.8003e+12	3.7529e+12	-4.6013e+13
H42	-2.939576	1.922264	-3.512506	2.7985e+13	-3.4565e+13	4.3985e+12
O43	-0.671643	0.241338	-4.012874	-1.8716e+13	-4.4823e+13	3.1531e+13
H44	0.081771	0.795290	-4.301634	-8.9900e+11	1.0225e+13	4.7634e+13
H45	-1.263379	0.650463	-3.376171	-1.5530e+13	8.1615e+12	1.4682e+13
O46	1.737682	3.087787	1.202103	2.1061e+13	-1.6832e+13	1.0944e+13

Continuation of Table B.11						
State #10	Coordinates (Å)			MWV ($amu^2 * bohr/sec$)		
#atom	x	y	z	v_x	v_y	v_z
H47	2.017933	3.761140	0.584051	-1.8640e+13	9.9883e+12	2.9995e+12
H48	1.317601	2.372808	0.709281	-1.1765e+12	-2.0930e+13	8.5259e+12
O49	-2.266726	2.268071	3.680352	3.5149e+13	7.5815e+13	3.1495e+13
H50	-1.330693	2.519085	3.684457	2.8589e+13	-3.6386e+13	-1.2002e+13
H51	-2.400708	1.325743	3.886253	5.3882e+13	-1.0222e+13	1.6711e+13
O52	3.785788	-1.302072	-2.473400	-3.3578e+13	-7.2817e+13	-9.4230e+12
H53	2.826468	-1.523676	-2.457539	-2.8355e+13	-2.2012e+13	-4.4032e+13
H54	4.193722	-2.100166	-2.832841	5.2166e+13	-1.1425e+12	2.1288e+13
O55	1.616273	-0.106942	-0.071486	-3.2333e+13	1.3419e+13	-5.7288e+13
H56	2.430043	-0.587906	0.245687	-4.0567e+12	4.5416e+13	-3.4469e+13
H57	1.321575	-0.617649	-0.865372	1.5083e+12	-3.6198e+13	-3.7039e+13
O58	-0.911029	-3.299292	-2.112128	6.9112e+13	2.0138e+13	2.6137e+13
H59	-0.762875	-3.528882	-1.186034	-1.7285e+13	-2.0851e+13	-6.4301e+11
H60	-1.051513	-4.067622	-2.663749	4.3316e+13	2.7318e+13	-4.2855e+13
O61	-3.602746	3.227615	1.672681	-4.0732e+13	5.0232e+13	2.8679e+13
H62	-4.401788	3.514523	2.117605	1.0905e+13	-1.5112e+13	4.9026e+13
H63	-3.083618	2.877367	2.439835	-3.0483e+13	-1.8637e+13	-2.8604e+12
O64	-2.101444	-0.433461	3.178166	-1.4184e+13	1.1759e+13	-4.2310e+13
H65	-1.798331	-1.052927	3.837133	1.8481e+13	1.5867e+13	-8.2102e+12
H66	-1.420632	-0.407919	2.436861	4.6525e+12	-3.6301e+13	-9.2730e+12
O67	3.877607	-1.093669	0.513038	-4.6348e+13	4.2846e+13	6.6052e+13
H68	4.106348	-1.342450	-0.406881	2.2409e+13	-5.8668e+13	4.8234e+13
H69	4.634524	-0.542249	0.755949	-1.0673e+13	1.0054e+13	-3.1349e+13
O70	1.893853	-3.147438	0.297489	-6.8108e+13	-8.0493e+12	-1.1066e+14

Continuation of Table B.11						
State #10	Coordinates (Å)			MWV ($amu^2 * bohr/sec$)		
#atom	x	y	z	v_x	v_y	v_z
H71	2.605156	-3.484949	0.840492	-5.0236e+12	-1.4227e+13	-6.2508e+13
H72	1.058472	-3.458931	0.697478	-1.7789e+13	-1.5337e+13	-4.2664e+13
O73	3.256615	1.096426	-2.105658	-3.2522e+13	2.8159e+13	-1.4141e+13
H74	2.546971	0.759348	-1.534702	1.3833e+13	-6.7090e+12	-5.0214e+12
H75	3.680688	0.240011	-2.364311	-2.9972e+13	-1.6049e+13	1.8479e+13
O76	-4.260783	0.367649	0.988834	-2.7209e+13	-4.4869e+13	3.2562e+13
H77	-3.818530	-0.023369	1.750574	3.8057e+13	7.0331e+12	-1.0646e+13
H78	-4.138662	-0.185822	0.196427	-1.0702e+14	2.6559e+12	-7.0495e+12
O79	2.284845	1.302561	4.420066	-8.2145e+13	3.1990e+13	-9.7234e+11
H80	1.589489	1.552865	5.033034	-1.5039e+13	-8.1777e+12	1.8535e+12
H81	2.135550	1.870352	3.656764	7.2938e+12	5.5905e+13	2.9513e+13
End of Table						

Table B.12: Vibrationally bound initial condition 11 of water $(H_2O)_{27}$ nanodroplet.

State #11	Coordinates (Å)			MWV ($amu^2 * bohr/sec$)		
#atom	x	y	z	v_x	v_y	v_z
O 1	-0.797471	3.596329	0.998973	-4.2052e+13	5.2631e+12	5.3039e+13
H 2	-1.729885	3.871700	1.075234	5.4347e+12	2.5892e+13	7.8393e+12
H 3	-0.454648	3.824422	1.872639	-7.3401e+12	-2.4519e+11	1.5447e+13
O 4	-1.915709	1.416113	-0.227774	2.1930e+13	-7.4089e+13	-7.5799e+13
H 5	-1.371749	2.004534	0.315641	3.1443e+13	1.5676e+13	-5.3126e+13

Continuation of Table B.12						
State #11	Coordinates (Å)			MWV ($amu^2 * bohr/sec$)		
#atom	x	y	z	v_x	v_y	v_z
H 6	-2.703349	1.223871	0.313662	-4.4632e+12	-2.9590e+12	-2.4361e+13
O 7	1.104690	-1.348838	-2.277075	8.9097e+13	-3.6263e+13	2.0820e+13
H 8	0.487535	-2.106448	-2.166033	1.2678e+13	4.0719e+11	-2.0618e+13
H 9	0.530811	-0.682755	-2.713574	4.8274e+13	1.6363e+13	9.3321e+12
O10	2.036032	-3.860480	-2.559244	8.3674e+12	-4.9023e+13	-7.3876e+12
H11	1.241031	-3.765574	-3.037920	-1.0694e+13	1.0398e+13	-1.1026e+13
H12	1.841402	-3.501374	-1.683562	3.4323e+13	2.0554e+12	-3.0974e+12
O13	5.256361	-0.232060	2.393970	3.8111e+13	-2.3117e+13	-8.8718e+12
H14	5.553933	0.400626	3.045509	-6.1956e+11	1.5882e+13	-2.3295e+13
H15	4.748030	-0.874342	2.892904	2.1924e+13	3.8958e+12	2.6127e+13
O16	0.515228	3.362633	3.363405	-1.2738e+13	2.0818e+13	-1.3217e+12
H17	0.415892	4.209946	3.808582	4.9795e+13	5.7636e+12	2.2332e+13
H18	1.163109	3.416407	2.573713	-3.8327e+13	2.7987e+13	-3.8942e+13
O19	-0.909283	-3.158902	0.478684	-9.4330e+12	1.4981e+13	4.1772e+13
H20	-1.509375	-3.493978	1.172310	2.2664e+13	1.4459e+13	5.9553e+13
H21	-0.888345	-2.193166	0.738708	2.5096e+13	-2.4108e+13	1.8606e+13
O22	-0.651796	-0.740894	1.188753	6.8631e+13	9.1669e+12	-5.9229e+13
H23	0.279037	-0.488708	0.895849	2.3608e+13	4.1876e+12	-1.5552e+13
H24	-1.137196	-0.168467	0.535373	1.6668e+13	2.6611e+13	4.3532e+13
O25	-4.228331	-3.105129	-0.706535	-4.3564e+13	8.0080e+12	-9.8245e+12
H26	-3.553613	-2.417347	-0.869838	-1.4760e+13	2.6113e+13	-1.7203e+13
H27	-5.016077	-2.659358	-0.381849	-1.6884e+13	4.5011e+13	-6.7090e+13
O28	2.572941	3.652754	-1.200864	-2.7448e+13	-3.1629e+13	1.5637e+13
H29	3.081904	2.850287	-1.412059	2.1772e+12	1.0454e+13	-9.2784e+12

Continuation of Table B.12						
State #11	Coordinates (Å)			MWV ($amu^2 * bohr/sec$)		
#atom	x	y	z	v_x	v_y	v_z
H30	2.325785	3.986532	-2.063750	-1.8240e+13	3.1298e+13	2.3729e+13
O31	1.733279	1.789784	-4.445860	-1.1006e+13	1.0520e+14	-2.7724e+12
H32	2.124697	2.560985	-4.839634	5.0348e+13	-1.1207e+13	-4.3610e+13
H33	2.269449	1.582459	-3.668738	1.2914e+13	3.4729e+13	-9.6570e+12
O34	-2.667066	-0.951463	-1.285245	5.0859e+13	-3.6693e+13	5.3445e+13
H35	-1.945923	-1.378798	-1.773251	4.1758e+13	1.5556e+13	4.0982e+13
H36	-2.975856	-0.313072	-1.953317	-2.0467e+13	-2.1741e+13	1.4851e+13
O37	-3.332356	-3.980525	1.742434	3.2758e+13	4.0247e+13	-4.8055e+13
H38	-3.702059	-3.748919	0.863983	1.6089e+13	2.1847e+13	-1.2187e+13
H39	-4.005961	-4.501812	2.177641	1.5769e+12	2.8994e+13	-8.9399e+12
O40	-2.830828	1.223498	-2.701671	3.7239e+13	-8.4369e+13	2.0629e+12
H41	-2.542469	1.761848	-1.918960	2.2079e+13	-3.7944e+13	2.2446e+13
H42	-3.042422	1.660843	-3.533931	-4.5782e+13	-1.7913e+11	1.9616e+13
O43	-0.674715	0.164050	-3.919808	1.8474e+13	-3.1120e+13	6.7472e+13
H44	0.039883	0.791156	-4.105703	-6.9438e+12	-7.7190e+12	-2.7395e+13
H45	-1.372252	0.546252	-3.388715	-1.8675e+13	-3.4082e+13	-1.0393e+13
O46	1.806968	3.045177	1.226933	4.6638e+13	-2.5652e+13	-1.2568e+12
H47	1.934079	3.589169	0.428848	1.2508e+13	-2.7078e+13	6.9710e+11
H48	1.411598	2.241401	0.884162	9.9775e+12	-3.6909e+13	6.4288e+13
O49	-2.145550	2.365459	3.759294	8.0766e+13	2.0023e+13	3.4045e+13
H50	-1.256577	2.650977	3.506312	-5.1796e+12	5.3033e+13	-1.8880e+13
H51	-2.278465	1.431121	3.599503	-5.3741e+12	3.3646e+13	-4.3675e+13
O52	3.698864	-1.475419	-2.472680	-3.9737e+13	-9.2298e+13	4.3480e+12
H53	2.886810	-1.857996	-2.803094	1.6573e+13	-4.4481e+13	-1.0301e+13

Continuation of Table B.12						
State #11	Coordinates (Å)			MWV ($amu^2 * bohr/sec$)		
#atom	x	y	z	v_x	v_y	v_z
H54	4.380206	-2.063809	-2.794323	9.4534e+12	-1.1920e+12	-1.1711e+13
O55	1.520933	-0.053764	-0.188806	-6.3124e+13	4.9971e+13	-4.9800e+13
H56	2.370322	-0.383142	0.181558	-5.4186e+12	-3.3336e+13	1.5997e+13
H57	1.349345	-0.674981	-0.930120	4.0908e+13	1.1587e+13	5.3277e+12
O58	-0.764457	-3.239107	-2.077792	6.9670e+13	3.8245e+13	1.6587e+13
H59	-1.144115	-3.515497	-1.189779	-1.7940e+13	3.3545e+13	-9.7815e+12
H60	-0.930804	-3.936125	-2.709990	-2.0178e+13	2.2507e+12	1.2017e+13
O61	-3.658915	3.326214	1.747846	-1.4885e+13	5.0509e+13	2.4230e+13
H62	-4.507152	3.564589	2.121205	-1.1543e+13	2.4566e+12	-7.7484e+12
H63	-3.190897	2.745712	2.372779	-2.6132e+13	1.7704e+13	4.6757e+13
O64	-2.148729	-0.390044	3.141528	-3.9184e+13	2.8408e+13	-3.9555e+11
H65	-2.003499	-1.009781	3.853548	-6.3944e+13	7.1720e+12	4.9228e+12
H66	-1.530757	-0.568353	2.428273	1.1357e+13	6.9034e+12	1.8011e+13
O67	3.809742	-1.038215	0.603157	-5.4567e+13	1.9971e+13	4.4621e+13
H68	4.012038	-1.654620	-0.105943	1.6598e+13	1.1752e+13	-6.6971e+12
H69	4.513709	-0.415318	0.842488	2.0664e+13	-2.5670e+13	6.0764e+12
O70	1.742880	-3.166091	0.042814	-7.6729e+13	-7.7563e+12	-1.4341e+14
H71	2.453999	-3.597854	0.518907	-4.4132e+13	-1.7809e+13	-2.0609e+13
H72	0.906099	-3.473865	0.429650	-3.1019e+13	1.1293e+13	-2.0759e+13
O73	3.152408	1.153421	-2.135647	-6.5091e+13	4.5371e+13	-1.3413e+13
H74	2.599922	0.902680	-1.357503	3.2100e+12	-1.3596e+13	8.3706e+12
H75	3.700243	0.380433	-2.310390	-1.2719e+13	-3.2026e+12	1.6160e+13
O76	-4.301457	0.294570	1.049789	-1.7927e+12	-4.4984e+13	3.2257e+13
H77	-3.648236	-0.233546	1.529851	-1.1385e+13	-2.0184e+13	7.2533e+12

Continuation of Table B.12						
State #11	Coordinates (Å)			MWV ($amu^2 * bohr/sec$)		
#atom	x	y	z	v_x	v_y	v_z
H78	-4.676807	-0.377551	0.466731	-5.6854e+13	-1.2803e+13	2.6635e+13
O79	2.133926	1.361344	4.416481	-6.9334e+13	2.7410e+13	2.5248e+12
H80	1.412645	1.499862	5.037746	-2.9286e+13	-1.4361e+13	-4.3875e+12
H81	2.170992	2.193463	3.941912	-3.3584e+12	2.8611e+13	2.7988e+13
End of Table						

Table B.13: Vibrationally bound initial condition 12 of water $(H_2O)_{27}$ nanodroplet.

State #12	Coordinates (Å)			MWV ($amu^2 * bohr/sec$)		
#atom	x	y	z	v_x	v_y	v_z
O 1	-1.261732	4.419615	0.211043	8.4489e+11	-6.2346e+13	1.7207e+13
H 2	-2.200851	4.339855	0.421257	-6.8467e+12	3.0628e+13	5.1044e+12
H 3	-0.819426	4.775866	0.982065	4.8263e+13	-5.3937e+13	1.3683e+12
O 4	-1.638475	1.843919	-0.163058	2.9219e+13	3.3536e+13	2.0255e+13
H 5	-0.965694	2.536857	-0.084116	1.8071e+13	-1.4848e+13	1.3240e+13
H 6	-2.297029	2.093597	0.495197	-4.2487e+13	8.7186e+12	-6.0594e+13
O 7	-0.214683	-0.752583	-1.707085	4.1694e+13	-1.0343e+13	1.0876e+12
H 8	-0.365281	-1.672621	-1.955190	-1.0045e+12	3.1490e+11	-2.5616e+13
H 9	-0.796928	-0.205370	-2.269384	1.5107e+13	1.1085e+13	2.9188e+13
O10	2.125564	-3.123552	-1.624381	3.6697e+12	-5.2932e+13	4.9344e+13
H11	1.230766	-3.252241	-1.908529	2.2374e+13	-3.8090e+13	2.7703e+13
H12	2.119949	-3.134225	-0.630460	1.5092e+13	-3.3927e+12	1.6089e+13

Continuation of Table B.13						
State #12	Coordinates (Å)			MWV ($amu^2 * bohr/sec$)		
#atom	x	y	z	v_x	v_y	v_z
O13	4.998475	-0.146997	2.200114	-3.4203e+13	2.8067e+12	1.0887e+14
H14	4.884667	0.795155	2.358817	-2.0667e+13	9.9606e+12	-4.8947e+13
H15	5.133736	-0.602498	3.031970	-4.5253e+13	7.1667e+13	7.4512e+13
O16	0.427758	2.718306	3.071755	-3.4669e+13	5.2573e+13	3.2686e+13
H17	0.647062	3.588827	3.402509	-1.1422e+13	4.1393e+12	3.2296e+13
H18	0.997870	2.601530	2.228134	-9.2297e+12	4.4828e+13	2.6243e+13
O19	-0.640719	-3.220385	0.710095	-4.8753e+13	2.6327e+13	2.6261e+13
H20	-1.279751	-3.793617	1.167697	-3.2051e+13	-2.8107e+13	-8.5772e+12
H21	-1.059040	-2.361317	0.675565	-3.9937e+13	-9.9570e+12	-4.8591e+13
O22	-1.168527	-0.600736	0.847498	-1.6761e+13	-6.4303e+13	-6.6902e+12
H23	-0.211249	-0.544081	0.693065	2.4020e+13	-9.0326e+13	-2.2731e+13
H24	-1.379270	0.152749	0.237312	6.5328e+13	2.2771e+13	2.9906e+13
O25	-4.098430	-3.093560	-0.320016	1.3433e+13	-3.5219e+12	2.8818e+12
H26	-3.741411	-2.216956	-0.528199	-9.7927e+12	-2.4085e+13	-8.1127e+13
H27	-5.045531	-3.012922	-0.436416	6.7359e+12	1.4948e+13	-4.7936e+13
O28	3.045863	3.922088	-0.819636	-1.4213e+13	5.1775e+13	-7.1455e+13
H29	3.127440	3.185464	-1.453360	3.5657e+13	5.1550e+12	-1.5065e+12
H30	2.651342	4.691658	-1.224575	1.4334e+13	7.5046e+12	-4.5831e+13
O31	1.784686	0.655771	-4.202698	5.2259e+13	3.8347e+13	-6.4451e+12
H32	1.117718	0.307820	-3.609676	1.2609e+13	1.8687e+13	-1.0219e+13
H33	2.441323	1.003407	-3.572998	-1.0091e+13	2.0932e+13	3.1497e+13
O34	-2.837907	-0.978253	-1.861107	1.4697e+13	-5.2871e+13	-7.7883e+11
H35	-3.628260	-0.583822	-1.459203	1.9731e+13	2.8766e+13	-6.9139e+11
H36	-3.009209	-1.103094	-2.793144	1.9434e+13	1.6146e+13	-3.9868e+12

Continuation of Table B.13						
State #12	Coordinates (Å)			MWV ($amu^2 * bohr/sec$)		
#atom	x	y	z	v_x	v_y	v_z
O37	-2.641196	-4.455243	1.797237	-5.0296e+13	1.1374e+13	1.7818e+13
H38	-3.332609	-3.815928	1.541621	-5.9125e+12	2.0847e+13	2.0270e+13
H39	-3.002762	-5.142140	2.359258	-1.6271e+13	-1.3583e+13	-1.2787e+13
O40	-2.813070	2.049642	-2.866580	1.9075e+13	-4.1496e+13	2.1270e+12
H41	-2.450010	1.746625	-2.026955	3.3156e+12	2.2468e+13	-1.5514e+13
H42	-2.985005	2.982636	-2.780451	4.3858e+13	-1.4934e+12	-4.7584e+11
O43	-1.125548	0.795564	-4.167071	-3.1585e+13	2.1917e+13	-2.7047e+13
H44	-0.304757	1.138376	-4.526663	-5.7051e+12	2.9979e+13	-6.6635e+12
H45	-1.830439	1.455104	-4.033668	-1.2644e+12	8.6272e+12	6.2145e+12
O46	1.747128	2.213739	1.115639	2.7083e+13	5.7649e+13	9.5350e+12
H47	2.143991	2.839873	0.483497	6.9407e+12	8.8926e+12	3.2283e+12
H48	1.586732	1.371409	0.634512	3.2632e+12	1.4221e+13	1.7346e+13
O49	-2.063050	1.994057	3.457517	-2.3526e+13	2.5420e+13	4.0869e+13
H50	-1.110580	2.132820	3.309604	-1.7544e+13	3.6759e+13	3.6577e+13
H51	-2.430418	1.118559	3.304783	1.5554e+13	1.0498e+13	-1.2757e+13
O52	3.803657	-1.272502	-2.560771	-2.9995e+13	-8.7406e+12	-3.5484e+13
H53	3.268024	-2.086438	-2.311461	3.6231e+13	-1.9136e+13	2.2390e+13
H54	4.303704	-1.535603	-3.331688	-1.2877e+13	-2.7909e+12	-1.3895e+13
O55	1.595552	-0.081764	-0.121163	3.5189e+13	1.5716e+13	-4.5383e+13
H56	2.299124	-0.774668	0.053766	-3.7958e+13	5.6320e+12	-2.7191e+13
H57	1.017588	-0.302813	-0.875918	-4.9089e+11	4.0287e+13	4.5484e+12
O58	-1.082124	-3.171071	-2.076792	-6.1140e+13	-5.4734e+13	-6.9188e+13
H59	-1.071901	-3.618901	-1.204041	-1.2061e+13	-1.6027e+13	-1.1527e+13
H60	-1.984721	-2.842741	-2.141123	-1.4608e+11	2.6831e+13	2.0363e+13

Continuation of Table B.13						
State #12	Coordinates (Å)			MWV ($amu^2 * bohr/sec$)		
#atom	x	y	z	v_x	v_y	v_z
O61	-3.429975	3.236458	1.556260	-4.2734e+13	-2.1357e+13	-7.0787e+12
H62	-4.123670	3.852823	1.790486	3.2607e+13	4.8667e+13	-1.0232e+13
H63	-2.895880	3.042022	2.368064	-2.8294e+13	9.4552e+12	-1.8164e+13
O64	-2.142843	-0.951156	3.055030	1.8780e+13	2.2510e+12	4.6561e+13
H65	-1.770117	-1.074274	3.926913	2.2851e+13	-1.6478e+13	6.9468e+11
H66	-1.438495	-0.784158	2.391038	-7.6467e+12	-3.1560e+13	2.3356e+12
O67	3.844669	-1.294137	0.258070	9.2791e+13	2.3577e+13	-1.7359e+13
H68	4.346215	-1.154148	-0.555281	3.5129e+13	-3.7907e+13	-3.7847e+12
H69	4.347018	-0.826995	0.942520	3.5832e+12	-1.4822e+13	2.5801e+12
O70	1.933443	-3.354766	1.088214	4.8140e+13	2.2522e+13	-1.2072e+14
H71	2.263066	-2.657816	1.652791	3.5124e+13	-1.4671e+13	-2.1845e+13
H72	0.956369	-3.316614	1.074965	7.9129e+12	4.0207e+13	-4.2019e+13
O73	3.311317	1.400912	-1.897391	-6.9610e+13	-6.5673e+13	4.1440e+13
H74	2.745001	0.841153	-1.332935	2.8653e+13	-4.3337e+13	2.1680e+13
H75	3.933448	0.790179	-2.292989	1.1246e+13	1.5258e+13	3.9226e+13
O76	-4.058366	-0.167136	0.477602	-3.7877e+13	5.1775e+13	4.9572e+13
H77	-3.331692	-0.484138	1.044333	-3.2614e+13	1.6764e+13	3.2413e+13
H78	-4.683996	0.342239	0.997340	-8.0626e+13	-2.9260e+13	-3.5184e+13
O79	2.803295	1.207046	4.315764	4.9488e+13	-4.7757e+13	-3.5486e+13
H80	2.786973	0.799661	5.177366	4.4957e+13	-1.6843e+13	-5.7022e+12
H81	1.947128	1.654748	4.177318	3.5411e+13	4.2248e+13	3.3835e+13
End of Table						

Table B.14: Vibrationally bound initial condition 13 of water $(H_2O)_{27}$ nanodroplet.

State #13	Coordinates (Å)			MWV ($amu^2 * bohr/sec$)		
#atom	x	y	z	v_x	v_y	v_z
O 1	-0.931411	3.613283	1.075146	-8.8672e+13	8.4935e+12	1.3858e+13
H 2	-1.828246	3.978476	1.175127	-2.5848e+13	-5.6993e+10	3.9430e+13
H 3	-0.579032	3.626469	1.969923	-3.7975e+13	-2.1045e+13	1.3422e+13
O 4	-1.858922	1.290584	-0.347685	2.2818e+13	-2.8183e+13	-4.7176e+13
H 5	-1.509303	2.161204	-0.080464	-1.4809e+13	-1.8191e+13	-2.0404e+13
H 6	-2.734866	1.339101	0.076624	6.4458e+12	-2.2118e+13	-6.4837e+12
O 7	1.225639	-1.389483	-2.269109	3.1792e+13	-5.8146e+11	-1.5396e+13
H 8	0.535812	-2.065663	-2.233110	-3.2406e+12	-2.5060e+12	5.4218e+12
H 9	0.859829	-0.788527	-2.942409	2.5950e+13	-2.8913e+13	-4.7134e+13
O10	2.083724	-3.963047	-2.601149	3.5403e+13	-5.3555e+13	-3.3369e+13
H11	1.241952	-3.770309	-2.967332	1.2186e+13	-2.3600e+13	2.2325e+13
H12	1.906903	-3.773074	-1.642309	-1.3509e+13	-6.0254e+13	-7.8210e+12
O13	5.363083	-0.269825	2.407602	6.7340e+13	-1.7842e+13	1.5581e+13
H14	5.510452	0.592082	2.804041	-2.3643e+13	1.5875e+13	-3.0966e+13
H15	4.792951	-0.758651	3.005899	2.2984e+12	3.7880e+13	2.8883e+13
O16	0.494265	3.444668	3.348157	3.6768e+12	5.4612e+13	-2.2272e+13
H17	0.870471	4.140013	3.886520	3.4221e+13	-4.7452e+12	1.2488e+12
H18	1.099398	3.375430	2.545933	2.3366e+13	-2.7563e+13	3.7366e+13
O19	-0.932373	-3.152530	0.587769	4.1332e+12	-2.9841e+12	4.3818e+13
H20	-1.504685	-3.589507	1.216829	-4.0908e+13	6.9503e+11	-2.2930e+13
H21	-0.860924	-2.185718	0.813393	-6.3776e+13	1.4073e+13	5.1162e+13
O22	-0.506228	-0.686910	1.053571	6.8874e+13	3.2181e+13	-5.8532e+13

Continuation of Table B.14						
State #13	Coordinates (Å)			MWV ($amu^2 * bohr/sec$)		
#atom	x	y	z	v_x	v_y	v_z
H23	0.346017	-0.402330	0.633005	-7.6731e+12	3.6435e+13	-5.7261e+13
H24	-1.110710	-0.070456	0.579730	-1.8049e+13	4.6574e+12	-2.7657e+13
O25	-4.305659	-3.034714	-0.711660	-3.4366e+13	5.6269e+13	-5.3329e+12
H26	-3.609641	-2.413990	-1.035076	-3.2140e+12	-1.2818e+13	5.2891e+12
H27	-5.181621	-2.771304	-0.998929	-1.0187e+13	-6.3417e+13	-7.2684e+13
O28	2.532158	3.601823	-1.168711	-1.2908e+13	-2.2287e+13	1.7617e+13
H29	2.968955	2.878138	-1.661990	-3.5849e+13	5.4900e+12	-4.7436e+13
H30	2.099677	4.153692	-1.820911	-3.5909e+13	4.2989e+12	3.1729e+13
O31	1.719055	2.007130	-4.436044	-1.0097e+13	1.1012e+14	9.8115e+12
H32	2.293823	2.230809	-5.161126	8.7450e+12	-6.9703e+13	-1.1680e+13
H33	2.249488	1.711400	-3.663805	-9.7148e+12	1.9135e+13	-1.2259e+13
O34	-2.582909	-1.085089	-1.178265	3.3704e+13	-9.2706e+13	5.3274e+13
H35	-1.704173	-1.261348	-1.542220	1.4788e+13	7.7480e+12	9.4502e+12
H36	-2.869959	-0.383112	-1.781854	3.8148e+13	-1.3921e+13	1.6375e+13
O37	-3.253885	-3.886892	1.634361	4.5850e+13	5.1872e+13	-5.7619e+13
H38	-3.667057	-3.622394	0.786216	-1.7909e+13	1.8301e+13	-2.5048e+12
H39	-3.942009	-4.337948	2.123796	1.4663e+13	1.2973e+13	-1.0389e+13
O40	-2.765245	1.065256	-2.711794	2.4908e+13	-5.6358e+13	-5.3288e+12
H41	-2.358547	1.293940	-1.835032	4.1431e+13	-1.0096e+14	1.3849e+13
H42	-3.366778	1.781208	-2.923306	-3.7045e+13	-1.1838e+13	8.6472e+13
O43	-0.587640	0.086430	-3.782446	5.7844e+13	-2.2252e+13	6.6588e+13
H44	-0.185423	0.788793	-4.312093	9.2129e+12	-3.5217e+13	-2.6419e+13
H45	-1.416017	0.523591	-3.479490	-9.9039e+11	-4.2314e+13	-7.2568e+12
O46	1.895219	2.980848	1.257212	3.8421e+13	-4.9721e+13	2.1168e+13

Continuation of Table B.14						
State #13	Coordinates (Å)			MWV ($amu^2 * bohr/sec$)		
#atom	x	y	z	v_x	v_y	v_z
H47	2.038506	3.210092	0.300143	1.4956e+13	-2.0605e+13	6.4213e+11
H48	1.664469	2.050758	1.168999	5.0724e+13	-1.3283e+13	2.6909e+13
O49	-2.013433	2.406121	3.797643	6.8473e+13	9.0582e+12	-1.3907e+12
H50	-1.144122	2.777693	3.587793	2.0310e+13	3.3500e+13	6.3338e+13
H51	-1.951298	1.452864	3.549374	4.2023e+11	2.4252e+12	3.9084e+13
O52	3.672593	-1.648425	-2.458267	6.7578e+12	-6.9388e+13	1.6550e+13
H53	2.837885	-2.166047	-2.579712	2.8602e+13	-3.9368e+13	4.5717e+13
H54	4.391314	-2.087487	-2.907402	-2.0720e+13	-3.0429e+13	-2.4218e+13
O55	1.458211	0.044741	-0.236088	-7.3566e+12	5.6763e+13	2.8858e+12
H56	2.207952	-0.303460	0.305619	-2.6981e+12	3.4402e+13	-4.7626e+13
H57	1.274992	-0.596806	-0.987911	-1.3748e+13	-1.0264e+13	-2.9488e+12
O58	-0.658450	-3.166415	-2.049241	4.3019e+13	4.1511e+13	1.4716e+13
H59	-0.841912	-3.244259	-1.105139	5.0548e+13	-5.4881e+12	2.4021e+13
H60	-1.215729	-3.763012	-2.536533	-5.0716e+13	3.7238e+13	4.1704e+13
O61	-3.668830	3.413837	1.810849	5.6798e+12	4.4630e+13	3.9871e+13
H62	-4.600403	3.626237	1.843899	-1.7597e+12	6.5539e+12	-4.6637e+13
H63	-3.254954	3.247706	2.671184	2.0021e+12	5.7018e+13	1.0869e+13
O64	-2.246287	-0.314557	3.127742	-4.3588e+13	3.8704e+13	-1.1596e+13
H65	-2.489477	-0.944565	3.814209	-5.9397e+13	2.0623e+13	-1.0721e+13
H66	-1.362334	-0.583999	2.765102	-1.7706e+13	-9.1314e+11	2.0840e+13
O67	3.702534	-1.030173	0.646934	-5.8397e+13	-9.8590e+12	4.0523e+12
H68	3.843425	-1.305101	-0.262908	-4.3313e+13	5.9782e+13	-2.3159e+13
H69	4.443831	-0.657810	1.155209	-3.4166e+13	-1.7603e+13	3.6935e+13
O70	1.586566	-3.185030	-0.224596	-7.7589e+13	-6.7065e+12	-1.2867e+14

Continuation of Table B.14						
State #13	Coordinates (Å)			MWV ($amu^2 * bohr/sec$)		
#atom	x	y	z	v_x	v_y	v_z
H71	2.125698	-3.648111	0.423020	-5.3418e+13	9.5999e+12	5.6145e+12
H72	0.664141	-3.282733	0.057338	-1.3249e+13	-1.7187e+12	-2.6553e+13
O73	3.028543	1.218629	-2.139247	-6.1914e+13	1.8110e+13	-3.8643e+12
H74	2.342601	0.976442	-1.497171	-4.3239e+13	1.7446e+13	-1.6682e+13
H75	3.448892	0.389574	-2.421001	-4.8231e+13	8.1789e+12	-1.2235e+13
O76	-4.277621	0.199024	1.110506	2.3684e+13	-3.5776e+13	3.3035e+13
H77	-3.864652	-0.311173	1.819505	-2.7919e+13	-3.3727e+12	2.8178e+13
H78	-4.956031	-0.356436	0.741148	-1.8579e+13	-2.7725e+13	4.2701e+13
O79	2.013554	1.412737	4.436990	-5.2264e+13	2.1611e+13	1.7978e+13
H80	1.156524	1.317686	4.856476	-3.6766e+13	-3.1817e+13	-3.3748e+13
H81	1.937983	2.266009	4.017697	-5.1868e+13	-4.2913e+12	-1.4519e+13
End of Table						

Table B.15: Vibrationally bound initial condition 14 of water $(H_2O)_{27}$ nanodroplet.

State #14	Coordinates (Å)			MWV ($amu^2 * bohr/sec$)		
#atom	x	y	z	v_x	v_y	v_z
O 1	-1.145884	3.634358	1.078667	-1.1116e+14	2.4611e+12	-2.2363e+13
H 2	-2.084341	3.735585	1.282768	-3.8144e+13	-4.8171e+13	2.1879e+13
H 3	-0.691500	3.470968	1.904022	-3.2998e+13	-3.8178e+12	-2.4205e+11
O 4	-1.844366	1.274070	-0.408373	7.0073e+12	2.6163e+12	-3.2790e+12
H 5	-1.405787	2.015095	0.106400	-1.0181e+13	-1.1461e+13	4.6078e+13

Continuation of Table B.15						
State #14	Coordinates (Å)			MWV ($amu^2 * bohr/sec$)		
#atom	x	y	z	v_x	v_y	v_z
H 6	-2.553609	0.972045	0.185967	1.4978e+13	-1.5917e+13	3.1217e+12
O 7	1.242570	-1.363884	-2.320918	-5.9270e+11	2.6830e+13	-2.7241e+13
H 8	0.591692	-2.075866	-2.194327	1.8535e+13	7.7284e+12	9.5354e+10
H 9	0.853752	-0.839973	-3.029118	-3.8746e+13	1.3241e+13	2.4191e+13
O10	2.162997	-4.084790	-2.681622	4.3889e+13	-7.2684e+13	-6.2483e+13
H11	1.293387	-4.043958	-3.090500	3.9041e+13	-3.5465e+13	-3.2209e+12
H12	1.982306	-4.154693	-1.736676	-1.1297e+13	-2.2061e+13	-1.2811e+12
O13	5.479758	-0.291489	2.468323	5.1054e+13	-3.1232e+12	2.9915e+13
H14	5.427965	0.660919	2.347035	-3.0098e+11	-8.8325e+12	-5.1917e+13
H15	4.953477	-0.560033	3.220754	2.9311e+13	2.8000e+13	2.9357e+13
O16	0.549158	3.548913	3.309612	4.2552e+13	4.3063e+13	-1.9168e+13
H17	0.879653	4.284808	3.818053	-6.1823e+12	3.8360e+13	-3.4647e+13
H18	1.067659	3.471718	2.464362	-4.3017e+12	5.3955e+13	-1.9003e+13
O19	-0.931712	-3.150652	0.674242	7.5725e+12	-1.6328e+12	2.7283e+13
H20	-1.774812	-3.624367	0.867062	-1.3055e+13	3.5330e+13	-9.6860e+12
H21	-0.879785	-2.161385	0.880740	2.8654e+13	-1.7277e+13	-1.3037e+13
O22	-0.455258	-0.617347	0.965641	-1.8635e+13	1.4138e+13	-7.0261e+12
H23	0.399914	-0.243429	0.563509	2.2291e+12	2.6086e+13	3.8232e+12
H24	-1.157642	-0.165735	0.521875	2.4487e+13	1.8942e+13	-5.0446e+13
O25	-4.379320	-2.938916	-0.713978	-4.6369e+13	4.6986e+13	-2.6715e+12
H26	-3.758196	-2.202777	-0.921908	8.7324e+12	2.5953e+13	3.2272e+13
H27	-4.858623	-3.224845	-1.492118	7.2599e+13	-6.0211e+13	-2.9240e+13
O28	2.506051	3.574611	-1.151486	-1.6483e+13	1.8884e+12	1.6357e+13
H29	2.744949	2.883223	-1.778514	-2.0121e+13	1.5512e+12	-6.2702e+12

Continuation of Table B.15						
State #14	Coordinates (Å)			MWV ($amu^2 * bohr/sec$)		
#atom	x	y	z	v_x	v_y	v_z
H30	1.792042	4.120535	-1.474997	-3.1943e+13	-2.3655e+13	2.1599e+13
O31	1.702802	2.208279	-4.429105	-5.1697e+12	8.6584e+13	-5.6435e+12
H32	2.177518	1.767137	-5.135460	-3.9302e+13	-2.9216e+13	1.9340e+13
H33	2.074027	1.870803	-3.587454	-3.1674e+13	1.8656e+13	3.0154e+13
O34	-2.511444	-1.285957	-1.097000	1.8993e+13	-1.1038e+14	4.5019e+13
H35	-1.645450	-1.584055	-1.397232	-8.4181e+11	-3.6799e+13	-1.6228e+13
H36	-2.857496	-0.612478	-1.713559	5.7959e+13	-1.9890e+13	-2.5048e+13
O37	-3.191817	-3.774770	1.507633	1.8135e+13	6.1948e+13	-6.7152e+13
H38	-3.796747	-3.500147	0.788294	-3.3042e+13	-7.8203e+12	3.0203e+12
H39	-3.638901	-4.350480	2.127292	4.7321e+13	-1.2936e+13	-7.9356e+12
O40	-2.727559	0.951080	-2.692265	1.3671e+13	-6.1647e+13	2.7253e+13
H41	-2.102293	1.173592	-1.927086	2.5087e+13	3.3206e+13	-3.3657e+13
H42	-3.463428	1.496434	-2.431539	-1.5594e+13	-4.0791e+13	7.1240e+12
O43	-0.448124	0.038208	-3.673805	7.7419e+13	-2.5214e+13	3.6039e+13
H44	-0.023893	0.632370	-4.303700	2.7658e+13	1.4047e+13	3.0120e+13
H45	-1.376551	0.334163	-3.718251	8.1695e+12	-4.1533e+12	-3.1908e+13
O46	1.970744	2.850285	1.325148	3.8662e+13	-7.4377e+13	5.1524e+13
H47	2.154955	3.227964	0.445904	1.6992e+13	-2.2390e+13	8.9493e+12
H48	2.048459	1.899056	1.160933	3.5662e+13	-1.6115e+11	-3.7886e+13
O49	-1.900528	2.452256	3.802630	4.7514e+13	3.1108e+13	1.1451e+13
H50	-0.994107	2.629922	4.060691	1.1979e+13	-2.6506e+13	2.5896e+13
H51	-1.921422	1.489057	3.682493	-7.7946e+11	-1.3055e+13	-1.0035e+13
O52	3.726781	-1.771136	-2.416483	4.8816e+13	-5.3750e+13	2.8721e+13
H53	2.935708	-2.330511	-2.292078	-2.8673e+13	-6.0789e+11	9.9838e+12

Continuation of Table B.15						
State #14	Coordinates (Å)			MWV ($amu^2 * bohr/sec$)		
#atom	x	y	z	v_x	v_y	v_z
H54	4.342457	-2.254473	-2.959129	1.5523e+13	-9.4572e+12	7.0449e+12
O55	1.482411	0.165186	-0.265619	3.4232e+13	6.3047e+13	-3.9077e+13
H56	2.299182	-0.160493	0.210016	1.9597e+13	-5.6790e+12	3.9639e+13
H57	1.333428	-0.472060	-1.066331	-5.6328e+12	2.8666e+13	-1.3100e+13
O58	-0.611669	-3.111110	-1.991312	-6.1006e+12	9.3525e+12	4.3863e+13
H59	-0.700916	-3.281004	-0.999643	-8.2225e+12	3.6128e+12	-6.6539e+12
H60	-1.480947	-3.255594	-2.376012	4.4687e+12	8.5562e+13	-5.9794e+12
O61	-3.626128	3.515898	1.869492	1.9022e+13	5.3180e+13	4.2675e+13
H62	-4.571541	3.656730	1.834407	8.9462e+11	9.9892e+12	-1.4115e+13
H63	-3.440873	3.233998	2.780305	1.7780e+13	-4.0379e+13	-1.4151e+13
O64	-2.339559	-0.226571	3.107863	-5.1588e+13	4.9841e+13	-1.0546e+13
H65	-2.636070	-0.879349	3.742151	1.6338e+13	-1.3317e+13	-2.5643e+12
H66	-1.631295	-0.638086	2.581412	-2.5395e+13	-5.6178e+12	-5.7105e+13
O67	3.550453	-1.050048	0.620199	-5.5747e+13	1.1367e+10	-4.2916e+13
H68	3.922749	-1.123519	-0.272807	-2.3402e+13	-5.3613e+13	-3.7950e+12
H69	4.324668	-0.743339	1.127022	-3.9936e+13	-1.9954e+13	5.9215e+13
O70	1.429327	-3.223198	-0.411067	-7.6111e+13	-2.9713e+13	-4.9992e+13
H71	2.077357	-3.228061	0.307179	3.3307e+13	9.7183e+13	-5.0905e+13
H72	0.556883	-3.215101	0.034182	9.3650e+11	1.8752e+12	1.5719e+13
O73	2.882508	1.229768	-2.173060	-8.5897e+13	-1.4788e+13	-2.5977e+13
H74	2.205643	1.074541	-1.479434	1.0805e+13	2.2038e+13	1.3740e+13
H75	3.227390	0.338669	-2.397651	-1.1404e+12	-1.9859e+11	-6.8929e+11
O76	-4.238593	0.124825	1.173054	2.6876e+13	-2.3364e+13	2.5483e+13
H77	-3.670792	-0.059906	1.937622	2.7525e+13	2.9371e+13	-3.6035e+12

Continuation of Table B.15						
State #14	Coordinates (Å)			MWV ($amu^2 * bohr/sec$)		
#atom	x	y	z	v_x	v_y	v_z
H78	-4.892337	-0.532906	0.991929	3.6850e+13	-4.8532e+13	4.6359e+13
O79	1.895206	1.450624	4.478709	-6.6813e+13	1.4657e+13	1.7796e+13
H80	1.133784	0.891576	4.618485	2.9829e+13	-6.8833e+13	-1.9271e+13
H81	1.577065	2.148415	3.894887	-4.2069e+13	-1.4126e+13	3.8098e+12
End of Table						

Table B.16: Vibrationally bound initial condition 15 of water $(H_2O)_{27}$ nanodroplet.

State #15	Coordinates (Å)			MWV ($amu^2 * bohr/sec$)		
#atom	x	y	z	v_x	v_y	v_z
O 1	-1.356480	3.590117	1.020817	-9.5312e+13	-4.4812e+13	-4.1037e+13
H 2	-2.313126	3.721332	1.164690	-8.9980e+11	4.7891e+13	-2.6634e+13
H 3	-0.911875	3.573514	1.875923	-2.6271e+13	2.1283e+13	-1.7419e+13
O 4	-1.813747	1.300600	-0.328872	1.4856e+13	2.0226e+13	5.5662e+13
H 5	-1.608959	2.136460	0.147796	-4.1981e+13	1.8826e+13	3.9488e+12
H 6	-2.731153	1.047729	-0.127679	-1.5653e+13	4.6246e+13	-1.8127e+13
O 7	1.240585	-1.285109	-2.351962	-3.1256e+12	4.1268e+13	5.8471e+12
H 8	0.842910	-2.119260	-2.029980	4.0497e+13	-2.6724e+12	2.6005e+13
H 9	0.490382	-0.785319	-2.791383	-2.5736e+13	-2.2398e+13	1.9427e+13
O10	2.258195	-4.244777	-2.794600	4.0891e+13	-8.0406e+13	-5.5385e+13
H11	1.458540	-4.250038	-3.359207	3.7373e+13	-2.3876e+13	-3.8698e+13
H12	1.957709	-4.118085	-1.890378	7.6180e+12	1.8144e+13	-3.0871e+13

Continuation of Table B.16						
State #15	Coordinates (Å)			MWV ($amu^2 * bohr/sec$)		
#atom	x	y	z	v_x	v_y	v_z
O13	5.544497	-0.301753	2.508299	9.3027e+12	1.2862e+12	2.2004e+13
H14	5.515287	0.591527	2.153570	3.3528e+13	-1.3391e+13	-3.9247e+13
H15	5.328305	-0.181670	3.436811	6.8683e+13	2.5118e+13	1.3926e+13
O16	0.640729	3.650233	3.265903	3.8432e+13	4.9564e+13	-2.5879e+13
H17	0.732178	4.544577	3.585937	-7.6503e+12	1.9867e+13	-4.0475e+13
H18	1.212796	3.378574	2.477811	4.0733e+13	-4.2466e+13	3.6472e+13
O19	-0.887452	-3.150276	0.685939	2.5431e+13	9.2656e+12	-9.5273e+11
H20	-1.728943	-3.301425	1.138699	1.3455e+13	-6.1462e+12	2.5937e+13
H21	-0.690335	-2.202839	0.781629	5.2695e+13	9.7554e+12	-2.0205e+13
O22	-0.539252	-0.579933	0.964740	-5.2299e+13	2.4562e+13	-2.8577e+12
H23	0.382642	-0.317756	0.853284	-3.6807e+13	-2.3537e+13	5.8822e+13
H24	-1.020452	-0.124337	0.234535	-1.6246e+12	1.0029e+13	2.5294e+13
O25	-4.489303	-2.861805	-0.708881	-4.3811e+13	2.1580e+13	-4.5194e+12
H26	-3.661216	-2.298185	-0.799447	-3.1358e+13	1.1915e+13	3.8806e+13
H27	-4.272309	-3.507019	-1.385339	1.4679e+13	-3.3248e+13	5.1238e+13
O28	2.457975	3.599302	-1.108866	-2.9934e+13	2.0700e+13	2.3084e+13
H29	2.817861	2.929774	-1.710898	2.6771e+13	4.1360e+12	3.3572e+13
H30	1.618424	3.911360	-1.445585	-1.1768e+13	-2.5025e+13	-6.5481e+12
O31	1.665323	2.343065	-4.422279	-2.9388e+13	4.0721e+13	1.2205e+13
H32	2.023605	1.715722	-5.061382	-1.2958e+13	3.1504e+13	-1.4595e+13
H33	2.008374	2.009950	-3.586276	1.2846e+13	3.1530e+13	-3.9258e+12
O34	-2.462697	-1.453702	-1.065658	3.2423e+13	-6.1334e+13	-3.1683e+11
H35	-1.616267	-1.902064	-1.109259	9.8763e+12	-1.3800e+12	6.6274e+13
H36	-2.530549	-0.621047	-1.561718	1.5997e+13	-5.8588e+12	3.2284e+13

Continuation of Table B.16						
State #15	Coordinates (Å)			MWV ($amu^2 * bohr/sec$)		
#atom	x	y	z	v_x	v_y	v_z
O37	-3.211343	-3.653608	1.388198	-3.4147e+13	5.6793e+13	-4.5456e+13
H38	-3.883404	-3.638475	0.665555	1.7989e+13	5.3501e+11	-3.0158e+13
H39	-3.228330	-4.443264	1.925230	3.6915e+13	-1.1271e+13	-4.2391e+13
O40	-2.696965	0.815944	-2.650713	1.5623e+13	-7.5506e+13	9.7294e+12
H41	-2.222554	1.354392	-1.994135	-5.2600e+13	1.3039e+13	3.4414e+13
H42	-3.598681	1.134664	-2.640856	3.3504e+12	-5.2012e+13	-4.8307e+13
O43	-0.311281	0.036702	-3.665573	6.9640e+13	1.7943e+13	-1.8425e+13
H44	0.196569	0.845336	-3.857797	-1.9381e+13	3.9227e+13	5.9954e+13
H45	-1.243296	0.250910	-3.655892	1.5834e+13	2.3339e+13	2.6365e+13
O46	2.073403	2.706133	1.386578	6.0450e+13	-6.3034e+13	2.5088e+13
H47	2.273241	3.185056	0.549808	1.1165e+13	-3.8734e+13	-1.3556e+12
H48	1.935328	1.769779	1.186600	-5.1352e+13	-1.2518e+13	-6.5997e+11
O49	-1.833419	2.477743	3.822959	1.1587e+13	1.0451e+13	6.4721e+12
H50	-0.909889	2.724880	3.945601	3.7292e+12	1.0034e+13	-5.8955e+13
H51	-1.907939	1.540817	3.657507	4.7950e+13	-4.2358e+12	2.1173e+13
O52	3.827992	-1.857532	-2.320753	4.7817e+13	-4.5115e+13	5.3483e+13
H53	2.975497	-2.086905	-2.690200	2.5544e+13	7.3677e+13	-4.8514e+13
H54	4.421240	-2.456005	-2.773839	2.2843e+13	-1.9731e+13	5.1662e+13
O55	1.567538	0.279131	-0.322410	4.3619e+13	2.6151e+13	-1.2803e+13
H56	2.288692	-0.223798	0.105916	4.4466e+12	5.2249e+13	-3.3521e+13
H57	1.320719	-0.350510	-1.055202	-1.4939e+13	5.2986e+13	2.7838e+11
O58	-0.657869	-3.103468	-1.916770	-3.7698e+13	9.3716e+11	2.1686e+13
H59	-0.918376	-3.373530	-1.032843	-1.8032e+13	-4.0754e+13	1.0444e+13
H60	-1.383114	-2.987611	-2.536560	1.8598e+13	-2.8557e+13	-2.3671e+13

Continuation of Table B.16						
State #15	Coordinates (Å)			MWV ($amu^2 * bohr/sec$)		
#atom	x	y	z	v_x	v_y	v_z
O61	-3.596537	3.613550	1.970739	6.7911e+12	4.5658e+13	5.6606e+13
H62	-4.543357	3.569511	1.857365	-2.9465e+12	-3.8994e+13	2.8272e+13
H63	-3.359101	3.048832	2.728471	-2.7095e+12	7.4198e+12	1.4297e+13
O64	-2.414214	-0.153443	3.065200	-1.9931e+13	3.8068e+13	-3.4106e+13
H65	-2.425990	-0.899969	3.657389	4.1824e+13	-2.8457e+12	-2.6612e+13
H66	-1.740799	-0.298247	2.370532	2.4677e+12	4.7853e+13	2.6198e+13
O67	3.454313	-1.061186	0.532660	-2.7486e+13	-3.3297e+13	-4.2035e+13
H68	3.936356	-1.551821	-0.165876	2.5343e+12	-1.5736e+13	1.3983e+13
H69	4.094376	-1.137733	1.261141	-3.0860e+13	-3.3789e+13	-1.5017e+13
O70	1.339281	-3.271734	-0.448647	-1.3041e+13	-1.9560e+13	-2.3843e+12
H71	1.927328	-2.524053	-0.327316	-6.0123e+13	5.0765e+13	-5.9574e+13
H72	0.834029	-3.506337	0.345432	6.0742e+13	-3.9615e+13	3.0156e+13
O73	2.718502	1.199532	-2.252516	-7.0841e+13	-1.4455e+13	-4.9693e+13
H74	2.355844	0.985485	-1.349839	-4.5360e+12	-4.3604e+12	-1.9063e+12
H75	3.220645	0.406628	-2.467539	1.2826e+13	1.3547e+13	-4.3474e+13
O76	-4.175520	0.084563	1.211227	3.4324e+13	-2.7552e+13	1.7753e+13
H77	-3.616420	0.183014	2.004692	-1.0139e+13	5.2075e+13	8.7865e+12
H78	-4.442628	-0.835370	1.190797	5.7182e+13	-4.6191e+12	-2.8182e+13
O79	1.765299	1.458639	4.511592	-6.0728e+13	-3.2189e+12	1.7077e+13
H80	1.455679	0.566300	4.389319	2.7261e+13	-4.1588e+12	-4.3718e+13
H81	1.177569	2.108599	4.089670	-4.2477e+13	-9.2878e+12	4.1231e+13
End of Table						

Table B.17: Vibrationally bound initial condition 16 of water $(H_2O)_{27}$ nanodroplet.

State #16	Coordinates (Å)			MWV ($amu^2 * bohr/sec$)		
#atom	x	y	z	v_x	v_y	v_z
O 1	-1.275673	4.543660	0.183835	1.6029e+13	-5.7232e+13	9.6466e+12
H 2	-2.066292	4.070751	0.497597	-1.6924e+13	7.9821e+12	-2.3418e+13
H 3	-1.063704	5.174981	0.875409	1.2329e+13	-4.4267e+13	2.9865e+13
O 4	-1.704554	1.788804	-0.199776	3.8721e+13	2.3823e+13	3.0285e+13
H 5	-1.104311	2.522674	-0.356513	1.1731e+13	9.8192e+12	1.7250e+13
H 6	-2.222394	1.970390	0.581241	6.4693e+12	-1.4625e+13	2.3572e+13
O 7	-0.257198	-0.699433	-1.749202	7.8828e+11	-3.3696e+13	3.2724e+13
H 8	-0.667504	-1.604465	-1.714253	5.2227e+13	-3.5256e+13	-3.8657e+12
H 9	-0.697249	-0.244843	-2.478751	-3.2019e+13	-2.9524e+13	3.3924e+13
O10	2.105184	-3.002209	-1.717139	1.6682e+13	-7.1818e+13	4.9601e+13
H11	1.212596	-3.020725	-2.029355	-3.5099e+12	-9.3494e+12	-1.3011e+13
H12	2.095164	-3.201956	-0.766509	5.5551e+12	1.0150e+13	7.6452e+12
O13	5.092209	-0.134939	2.014768	-5.6323e+13	-1.1082e+13	6.9143e+13
H14	4.777361	0.425052	2.739892	4.5452e+13	7.2342e+13	-1.7013e+13
H15	5.429437	-0.943108	2.413907	-3.7964e+13	1.8809e+13	8.6459e+13
O16	0.489137	2.593917	3.038265	-1.9861e+13	7.6552e+13	-9.2396e+11
H17	0.686785	3.509385	3.235844	-8.9684e+11	1.6346e+13	5.3318e+12
H18	0.985210	2.429571	2.134851	-4.1980e+12	-9.3745e+12	1.5962e+13
O19	-0.567078	-3.262683	0.653505	-2.7356e+13	1.1672e+13	2.5375e+13
H20	-1.195423	-3.754991	1.256819	2.9471e+13	-8.9899e+12	5.7274e+12
H21	-0.641650	-2.297665	0.836843	-2.9165e+13	1.6104e+13	5.6250e+12
O22	-1.103462	-0.457980	0.841824	-5.0156e+13	-6.8113e+13	5.8320e+12

Continuation of Table B.17						
State #16	Coordinates (Å)			MWV ($amu^2 * bohr/sec$)		
#atom	x	y	z	v_x	v_y	v_z
H23	-0.222973	-0.021801	0.639008	5.5384e+12	-4.1301e+13	2.7542e+13
H24	-1.561760	-0.107013	0.054402	-4.9793e+13	2.8544e+13	4.3809e+13
O25	-4.110358	-3.093365	-0.296375	9.1600e+12	3.4675e+12	-3.3248e+13
H26	-3.846278	-2.212224	-0.047072	1.1356e+12	-1.4604e+12	-2.1356e+13
H27	-5.048353	-3.033541	-0.095405	-2.3695e+12	2.3740e+13	-2.4758e+13
O28	3.050138	3.798482	-0.665391	1.1413e+13	6.8338e+13	-8.0722e+13
H29	3.198810	3.194209	-1.409217	-6.0489e+13	-3.0718e+12	-1.5490e+13
H30	2.533911	4.547103	-0.958461	1.2683e+13	2.1053e+13	-2.8155e+13
O31	1.651055	0.578058	-4.188231	7.7282e+13	4.4125e+13	-1.0216e+13
H32	1.252427	-0.001071	-3.538253	-3.3925e+13	4.0674e+13	-5.0148e+11
H33	2.396817	0.978875	-3.712815	1.8168e+13	-2.0709e+13	7.2258e+12
O34	-2.901985	-0.887645	-1.871504	4.7425e+13	-3.9421e+13	1.3682e+13
H35	-3.625318	-0.441970	-1.410201	-1.6966e+13	-4.8968e+13	-1.3737e+13
H36	-3.134787	-0.933318	-2.796377	2.4936e+12	-5.1594e+13	2.1940e+12
O37	-2.555592	-4.466089	1.762580	-3.7711e+13	-3.6606e+11	2.0136e+13
H38	-3.246656	-4.218299	1.120526	-2.2982e+13	7.2046e+13	7.2344e+13
H39	-2.886970	-5.004305	2.480067	-5.4549e+12	-1.9304e+13	-1.4716e+13
O40	-2.869148	2.131211	-2.844289	3.2943e+13	-4.6054e+13	-3.3635e+13
H41	-2.527255	1.863140	-1.988420	1.2090e+13	-1.4251e+13	1.2934e+13
H42	-3.286008	2.971916	-2.655848	3.2460e+13	7.3096e+12	3.5206e+12
O43	-1.047267	0.706274	-4.110601	-4.6348e+13	4.8779e+13	-2.7240e+13
H44	-0.269231	1.063245	-4.563690	-1.9329e+13	3.4838e+13	-4.9721e+12
H45	-1.607298	1.453892	-3.857112	-1.1571e+13	1.4489e+13	-5.0757e+13
O46	1.714614	2.102747	1.040161	3.2116e+12	5.0152e+13	5.6057e+13

Continuation of Table B.17						
State #16	Coordinates (Å)			MWV ($amu^2 * bohr/sec$)		
#atom	x	y	z	v_x	v_y	v_z
H47	2.191727	2.793111	0.547146	-2.0957e+13	1.7480e+13	8.2471e+11
H48	1.701012	1.237687	0.539727	-2.8912e+12	6.0852e+12	2.7423e+13
O49	-2.034298	1.943785	3.354544	-1.6565e+13	4.0452e+13	6.3578e+13
H50	-1.047094	2.128298	3.202252	9.6927e+12	-7.7787e+13	-1.8825e+13
H51	-2.214505	1.000581	3.412716	-2.0441e+13	7.1155e+12	-1.2636e+13
O52	3.863722	-1.247648	-2.477370	-2.7287e+13	-3.1938e+13	-4.8071e+13
H53	3.064983	-1.788039	-2.359406	-3.8975e+12	-4.1900e+11	-8.4160e+12
H54	4.330698	-1.614410	-3.226926	1.0519e+13	2.8771e+13	-2.1627e+13
O55	1.526317	-0.117079	-0.033983	3.1810e+13	1.4746e+13	-4.4040e+13
H56	2.401174	-0.581062	0.121403	4.4890e+13	2.3118e+13	-5.0946e+11
H57	0.977702	-0.539308	-0.765307	2.0876e+12	-1.6927e+13	-4.7844e+12
O58	-0.959181	-3.098804	-1.936574	-6.4047e+13	-1.9767e+13	-7.4268e+13
H59	-0.900786	-3.289482	-0.971493	-1.3223e+13	-3.9402e+13	-4.6343e+13
H60	-1.895075	-3.059397	-2.140427	-1.3359e+13	3.1163e+13	-2.1019e+13
O61	-3.327400	3.283503	1.592288	-5.0135e+13	-1.0835e+13	-3.6540e+13
H62	-4.253153	3.368011	1.831138	-4.2889e+12	4.8636e+13	2.6068e+13
H63	-2.927411	2.764523	2.357681	-1.3462e+13	2.0593e+13	2.9655e+13
O64	-2.214642	-0.927797	2.999669	5.6905e+13	-2.7741e+13	9.7054e+12
H65	-1.823241	-1.088542	3.854591	-1.9245e+13	2.4701e+13	2.2901e+13
H66	-1.571805	-0.680862	2.319507	1.8221e+13	1.5772e+13	1.4444e+13
O67	3.662023	-1.330336	0.273744	1.0201e+14	1.0950e+13	-2.6244e+12
H68	3.968280	-1.248997	-0.645593	3.6700e+12	4.9980e+13	-2.8252e+12
H69	4.182318	-0.753517	0.884241	1.4866e+12	-6.5008e+12	5.5841e+13
O70	1.853420	-3.405239	1.315730	2.1668e+13	3.0645e+13	-1.1029e+14

Continuation of Table B.17						
State #16	Coordinates (Å)			MWV ($amu^2 * bohr/sec$)		
#atom	x	y	z	v_x	v_y	v_z
H71	2.111598	-2.537871	1.623964	6.2271e+12	-1.5538e+13	3.0186e+13
H72	0.882000	-3.466289	1.295153	8.8340e+12	-6.5489e+12	3.4083e+12
O73	3.424899	1.510270	-1.990347	-3.9555e+13	-2.9692e+13	5.0832e+13
H74	2.693378	1.224798	-1.426042	-4.9475e+12	-6.5091e+13	1.2369e+12
H75	3.795220	0.657318	-2.252893	-1.6721e+12	-5.9661e+12	-3.1177e+13
O76	-3.960565	-0.269622	0.413057	-5.9113e+13	4.9450e+13	1.3389e+13
H77	-3.201560	-0.699497	0.810500	-1.5425e+13	4.1651e+13	1.0155e+13
H78	-4.143170	0.516174	0.932021	-3.3987e+13	-1.8147e+13	4.8087e+13
O79	2.689494	1.300954	4.378121	5.5832e+13	-4.0736e+13	-2.6526e+13
H80	2.399707	0.974789	5.228786	5.8331e+13	-3.1315e+13	5.0320e+12
H81	1.920210	1.439939	3.809932	-5.6286e+12	-1.2508e+13	3.5891e+13
End of Table						

Table B.18: Vibrationally bound initial condition 17 of water $(H_2O)_{27}$ nanodroplet.

State #17	Coordinates (Å)			MWV ($amu^2 * bohr/sec$)		
#atom	x	y	z	v_x	v_y	v_z
O 1	-1.239269	4.321701	0.242511	1.8662e+13	-3.4015e+13	2.9599e+13
H 2	-2.067192	4.283772	0.742251	2.2711e+13	-5.3115e+13	3.8818e+13
H 3	-0.592061	4.367336	0.948600	4.1123e+13	-4.0461e+13	-2.1428e+13
O 4	-1.604447	1.850080	-0.150352	-8.4112e+11	-1.4174e+13	-4.1592e+12
H 5	-1.100401	2.674611	0.026108	-2.4722e+13	2.0571e+13	-1.2804e+13

Continuation of Table B.18						
State #17	Coordinates (Å)			MWV ($amu^2 * bohr/sec$)		
#atom	x	y	z	v_x	v_y	v_z
H 6	-2.479946	2.232752	0.067226	-1.1419e+13	-2.4764e+13	-2.5265e+13
O 7	-0.109414	-0.752395	-1.747049	5.9280e+13	-2.7690e+12	-3.9785e+13
H 8	-0.377649	-1.656176	-1.996383	1.2715e+13	1.2955e+13	-1.8865e+12
H 9	-0.686406	-0.133075	-2.224354	1.3805e+13	1.2355e+13	-2.3363e+13
O10	2.160903	-3.210202	-1.527465	2.3538e+13	-3.6779e+13	2.5984e+13
H11	1.294237	-3.521297	-1.815353	3.6324e+13	-1.9001e+13	6.9146e+12
H12	2.221434	-3.384491	-0.566595	-6.5328e+12	-4.0234e+13	4.1279e+12
O13	4.945614	-0.110208	2.442576	-3.0218e+13	4.4480e+13	1.3400e+14
H14	4.553337	0.687708	2.056551	-3.9993e+13	-4.1740e+13	-4.6497e+13
H15	4.625352	-0.029749	3.347294	-7.5564e+13	3.7093e+13	7.6144e+12
O16	0.364080	2.833340	3.171655	-3.3389e+13	5.2304e+13	6.2660e+13
H17	0.553349	3.642937	3.639780	1.4418e+13	1.7391e+13	-1.4618e+12
H18	0.938959	2.701908	2.391409	1.0287e+13	2.8544e+13	2.9607e+13
O19	-0.749763	-3.188376	0.731184	-6.0114e+13	8.8133e+12	-8.7908e+12
H20	-1.326973	-3.822351	1.186559	1.3128e+13	2.3176e+13	1.0462e+13
H21	-1.373549	-2.479981	0.477342	-2.9676e+13	-4.2270e+13	1.8757e+13
O22	-1.139046	-0.702564	0.805589	1.5398e+13	-4.8700e+13	-1.3954e+13
H23	-0.283504	-1.035268	0.577951	8.6021e+11	3.5992e+13	-3.2046e+13
H24	-1.164309	0.246416	0.574753	3.9052e+13	-2.1010e+12	1.4533e+13
O25	-4.077020	-3.079679	-0.320346	1.4573e+13	8.6330e+12	8.7911e+11
H26	-3.576930	-2.547655	-0.959044	9.8019e+12	-3.1417e+13	-2.7663e+13
H27	-4.975876	-3.150107	-0.626534	9.3657e+12	-2.8429e+13	-1.5297e+13
O28	3.014020	4.000764	-0.948886	-1.3284e+13	2.7278e+13	-6.4957e+13
H29	3.348715	3.191694	-1.377114	3.3842e+12	-1.9167e+13	2.7547e+13

Continuation of Table B.18						
State #17	Coordinates (Å)			MWV ($amu^2 * bohr/sec$)		
#atom	x	y	z	v_x	v_y	v_z
H30	2.747098	4.592260	-1.650607	4.0277e+12	-2.0917e+13	-4.3274e+13
O31	1.865917	0.751843	-4.191989	2.2263e+13	5.3204e+13	4.5920e+12
H32	1.260322	0.096386	-3.820238	5.2908e+13	-3.6978e+13	-3.4251e+13
H33	2.349462	1.107676	-3.437805	-1.0554e+13	-1.0626e+13	4.2678e+13
O34	-2.856729	-1.080749	-1.876444	-3.2248e+13	-3.5766e+13	-2.3740e+13
H35	-3.118581	-0.329700	-1.311949	9.5071e+13	-1.8799e+13	6.8436e+13
H36	-2.882677	-0.735490	-2.779142	2.4299e+13	3.8255e+13	1.9729e+13
O37	-2.747026	-4.421600	1.836880	-5.8640e+13	2.1825e+13	2.4315e+13
H38	-3.447318	-3.894364	1.428024	-1.4641e+13	-1.9803e+13	-6.3091e+13
H39	-3.155973	-5.190872	2.224636	-1.3732e+13	-1.4720e+13	-1.6677e+13
O40	-2.801615	2.007630	-2.815890	1.9800e+12	-3.7364e+12	5.7163e+13
H41	-2.269479	1.811285	-1.995628	2.1274e+13	1.3709e+13	8.2565e+12
H42	-2.826387	2.961054	-2.904444	-9.7378e+12	-7.6594e+12	-2.6762e+13
O43	-1.144610	0.807234	-4.231047	1.0514e+13	-6.8394e+12	-3.6132e+13
H44	-0.397203	1.235994	-4.635104	9.8210e+12	-1.8401e+13	-1.5267e+13
H45	-1.747757	1.431650	-3.801108	-4.0777e+12	-1.8878e+13	3.0597e+13
O46	1.806346	2.341138	1.107167	3.2372e+13	6.5942e+13	-9.6244e+12
H47	2.221798	2.919548	0.445818	-2.6284e+12	1.7393e+13	-1.1366e+13
H48	1.812724	1.438855	0.735579	2.4372e+13	1.3017e+13	-3.1738e+12
O49	-2.137045	2.055291	3.520298	-2.7975e+13	1.4560e+13	1.5144e+13
H50	-1.203692	2.378480	3.449026	-3.6054e+13	8.2878e+13	7.8868e+12
H51	-2.060114	1.091889	3.371780	-7.6903e+12	-8.8429e+12	4.5646e+13
O52	3.771530	-1.304107	-2.603197	-3.1748e+12	-2.0686e+13	-4.5634e+12
H53	3.133627	-1.985670	-2.326973	-5.6542e+13	2.1069e+13	-3.6089e+13

Continuation of Table B.18						
State #17	Coordinates (Å)			MWV ($amu^2 * bohr/sec$)		
#atom	x	y	z	v_x	v_y	v_z
H54	4.069615	-1.585921	-3.465227	-5.1973e+13	-1.5103e+13	-1.5391e+13
O55	1.655568	-0.026654	-0.198443	3.3699e+13	3.0739e+13	-2.7399e+13
H56	2.404242	-0.664437	-0.119925	5.7658e+13	4.7402e+12	5.2953e+12
H57	0.974618	-0.383698	-0.852800	-4.1410e+12	-1.5022e+13	-4.2866e+12
O58	-1.205513	-3.289501	-2.190794	-5.7483e+13	-5.4165e+13	-4.6370e+13
H59	-0.955700	-3.620283	-1.320620	2.0720e+13	-8.0569e+12	-3.9793e+12
H60	-1.945564	-2.688988	-2.026990	6.1216e+12	6.0537e+12	7.2965e+11
O61	-3.500703	3.219032	1.537498	-2.3014e+13	-2.0763e+12	-1.9880e+13
H62	-3.979144	4.001740	1.794428	-3.9571e+12	-1.0712e+13	3.8375e+13
H63	-3.132433	2.735252	2.320055	-2.9890e+13	-4.3995e+13	7.8515e+12
O64	-2.128837	-0.918704	3.173749	3.4420e+11	3.2982e+13	6.5339e+13
H65	-1.594293	-1.305324	3.866653	1.7078e+13	-4.2248e+13	-2.0458e+13
H66	-1.655024	-1.015174	2.321249	-3.6673e+13	-2.6108e+13	-1.0461e+13
O67	4.001588	-1.263971	0.204390	6.3211e+13	8.4785e+12	-2.7459e+13
H68	4.560301	-1.468348	-0.552177	3.2124e+13	-2.6295e+13	7.6767e+12
H69	4.563433	-0.993587	0.965008	5.1661e+13	-3.7756e+13	-1.8009e+13
O70	2.010036	-3.309622	0.848159	2.8996e+13	2.1142e+13	-1.0210e+14
H71	2.603575	-2.701667	1.298197	3.9755e+13	5.9955e+12	-7.1487e+13
H72	1.072121	-3.108807	1.015339	2.5815e+13	6.9955e+12	1.8468e+13
O73	3.185318	1.277332	-1.813194	-4.2515e+13	-4.5715e+13	4.1718e+13
H74	2.693778	0.784149	-1.121594	-6.0203e+13	1.6897e+13	1.0815e+13
H75	3.988082	0.790920	-2.040547	-2.6535e+13	-1.8661e+13	2.2568e+13
O76	-4.126180	-0.066901	0.554757	-3.3984e+13	5.2145e+13	4.4006e+13
H77	-3.719174	-0.327756	1.393663	-2.2326e+13	4.1467e+12	2.7075e+13

Continuation of Table B.18						
State #17	Coordinates (Å)			MWV ($amu^2 * bohr/sec$)		
#atom	x	y	z	v_x	v_y	v_z
H78	-5.040224	0.075243	0.805742	-3.2393e+13	-2.1911e+13	-5.0757e+13
O79	2.910484	1.114682	4.242466	6.2045e+13	-4.8217e+13	-3.5093e+13
H80	2.956223	0.800825	5.139544	5.6415e+12	1.0213e+13	-9.2006e+11
H81	2.218186	1.781755	4.231842	1.5871e+13	6.3183e+11	-3.1951e+13
End of Table						

Table B.19: Vibrationally bound initial condition 18 of water $(H_2O)_{27}$ nanodroplet.

State #18	Coordinates (Å)			MWV ($amu^2 * bohr/sec$)		
#atom	x	y	z	v_x	v_y	v_z
O 1	-1.194122	4.256927	0.335928	2.4462e+13	-3.9380e+13	5.0956e+13
H 2	-1.854876	3.904279	0.971723	3.5756e+13	3.8983e+12	3.8042e+13
H 3	-0.319688	4.234175	0.726422	8.4377e+12	-2.3387e+12	-6.3743e+12
O 4	-1.639306	1.791007	-0.194008	-3.0106e+13	-5.9221e+13	-4.2392e+13
H 5	-1.369146	2.737540	-0.198959	-7.6223e+13	6.1103e+12	6.3051e+12
H 6	-2.518520	1.730114	0.216418	6.7284e+12	-3.1724e+13	4.1010e+13
O 7	0.002268	-0.755195	-1.862087	5.2346e+13	-2.8276e+12	-7.6550e+13
H 8	-0.239932	-1.667612	-2.128134	2.6095e+13	-1.1259e+13	-2.1136e+13
H 9	-0.287752	-0.181358	-2.584153	7.2894e+13	-1.4538e+13	-6.7683e+13
O10	2.213143	-3.270745	-1.590806	2.2646e+13	-2.3280e+13	-9.2012e+13
H11	1.482316	-3.702696	-2.077603	3.1702e+13	-1.7433e+13	-5.6366e+13
H12	2.059610	-3.426755	-0.611971	-4.3833e+13	4.8820e+12	-2.5407e+13

Continuation of Table B.19						
State #18	Coordinates (Å)			MWV ($amu^2 * bohr/sec$)		
#atom	x	y	z	v_x	v_y	v_z
O13	4.851041	-0.002335	2.686767	-6.6808e+13	5.0600e+13	1.0381e+14
H14	4.530136	0.355178	1.854951	3.9791e+13	-1.6394e+13	-9.0993e+12
H15	4.109443	0.192854	3.285103	-3.2970e+13	3.3451e+13	-6.4906e+12
O16	0.337176	2.957580	3.297069	5.3544e+12	6.2847e+13	5.3413e+13
H17	0.658083	3.789322	3.648774	7.8646e+12	1.6887e+13	1.5696e+12
H18	0.809220	2.727536	2.438957	-3.6166e+13	9.0966e+12	7.3733e+12
O19	-0.853519	-3.208977	0.694369	-3.6164e+13	-3.0179e+13	-2.6445e+13
H20	-1.248556	-3.883799	1.299410	-1.6019e+13	-3.0609e+12	6.8736e+11
H21	-1.444637	-2.416614	0.731562	8.3948e+12	2.5459e+13	5.5450e+13
O22	-1.105288	-0.735041	0.772454	1.2717e+13	1.1611e+13	-1.9761e+13
H23	-0.202950	-0.895089	0.454961	-1.5572e+13	3.0389e+13	4.0379e+12
H24	-1.353105	0.183916	0.586276	-2.4306e+13	-1.7497e+13	-2.6108e+13
O25	-4.044300	-3.078913	-0.317542	1.4076e+13	-7.0501e+12	-4.2117e+12
H26	-3.689662	-2.497421	-1.001924	-1.9213e+13	3.7758e+13	1.2693e+13
H27	-4.882370	-3.397568	-0.645190	1.3294e+13	-4.2208e+13	2.4129e+13
O28	2.994760	4.013719	-1.068172	-1.1793e+13	-1.8047e+13	-5.9139e+13
H29	3.213188	3.093644	-1.293949	-6.2283e+12	-5.6254e+12	-6.1892e+11
H30	2.712473	4.370467	-1.910055	-1.3558e+13	-1.7102e+13	-1.5864e+13
O31	1.888814	0.849628	-4.158510	-8.1288e+11	4.0371e+13	2.6179e+13
H32	1.745077	-0.104622	-4.235777	7.0921e+13	3.1239e+12	-6.3605e+13
H33	2.330651	1.050078	-3.315979	1.3627e+13	9.7162e+12	-1.5888e+13
O34	-2.922104	-1.142720	-1.905520	-2.5453e+13	-3.5226e+13	-4.1450e+12
H35	-2.536047	-0.858724	-1.065112	4.6421e+13	-5.4054e+13	-1.3391e+13
H36	-2.803271	-0.366396	-2.485131	-7.4375e+12	4.3867e+13	6.6670e+13

Continuation of Table B.19						
State #18	Coordinates (Å)			MWV ($amu^2 * bohr/sec$)		
#atom	x	y	z	v_x	v_y	v_z
O37	-2.897951	-4.367186	1.870601	-8.7494e+13	2.4974e+13	2.0270e+11
H38	-3.224587	-4.196146	0.973428	4.9772e+13	-2.2122e+13	-1.7001e+13
H39	-3.160925	-5.260980	2.070040	8.8467e+12	-4.6127e+12	-1.0197e+13
O40	-2.780254	2.007399	-2.668887	1.7639e+13	1.1821e+13	7.5303e+13
H41	-2.335068	2.131040	-1.829158	-1.8285e+13	1.8808e+13	5.1229e+13
H42	-3.051349	2.867726	-2.990811	-5.5914e+13	-2.7393e+13	1.6118e+12
O43	-1.106746	0.743496	-4.287574	3.4150e+13	-3.9540e+13	-1.9342e+13
H44	-0.261827	1.160174	-4.498820	1.7045e+13	-3.2306e+13	4.0545e+13
H45	-1.667103	1.439389	-3.934833	8.8049e+12	-1.5896e+13	-2.5403e+13
O46	1.875491	2.478860	1.089224	2.6423e+13	7.0777e+13	-3.1209e+12
H47	2.122278	3.125155	0.406426	-6.0055e+12	2.0994e+13	-4.6671e+12
H48	1.713915	1.631108	0.644288	-2.1240e+13	4.5722e+13	-2.4215e+13
O49	-2.232751	2.079279	3.533849	-5.1381e+13	5.9220e+12	-4.9286e+11
H50	-1.334365	2.432300	3.398920	-2.7787e+11	-1.9775e+13	-1.7306e+12
H51	-1.987648	1.172157	3.751705	-2.0912e+13	7.9988e+12	3.3444e+13
O52	3.745891	-1.369622	-2.608458	-2.3266e+13	-2.7681e+13	1.2064e+13
H53	2.992886	-1.896477	-2.238496	3.2386e+13	-4.4562e+13	-2.5542e+12
H54	3.827462	-1.477020	-3.555046	-2.6298e+13	1.6213e+13	3.2494e+12
O55	1.741225	0.002851	-0.209255	3.1948e+13	-6.0350e+12	1.3252e+13
H56	2.495016	-0.544216	-0.021011	-4.9171e+12	2.9148e+13	1.3734e+13
H57	1.176760	-0.404944	-0.923775	3.1143e+13	-2.3689e+12	1.4885e+13
O58	-1.285160	-3.379455	-2.253014	-2.2310e+13	-3.4032e+13	-1.8172e+13
H59	-1.078347	-3.670715	-1.365289	-4.7011e+13	-9.4116e+11	1.8908e+12
H60	-1.928408	-2.658678	-2.148607	-8.8405e+12	-8.4599e+11	-4.0423e+13

Continuation of Table B.19						
State #18	Coordinates (Å)			MWV ($amu^2 * bohr/sec$)		
#atom	x	y	z	v_x	v_y	v_z
O61	-3.519130	3.217444	1.520511	7.7902e+12	-6.6040e+12	8.7768e+12
H62	-4.146075	3.765099	1.990312	-2.6749e+13	-3.3342e+13	-1.1156e+13
H63	-3.130117	2.604122	2.186565	1.2197e+13	9.4810e+12	-3.6749e+13
O64	-2.119950	-0.844658	3.292899	8.8038e+12	3.9876e+13	5.2146e+13
H65	-1.724085	-1.594301	3.737104	-4.9972e+13	-2.7424e+13	-5.0820e+12
H66	-1.814728	-0.882704	2.373089	6.8995e+12	5.0048e+13	2.8457e+13
O67	4.142097	-1.259226	0.164542	5.4738e+13	-4.2437e+12	-1.6824e+13
H68	4.453452	-1.630840	-0.666807	-7.7846e+12	-7.6165e+12	-4.4615e+12
H69	4.736091	-1.306922	0.921094	3.4483e+13	-4.8252e+13	-9.5840e+12
O70	2.075147	-3.282335	0.761547	3.9899e+13	1.4627e+13	1.3946e+13
H71	2.693245	-2.532506	0.720067	-1.3491e+13	2.5785e+13	-4.6074e+13
H72	1.210202	-2.979513	1.091951	4.6016e+12	2.1001e+13	-8.8440e+12
O73	3.124604	1.255924	-1.748902	-2.2241e+13	8.9046e+11	1.3845e+13
H74	2.357436	0.927944	-1.236799	-1.0137e+13	6.4996e+13	7.9690e+12
H75	3.557412	0.384175	-1.896345	-3.9572e+13	-2.4047e+13	-1.3556e+13
O76	-4.165829	0.044560	0.639404	-2.3840e+12	5.9803e+13	4.0050e+13
H77	-4.055083	-0.345163	1.508389	-6.6137e+13	-8.7837e+12	1.5713e+13
H78	-5.091032	-0.118091	0.459757	1.7015e+13	-2.6380e+13	-3.3355e+13
O79	3.034339	1.021050	4.180920	5.6955e+13	-4.5926e+13	-2.5025e+13
H80	2.893119	0.965366	5.124070	-2.0805e+13	3.3922e+13	-1.7245e+13
H81	2.329048	1.552966	3.806135	1.2299e+13	-4.8001e+13	-5.4701e+13
End of Table						

Table B.20: Vibrationally bound initial condition 19 of water $(H_2O)_{27}$ nanodroplet.

State #19	Coordinates (Å)			MWV ($amu^2 * bohr/sec$)		
#atom	x	y	z	v_x	v_y	v_z
O 1	-1.154634	4.159275	0.449728	2.0720e+13	-5.7401e+13	6.2876e+13
H 2	-1.767685	4.387783	1.166330	-5.0169e+12	6.6224e+13	-4.8150e+12
H 3	-0.240850	4.222971	0.740692	2.8170e+12	4.7880e+12	1.1471e+13
O 4	-1.766982	1.680181	-0.261390	-8.9970e+13	-4.9044e+13	-1.7566e+13
H 5	-1.388044	2.550164	0.051989	2.8647e+13	-6.0328e+13	4.4294e+13
H 6	-2.570132	1.500683	0.250928	-2.5078e+13	-8.1772e+12	-1.1065e+13
O 7	0.108590	-0.776413	-2.047827	6.3154e+13	-1.7571e+13	-9.5925e+13
H 8	-0.068272	-1.712653	-2.181138	3.6153e+12	-1.1391e+13	-8.6545e+12
H 9	0.070720	-0.338257	-2.906374	6.8469e+11	-2.7364e+13	-1.6024e+13
O10	2.239400	-3.314853	-1.829588	1.3729e+13	-2.1279e+13	-1.3374e+14
H11	1.719705	-3.797861	-2.478105	-1.0742e+13	-3.2728e+13	-4.0801e+13
H12	1.985565	-3.497927	-0.912252	3.3066e+13	-2.0991e+13	-3.7926e+13
O13	4.758182	0.047294	2.817867	-6.3031e+12	-9.0817e+12	2.2163e+13
H14	4.864783	0.484279	1.976604	2.8593e+13	4.5793e+13	3.4671e+13
H15	4.115292	0.526882	3.357555	4.0598e+13	4.2898e+13	2.2744e+13
O16	0.350432	3.065760	3.376209	1.1486e+13	5.6947e+13	2.7039e+13
H17	0.691513	3.901972	3.693356	-1.5080e+13	1.1316e+13	4.1640e+13
H18	0.794525	2.921876	2.532297	2.2305e+13	-7.2840e+12	-8.0057e+12
O19	-0.913482	-3.280113	0.650383	-1.1951e+13	-4.3145e+13	-2.4930e+13
H20	-1.385894	-3.872294	1.236893	-3.4551e+13	-7.3797e+12	1.2987e+13
H21	-1.108451	-2.377049	0.876003	3.0275e+13	2.2172e+13	-2.6794e+13
O22	-1.099505	-0.671852	0.730342	1.5115e+13	5.6018e+13	-2.9660e+13

Continuation of Table B.20						
State #19	Coordinates (Å)			MWV ($amu^2 * bohr/sec$)		
#atom	x	y	z	v_x	v_y	v_z
H23	-0.122635	-0.640229	0.578037	2.4971e+13	4.3525e+12	4.3155e+13
H24	-1.409287	0.141694	0.272027	-2.9935e+13	-4.9360e+12	-1.9434e+13
O25	-4.009313	-3.097873	-0.322305	9.7908e+12	-1.0493e+13	-5.9333e+12
H26	-4.041542	-2.308781	-0.883246	-1.1050e+13	4.8782e+12	1.9181e+13
H27	-4.752852	-3.648149	-0.572327	2.2688e+13	-2.3557e+13	3.3497e+12
O28	2.959604	3.937185	-1.174130	-1.8142e+13	-5.3513e+13	-4.3987e+13
H29	3.404488	3.129082	-1.485754	2.2856e+13	2.1760e+13	-4.8291e+13
H30	2.561285	4.330026	-1.950672	-2.2324e+13	-7.2649e+12	1.5532e+12
O31	1.860886	0.917005	-4.127735	-1.6234e+13	2.5101e+13	1.2925e+13
H32	2.361637	0.219399	-4.556540	5.5778e+13	6.3859e+13	-4.9262e+13
H33	2.368568	1.160772	-3.319817	-3.3212e+13	4.5310e+13	1.8109e+13
O34	-2.942918	-1.189849	-1.880091	-1.0935e+13	-2.4512e+13	2.8463e+13
H35	-2.233501	-1.204734	-1.218644	3.9871e+13	-2.6184e+12	-4.1347e+13
H36	-3.085306	-0.283147	-2.177287	-2.0324e+13	3.5945e+12	2.5173e+13
O37	-3.051733	-4.333998	1.862249	-6.4209e+13	1.5845e+13	-3.5985e+12
H38	-3.314124	-4.053769	0.956232	-6.9235e+13	2.8314e+13	2.4797e+13
H39	-3.128042	-5.277020	1.985865	-1.0836e+13	1.8535e+12	-3.6695e+13
O40	-2.748183	2.024913	-2.547076	5.2652e+12	4.7065e+12	4.9890e+13
H41	-2.484973	2.048672	-1.599959	3.4756e+12	-3.7531e+13	-1.1111e+13
H42	-3.508357	2.607050	-2.652643	-3.6186e+13	-4.8503e+13	6.6612e+13
O43	-1.004448	0.645857	-4.314178	6.4388e+13	-5.1817e+13	-3.2457e+12
H44	-0.099993	1.013989	-4.264382	1.1282e+13	4.0022e+12	6.1817e+12
H45	-1.559427	1.251976	-3.772762	3.5551e+13	-4.1055e+13	4.1407e+13
O46	1.893745	2.630758	1.079775	-8.0585e+12	8.3481e+13	2.4547e+12

Continuation of Table B.20						
State #19	Coordinates (Å)			MWV ($amu^2 * bohr/sec$)		
#atom	x	y	z	v_x	v_y	v_z
H47	2.244178	3.282280	0.450811	2.9517e+13	-7.2056e+12	-1.3477e+13
H48	1.605448	1.830534	0.609562	-9.0093e+11	2.0498e+13	1.4669e+12
O49	-2.305505	2.073911	3.519359	-4.0707e+13	-3.7136e+10	-1.0832e+13
H50	-1.387859	2.357034	3.652098	-6.5674e+12	-5.6818e+13	5.8566e+13
H51	-2.420918	1.155432	3.802329	-8.3851e+12	-1.5654e+12	-1.7676e+13
O52	3.682484	-1.416472	-2.559883	-2.9833e+13	-2.0507e+13	2.4796e+13
H53	3.293053	-2.286605	-2.310991	-3.3603e+12	-2.3366e+13	2.1355e+13
H54	3.844272	-1.389978	-3.503821	4.1549e+13	1.4011e+13	1.6229e+13
O55	1.739588	-0.027140	-0.127145	-1.5762e+13	-2.1546e+13	6.7594e+13
H56	2.662444	-0.376703	0.037319	-1.1647e+13	8.7541e+11	4.8939e+12
H57	1.351934	-0.469709	-0.928201	1.7857e+13	-1.7940e+12	-2.5928e+13
O58	-1.306400	-3.420627	-2.271515	-4.6813e+12	-9.0177e+12	4.1532e+12
H59	-1.488670	-3.507724	-1.318178	-3.4110e+13	3.8314e+13	-1.7832e+13
H60	-2.007892	-2.854008	-2.613574	-4.7376e+12	-4.3890e+13	-6.3980e+13
O61	-3.468734	3.199371	1.530329	2.9494e+13	-7.9785e+12	1.4411e+13
H62	-4.343869	3.509994	1.781726	-2.0455e+13	-2.4302e+13	-7.0372e+13
H63	-3.150556	2.709164	2.329409	2.4727e+13	1.1899e+13	3.2740e+13
O64	-2.109321	-0.745507	3.397531	4.9381e+12	5.6187e+13	4.9315e+13
H65	-2.211973	-1.685158	3.570446	-6.9228e+13	1.3341e+13	-3.2725e+13
H66	-1.539541	-0.654222	2.604248	2.7783e+13	1.3182e+13	2.4954e+13
O67	4.229736	-1.287647	0.141392	4.1771e+13	-2.5430e+13	-1.5125e+13
H68	4.520172	-1.501635	-0.760716	-5.7863e+12	4.4171e+13	-1.6125e+13
H69	4.826626	-1.607449	0.813682	-1.4869e+13	-9.4114e+12	1.1968e+13
O70	2.135419	-3.224491	0.814440	2.2264e+13	3.0901e+13	2.0382e+13

Continuation of Table B.20						
State #19	Coordinates (Å)			MWV ($amu^2 * bohr/sec$)		
#atom	x	y	z	v_x	v_y	v_z
H71	2.685280	-2.440541	0.770104	-6.6063e+12	1.3253e+13	4.6169e+13
H72	1.212429	-3.033602	0.994978	-5.6633e+12	-1.1576e+13	-5.1689e+12
O73	3.111001	1.297978	-1.790952	9.3822e+12	3.7626e+13	-4.4901e+13
H74	2.498588	1.101913	-1.039162	1.9908e+13	-1.5741e+13	9.7830e+12
H75	3.444173	0.398161	-1.885037	1.7031e+13	6.0791e+12	9.4021e+12
O76	-4.169874	0.152757	0.740231	8.6027e+12	6.4059e+13	4.8177e+13
H77	-4.274915	-0.358905	1.536752	-2.7844e+13	-1.8292e+13	-2.1520e+13
H78	-4.706586	-0.170844	0.014815	7.2319e+13	-1.7757e+13	-1.8244e+13
O79	3.076440	0.966248	4.150920	-2.8266e+13	-1.9716e+12	2.0665e+12
H80	2.756819	1.176101	5.030962	-1.2730e+13	2.1714e+13	-1.3346e+13
H81	2.419250	1.244066	3.507397	-1.8957e+12	-2.1618e+13	-7.1603e+12
End of Table						

Table B.21: Vibrationally bound initial condition 20 of water $(H_2O)_{27}$ nanodroplet.

State #20	Coordinates (Å)			MWV ($amu^2 * bohr/sec$)		
#atom	x	y	z	v_x	v_y	v_z
O 1	-1.090677	4.036810	0.569356	4.5615e+13	-6.4494e+13	5.4784e+13
H 2	-1.850332	4.401409	1.018918	-3.3567e+13	-5.8061e+13	-1.4711e+13
H 3	-0.277259	4.337038	0.976786	-7.2115e+12	4.4901e+12	3.8646e+13
O 4	-1.964234	1.569932	-0.224593	-1.0464e+14	-4.2607e+13	6.7455e+13
H 5	-1.459654	2.341364	0.121431	-7.4140e+11	1.4342e+13	-4.7565e+13

Continuation of Table B.21						
State #20	Coordinates (Å)			MWV ($amu^2 * bohr/sec$)		
#atom	x	y	z	v_x	v_y	v_z
H 6	-2.801948	1.708961	0.269919	-2.5900e+13	7.6541e+12	1.4818e+12
O 7	0.234888	-0.840124	-2.220492	5.2202e+13	-4.5810e+13	-8.4458e+13
H 8	0.006235	-1.778685	-2.228255	3.1543e+13	-3.6335e+12	9.5206e+11
H 9	-0.092970	-0.436196	-3.072442	-1.3211e+13	6.5863e+12	-8.1392e+12
O10	2.253549	-3.392591	-2.093364	2.7539e+12	-5.6358e+13	-1.1614e+14
H11	1.566182	-3.940559	-2.444172	-4.8662e+13	-1.6938e+13	2.0648e+13
H12	2.326912	-3.520667	-1.110453	3.6614e+13	3.0434e+13	-3.5947e+13
O13	4.806494	0.015328	2.788853	5.0020e+13	-1.6098e+13	-3.8297e+13
H14	5.181615	0.697843	2.234995	4.2747e+13	3.9474e+12	2.8056e+13
H15	4.575280	0.415320	3.633151	2.5872e+13	-6.3892e+13	2.4558e+13
O16	0.374864	3.154707	3.414579	2.2332e+13	3.9101e+13	9.5987e+12
H17	0.646081	3.920276	3.921019	-5.3115e+12	-6.0257e+12	2.7675e+13
H18	0.990273	3.153836	2.661183	-5.5081e+12	3.8475e+13	3.5565e+13
O19	-0.916548	-3.355562	0.602984	-1.0403e+13	-1.3620e+13	-2.3039e+13
H20	-1.641830	-3.672386	1.153498	-3.4385e+12	1.8888e+12	-4.1415e+13
H21	-1.104366	-2.404145	0.488319	2.9874e+13	-3.9059e+13	-5.2437e+13
O22	-1.032893	-0.585350	0.699108	4.5561e+13	3.8561e+13	-4.5524e+12
H23	-0.097610	-0.390107	0.688340	2.9427e+13	9.8865e+12	9.1353e+11
H24	-1.387562	0.237810	0.278859	-2.1674e+13	5.1497e+12	2.8445e+13
O25	-4.010898	-3.130210	-0.318413	-1.1806e+13	-1.4722e+13	-2.2476e+11
H26	-3.679822	-2.432790	-0.931237	7.2338e+13	-4.3056e+13	-2.5856e+12
H27	-4.652624	-3.619688	-0.844604	1.6322e+13	3.0831e+13	-5.5889e+13
O28	2.932547	3.831324	-1.255121	-9.6386e+12	-4.5940e+13	-3.0555e+13
H29	3.362404	3.117249	-1.751924	-4.2967e+13	-2.8093e+13	-2.8804e+13

Continuation of Table B.21						
State #20	Coordinates (Å)			MWV ($amu^2 * bohr/sec$)		
#atom	x	y	z	v_x	v_y	v_z
H30	2.318405	4.301514	-1.816368	-2.9323e+13	-1.2422e+13	1.9536e+13
O31	1.811954	0.974806	-4.118010	-2.9615e+13	3.7185e+13	-4.9342e+12
H32	2.579301	0.959461	-4.679610	-2.3131e+12	1.0205e+14	-5.2592e+12
H33	2.195412	1.211989	-3.259139	-1.3896e+13	-2.6891e+13	9.2592e+12
O34	-2.966856	-1.205141	-1.797712	1.0715e+12	2.2136e+13	4.9098e+13
H35	-1.997532	-1.200730	-1.692965	1.0995e+13	-2.9196e+13	-5.8599e+13
H36	-3.151052	-0.347961	-2.203018	-3.6095e+13	-2.6184e+13	-3.1435e+13
O37	-3.169939	-4.299942	1.860776	-5.7537e+13	1.8942e+13	8.3890e+12
H38	-3.731549	-3.768653	1.279844	-2.7923e+13	3.3159e+13	2.1706e+13
H39	-3.304952	-5.220417	1.636484	-2.3977e+13	1.9492e+13	-4.3555e+13
O40	-2.759901	1.997176	-2.490212	-1.0939e+13	-3.6744e+13	-3.6116e+12
H41	-2.252356	1.956809	-1.648491	1.4616e+13	1.8508e+13	1.6894e+13
H42	-3.645888	2.282576	-2.250256	-2.9094e+12	-2.5455e+13	4.4016e+13
O43	-0.852256	0.544712	-4.282004	8.1016e+13	-6.8748e+13	2.8096e+13
H44	-0.039725	1.029565	-4.464337	9.1869e+12	2.1194e+13	-1.6392e+13
H45	-1.446218	1.051638	-3.709559	3.4606e+12	4.1709e+13	-2.5794e+13
O46	1.859452	2.793734	1.076112	-2.2568e+13	7.7533e+13	-9.4605e+12
H47	2.371850	3.229234	0.366288	-3.8171e+12	1.3713e+13	1.0975e+12
H48	1.647210	1.892607	0.792017	7.4988e+12	-6.9467e+12	5.1958e+13
O49	-2.364783	2.044109	3.535779	-3.0124e+13	-1.9935e+13	2.2038e+13
H50	-1.445938	2.261356	3.749462	-7.1517e+12	8.3513e+11	-3.2723e+13
H51	-2.541828	1.090617	3.468524	2.0420e+13	-8.8531e+12	-3.7425e+13
O52	3.667540	-1.416580	-2.483481	1.0355e+13	1.8872e+13	3.7912e+13
H53	2.923518	-2.092443	-2.503813	-3.3042e+13	7.2670e+13	-2.5190e+13

Continuation of Table B.21						
State #20	Coordinates (Å)			MWV ($amu^2 * bohr/sec$)		
#atom	x	y	z	v_x	v_y	v_z
H54	4.170558	-1.589169	-3.283808	3.5570e+13	-4.5897e+13	3.8015e+13
O55	1.697184	-0.072588	-0.005141	-3.7321e+13	-1.3024e+13	5.1285e+13
H56	2.484881	-0.605483	0.179676	4.6275e+12	-4.5312e+13	1.5397e+12
H57	1.294285	-0.396285	-0.839637	-1.0457e+13	-4.9587e+12	4.9559e+13
O58	-1.298131	-3.416884	-2.267470	1.9392e+13	1.0765e+13	4.9424e+11
H59	-1.611188	-3.386291	-1.338372	-2.9017e+12	-2.4818e+13	5.6106e+12
H60	-2.023327	-3.231719	-2.860228	-1.2915e+13	-4.2803e+13	6.7672e+12
O61	-3.400859	3.199768	1.540128	3.5743e+13	8.2875e+12	-8.0202e+12
H62	-4.353542	3.114066	1.448467	1.4736e+13	-6.7312e+13	1.4688e+12
H63	-3.172414	2.864879	2.436699	-2.1198e+13	6.8708e+12	-1.9870e+13
O64	-2.094214	-0.634241	3.479941	5.8695e+12	5.1188e+13	2.4252e+13
H65	-2.689035	-1.378397	3.362391	-5.0301e+13	5.5805e+13	5.8943e+12
H66	-1.650212	-0.600246	2.619725	-2.7261e+13	1.6812e+13	-1.9004e+13
O67	4.257505	-1.312805	0.118258	2.8991e+12	-4.2332e+12	-2.6883e+12
H68	4.623306	-1.450471	-0.766742	-1.5085e+13	-2.7303e+13	-1.0085e+13
H69	4.940748	-1.542744	0.749296	1.1050e+13	3.5215e+13	-1.1937e+13
O70	2.160510	-3.178069	0.826710	-1.2294e+12	2.1461e+13	-6.8069e+12
H71	2.541214	-2.338752	1.102601	-1.3443e+13	-9.8043e+12	2.8440e+13
H72	1.203174	-3.162057	0.975617	7.8763e+12	-3.3873e+13	-3.3880e+12
O73	3.154545	1.358300	-1.880432	3.8430e+13	3.5602e+13	-5.8777e+13
H74	2.578048	1.104283	-1.151291	2.2680e+13	-4.4528e+13	-5.6521e+12
H75	3.625422	0.532573	-2.093479	-2.2067e+13	2.7428e+11	-1.6302e+12
O76	-4.152619	0.272734	0.813009	2.9331e+12	4.4297e+13	2.1891e+13
H77	-4.287065	-0.384348	1.499655	2.4195e+13	3.4151e+13	1.6609e+13

Continuation of Table B.21						
State #20	Coordinates (Å)			MWV ($amu^2 * bohr/sec$)		
#atom	x	y	z	v_x	v_y	v_z
H78	-3.995142	-0.210565	-0.018725	1.1383e+14	2.5823e+13	1.4267e+13
O79	2.947166	1.002579	4.195174	-8.5595e+13	3.3401e+13	4.1102e+13
H80	2.617987	1.417163	4.998645	-2.8344e+13	3.5161e+13	-9.7690e+11
H81	2.291170	1.169906	3.512872	-1.1912e+13	-5.5698e+12	-2.0820e+12
End of Table						

Table B.22: Vibrationally bound initial condition 21 of water $(H_2O)_{27}$ nanodroplet.

State #21	Coordinates (Å)			MWV ($amu^2 * bohr/sec$)		
#atom	x	y	z	v_x	v_y	v_z
O 1	-1.007248	3.897609	0.647081	3.2578e+13	-7.5313e+13	3.5445e+13
H 2	-1.898865	3.816813	1.023423	1.5594e+13	-4.2875e+13	-1.6921e+13
H 3	-0.466038	4.161052	1.396439	-2.2714e+13	-5.7533e+13	4.5895e+13
O 4	-2.139963	1.554010	-0.062798	-6.1832e+13	2.2877e+13	8.8662e+13
H 5	-1.502156	2.301079	0.064691	5.2416e+12	-3.2593e+13	2.3479e+13
H 6	-2.823147	1.828721	0.571153	3.8128e+12	2.4454e+13	3.8262e+13
O 7	0.337092	-0.933916	-2.350534	5.6405e+13	-5.6538e+13	-4.7143e+13
H 8	0.178042	-1.873172	-2.531827	9.2751e+12	-3.0390e+12	-5.0781e+13
H 9	-0.091195	-0.449819	-3.080223	-7.7380e+11	1.0915e+13	9.4275e+12
O10	2.227064	-3.521771	-2.297790	-3.4750e+13	-6.7026e+13	-8.1054e+13
H11	1.346952	-3.852863	-2.187801	-5.3709e+12	2.4785e+13	-7.7859e+12
H12	2.464169	-3.324840	-1.375188	2.9790e+13	1.4908e+13	-1.5777e+13

Continuation of Table B.22						
State #21	Coordinates (Å)			MWV ($amu^2 * bohr/sec$)		
#atom	x	y	z	v_x	v_y	v_z
O13	4.932083	-0.041881	2.692518	7.1945e+13	-2.8476e+13	-4.9737e+13
H14	5.385845	0.803346	2.623985	8.3932e+12	6.2742e+11	5.2502e+13
H15	4.431818	0.056158	3.515102	-5.4327e+13	-4.2376e+13	-5.1204e+13
O16	0.415317	3.225613	3.435854	9.4031e+12	2.2417e+13	4.8205e+12
H17	0.609863	3.853777	4.131353	2.1117e+13	4.8906e+12	3.2629e+12
H18	1.027113	3.350866	2.655510	2.3035e+13	3.5550e+13	2.3949e+12
O19	-0.923738	-3.381874	0.512148	-5.8389e+12	-8.1016e+12	-5.8051e+13
H20	-1.689771	-3.656777	1.082431	1.6725e+13	-9.9363e+11	1.1661e+13
H21	-0.972766	-2.383295	0.568460	7.9628e+12	1.1388e+13	3.9975e+13
O22	-0.937367	-0.547380	0.732647	4.9816e+13	-1.5047e+11	4.1914e+13
H23	0.005083	-0.342408	0.725679	-1.1798e+13	1.9642e+12	2.0433e+13
H24	-1.327654	0.292771	0.376800	3.5895e+13	7.5782e+12	-1.4411e+13
O25	-4.035104	-3.157515	-0.356781	-6.9994e+12	-1.8689e+13	-1.9796e+13
H26	-3.428196	-2.478261	-0.696845	-2.7327e+13	3.1934e+13	7.8914e+12
H27	-4.628518	-3.389906	-1.070349	-8.2908e+12	4.5718e+13	-2.3858e+13
O28	2.906318	3.757868	-1.304800	-2.7025e+13	-3.0287e+13	-1.8350e+13
H29	2.983234	2.901257	-1.745583	-9.3435e+12	-1.4377e+13	7.5398e+12
H30	2.137895	4.215524	-1.643658	-1.4193e+13	1.2876e+12	2.5033e+13
O31	1.759072	1.063006	-4.159374	-2.9793e+13	4.9525e+13	-4.0957e+13
H32	2.296818	1.692231	-4.635236	-5.1381e+13	7.6747e+13	4.3634e+13
H33	2.085334	1.062811	-3.235287	5.0446e+12	6.9800e+12	-1.9759e+13
O34	-2.937620	-1.141080	-1.706677	2.8920e+13	4.1746e+13	3.3849e+13
H35	-2.035066	-1.235188	-2.031682	3.3337e+11	-2.9281e+12	-9.6381e+11
H36	-3.348332	-0.534630	-2.332608	-2.9100e+13	-1.3009e+13	2.3026e+13

Continuation of Table B.22						
State #21	Coordinates (Å)			MWV ($amu^2 * bohr/sec$)		
#atom	x	y	z	v_x	v_y	v_z
O37	-3.285414	-4.252371	1.880500	-5.8359e+13	2.8420e+13	3.9675e+12
H38	-3.746625	-3.662067	1.274284	1.0615e+13	5.0465e+12	-1.3114e+13
H39	-3.406233	-5.101709	1.450031	5.7113e+12	1.0145e+12	9.5597e+12
O40	-2.789767	1.908819	-2.529176	-1.3965e+13	-5.3998e+13	-3.9155e+13
H41	-2.354696	1.707075	-1.698589	-5.1896e+13	-6.6494e+13	-1.8546e+13
H42	-3.670374	2.197682	-2.304708	-1.1193e+13	5.6072e+12	-3.7943e+13
O43	-0.713317	0.451234	-4.200546	5.9744e+13	-3.2942e+13	3.7931e+13
H44	0.166395	0.783800	-4.448788	2.4068e+13	-5.8129e+13	3.0328e+13
H45	-1.415473	1.085937	-4.131901	1.1000e+13	-2.4209e+13	-3.5930e+13
O46	1.802155	2.938036	1.082073	-2.8287e+13	6.1876e+13	6.1292e+12
H47	2.217531	3.273841	0.261687	-2.4426e+13	4.1934e+13	-1.9515e+12
H48	1.823672	1.986172	0.976049	7.4624e+12	1.1519e+13	1.7126e+13
O49	-2.409653	2.012040	3.575364	3.0614e+12	-1.0626e+13	8.8330e+12
H50	-1.538748	2.423884	3.438552	-1.9295e+13	4.9208e+13	-4.7848e+12
H51	-2.301500	1.037132	3.631463	-3.2527e+11	-2.2084e+12	5.8657e+13
O52	3.717450	-1.335153	-2.424617	3.6504e+13	5.5213e+13	2.3954e+13
H53	2.827567	-1.700285	-2.583590	-1.1454e+13	2.3511e+13	-1.1587e+13
H54	4.269184	-1.933372	-2.933247	-8.9033e+12	-3.8030e+13	3.7222e+13
O55	1.642556	-0.104521	0.079890	-1.8727e+13	-1.3862e+13	3.2872e+13
H56	2.466513	-0.603445	0.147905	-1.4690e+13	2.4333e+13	-6.5105e+12
H57	1.115424	-0.423985	-0.711737	2.3323e+12	-3.3652e+12	-2.0915e+13
O58	-1.251165	-3.382888	-2.248430	2.7893e+13	1.8348e+13	1.4401e+13
H59	-1.262016	-3.818267	-1.386809	7.8297e+13	-3.8271e+13	-1.6708e+12
H60	-2.058499	-3.583545	-2.714484	1.2280e+13	-5.2457e+13	2.8445e+13

Continuation of Table B.22						
State #21	Coordinates (Å)			MWV ($amu^2 * bohr/sec$)		
#atom	x	y	z	v_x	v_y	v_z
O61	-3.368859	3.212976	1.519034	1.0778e+13	1.7294e+12	-9.1064e+12
H62	-4.233366	2.813756	1.393255	3.5247e+12	-1.4057e+13	9.6231e+11
H63	-2.953528	2.708665	2.265840	-1.1117e+13	-4.2929e+13	2.1575e+12
O64	-2.090164	-0.526670	3.464023	4.0344e+12	5.8097e+13	-3.3849e+13
H65	-2.888538	-1.027227	3.639064	8.0346e+12	2.2700e+13	3.4102e+13
H66	-1.718481	-0.745608	2.582208	-1.4267e+13	-5.5092e+13	2.1542e+13
O67	4.231148	-1.305307	0.124946	-4.8560e+13	1.8045e+13	2.2479e+13
H68	4.352277	-1.697852	-0.738406	1.5414e+13	-2.1448e+13	1.7364e+13
H69	4.987997	-1.188793	0.709591	9.7740e+12	3.3111e+13	-3.8099e+13
O70	2.141241	-3.155579	0.772410	-2.0194e+13	6.6458e+12	-4.2226e+13
H71	2.472424	-2.471111	1.368713	5.1351e+12	-2.7669e+13	2.5823e+13
H72	1.226339	-3.336698	1.045284	-3.2125e+11	-1.7003e+13	6.2875e+12
O73	3.216178	1.344434	-1.974505	1.8437e+13	-3.6692e+13	-3.8053e+13
H74	2.779966	1.140808	-1.134905	4.5361e+13	-1.2131e+13	-1.0738e+13
H75	3.702560	0.567307	-2.318284	2.8191e+13	-4.8960e+12	-9.8003e+12
O76	-4.127252	0.351863	0.822057	2.4770e+13	2.3851e+13	5.8536e+12
H77	-4.189692	-0.136629	1.653342	-2.5348e+13	5.4844e+13	2.7788e+13
H78	-3.370167	-0.045412	0.380840	3.5880e+13	2.8075e+13	1.5095e+13
O79	2.775606	1.079153	4.295575	-8.4065e+13	3.9185e+13	5.0355e+13
H80	2.314287	1.642519	4.915692	-4.4668e+13	2.5855e+13	-4.2954e+12
H81	2.270177	1.153231	3.484057	3.5807e+12	7.7950e+11	-6.5512e+12
End of Table						

Appendix C

X-RAY ABSORPTION SPECTRA FOR WATER MOLECULES WITH DIFFERENT SIZES

C.1 Water Pentamer Geometry

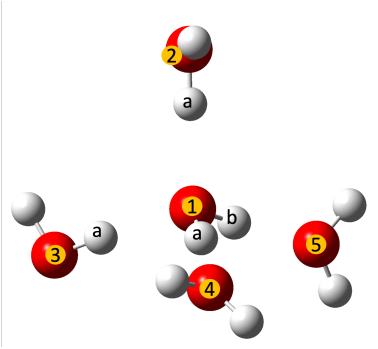

Figure C.1: The pentamer water cluster used in our simulation.

Atom 1	Atom 2	Distance (Å)
1	2	2.85899
1	3	2.86620
1	4	2.86482
1	5	2.84075
1	2a	1.88757
1	3a	1.89535
4	1a	1.89906
5	1b	1.87086

Table C.1: O–O distance and O–H distance between the center water and the rest in the water pentamer cluster.

C.2 XAS simulation for Water Monomer and Dimer

Similar procedures used in computing XAS for water pentamer were performed with water monomer and dimer. For water monomer, very accurate setup in the RASCI calculations were used due to its small system size. RASCI setups for neutral water monomer were as followed: RAS 1 included the only $1s$ orbitals with two electrons; RAS 2 included all four valence/inner-valence orbitals and eight electrons; RAS 3 included all the unoccupied orbitals with orbital energies up to 2 Hartree ($\approx$ 54.42 electronVolt). Up to one hole is allowed in RAS 1 while up to 3 electrons are allowed in RAS 3 to capture enough dynamic correlation. For cation species, RAS 2 included 7 electrons. A global shift of 5.0 eV has been applied to both the neutral and cationic species, to remediate the scalar relativistic effects not considered in the calculation. As up to triple excitations and a relatively large portion of virtual orbitals are included in the configuration interaction, the dynamic correlation can be considered completely recovered.

The RASCI setups for neutral water dimer were as followed: RAS 1 included the two $1s$ orbitals with four electrons; RAS 2 included all eight valence/inner-valence orbitals and sixteen electrons; RAS 3 included all the unoccupied orbitals with orbital energies up to 2 Hartree ($\approx$ 54.42 electronVolt). Up to one hole is allowed in RAS 1 while up to 2 electrons are allowed in RAS 3 to capture enough dynamic correlation. For cation species, RAS 2 included 15 electrons. For signals in the region of inner-valence/valence holes, a global shift of 7.2 eV is applied, while 9.8 eV shift is applied to the pre-edge region. The difference is due to the fact that the dynamic correlation is not fully recovered upon the frozen virtual approximation.

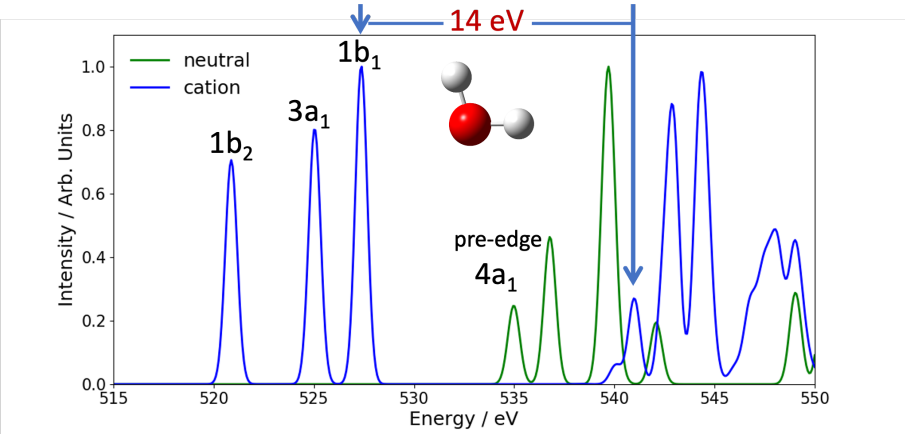

Figure C.2: Computed spectrum for water monomer.

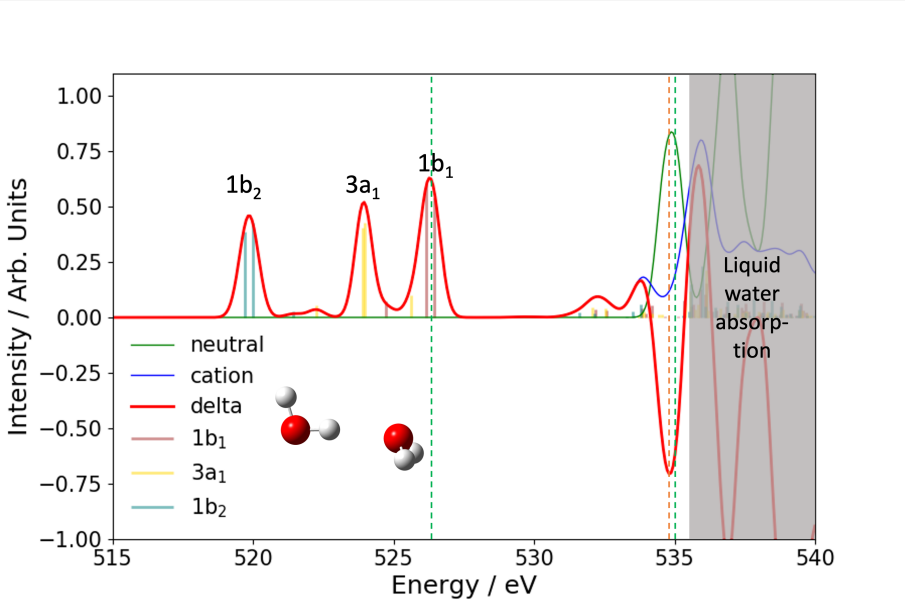

Figure C.3: Computed spectrum for water dimer with 1s core-hole from both water in our simulation.

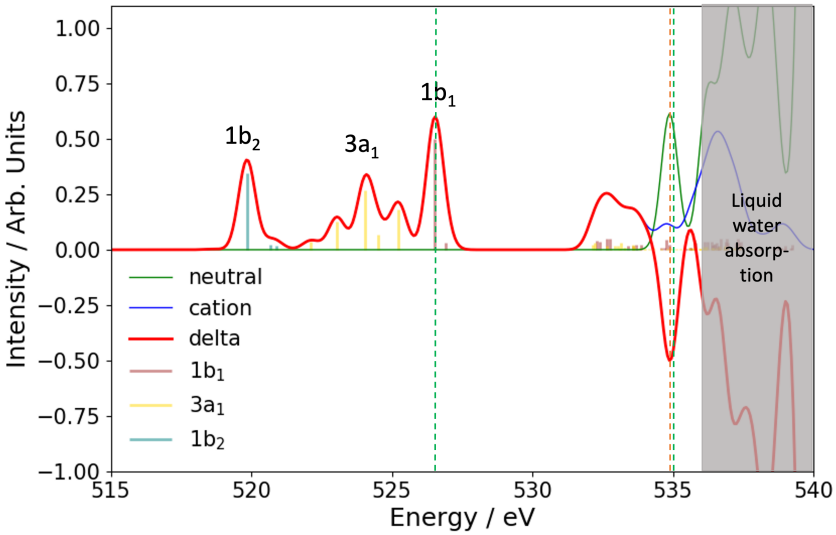

Figure C.4: Computed spectrum for pentamer with 1s core-hole from central water in our simulation. For signals in the region of inner-valence/valence holes, a global shift of 12.5 eV is applied, while 14.8 eV shift is applied to the pre-edge region.